DISSERTATION

EXPERIMENTAL INVESTIGATION OF AN ADVANCED ORGANIC RANKINE VAPOR COMPRESSION CHILLER

Submitted by

Alex Michael Grauberger

Department of Mechanical Engineering

In partial fulfillment of the requirements

For the Degree of Doctor of Philosophy

Colorado State University

Fort Collins, Colorado

Spring 2022

Doctoral Committee:

Advisor: Todd Bandhauer

Jason Quinn
Bret Windom
Sybil Sharvelle

ABSTRACT

EXPERIMENTAL INVESTIGATION OF AN ADVANCED ORGANIC RANKINE VAPOR COMPRESSION CHILLER

Thermally driven chilling technologies convert heat into cooling. These systems can support increasing cooling demands using waste heat in a variety of applications. Commercial thermally driven chilling technologies suffer from several implementation challenges, including high capital costs, limited equipment lifecycles, rigid working principles, and large physical formats, and thus are not implemented widely. Organic Rankine vapor compression cooling systems are a pre-commercial technology which can address the limitations of commercial alternatives. Organic Rankine vapor compression cooling systems couple an organic Rankine power generation cycle to a standard vapor compression chilling cycle. These systems can use benign, pressurized refrigerants as working fluids which allows for reduced heat exchanger costs over commercial thermally driven alternatives without environmentally impactful fugitive emissions. Refrigerants are released from cooling technologies during charging, leaking connections, and/or improper/unregulated disposal. Furthermore, the coupling of the two individual cycles allows the use of high-speed compression and expansion machinery as well as multiple methods of heat recuperation. High-speed fluid machinery and heat recuperation strategies reduce the format and cost of the technology while simultaneously improving the longevity and operational flexibility.

Current organic Rankine vapor compression efforts are limited from an absence of experimental validation. This study aims to fill this research gap through investigating a prototype organic Rankine vapor compression system enhanced with a high-speed, centrifugal turbo-compressor, sub cycle and cross cycle heat recuperation, compact heat exchanger technologies, and benign, next-generation refrigerants at an

industry-relevant scale of 300 kW. A thermodynamic model was created and a system heat-to-cooling coefficient of performance (COP) of 0.65 was simulated with 91°C liquid waste heat, 30°C condenser coolant, and 7°C chilled water delivery where a 5°C inlet to outlet temperature difference was specified for each stream. A full-scale prototype was fabricated and tested following standards for performance rating of commercial water chilling technologies to validate the performance simulation. Experimental testing of the prototype yielded a thermal COP of 0.56 and a cooling duty of 264 kW under its baseline operating conditions. The baseline test conditions were identical to the simulated conditions except the temperature difference across the condensers, which was 1.7°C greater due to a 25.6% lower condenser coolant flowrate. The lower condenser coolant flowrate, a vapor compression condenser refrigerant outlet vapor mass quality of 6.2% instead of the modeled 1°C of subcooling, and elevated system pressure losses limited the efficiency and cooling duty of the prototype over the simulated values. A scenario analysis on the test data was complete to show the prototype could surpass the simulated performance prediction with a COP of 0.66 at 300 kW of cooling if the operational limitations associated with prototype were corrected. This performance is competitive with commercial single-effect absorption systems and is possible because the turbomachinery efficiencies were high. The isentropic efficiency values for the turbine and compressor were 76.7% and 84.8% respectively at the baseline conditions during experimentation and the two devices had a 100% power transmission efficiency within experimental error.

Following the assessment of baseline performance, operational characteristics of the technology were quantified at off-design boundary conditions and normalized to those of the baseline to identify performance trends. It was shown that prototype thermal performance generally improved with increasing waste heat supply temperature, increasing chilled water delivery temperature, decreasing condenser coolant temperature, and decreasing chilling duty. These trends are consistent with performance simulations in literature. However, performance improvements at off-design operation were

often challenged by variations in turbine and compressor efficiency as well as the efficacy of heat recuperation strategies. Such changes to component performance characteristics at varying boundary conditions have not been previously quantified in practice and, thus, have historically been neglected in analytical investigations of organic Rankine vapor compression systems. Understanding the off-design component performance characteristics allows for the creation of validated organic Rankine vapor compression performance models. Such models will be critical to understanding the true energy savings potential of organic Rankine vapor compression systems as they are continuously investigated.

ACKNOWLEDGMENTS

First, I would like to thank Dr. Todd Bandhauer for advising me since I was first brought into his laboratory as an undergraduate intern. During my time at the REACH CoLab, I was fortunate to have the opportunity to contribute to a diverse set of research challenges. Dr. Bandhauer showed me how to approach each challenge with enthusiasm, persistence, and curiosity. I aspire to continue approaching challenges (in all areas of my life) as Dr. Bandhauer showed me, and to use the skills he fostered to pursue the toughest research challenges our society faces as my career continues to develop.

Regarding this research effort, the development and experimentation of the prototype would not have been possible without the support of my colleagues, specifically Derek Young. Derek was an invaluable asset at all stages of the project and was always eager to help me when I felt overwhelmed or unsure. Other lab members deserving of recognition are Christian Dahm, Ben Platt, Brandi Grauberger, Katie Plese, and Kaitlyn Baker for assisting in prototype fabrication, the calibration of instrumentation, and/or the collection of experimental data.

The prototype development effort also would not have been possible without the custom hardware produced by project partners Barber Nichols Inc. and Modine Manufacturing. Recognition is also given to the Office of Energy Efficiency and Renewable Energy of the United States Department of Energy for the financial support of the project under contract DE-EE0008325.

Finally, I would like to thank my family and friends for their support. A special thanks is owed to my loving wife, Kymbre Grauberger. Her unwavering support allows me to pursue (and sometimes accomplish) my wildest dreams. I cannot wait to see what other incredible adventures we get to share in as we continue to grow together.

TABLE OF CONTENTS

LIST OF TABLES

LIST OF FIGURES

LIST OF SYMBOLS

Symbol	*Description*	*Units*
A	Flow area	m^2
COP	Coefficient of performance	$kW\ kW^{-1}$
Cp	Specific Heat Capacity	$kJ\ kg^{-1}\ K^{-1}$
D	Diameter	m
Ds	Specific Diameter	-
E	Measurement uncertainty	var.
$\dot{E}$	Energy transfer rate	kW
EB	Energy Balance	%
FC	Heat exchanger fouling coefficient	-
FP	Heat exchanger fouling parameter	$m^2\ K^{-1}\ kW^{-1}$
g	Gravitational constant	$m\ s^{-2}$
G	Gravitational correction constant	$m^2\ s^2$
h	Enthalpy	$kJ\ kg^{-1}$
H	Refrigerant column height	m
Had	Isentropic enthalpy change across turbine or compressor	$kJ\ kg^{-1}$
k	Student T coverage factor for 95% confidence	-
$LMTD$	Log mean temperature difference	K
$Load$	Percent cooling load of the full-load value	%
$\dot{m}$	Mass flow rate	$kg\ s^{-1}$
N	Number of measurement variables	-
$NPSH$	Net positive suction head	m
Ns	Specific Speed	-
P	Absolute pressure	kPa
PLV	Part load value	-
$\dot{Q}$	Heat transfer rate	kW

R	Fluid gas constant	J kg^{-1} K^{-1}
s	Standard deviation	var.
SEE	Standard error of estimate	var.
T	Temperature	°C
$T\mathrm{A}$	Absolute temperature	K
U	Calculation uncertainty	var.
UA	Thermal conductance	kW K^{-1}
$\dot{V}$	Volumetric Flow Rate	m^{3} hr^{-1}
$\vec{V}$	Velocity	m s^{-1}
$\dot{W}$	Work transfer rate	kW
x	Unaltered measurement readout	var.
y	Calibration standard readout	var.
z	Corrected measurement readout	var.
Z	Compressibility factor	-

Greek

$\hat{\beta}$	Calibration factor	var.
δ	Scaling pressure coefficient	-
η	Efficiency	-
θ	Scaling velocity coefficient	-
ε	Heat exchanger effectiveness	-
ψ	Scaling expansion coefficient	-
γ	Ratio of specific heats (pressure to volume)	-
ρ	Density	kg m^{-3}
ω	Rotational speed	kRPM

Subscripts

0	Offset
1	Gain
#%	Relating to a percent chilling load for part load testing
abs	Relating to the absolute pressure transmitter
adj	Adjusted parameter

avg	Average parameter
B	Bias
cc	Cooling cycle
cc,#	Relating to a specific cooling cycle state point
ccond	Relating to the cooling cycle condenser
clean	Relating to a specific variable for fouling correction
cold	Relating to the lower quality thermal stream
comp	Relating to the compressor
condp	Relating to condenser loop pump
cor	Corrected for turbo-compressor performance mapping
cr	Critical
cs	calibration standard
EC	Electrical Equivalent
econ	Relating to the economizer
eg	Ethylene glycol water mixture parameter
eq	Equivalent
evap	Relating to the evaporator
ext	Relating to an external fluid stream
fract	Specified fraction of a total value
gen	Relating to the generator
high	Heat supply temperature
hot	Relating to the higher quality thermal stream
II	Second law
ILMTD	Relating to a specific variable for fouling correction
in	Relating to an inlet or input
low	Chilling delivery temperature
LMTD	Relating to a specific variable for fouling correction
max	Maximum
medium	Initial heat rejection temperature
o	total property including the effects of kinetic energy
ORC	Organic Rankine cycle

out	Relating to an outlet or output
P	Pressure based variable
pc	Power cycle
pc,#	Relating to a specific power cycle state point
pcond	Relating to the power cycle condenser
pinch	Pinch temperature
pump	Relating to the pump
r	Refrigerant parameter
R	Random
range	Relating to a specific variable for fouling correction
recup	Relating to the recuperator
ref	Reference condition
s	Outlet condition from an isentropic process
sat	Saturated vapor mass quality variable
sc	Subcooled liquid flow regime
sh	Superheated vapor flow regime
shaft	Relating to transfer efficiency of the turbo-compressor
slhx	Relating to the suction line heat exchanger
small	Relating to a specific variable for fouling correction
T	Total
test	Value from an experimental test point
TH	Thermal
tp	Two-phase fluid flow regime
tpsc	Two-phase fluid transition to or from a subcooled state
tpsh	Two-phase fluid transition to or from a superheated state
ts	Total to static
tt	Total to total
turb	Relating to the turbine
V	Velocity based variable
VC	Vapor compression cycle
w	Water parameter

Chapter 1 Introduction

1.1. Background

Climate change and globalization have created a growing demand for comfort cooling. The International Energy Agency projects the number of comfort cooling technologies will more than triple by 2050 from the stock in 2018 as outlined in Figure 1-1 [1]. The majority of this growth is dominated by developing nations such as India, China, and Indonesia where populations are purchasing a cooling technology for the first time. Considering the purchasing power of these nations, these cooling technologies will be less efficient and implement more environmentally harmful refrigerants than alternative commercially available systems.

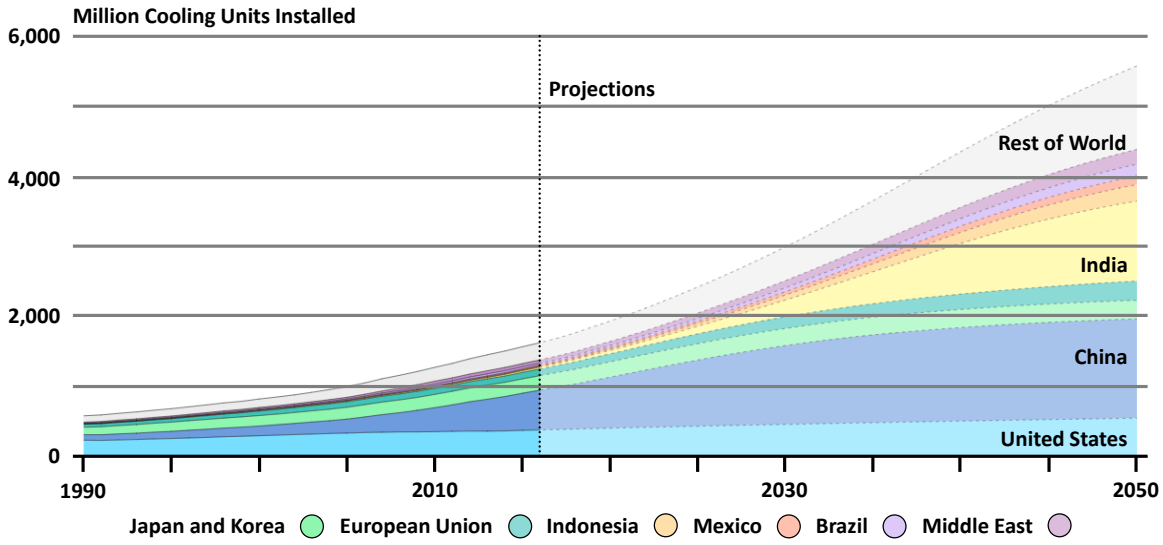

Figure 1-1 Global projection of installed comfort cooling technologies to 2050 (Adapted from [1])

The rapid adoption of inferior cooling technologies in developing nations over the upcoming decades will have a two-fold effect. First, developing regions must expand their already strained electric generation infrastructure to power the technologies. It is projected that an additional 4.18 trillion kWh, more energy than United States utilities produced in 2019, will be required for comfort cooling by 2050 [1,2]. This added energy generation will drastically increase the atmospheric release of carbon dioxide

and other greenhouse gases as China, Indonesia, and India are reliant upon inefficient, fossil fuel driven power generation methods that result in national emission factors (the ratio of carbon dioxide equivalent emissions released to electricity produced) surpassing twice that of the global average [3]. The second implication is that refrigerants implemented in the technologies have an appreciably greater environmental impact than the emissions from power production (per unit mass) when leaked during operation or released from improper disposal [4]. In fact, up to 26% of the emissions related to air conditioning are from the fugitive emission of refrigerants [5]. While a daunting feat to accomplish, these challenges could be curtailed with a combination of policy implementation and enforcement, technology development, and adoption of sustainable practices (an example of which is increasing thermostat settings by 1°C) as projected in Figure 1-2 [1].

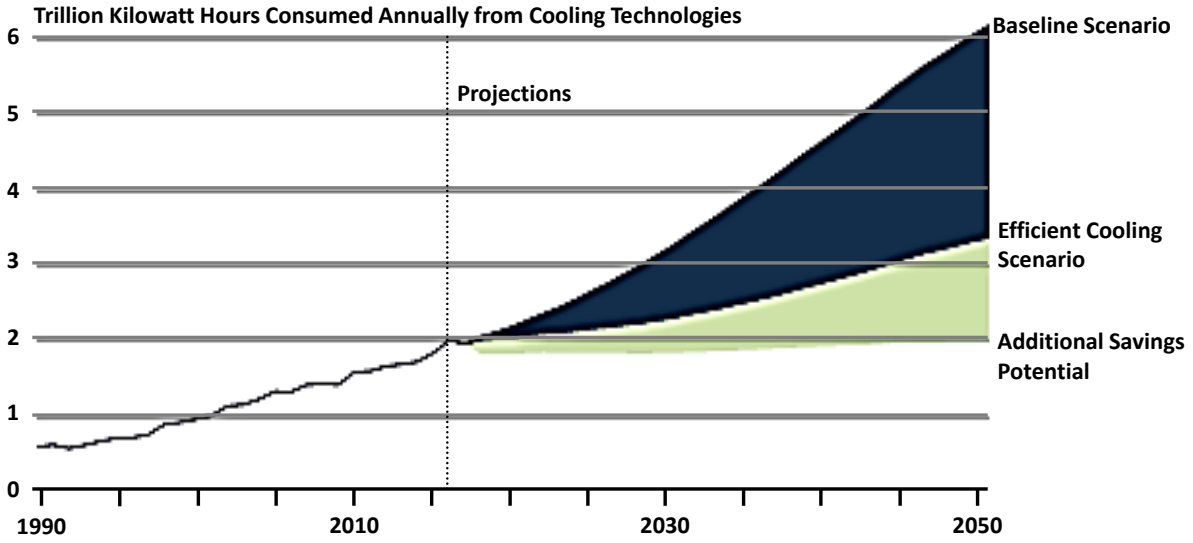

Figure 1-2 Estimated global generation capacity increases required to satisfy cooling demand to 2050 (Adapted from [1])

Current efforts by governmental and private sectors to mitigate challenges related to growing cooling demand have had a limited effect. More than 100 nations have vowed to reduce their usage of hydrofluorocarbon refrigerants and other potent greenhouse gases following the Kigali Amendment to the Montreal Protocol [6]. However, the full effect of this phasedown (with agreeing nations reducing

usage by 80%) will not be seen until 2047. Furthermore, there are inherent challenges with implementing and enforcing universal energy and climate policies, especially in developing nations [1]. In the private sector, philanthropic foundations and organizations have sponsored research and development efforts, commercialization activities, and installations of new or alternative sustainable cooling technologies [7–11]. While novel solutions are being investigated, the technologies required to meet future sustainability targets (including those already commercially available) are continuously disregarded for less expensive units. This is especially true in emerging economies where citizens are purchasing a cooling technology for the first time [1]. In order for an alternative cooling technology to viably address challenges related to growing global cooling demand, it must be inherently efficient, environmentally benign, and available at a cost point which is competitive with incumbent solutions.

While no singular technology will be capable of serving all climates and cooling applications, a promising technical solution capable of addressing numerous concerns related to global cooling demand is district cooling [1,12–17]. District cooling systems aggregate numerous cooling loads to a single, centralized plant which serves each load by pumping a chilled solution (typically water or a glycol brine) to each application through insulated piping networks as shown in Figure 1-3. Distributed cooling is generated using large industrial chillers, which are inherently more efficient than commercial, residential, and single room alternatives [1,18]. This improvement in efficiency can significantly reduce growing electricity demand and the resulting greenhouse gas emissions from space cooling. Also, because the district cooling plant is controlled by a utility or building manager, sophisticated operational strategies and sustainable practices (whether mandated through regulation or implemented independently) are easily adopted and verified to further increase energy efficiency and improve the economic viability of the technology [19]. In addition, district cooling systems are easier to monitor for leaks and are simpler to recover refrigerant from at the end of their useful life [20]. Refrigerant recovery and leak monitoring of centralized cooling plants is an important advantage of district cooling as lifetime leakages from single

room/apartment cooling technologies during operation, recharging, and improper (or unregulated) disposal can be as high as 170% the initial system charge [3]. Further benefits to district cooling systems include the lifecycle of their chilling technologies (up to three times greater than alternatives [20]) and their ability to be combined with local renewable energy resources, sustainable energy technologies, and energy storage systems to further reduce consumption of non-renewable energy and greenhouse gas emissions while increasing their resiliency [21].

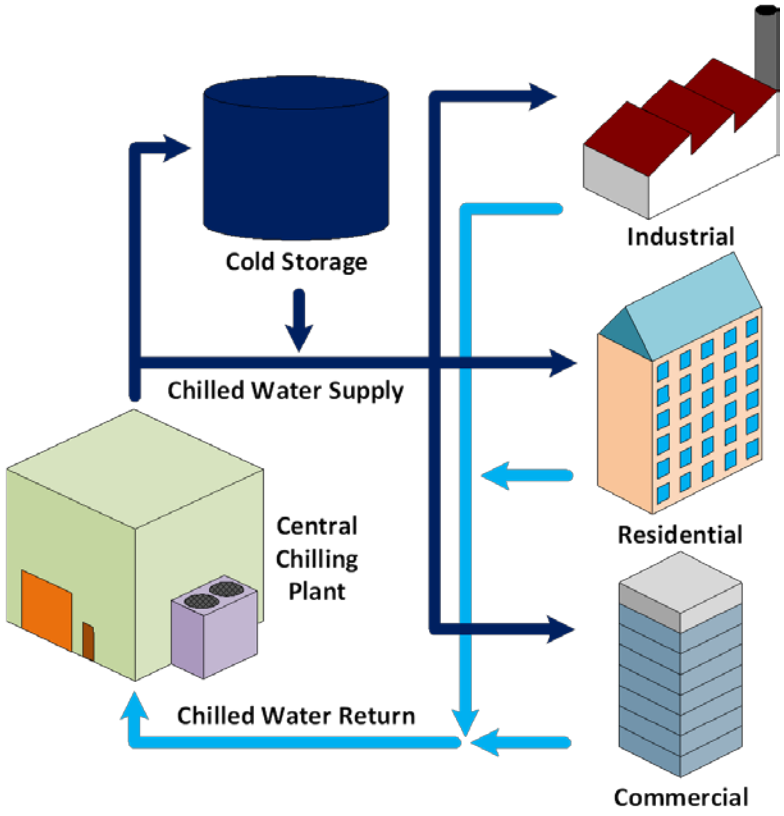

Figure 1-3 Typical layout of a district cooling system

A barrier to the adoption of district cooling systems is that they require extensive planning and construction to integrate with facilities. This makes retrofits into existing infrastructure very challenging and often too costly to pursue without subsidization [22]. However, this does not stifle the relevance of district cooling in developing nations. For example, up to 75% of the buildings required for the population projected for India in 2030 have yet to be constructed [12].

1.2. District Cooling Systems

The fundamental component of all district cooling systems is the chilling technology which satisfies the distributed cooling loads. Three primary chilling technologies are used in district cooling plants: electrical chillers, thermally driven chillers, and direct heat exchange systems [23]. Table 1-1 provides a general overview of these differing technologies for district cooling applications.

Table 1-1 General overview of district cooling chilling technologies (Adapted from [23])

Chilling Technology	***Energy Sources and Conversion Technologies***	***Challenges and Considerations***	***Benefits and Opportunities***
Electric Chiller	Energy Source: Electricity Conversion Technology: Electric chillers	• Requires reliable electricity • May not be competitive when electricity is subsidized to commercial and residential entities • Carbon emissions dependent upon energy source	• Despite utilizing electricity, are much more efficient than other residential and commercial air-conditioning units • Generally implement less environmentally impactful refrigerants than discrete electric solutions
Direct Heat Exchange System	Energy Sources: Natural or anthropic heat sinks Conversion Technologies: Heat exchangers and pumps	• Requires heat sink and cooling loads to be collocated • Could require backup cooling • Environmental permitting often required • Cooling availability may be seasonal	• Use of renewables results in low carbon emissions • Highly efficient utilization of electricity reduces peak demand • Most systems use no refrigerants
Thermally Driven Chiller	Energy Sources: Heat captured from wasted/renewable streams or generated from primary fuels Conversion Technologies: Absorption chillers, adsorption chillers, and steam turbine chillers	• Carbon emissions dependent upon heat source • Efficiency proportional to the quality (temperature) of heat available	• When combined with primary generators, production of electricity, heating, and cooling allows year-round operation • Peak electrical and cooling demand are matched when driven by waste heat from power generation sources • Most commercial solutions use environmentally benign refrigerants

Electric chillers for district cooling employ the vapor compression cycle shown in Figure 1-4. The distributed chilling stream is regenerated by rejecting the heat removed from network cooling loads to

vaporize a low temperature two-phase refrigerant mixture in the evaporator of the vapor compression cycle (1-2). This two-phase mixture is produced by rapidly depressurizing a liquid refrigerant through an expansion device (4-1). Once vaporized in the evaporator, the refrigerant is pressurized to the liquid refrigerant pressure using an electric compressor (2-3). The cycle is completed by liquifying this high-pressure vapor in a condenser (3-4) by rejecting heat to a lower temperature medium thus producing liquid refrigerant for expansion.

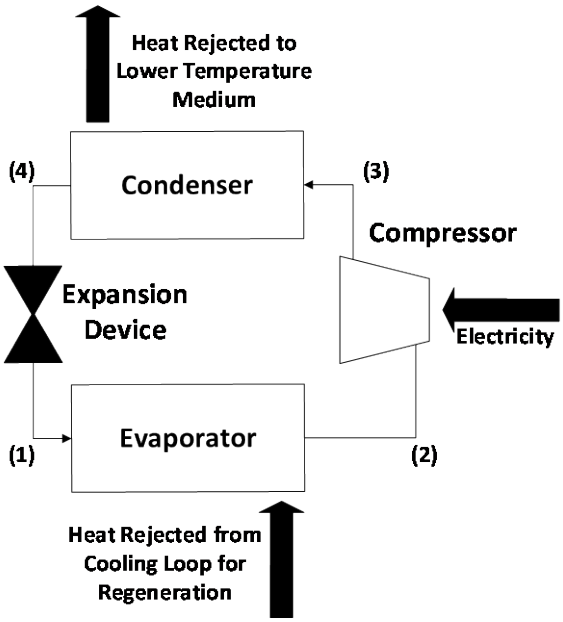

Figure 1-4 Process flow diagram of a standard vapor compression cycle for district cooling

Electric chillers are the most prolific chilling technologies for district cooling systems considering their reliability, simple operational strategy, and high efficiency [13]. While district chilling with electric chillers is around 50% more efficient than cooling with individual building, home, or single-room air-conditioning units [23], most electric chillers still operate using traditional refrigerants [24], and the cooling they deliver is only as sustainable and reliable as the electricity used to power them. Currently, the pairing of electric chilling with renewable power generation remains niche due to the high capital costs of renewable generation devices and discrepancies between peak cooling demand and peak renewable electrical generation [1].

Direct heat exchange systems for district cooling applications chill the water/brine for the distributed loads by rejecting the network cooling load to a thermal heat sink. Examples of such heat sinks include shallow geothermal wells, deep water from oceans, rivers, lakes or aquifers, and regasification points on natural gas pipelines [21]. When using the ocean as a heat sink, cool water at depths between 700 and 1,000 meters (where temperatures are near 5°C [25]) is pumped through a heat exchanger and returned to the ocean surface. The distributed cooling stream is cooled in the heat exchanger, but the ocean water is heated. Direct exchange chilling is the most sustainable option for district cooling systems as it uses no harmful refrigerants and requires only enough energy to overcome pumping losses in the distribution network. However, these systems require significant capital investment to interface the distribution network with the heat sink (between seven and sixteen times greater than alternative methods [26]) and are niche due to their geographic limitations.

The final technologies capable of satisfying district cooling loads are thermally driven chillers. Most thermally driven chillers use the same underlying thermodynamic cycle as electrically driven chillers (shown in Figure 1-4) to produce chilled water/brine for the distributed cooling network [27]. However, thermally driven chillers primarily use thermal energy (heat) to compress the refrigerant instead of electricity. Thermal compressors implemented on district cooling scale thermally driven chilling technologies include sorption-based compressors (solid (adsorption) and liquid (absorption) state), and heat engine driven compressors (steam turbine and organic Rankine cycle). The most prolific thermally driven chiller for district cooling applications is the absorption chiller implementing an environmentally benign working fluid pair of lithium bromide (absorbent) and water (refrigerant) [13]. Figure 1-5 presents the working principle of a simple absorption thermal compressor.

First, vapor refrigerant from the evaporator (1) is absorbed into an aqueous solution of the absorbent and refrigerant (2) in the absorber. This process releases heat which must be rejected. The solution leaves the absorber with a greater refrigerant concentration (3) where it is pumped to the

generator (3-4) using a pump. The pump consumes significantly less energy to pressurize the liquid mixture than a compressor would consume to pressurize the vapor leaving the evaporator. The high-pressure solution enters the generator (4) where it is heated. As the solution is heated, it releases vapor refrigerant thus dropping its refrigerant concentration. The generated vapor refrigerant is sent to the condenser (5) and the solution with a lesser refrigerant concentration is sent to a throttling valve (6). Throttling the solution (6-2) reduces its pressure such that it can absorb more refrigerant in the absorber.

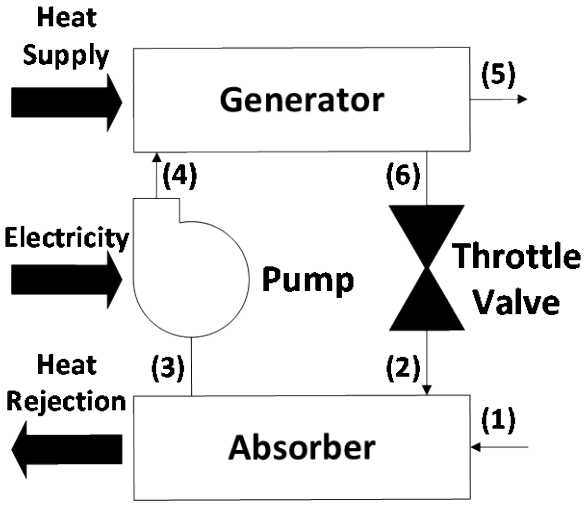

Figure 1-5 Process flow diagram of an absorption cycle thermal compressor

Thermally driven chillers can deliver practically emission-free cooling (when implementing benign working fluids) if operated using renewable or otherwise wasted heat supplies. Thus, thermally driven chilling-based district cooling networks could offer a sustainable solution to growing global cooling demand if the systems can be collocated with low emission heat sources. One viable waste heat source for thermally driven district cooling systems in the near term is exhaust and/or coolant from localized power generation technologies such as reciprocating engines or gas turbines [28–31].

1.3. Combined District Cooling and Power Generation

Coupling localized primary fuel driven generators with thermal energy distribution networks (including district cooling) is recognized as a sustainable energy solution in energy policies for both

developed and developing nations alike [32–37]. Such systems offer improvements to energy efficiency, resiliency, and security over grid scale power generation which is a sustained and significant source of waste heat. In 2019, 65% of the energy supplied to generate grid scale power in the United States was lost as waste heat during its conversion to electricity [38]. This translated to a total energy loss of 24.2 quads (~7.09 trillion kWh) as shown in Figure 1-6.

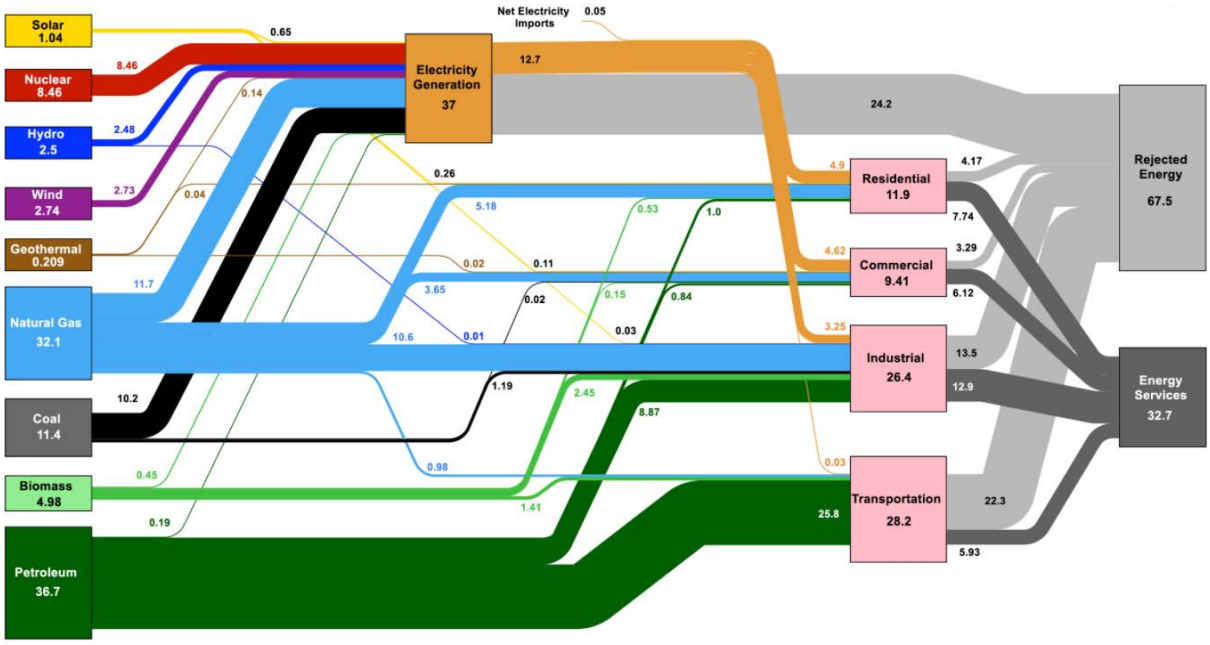

Figure 1-6 Estimated energy flow (quads) for the United States in 2019 (Taken from [38])

Shifting power generation from centralized to dispersed, localized infrastructure avoids this energy penalty by allowing the capture and utilization of waste heat. Figure 1-7 presents the energy flow diagram for a typical combined power generation and thermally driven-based district cooling network for localized energy distribution [39]. While the localized primary generation devices have slightly lesser electrical efficiencies than their grid scale counterparts, the capture and conversion of waste heat through thermally driven chillers overall improves their energy efficiency. Heat rejected from the combined system is a result of thermally driven chiller inefficiencies and limitations to the quantities of waste heat which can be captured from primary generation exhaust streams.

Combining localized power generation and thermally driven district cooling doubles the efficiency of power generation and is immediately capable of addressing challenges related to growing global cooling demand. However, the combined power and cooling systems have seen limited implementation despite their sustainable benefits and ability to reduce energy expenditures. In the United States, there are nominally 4,750 installations of localized power generation systems with waste heat capture [40]. Only 30% of the well documented projects (~70 installations) incorporate thermally driven chilling technologies while many of the remaining systems reject heat during summer months without capture [41]. The primary reason there is a limited number of combined localized power generation and thermally driven district cooling systems is that the available thermally driven chilling technologies are unable to generate sufficient energy savings to offset their prohibitive capital costs. Currently, only critical infrastructure and long-established entities with significant, consistent thermal and electrical loads can justify installing the combined energy system [42]. To proliferate the adoption of the proposed technology outside of institutional campuses, hospitals, and airports [43], a thermally driven chilling technology capable of serving district cooling demands must be developed for a cost competitive with incumbent technologies.

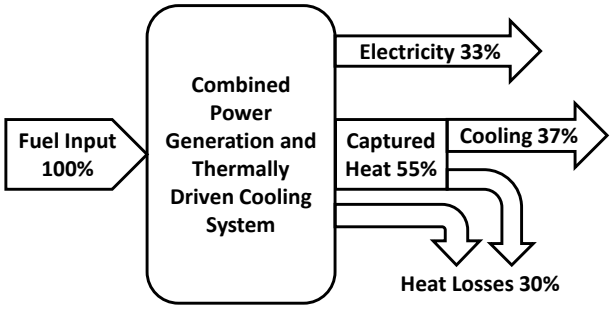

Figure 1-7 Energy flow diagram for a multi-generation system (Adapted from [39])

1.4. Research Objectives

The prohibitive cost of commercially available thermally driven chilling technologies has limited the adoption and proliferation of district cooling systems driven by waste heat from localized power

generation systems. The current study presents an experimental investigation of an alternative thermally driven chilling technology, organic Rankine vapor compression cooling, with the potential for cost and efficiency enhancements over the incumbent commercial solutions. An organic Rankine vapor compression system produces cooling using a vapor compression (cooling) cycle which is driven by mechanical energy created through a waste heat driven organic Rankine (power) cycle. The cooling and power cycles can be further integrated using advanced heat recuperation schemes to improve efficiency. This investigation is the first to experimentally assess the three primary organic Rankine vapor compression heat recuperation strategies presented in literature. The investigation is also the first to experimentally assess the technology at a scale and operating conditions relevant for district cooling applications. Furthermore, the technology used environmentally benign, next generation refrigerants as working fluids which has not been previously demonstrated. These working fluids reduce the environmental impact of the system and allow the use of compact equipment (aluminum brazed heat exchangers and high-speed turbomachinery) to further reduce the size, complexity, and, potentially, cost of the technology. The primary goals for this effort were to design, manufacture, and experimentally validate the operational and performance characteristics of the advanced organic Rankine vapor compression technology over a wide range of conditions relevant for district cooling applications. The learnings from this effort are intended to guide future organic Rankine vapor compression technoeconomic investigations and design studies to progress the technology towards a status where it is capable of addressing some of the challenges related to growing global cooling demand.

1.5. Dissertation Organization

This dissertation presents an investigation of a novel organic Rankine vapor compression prototype for district cooling applications. Chapter Two provides a comprehensive review of thermally driven cooling systems to identify the knowledge gaps addressed in this study. Chapter Three presents a baseline performance simulation of a novel thermally driven organic Rankine vapor compression cooling

system. The simulation spans boundary conditions, technical assumptions, results, and calculations verifying the adequacy of critical prototype components. Chapter Four presents the prototype system architecture and experimental methods used to quantify its performance. Chapter Five presents and discusses the experimental results and the associated implications. Lastly, the conclusions and recommendations for future research are given in Chapter Six. References cited throughout the text are listed in Chapter Seven. Several appendices are also provided with supporting information at the end of this document. Appendix A presents hand calculations to validate the performance simulation, which is also used in the evaluation of experimental data. Appendices B through E provide further details regarding the design, operation, and maintenance of the experimental system. Hand calculations used to validate the experimental data reduction methods are given in Appendix F.

Chapter 2 Literature Review

The preceding chapter outlined the demand for a technical solution to the rapid proliferation of cooling technologies in developing nations. One attractive solution, especially for near term urban development, is to pair thermally driven chilling-based district cooling networks with localized primary generation devices. This combined generation of cooling and electricity could sustainably satisfy the growing energy demands of developing nations in the near term and facilitate the adoption of purely renewable based district cooling systems in the future. However, the transition from discrete electric to centralized thermally driven cooling systems requires improvements to the cost and performance characteristics of thermally driven technologies over commercially available systems. The focus of this chapter is to review the status of thermally driven chilling technologies to identify a research and development pathway with the potential to yield significant advances for thermally driven chillers over the state of the art. This review will be guided by characterizing thermally driven chilling technologies capable of supporting district cooling applications by their working principle, efficiency, cost, and opportunity for improvement. Following this assessment, specific research gaps will be identified for the technology with the greatest potential, and the focus of the current research effort will be presented.

2.1. Overview of Thermally Driven Chillers for District Cooling

District cooling systems most often implement water cooled, electrically driven vapor compression chillers as their primary cooling technology [13]. These technologies are performance rated with condenser coolant inlet temperatures of 30°C while delivering chilling at 7°C [44]. Thermally driven chillers must be capable of operating at these conditions to proliferate their adoption into district cooling applications. Furthermore, thermally driven chillers must be capable of delivering their chilling duty through a liquid stream that can be readily distributed across a cooling network. Chilling duties for district cooling networks vary from 210 to 35,170 kW while it is estimated that the most cost effective district

cooling chiller capacity is 8,800 kW [45]. Lastly, the thermally driven cooling technology must also be capable of operating off waste heat sources of common primary generation devices which the technology would be paired with for the proposed application. The most common primary generation devices for localized power generation (~57% of installations [40]) are reciprocating engines which generate most of their waste heat in the form of coolant (from 88°C to 110°C) and exhaust (from 380°C to 540°C) [46]. Some reciprocating engines may also reject small amounts of heat from oil and charge air coolers.

The commercial state of the art thermally driven chilling technology used in district cooling applications is the absorption refrigeration machine. The basic working principle of an absorption chiller is shown in Figure 2-1. This cycle uses a condenser, expansion device, and evaporator much like a vapor compression system, but uses a thermal compressor in place of a traditional electric or mechanical compressor. The thermal compression begins in the absorber which contains a strong liquid mixture of the refrigerant and an absorbent (strong with absorbent). The vapor refrigerant leaving the evaporator is absorbed into this mixture to increase the liquid refrigerant concentration before it is pumped to a high pressure in the weak solution pump. The absorption process releases heat, and, therefore, the absorber must reject this energy to a lower temperature medium. After the weak solution (concentrated with refrigerant) is pumped to a higher pressure, it enters the generator where the heat is supplied to the system. Here, the heat added to the system vaporizes a portion of the refrigerant from the weak mixture to be sent to the condenser. The now strong mixture that remains is throttled to a lower pressure in the strong solution expansion device for the cycle to repeat.

The most viable working pair for use in commercial absorption chillers for district cooling applications is an environmentally benign working pair of lithium bromide (absorbent) and water (refrigerant) [47]. The other commercially available working pair is ammonia (refrigerant) and water (absorbent), which is better suited for chilling applications below 0°C or heat pumping [48]. Lithium bromide water absorption chillers are best suited for waste heat sources between 80°C and 120°C but can

utilize higher quality heat sources (from 120°C to 170°C) if multiple generators are integrated with the chiller [27]. Absorption chillers with two generators (double effect) have improved efficiencies over single effect units [49], but systems with three or more effects provide diminishing performance returns [50,51].

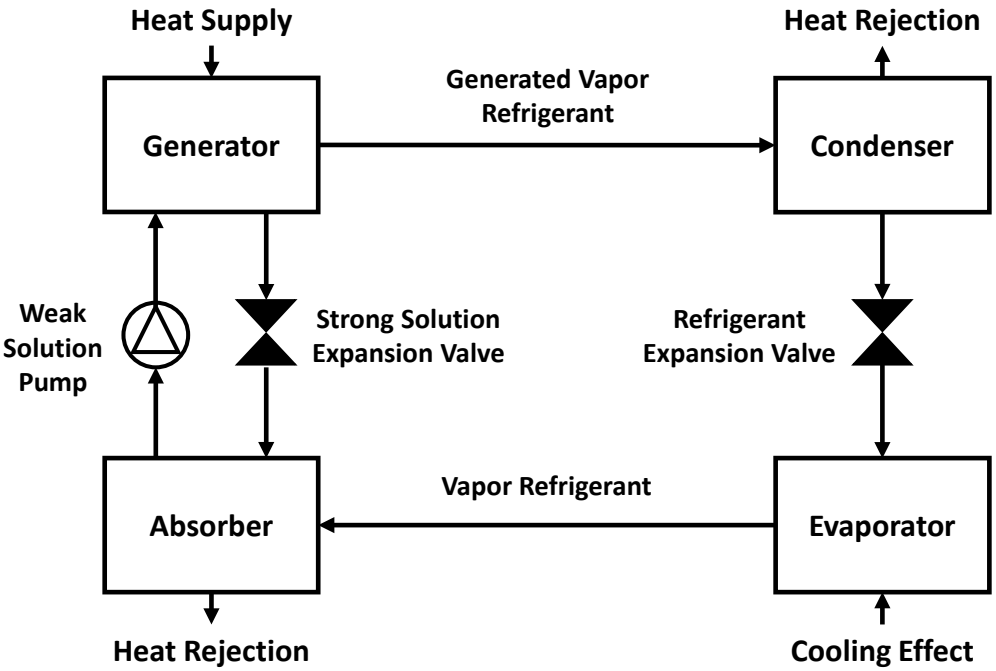

Figure 2-1 Working principle of an absorption refrigeration system

Another commercial thermally driven chilling technology for district cooling applications is adsorption refrigeration. The basic working principle of an adsorption chiller is shown in Figure 2-2. Adsorption systems work using a solid-refrigerant (adsorbent-adsorbate) pair to produce a cooling effect using heat. The cycle begins with the heating of an isolated solid sorbent bed saturated with refrigerant (V1 and V2 closed). As the bed temperature increases, it releases vapor refrigerant which pressurizes the bed. Once the condenser pressure is reached, the valve between the bed and condenser (V1) is opened. Heat is continually added to the bed to release additional vapor as the process is endothermic. Energy is rejected from the condenser to liquify the adsorbate where it collects in a liquid receiver. Once a minimum refrigerant concentration is reached in the bed, the bed is once again isolated (V1 and V2 closed) and heat

is rejected from the bed until it reaches the evaporator pressure. At this point, the valve between the bed and evaporator opens (V2) and liquid refrigerant in the receiver is allowed to flow through the expansion valve. Throttling of adsorbate to the evaporator pressure across the expansion valve converts the liquid to a low-temperature two-phase mixture. As this mixture evaporates in the evaporator, it removes heat from a process loop producing a cooling effect. The resulting vapor is then adsorbed in the bed until it once again becomes saturated with adsorbate. The bed continually rejects heat during this process as it is exothermic. At this point, valves V1 and V2 are closed, and the full cycle can repeat.

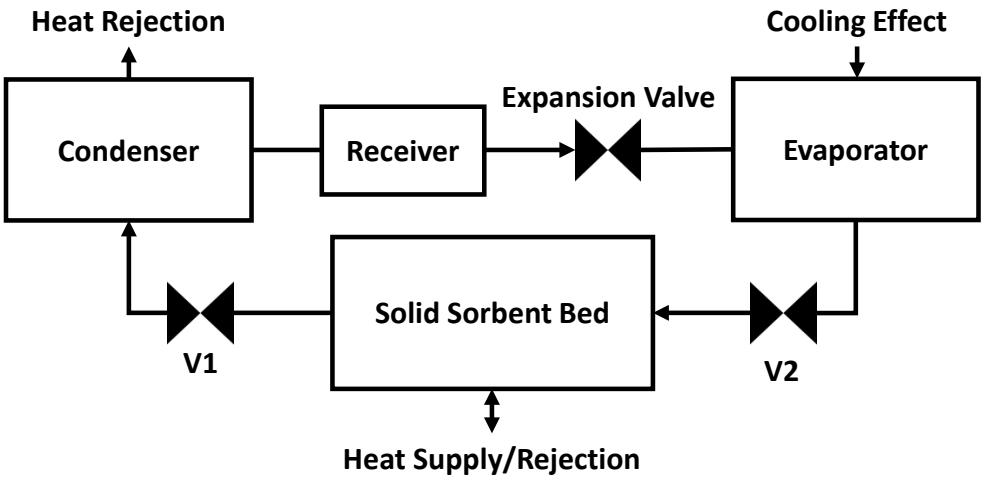

Figure 2-2 Working principle of an adsorption refrigeration system

The most viable working pair for use in commercial adsorption chillers for district cooling applications is an environmentally benign working pair of silica gel (adsorbent) and water (adsorbate) [52]. This working pair is best suited for waste heat sources between 60°C and 90°C [27]. To counteract their intermittent working principle, adsorption chillers typically have multiple solid sorbent beds in parallel [53]. When two beds are used, one bed desorbs refrigerant to the condenser while the other resorbs refrigerant from the evaporator. Multibed adsorption also allows for heat and mass recovery between beds which improves performance [54–57]. Three or more adsorption beds are required for continuous operation [58].

The final commercial thermally driven chilling technology for district cooling applications is steam turbine refrigeration. The basic working principle of a steam turbine chiller is shown in Figure 2-3. Simply put, this cycle consist of a commercial vapor compression chiller with its electric motor replaced by a steam turbine and a steam condenser stacked above its refrigerant condenser [59]. The energy supplied by the steam turbine is produced by expanding high pressure steam to translate the energy of the fluid to shaft power. Once expanded, the low-pressure steam is condensed, and either recycled to produce additional steam for expansion or rejected as grey water.

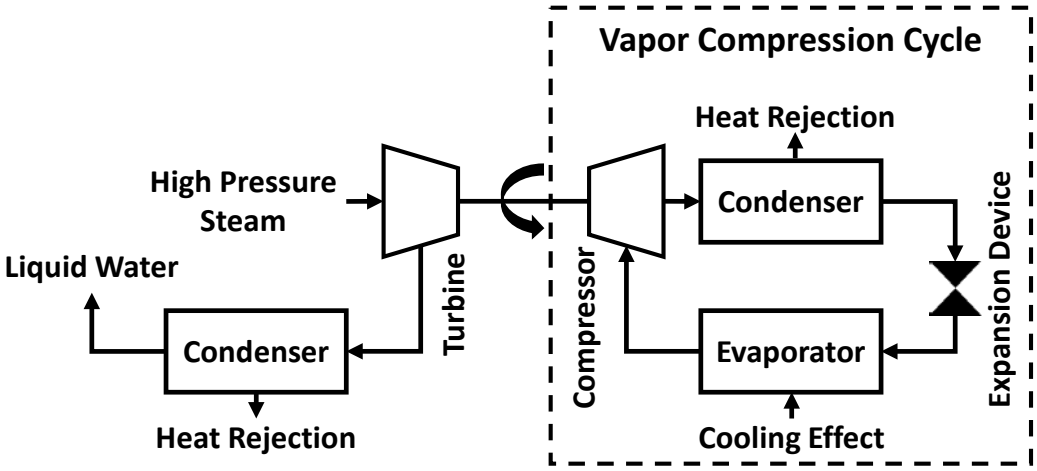

Figure 2-3 Working principle of a steam turbine refrigeration system

Currently, steam turbine chillers are only commercially available with R134a as the vapor compression cycle refrigerant [60]. These systems are best suited to consume steam between 95 kPa and 1,150 kPa that is superheated to temperatures reaching 315°C [61]. Increasing steam pressure and superheating increases the thermal performance of steam turbine refrigeration systems.

While a precommercial technology, organic Rankine vapor compression refrigeration is another thermally driven chilling technology which is viable for district cooling applications. The basic working principle of an organic Rankine vapor compression chiller is shown in Figure 2-4. Much like the steam turbine chiller, the organic Rankine vapor compression chiller drives a standard vapor compression cycle

using a vapor expansion turbine. However, the organic Rankine vapor compression cycle uses an organic working fluid for the turbine in place of steam. The use of an organic fluid requires the expanded vapor to be condensed, pressurized, and vaporized for expansion in a closed loop. If the same organic fluid is utilized in the organic Rankine and vapor compression cycle, a common condenser can be utilized to reduce system complexity.

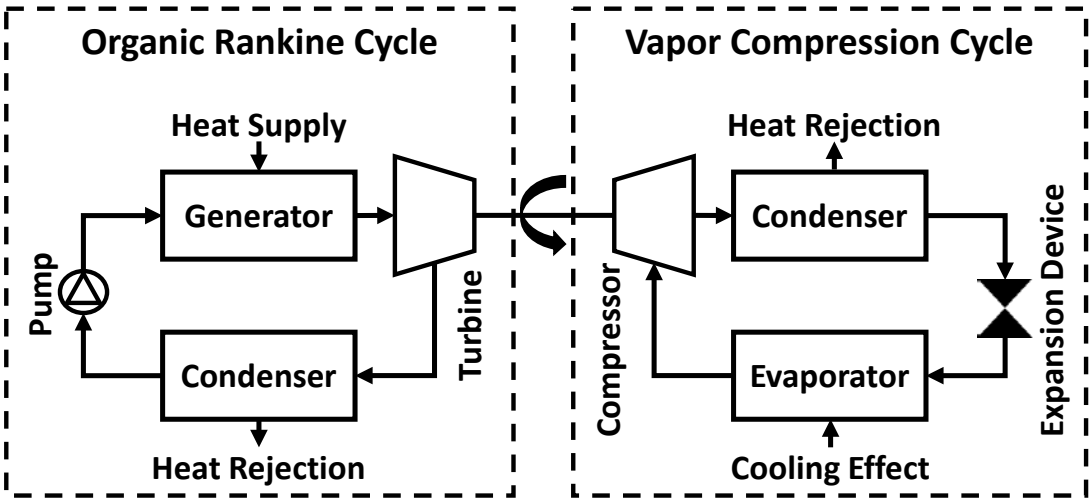

Figure 2-4 Working principle of an organic Rankine vapor compression refrigeration system

Organic Rankine vapor compression chillers can optimally perform at driving source temperatures between 60°C and 360°C, cooling supply temperatures as low as -5°C, and ambient temperatures as high as 67°C using various working fluids [62,63]. Other thermomechanical cycle driven chillers, including Stirling, Brayton, and Ericson, could also support district cooling applications but currently have unsolved technical challenges and are prohibitively costly compared to commercially available organic Rankine machines [64]. While similar to organic Rankine vapor compression refrigeration, ejector refrigeration systems are excluded from the comparison of thermally driven cooling technologies as they have rigid operational requirements and are incapable of providing the required chilling temperature at standard ambient conditions without disproportionally high driving temperatures and low efficiencies [65–70].

Desiccant systems are also excluded from further discussion as the working principle of solid and liquid based systems (which directly condition air) cannot readily support dispersed cooling applications [71,72].

2.2. Cost and Performance Comparison of Thermally Driven Chillers

The previous section presented several technically viable thermally driven cooling technologies which could be paired with localized power generation devices to deliver sustainable district cooling loads using waste heat. However, for district energy systems to be adopted over traditional solutions in expanding urban developments of rapidly growing nations, they must also yield a reasonable return on investment over traditional power purchasing agreements [73]. The initial (capital) cost and energy conversion efficiency of thermally driven cooling technologies are two of the primary variables which can be used to assess the economic viability of the proposed district energy system [74]. Historically, the combined cost and performance characteristics of thermally driven chillers have been the limiting factor to the proliferation of their adoption into district energy systems, and must be improved to facilitate an energy transition [42,43,75]. The cost and performance variables for the commercial thermally driven cooling technologies presented in the previous sections are listed in Table 2-1. Also listed are the ranges of capacities in which the technologies are available for purchase. Systems with larger capacities benefit from economies of scale and generally have superior efficiencies. For example, the relative capital cost of a single effect lithium bromide water absorption chiller increases 160% and its efficiency decreases 5.4% when its full scale capacity is decreased from 1,550 kW to 175 kW under similar operating conditions [76].

Table 2-1 Comparison of commercial thermally driven chilling technologies

Technology	***Working Fluids***	***Capacity [kW]***	***Capital Cost [$ kW^{-1}]***	η_{II} ***[%]***	***References***
Single Effect Absorption	Lithium Bromide/Water	35-7,000	548-1,826	21-31	[27,42,76,79]
Double Effect Absorption	Lithium Bromide/Water	20-11,630	609-1,004	26-38	
Dual Bed Adsorption	Silica Gel/Water	11-1,178	~906	19-24	[27,53,77]
Steam Turbine	Steam/R134a	2,100-9,850	582-959	26-29	[59,61,78]

Performance, cost, and capacity values presented in Table 2-1 were taken or derived from a number of sources [27,42,53,59,61,76–79]. The capital costs include installation but do not include the cost of the primary generation device and waste heat recovery system required to drive the chiller. The monetary values in Table 2-1 were scaled to fiscal year 2019 through the Chemical Engineering Plant Cost Index from *Chemical Engineering Magazine* and normalized by capacity for direct comparison [80]. As detailed in the previous sections, the presented commercial thermally driven cooling technologies require different driving sources to operate. It is well known that performance improvements to thermally driven cooling technologies are recognized by increasing the driving source temperature, decreasing the heat rejection temperature, or increasing the cooling delivery temperature. Thus, Table 2-1 reports the performance of each technology using the second law efficiency (η_{II}). This metric (Equation (2.1)) takes the ratio of efficiencies for a thermally driven chilling technology where the numerator is the true efficiency of the system and the denominator is its maximum theoretical efficiency. The maximum theoretical efficiency of a thermally driven chiller (Equation (2.2)) is derived using Carnot Principles and is solely dependent on the absolute source (high), initial heat rejection (medium), and cooling delivery (low) temperatures (*TA*) for a given technology [81]. The true and maximum theoretical efficiency used to assess second law efficiency is the thermal coefficient of performance (COP_{TH}), which is the ratio of the cooling energy produced by a system to the heat energy supplied.

Considering the comparison in Table 2-1, no commercial thermally driven chilling technology in its current state is clearly superior to the state of the art, single effect lithium bromide water absorption. While excluded from Table 2-1, results of recent analytical investigations into organic Rankine vapor compression chillers have also shown competitive cost [82,83] and performance [64] characteristics to the state of the art while experimental studies have demonstrated chilling duties approaching those required for district cooling [84]. These results were excluded to prevent an erroneous comparison between a precommercial technology and mature commercial solutions. As no technology shows clearly

superior cost and performance characteristics to the state of the art or has yet to be commercialized, further research and development efforts are required to bolster the economic viability of thermally driven chillers if they are to be integrated with traditional generation devices in district energy systems.

$$\eta_{II} = \frac{COP_{TH}}{COP_{TH,max}} \tag{2.1}$$

$$COP_{TH,max} = \frac{\left(1 - \frac{TA_{medium}}{TA_{high}}\right)}{\left(\frac{TA_{medium}}{TA_{low}} - 1\right)} \tag{2.2}$$

2.3. Opportunities and Challenges for Thermally Driven Chillers

The economic characteristics of thermally driven chilling technologies (combination of cost and performance) currently limit their adoption into district energy systems. Furthermore, opportunities to improve these characteristics are not equally distributed amongst technical options due to challenges with their differing working principles and levels of technical maturity. This section presents a deeper investigation into the thermally driven chilling technologies presented in the previous sections to determine which solution could best support an energy transition capable of addressing global challenges relating to cooling through continued research and development.

2.3.1. Absorption

As the commercial state of the art, there has been a substantial amount of research focused on improving the cost and performance characteristics of absorption chillers. As previously mentioned, the efficiency of absorption chillers can be increased using multi-effect generation strategies. Working principles of multi-effect generators (including series, parallel, and reverse parallel) are detailed in a study by Farshi et al. [49]. An alternative approach to utilizing a multi-effect generator is to implement multiple thermal compressors in series. Absorption chillers with two thermal compressors in series (or half-effect

absorption) can take advantage of lower temperature driving sources but have inferior real and second law efficiencies compared to single-effect systems. Performance comparisons of absorption generation strategies from half to triple-effect are presented by Gebreslassie et al. [50] and Maryami and Dehghan [51]. For the proposed application, altering the effect of an absorption chiller is not viable if doing so places the required driving temperature of the technology outside the range of values presented for reciprocating engine coolant streams. If the required driving temperature surpasses the coolant temperature, only a portion of the waste heat in the exhaust of the reciprocating engine can be utilized to drive the system. Alternatively, if the required driving temperature falls below the coolant temperature, the entirety of waste heat available in the coolant and a larger portion of the waste heat in the exhaust of the reciprocating engine can be utilized to drive the system, but at an efficiency penalty.

Another strategy to increase the efficiency of absorption chillers is to implement methods of heat recuperation. Figure 2-5 shows the most common methods of heat recuperation investigated in the literature for absorption chillers. Most commercial absorption chillers employ solution heat exchangers on each of their thermal compression stages. This heat exchanger preheats the weak solution entering the generator with the strong solution leaving, which benefits both the generator and absorber by reducing the thermal loads required to generate vapor and reject the heat of absorption respectively. In single effect systems, a solution heat exchanger can improve thermal performance as much as 44% [85]. Another heat exchanger used to increase the performance of an absorption chiller is a precooler (or refrigerant heat exchanger). This unit precools the refrigerant entering the primary expansion device using the vapor leaving the evaporator to increase the heat of vaporization available in the evaporator and, thus, the cooling duty. However, a refrigerant heat exchanger also increases the temperature of the vapor entering the absorber, which increases the absorber cooling load and negates most of its benefit [85,86]. While not technically a recuperative heat exchanger, a rectifier is implemented on some absorption systems to remove trace amounts of absorbent that vaporize in the generator with the refrigerant. The

cooling load required to accomplish this can be provided by the same medium as the absorber and condenser or from the weak solution before it enters the generator. The final common recuperation strategy is to employ a generator absorber heat exchanger. This device allows some of the heat of absorption to be used in the generation process when there is appreciable thermal overlap between the absorber and generator. This ultimately increases the heat input to the system and decreases the cooling required by the absorber. Efficiency improvements as high as 40% can be recognized using this strategy over a traditional single-effect system with a solution heat exchanger, but doing so requires specific fluid properties and operating conditions to recognize the benefits [87]. When using a generator absorber heat exchanger, the use of a refrigerant heat exchanger becomes more prevalent because the heat taken from the refrigerant prior to the primary expansion device can now be rejected to the generator instead of increasing the thermal loading of the absorber.

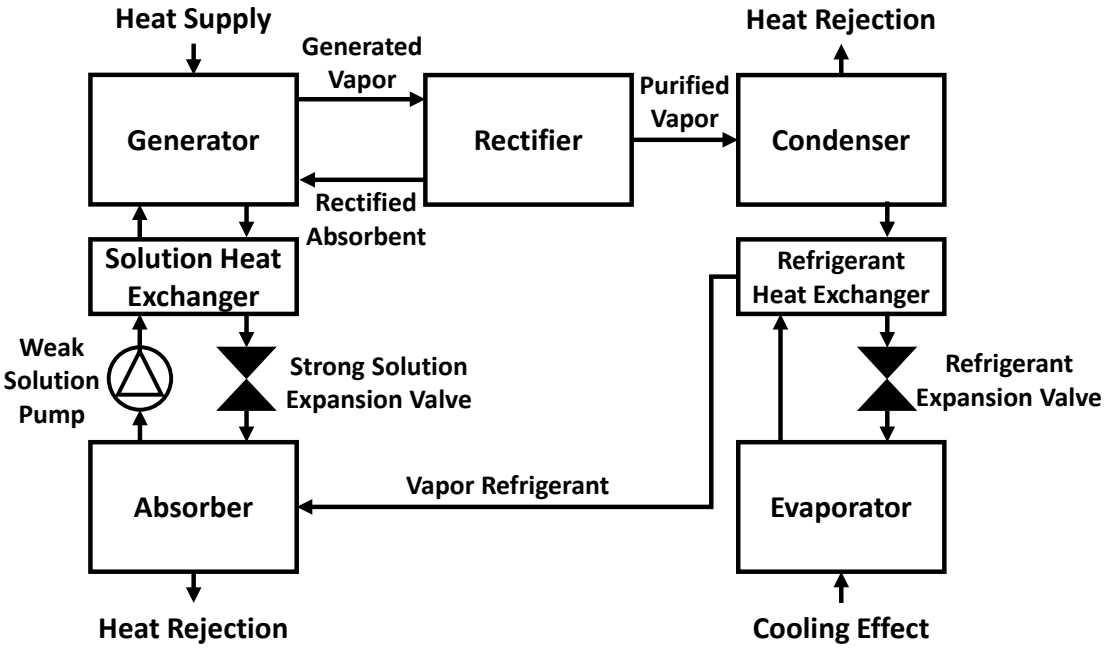

Figure 2-5 Methods of heat recuperation for absorption refrigeration systems

The performance of an absorption refrigeration cycle not only depends upon its configuration, but also the thermophysical properties of its working fluid pair [88]. The two most common mixtures used

in commercial absorption refrigeration devices are ammonia water (where ammonia is the refrigerant) and lithium bromide water (where water is the refrigerant). While both working pairs have negligible environmental implications, finding suitable alternatives to them has been a significant focus of absorption refrigeration research and development efforts due to their inherent challenges [47]. Ammonia and water as an absorption working pair can effectively utilize a generator absorber heat exchanger but requires rectification, is toxic, corrosive to copper, mildly flammable, and, as previously mentioned, better suited for chilling applications below 0°C or heat pumping. Lithium bromide and water as an absorption working pair has no safety concerns and is non-volatile (rectification is not required) but operates under vacuum, is prone to crystallization, expensive, and highly reactive. Vacuum based chilling technologies are prone to contamination from air ingress and require larger piping networks and heat exchangers due to a heightened intolerance to pressure loss [89]. Larger components not only increase the physical size of the system, but also the cost.

Alternative absorbents for absorption chillers are categorized as either ionic liquids, inorganic salts, or organic compounds [90]. Inorganic salt absorbents, like lithium bromide, have been heavily investigated due to their simplicity. However, due to their similarities, these absorbents have many of the same challenges associated with them as lithium bromide. One promising alternative to lithium bromide for low temperature applications is lithium chloride, which is slightly less prone to crystallization [91–95]. Alternatively, ionic liquids are low-temperature molten salts which, when they replace inorganic salts as the absorbent in absorption working pairs, eliminate the possibility of crystallization and reduce the risk of side reactions. Like lithium bromide, ionic liquids are generally non-toxic and are non-volatile. However, ionic liquid based working pairs have high viscosities (resulting in greater pumping energy consumption and heat exchanger pressure loss) and are more costly than inorganic salt and organic based working pairs [90]. Furthermore, a performance comparison by Khamooshi et al. showed no ionic liquid-based working pairs yield recognizable efficiency improvements over lithium bromide water at comparable operating

conditions [88]. Lastly, working pairs based off organic molecules have received increased attention due to several advantages they have over ionic liquids and inorganic salts including: an avoided risk of corrosion and crystallization, lower relative cost, minimal toxicity, an ability to operate at lower driving temperatures with moderate pressures, possibility to cool below 0°C, and lower viscosities [96]. Some of the working pairs investigated show promising thermal efficiencies to lithium bromide water, especially at lower driving temperatures, but are based upon flammable, toxic, or high global warming potential compounds. Some researchers have begun investigations into absorption working pairs which combine ionic liquids with hydrofluoroolefins (next generation, low global warming potential refrigerants) which show promising results for low temperature applications [97–99].

Despite its technical challenges and hundreds of investigated alternatives, lithium bromide water remains the most popular absorption refrigeration working pair due to its superior performance characteristics [47]. As no alternative working pair has been performance competitive with lithium bromide and water, other researchers have focused their efforts on mitigating the challenges associated with its use. One of the primary challenges associated with lithium bromide water is the possibility of crystallization. Crystallization is an event where solid lithium bromide precipitates out of the aqueous working pair when its concentration exceeds the solubility limit, which is both pressure and temperature dependent. Crystallization results in significant performance degradations, and, if severe enough, can decommission an absorption chiller by clogging its piping. This phenomenon is most prone to occur at the exit of the strong side of the solution heat exchanger where the solution with the highest absorbent concentration is at its lowest temperature. A technology review by Wang et al. details operational modes that cause crystallization and control strategies (self-decrystallization, over-concentration, evaporator pressure, and process water flow) to prevent its occurrence [100]. Another proven strategy to mitigate crystallization is to add ethylene glycol to the aqueous solution of lithium bromide and water, which increases the crystallization threshold of the system by ~10% without greatly impacting its

thermodynamic performance [101]. With these considerations, crystallization now most often results from a loss of system controls or vacuum pressure due to air ingress or gas generation from side reactions between lithium bromide and process equipment [100,102]. To mitigate the risk of crystallization and side reactions between lithium bromide water and process equipment (which are exacerbated in the presence of air), modern lithium bromide water absorption chillers are factory equipped with purging mechanisms that trap non-condensable gasses in the system for removal via an external vacuum pump [102]. Some manufacturers have also recently implemented titanium generators, copper-nickel alloy condensers, and stainless-steel solution heat exchangers into their lithium bromide water absorption chillers to further reduce the risk of side reactions and improve system longevity [103].

After reviewing the developments into absorption technology presented in the literature, opportunities to improve the economic viability of the technology for the proposed application are confirmed to be limited by its technical maturity [42]. Some recent advances, such as tailoring absorption chillers to operate at higher or lower temperatures with novel working fluid pairs and various generation strategies, are irrelevant for the waste heat sources most prevalent within district energy installations. Other advancements which sacrifice capital cost for improved longevity generally yield no net benefit to overall economic characteristics [74]. Considering cost to performance compromises and the limitations of the underlying technology, absorption systems integrated with compressors [104–107] and ejectors [108–111] or hybridized with other technologies [47,105,106,111–114] were not detailed in this analysis. While outside of the scope of this investigation, there is ongoing research into utilizing absorption cycles for heat pumping, heat transformation, and dehumidification [115–118]. The relevance behind this research is that gas-fired absorption heating systems have considerably higher fuel to heating efficiencies (often surpassing 100%) than traditional gas fired boilers and water heaters which helps overcome their prohibitive costs [119]. These efforts, as well as those allowing absorption cycles to operate at lower driving or higher rejection temperatures, appear to guide most of the recent absorption cycle

developments. With these considerations, absorption chilling will be excluded from further investigation for the proposed district energy application.

2.3.2. Adsorption

As a less mature technology, research into adsorption chillers has largely focused on improving the economic characteristics of the technology through addressing its technical limitations. As mentioned previously, the intermittent working principle of adsorption technology requires a chiller to have a minimum of three solid sorbent beds to deliver a continuous cooling duty. This severely limits the economic viability of adsorption chillers as their beds require a large mass of sorbent, which is both costly and difficult to integrate into a compact packaged system [120]. Thus, a considerable number of studies seek to improve the uptake characteristics (capacity, variation in uptake, and specific cooling energy) of adsorption chiller working pairs to reduce the mass of sorbent required for a multi-bed system. Uptake capacity (mass adsorbate held per mass adsorbent), variation in uptake (uptake capacity at saturated adsorption less that at complete desorption), and specific cooling energy (cooling energy per mass adsorbent) are tailored by altering both the physical and chemical properties of an adsorbent.

Regarding chemical properties, adsorption chilling working pairs fall into one of three categories: physical working pairs, chemical working pairs, and composite working pairs [121]. Physical adsorbents uptake refrigerant through van der Waal forces [122]. These weak, intermolecular forces allow physical sorbents to release refrigerant at relatively low temperatures (as low as 50°C), but require a large, interconnected surface area throughout their microstructure to attract and hold onto refrigerant [123]. Chemical adsorbents bond to refrigerant through a chemical reaction (electron transfer, atomic rearrangement, and/or bond rupture/formation) on the adsorbent surface [124]. These chemical reactions require more time and energy transfer than van der Waal adsorption but allow chemical adsorbents to have superior uptake capacities to physical adsorbents. Composite adsorbents combine

chemical and physical adsorbents to improve performance over chemical or physical adsorbents alone. Adsorbents can be composited through simple mixture (blending grains of different adsorbents), impregnation (dissolving the chemical adsorbent in a solution to transport it to cavities within the physical adsorbent where it is deposited by drying the solution), and consolidation (compressing mixed or impregnated composites into a more compact form). As with absorption working pairs, a substantial number of adsorption pairs have been investigated for use, but only a few of the most common pairs are utilized in commercial devices due to their dependable performance and cost effectiveness [125]. The most common working pairs are silica gel/water, activated carbon/methanol, activated carbon/ammonia, zeolite/water, and activated carbon and metal chloride composite/ammonia [126]. Of these, silica gel/water is best suited for district cooling due to the high cost and required driving temperatures (200°C to 300°C) for zeolite, the inferior uptake characteristics of activated carbon, and the properties of ammonia and methanol which are best suited for cooling applications below 0°C [53]. Other common refrigerants such as hydrofluorocarbons, hydrochlorofluorocarbons, and hydrofluoroolefins are not widely investigated due to their poor uptake characteristics [121]. Much of the current research regarding adsorption chiller working pairs is focused upon metal organic frameworks (a relatively new physical sorbent with favorable uptake characteristics) and composited materials to improve their hydrothermal stability, manufacturability, and cost competitiveness [127].

The favorable uptake characteristics of metal organic frameworks for adsorption chilling are a result of the high surface area of the material (as high as 5,500 $m^2 g^{-1}$ [123]). Other physical properties of adsorbents (including size, shape, and packing) can also be optimized to improve uptake characteristics. The simplest solid sorbent bed design, and worst performing, consists of granular, fibrous, and/or pelletized sorbent packed around tube bundles which transfer heat to/from the bed. Heat transfer resistance to/from the sorbent greatly affects the thermal performance of adsorption chillers [128]. As heat transfer resistance increases, greater reaction times and/or quantities and qualities of energy are

required for refrigerant uptake and release. Heat transfer to a sorbent bed can be improved using extended surfaces or heat pipes over traditional tube bundles, compressing sorbent or mixing it with metallic grains, and/or adhering sorbent to heat transfer surfaces [129–132]. Other important properties are those which prevent sorbent cracking and agglomeration as and adsorption bed cycles [128]. Cracking increases the heat transfer resistance of a sorbent bed while agglomeration increases its mass transfer resistance (which has a similar effect to increased heat transfer resistance). While research into bed design and the physical properties of sorbents has reduced cycle times, there has yet to be a significant breakthrough which simultaneously reduces the size and cost of solid sorbent beds for adsorption chillers [91].

An alternative approach to increase the economic viability of adsorption chilling is to improve its efficiency through cycle design optimization. As previously mentioned, adsorption systems with multiple adsorbent beds can see efficiency improvements with heat and mass recovery. Mass recovery for adsorption chillers requires a mass recovery valve between two solid sorption beds. When one bed is at its minimum adsorbate concentration (condenser pressure), the other is at its maximum concentration (evaporator pressure), and both beds are isolated from the rest of the cycle, the mass recovery valve is opened for a brief period to stabilize the pressures. Reducing the pressure in the minimum concentration bed and elevating it in the maximum concentration bed reduces the thermal loads required to set the pressure in each bed for the next cycle and reduces cycle time. This, however, is at the slight expense of some mass transfer between the two beds requiring slightly more adsorbent and adsorbate in each bed to maintain capacity. Alternatively, heat recovery between beds uses a closed fluid loop to reduce the thermal loads required to simultaneously desorb one bed while a parallel bed is resorbing. The fluid loop transfers the exothermic heat of adsorption from the resorbing bed to the desorbing bed and the endothermic heat of desorption from the desorbing bed to the resorbing bed. The heat source of the system is integrated into the fluid loop after the resorbing bed (before the desorbing bed) while the heat

sink of the system is integrated after the desorbing bed. When the desorbing bed is at its minimum concentration and the resorbing bed is at its maximum, the flow direction of the fluid loop is reversed for heat recovery during the next sorption cycle. Both heat and mass recovery are already incorporated into commercial adsorption chillers and their implications to performance are represented in Table 2-1. An adsorption cycle diagram illustrating heat and mass recovery is shown in Figure 2-6 where Bed A is desorbing, and Bed B is resorbing.

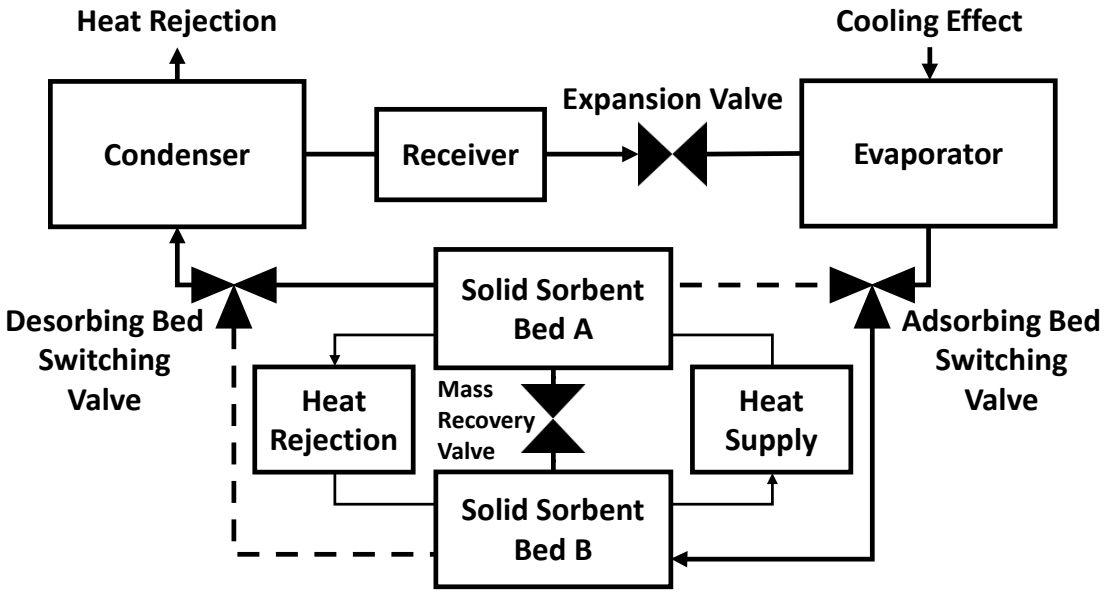

Figure 2-6 Cycle diagram of an adsorption chiller with heat and mass recovery

One idealized form of heat recovery, which has yet to be demonstrated in practice [129], is thermal wave adsorption chilling. A recent review by Alahmer et al. details several design renditions of thermal wave technology which computationally show highly competitive efficiencies over other thermally driven chillers by transferring 100% of the heat of adsorption to the desorbing bed and 100% of the heat of desorption to the adsorbing bed [133]. While thermodynamically feasible, this mode of operation would only be possible if the beds desorbed/adsorbed adsorbate isothermally, had negligible heat capacities, and were adiabatic parallel to the flow direction of the heat recovery loop [134]. Similar to absorption studies, other methods of performance improvement to adsorption systems presented in

literature appear superfluous for the proposed application considering the performance and cost limitations of the underlying cycle. These include cascaded adsorption [129,133,135], compression adsorption [136], desiccant adsorption [137], ejector adsorption [138,139], and thermoelectric adsorption [140].

Considering the challenges related to the working principle of adsorption chillers, further research into the technology for the proposed application is unlikely to yield significant improvements to its economic viability. From this investigation, the trajectory of adsorption chiller research is currently aimed to improve the cost and longevity of high-performance sorbents like metal organic frameworks and to demonstrate the practicality of advanced operationally strategies such as thermal wave. Considering thermal wave adsorption could be demonstrated and reliable, high-performance sorbents could be developed cost effectively, it is unclear that the economic characteristics of the resulting adsorption technology would surpass those of the current commercial state of the art. Thus, adsorption chilling will be excluded from further investigation for the proposed district energy application.

2.3.3. Steam Turbine

Research directly into steam turbine chillers is largely limited in peer reviewed literature. However, the steam turbines, steam condensers, and vapor compression chillers which combine to form a steam turbine chiller are highly mature technologies individually. Currently, the cost of vapor compression chillers is approximately \$500 kW^{-1} at a scale of 2,100 kW [80,141]. Considering the cost of steam turbine chillers presented in Table 2-1 (\$582 to \$959 kW^{-1}), anywhere from 14% to 48% of the technology cost is attributed to the steam turbine and steam condenser. The cost of the steam turbine is largely independent of the chiller capacity due to its significant machining requirements [59]. This is one of the reasons steam turbine chillers are not commercially available at the lower range of capacities relevant for district cooling. Thus, there is significant opportunity to improve the economic characteristics

of this system if the turbine could be optimized for cost. During this optimization, the performance of the turbine could be adjusted to better suit the operating conditions of vapor compression chillers with environmentally benign working fluids. Currently, commercial steam turbine chillers are only available with R134a as the working fluid in the vapor compression cycle, which is now a controlled refrigerant under the Kigali Amendment to the Montreal Protocol [142].

A challenge obstructing the design optimization of steam turbines for steam turbine chillers is that their operating conditions and physical construction largely effect their efficiency [143]. As a working fluid, steam has a relatively low density (resulting in significant volumetric flow rates) and molecular weight (resulting in substantial energy release as it is expanded [144]). Thus, in order to speed match the compressor, steam turbines on steam turbine chillers must have multiple stages with large diameter blades to maintain efficient operation [145]. For Johnson YST steam turbine chillers, as many as seven expansion stages are used to balance speed, volumetric flow, and energy release [78]. A turbine with a greater rotational speed could operate efficiently with a smaller form factor and fewer expansion stages but would adversely affect the performance of the compressor [143].

In addition to limiting turbine design optimization, the use of steam presents several technical challenges that limit the economic viability of steam turbine chillers. As a wet fluid, steam expanded through a turbine has the potential to form liquid droplets in the process stream which can erode the final blade stages of the device. Eroded turbine blades reduce performance and upset the balance of the machine. Mineral deposition within the turbine has a similar effect as erosion and is a result of impurities in the working fluid. These impurities enter the system through water makeup which is required even if steam is recycled to the turbine in a closed loop [145]. Both erosion and mineral deposition are mitigated through sufficiently superheating the steam prior to its expansion. To further mitigate the risk of mineral deposition, the working fluid is treated with filters, coagulants, softeners, demineralizers, deaerators, and chemical dosing units prior to entering the system [146]. Despite these precautions, degradation of the

steam turbine is inevitable and generally requires the unit to be replaced at least once throughout the lifecycle of a steam turbine chiller [147,148]. Another component susceptible to replacement is the steam condenser, which can be corroded from air ingress [147]. Air ingress at the steam condenser is possible as it operates under vacuum (~10 kPa absolute [61]) to improve turbine performance. This challenge is mitigated in commercial systems through purging the condenser with a vacuum pump. As previously mentioned, a chilling technology operating under vacuum has a heightened intolerance to pressure loss and requires larger, costlier components. Thus, there is also a limited opportunity to optimize the design of the steam condenser.

Opposed to the alternative thermally driven chilling technologies investigated in this chapter, steam turbine chillers cannot directly consume waste heat from reciprocating engines. Instead, waste heat must first be converted to steam using waste heat boilers or heat recovery steam generators [149]. These devices require as many as three heat exchangers to efficiently preheat, vaporize, and superheat steam considering the large difference in fluid density between saturated states [145]. Furthermore, much like multi-effect absorption chillers, the steam generation technologies require waste heat at temperatures surpassing the range of values presented for reciprocating engine coolant streams.

Steam turbine chillers were initially found to be cost and performance competitive with the commercial state of the art in the comparison presented in Table 2-1. However, further investigation revealed several considerable hidden costs associated with the technology and a limited opportunity to improve its economic characteristics. These hidden costs and limitations are consequence of using steam as a process fluid. While steam turbine chillers will be excluded from further investigation, it is recognized that a similar system using a working fluid alternative to steam could overcome the limitations and avoid the hidden costs to yield competitive economic characteristics for the proposed district energy application.

2.3.4. Organic Rankine Vapor Compression

Organic Rankine vapor compression chilling is a precommercial thermally driven chilling technology which may be capable of addressing the challenges of steam turbine chillers while capitalizing on their opportunities for improved economic characteristics over the state-of-the-art alternative. From a technical perspective, organic Rankine vapor compression chillers operate similarly to steam turbine chillers with closed loop steam recycling. However, the use of an organic fluid as a working fluid over steam in the sub cycle driving the turbine fundamentally changes the characteristics of the technology. For example, organic molecules have greater molecular weights and vapor densities than steam, which allows organic Rankine expanders to have fewer expansion stages and smaller formats without prohibitive speeds or reduced efficiencies. Organic molecules also have a lower latent heat of vaporization and critical temperature than steam which reduces the irreversibilities of heat transfer in the generator [144,150]. Regarding the generator, organic molecules maintain a similar density as they are vaporized, which allows the generator to be a single heat exchanger. Opposed to steam, organic molecules can be selected to have moderate saturation pressures in the condenser of the driving cycle to reduce its sizing requirements and risk of air ingress over a condenser operating under vacuum. Furthermore, organic molecules are chemically pure, and most are either dry or isentropic. Such fluids eliminate the risk of liquid droplet formation and sediment deposition within the turbine which can more than double its useful life over a steam device [151]. Lastly, organic molecules vaporize at lower temperatures than steam which allows an organic Rankine vapor compression chiller to utilize both exhaust and coolant waste heat from a reciprocating engine generator.

While the use of organic molecules in organic Rankine vapor compression chillers largely address the technical limitations of steam turbine chillers, the consequences of their implementation must also be considered. As liquids, organic molecules have lesser densities and greater viscosities than water, which increases pumping power demand, system pressure losses, and heat exchanger sizing requirements

[145,152]. Pressure loss effects and heat exchanger sizing requirements can be minimized through selecting a higher-pressure working fluid. As previously mentioned, the organic Rankine cycle and vapor compression cycle can also share a common condenser if they use the same fluid. Regarding pumping power, as much as 20% of the energy produced by the turbine of an organic Rankine cycle is consumed by its pump (opposed to less than 1% for a steam cycle) [145]. Increasing the latent heat of vaporization or critical temperature of an organic fluid reduces pumping power requirements but increases the irreversibilities in the generator. Thus, to minimize energy consumption, the efficiency of the pump should be high. Efficiencies for organic fluid pumps generally fall between 10% and 25% although efficiencies as high as 60% are technically feasible [145]. Further considerations for organic molecules include their flammability, toxicity, corrosivity, global warming potential, thermal stability, and cost [153].

A considerable number of fluid optimization studies have been performed to determine optimal working fluids for organic Rankine vapor compression systems. The majority of investigations are summarized in recent literature reviews for both single and dual fluid systems [62,63]. An important observation from the fluid optimization studies is that hydrofluoroolefins (which are environmentally benign) show optimal performance characteristics at conditions representative of those presented for the proposed application. However, given differing boundary conditions and optimization targets, there is no single fluid (or fluid combination) that always yields a superior outcome. From the review by Bao et al. [63], it can be generalized that dual fluid systems yield performance improvements over single fluid systems, but have challenges with power transmission and sealing and are incapable of sharing a single condenser [154].

In addition to fluid optimization, the economic viability of organic Rankine vapor compression chillers could be improved through cycle design optimization. Like those for absorption chillers, several methods of heat recuperation have been investigated for organic Rankine vapor compression chillers. The first, and most common, rejects the sensible energy remaining at the turbine discharge to the pump

discharge through a recuperator. The recuperator reduces the heat transfer required in both the generator and condenser of the organic Rankine cycle which improves thermal performance as much as 47% [155]. Recuperators are more effective when a dry working fluid is used, the turbine has a low isentropic efficiency, and/or there is considerable superheating at the inlet of the turbine [151]. Analogous to the refrigerant heat exchanger in an absorption system, a suction line heat exchanger rejects sensible energy at the discharge of the vapor compression cycle condenser to the discharge of the evaporator [83]. This increases the latent heat available for cooling in the evaporator which increases the capacity of the chiller. It also increases the inlet temperature of the compressor which reduces the risk of liquid entering or forming within the device. However, an elevated compressor inlet temperature results in an elevated compressor discharge temperature which increases the heat rejection duty in the vapor compression cycle condenser and negates some of the suction line heat exchanger performance benefits [156]. Thus, an economizer can be used to transfer the additional sensible energy at the compressor discharge to the pump discharge [157]. Recuperating heat from the vapor compression cycle to the organic Rankine cycle allows for sub cycle efficiency improvements beyond what is possible for discrete systems. The heat from the economizer should be added to the pump discharge after that of the recuperator if the compressor discharge has a higher temperature than the turbine discharge. When integrated into an organic Rankine vapor compression system with a recuperator, an economizer and suction line heat exchanger can yield thermal performance improvements beyond 20% [156,157]. In addition to improving thermal performance, heat recuperation within an organic Rankine vapor compression system can reduce the overall cost of the technology. This is because heat recuperation reduces the sizing requirements of phase change heat exchangers and can leverage advances in compact heat exchanger technologies [156,158–160]. Compact heat exchangers can be made with low-cost materials, have small volumes (reducing fluid charge requirements), and perform best with moderate pressure fluids which can tolerate pressure loss.

Other advanced cycle configurations investigated outside of heat recuperation include: using multistage compression/expansion with intercooling/reheating [155], evaporating at multiple pressure levels to deliver chilling loads of varying thermal quality [161], using a flash tank expansion process with series compression to increase chilling load [63], cascading generation for multi-temperature waste heat inputs [162], using transcritical organic Rankine cycles for wet fluids [163], implementing zeotropic working fluids [164,165], and incorporating parallel turbines for simultaneous power export and chilling production [166]. These strategies could increase the energy savings potential of an organic Rankine vapor compression chiller but would inevitably increase investment cost and complicate operation. Further investigation into highly advanced cycle designs for organic Rankine vapor compression chillers is currently unwarranted considering the cost, operational characteristics, and design limitations of the basic cycle are still not well understood.

Organic Rankine vapor compression chillers can address the technical limitations of steam turbine chillers and could recognize both cost and performance improvements over the state-of-the-art alternative using compact heat exchanger technologies for heat recuperation. However, as a precommercial technology, the understandings regarding organic Rankine vapor compression chillers are mostly theoretical. Continued investigation into the technology is necessary to better understand the practical aspects of the system before its viability for the proposed district energy system can be properly assessed.

2.4. Assessment of Research Opportunities for Organic Rankine Vapor Compression Chillers

Thermally driven chillers could sustainably support growing cooling demands in developing nations when integrated with localized power generation technologies to supply district cooling. Absorption chillers are not economically viable for this application because of their high capital cost and low efficiency. Furthermore, as the longstanding commercial state of the art, the maturity of absorption

chillers has exhausted opportunities to improve their economic characteristics for comfort cooling. Other commercial options such as adsorption and steam turbine chilling are also unlikely to improve beyond the state of the art due to the technical limitations of their working principles. However, a precommercial technology, organic Rankine vapor compression chilling, shows opportunity to overcome the challenges of incumbent solutions to match or surpass the economic characteristics of the state of the art. These opportunities and efforts made to recognize them are detailed in a number of recent literature reviews which detail ongoing organic Rankine vapor compression chiller developments [62,64,154,167,168].

Most investigations into organic Rankine vapor compression technology seek to understand system performance characteristics with different working fluids, operating conditions, and/or cycle configurations through analytical models. Early investigations showed the importance of key design variables such as turbomachinery efficiency, pinch temperature, subcooling/superheating, and heat exchanger effectiveness. Li et al. showed the isentropic efficiencies of the turbine and compressor in an organic Rankine vapor compression cycle have the strongest impact on full system performance characteristics [169]. Pinch temperatures are the minimum temperature differences in counter flow, phase change heat exchangers between the saturated working fluid (vapor or liquid) and the process fluid heating or cooling it. Nasir et al. showed performance improvements are realized by reducing pinch temperatures in each heat exchanger [170]. Minimizing the pinch temperature increases the working fluid saturation pressure in the generator and evaporator and decreases the saturation pressure in the condenser which increases the work potential of the turbine and decreases the work requirement of the compressor. However, reducing the pinch temperature in a heat exchanger increases its physical size. Kim and Perez-Blanco showed increasing generator superheating can yield improvements to organic Rankine vapor compression thermal performance [171]. Increasing generator superheating also reduces the risk of droplet formation in the expander. Wang et al. showed increasing condenser subcooling yields considerable performance benefits to the cooling cycle [156]. However, Nasir and Kim showed that

increasing condenser subcooling also reduces power cycle thermal efficiency, which negates the benefit of increasing the value [154]. Furthermore, Wang and Peterson detailed that, when a recuperator is installed into an organic Rankine vapor compression system, increasing the degree of subcooling in the condenser can cause partial condensation in the vapor side of the recuperator [158]. Partial condensation in the recuperator results in a two-phase fluid entering the condenser, which causes flow distribution challenges. As detailed in the previous section, an economizer and suction line heat exchanger can be used in addition to a recuperator to improve thermal performance. Similar to decreasing pinch temperatures, Wang et al. showed increasing the effectiveness value of recuperative heat exchangers improves system performance but at a diminishing return considering the physical size of the device also increases [156].

Unfortunately, the early investigations showing the importance of maximizing or minimizing key design variables generally fail to indicate what values are practically achievable. Thus, several authors have incorporated heat exchanger and/or turbomachinery sizing calculations into their performance models to further assert the performance claims of the technology. One pivotal investigation by Young et al. showed that both the performance and cost of organic Rankine vapor compression technology could compete with the state of the art using next generation, low global warming potential refrigerants [82]. The system optimization modeled yielded a system cost of ~420 \$ kW^{-1} (adjusted to 2019 value [80]) with an exergetic efficiency of 23% using R1234ZE(E) (global warming potential of 6) as the working fluid in both cycles. When optimized for performance instead of economic returns, an exergetic efficiency of 30% was found to be achievable, though this was with R134a as a refrigerant. These results are relevant for the proposed application considering the technology was modeled at boundary conditions and a scale representative of reciprocating engine waste heat driven district cooling plants. However, the performance model did not consider compact heat exchanger technologies or any heat recuperation

methods, both of which could simultaneously improve organic Rankine vapor compression cost and performance characteristics.

To the best knowledge of the author, no thermo-economic modeling has been performed on an organic Rankine vapor compression chiller at relevant boundary conditions and scale for the proposed application while considering low global warming potential working fluids, all simple forms of heat recuperation, and compact heat exchanger technologies. The modeling methods of Young et al. and other authors (such as Mounier et al. [172]) could be expanded to fill this research gap, but would have one severe limitation. These models do not consider how a system performs outside of its designated operating conditions, where chillers spend 99% of their lifecycle [44]. Thus, there would be little confidence in the economic results (payback period, internal rate of return, or others) used to determine the viability of a system which were generated using the performance results of such an analysis.

Some authors have predicted off-design performance trends through analytical parametric analysis [170,171]. However, these results are inherently erroneous as many design variables are interdependent and cannot be individually assessed through computation [159]. Conversely, two authors (Garland et al. [84] and Demierre et al. [173]) attempted to create off-design performance models for organic Rankine vapor compression systems by compiling individual component performance models and fixing design parameters. However, the authors showed that experimental data was required to adjust their methodology to yield accurate results. A similar model could be investigated for the proposed system to assess the energy savings potential of an organic Rankine vapor compression system over its entire lifecycle and its initial cost using key design parameters. However, like the previous models, experimental data would be required to validate or correct the modeling results. To date, there are six experimental organic Rankine vapor compression systems which have been detailed in peer reviewed literature. These investigations are summarized in Table 2-2 beginning with the first organic Rankine vapor compression prototype study in 1975 by Prigmore and Barber [174].

Table 2-2 Comparison of experimental organic Rankine vapor compression investigations

Study	*Heat Source*	*Rejection Medium*	*Cooling Delivery*	*Compressor/ Expander*	*Working Fluid(s)*	*Cooling Duty*	*Heat Recuperation*
Prigmore & Barber 1975	101.7°C Water	29.4°C Water	12.8°C Air	Piston/Radial, Gearbox and pulley coupling	R113/ R12	~10.6 kW	Recuperator
Biancardi et al. 1982	<149°C Water	~35°C Water	7°C Water	Centrifugal/Radial, Directly coupled	R11	<73 kW	None
Wang et al. 2011	200°C Oil	48.9°C Air (tested at 22°C)	32°C Air (tested at 22°C)	Scroll/Scroll, Directly coupled	R245fa/ R134a	5 kW	Recuperator
Demierre et al. 2012-2014	Expander inlet temp. 95°C to 123°C Oil	Saturation temp. 25°C to 36°C Water	Saturation temp. 1°C to 20°C Water	Centrifugal/Radial Directly coupled	R134a	~10 kW	None
Garland et al. 2018	106°C Air	15°C Air (tested at 27.5°C)	16°C Water (tested at ~37.5°C saturation temp.)	Centrifugal/Radial, Magnetically coupled with hermetic seal	HFE7000/ R134a	<175 kW	Recuperator
Liang et al. 2021	94.6°C Water	14.1°C to 25.1°C Water	-5.6°C Air	Scroll/Scroll, pulley coupled	R245fa/ R134a	<1.8 kW	None

The prototype system by Prigmore and Barber was designed to deliver chilled air for comfort cooling using heat from solar thermal flat-plate collectors. A COP of 0.5 was experimentally verified, the expander efficiency was 72%, the compressor efficiency was 85%, and the pump efficiency was 17%. The turbine was a high-speed device which drove a low-speed compressor using both a gearbox and a pulley. The expander shaft was also connected to a motor generator which could export power in the absence of cooling demand or drive the compressor in the absence of solar thermal irradiation. The unoptimized system was two-thirds the size of a comparable absorption machine, simulated to outperform absorption at some off-design conditions, and had significant mechanical losses between the turbine and compressor which reduced thermodynamic efficiency on the order of 10%. The pump also cavitated causing operational challenges. The authors suggested using a directly coupled, high speed turbine and compressor to increase operational flexibility, reduce mechanical losses, and reduce system cost as much as 70% at the slight expense of efficiency.

Shortly following the Prigmore and Barber investigation, Biancardi et al. developed a prototype organic Rankine vapor compression system in 1982 and performed a field validation of the technology [175]. The system used a single fluid but had separate condensers to increase the operational flexibility of the technology. The focus of this effort was to use the system as a solar driven heat pump, but tests were also performed to understand the performance as a chiller. Thermal COPs between 0.50 and 0.75 were determined when testing the system over a range of conditions. Following the suggestion of the previous study, the turbine was directly coupled to the compressor, and the device was designed to operate at 40 kRPM with a combined efficiency surpassing 60%. A challenge with this investigation is that the overall system performance at specific conditions is not explicitly stated, nor are the pump, turbine, and compressor efficiencies. Neither a motor nor generator was incorporated with the turbo-compressor, but a natural gas heater was integrated with the solar thermal hot water driving loop to boost system heat input during periods of inadequate solar irradiance. The pump in the system required up to 15°C of subcooling to operate without cavitation and the system was able to load follow. The refrigerants investigated by Prigmore and Barber and Biancardi et al. were banned under the Montreal Protocol [6].

Recent experimental organic Rankine vapor compression investigations begin with a study by Wang et al. in 2011 [159]. The system was designed to support comfort cooling applications in extreme environments using waste heat. The turbine and compressor were directly coupled, but dynamically sealed as the devices were low-speed, positive displacement units. Testing could not be complete at the design conditions, yielding a COP of 0.48 with the same evaporator and condenser temperature. The expander efficiency ranged between 70% and 84% while the efficiencies of the compressor and pump were not explicitly stated. This was the first system to investigate compact heat exchangers which, when successfully implemented, improved the COP to 0.6 [158]. There were notable challenges with the fabrication of the compact heat exchanger used for the generator and recuperator, and the low-speed compressor was unable to adequately perform at off-design.

Demierre et al. developed a prototype in 2014 [176], which was similar to that of Biancardi et al. The system used a single fluid, no heat recuperation, separate condensers, and high-speed, directly coupled turbomachinery to deliver heat pumping. Several experimental data points were relevant for chilling with COPs ranging between 0.40 and 0.52. The turbine and compressor had efficiencies just under 70% for these conditions at speeds around 190 kRPM while between 18% and 38% of the turbine work was required by the pump (the greater of which occurred at transcritical power cycle operation). The efficiency of the turbomachinery was consistent over a range of conditions and should be greatly improved at a larger scale.

Garland et al. created a dual fluid organic Rankine vapor compression system in 2018 which used high speed turbomachinery but was hermetically sealed using a magnetic shaft coupling [84]. This was the largest experimental system to date but had unique operating conditions where the condenser temperature was lower than that of the evaporator. Compact heat exchangers were successfully developed for the prototype including a power cycle recuperator. The turbine and compressor were designed to have efficiencies surpassing 80% with a transfer efficiency of 93% at 30 kRPM. No information relating to the pump was presented other than it limited system performance at high organic Rankine cycle loads. The system was only tested at off-design with a different working fluid in the cooling cycle which limited performance. COPs ranged between 1.68 and 1.80 while the design was 2.1.

The most recent experimental organic Rankine vapor compression investigation was presented by Liang in 2021 [177]. This investigation was the first to investigate transient operational modes and provide chilling below 0°C. A pulley coupled turbine and compressor (both low-speed devices) was investigated to determine the effect of varying the speed ratio between the two. The authors found a small tradeoff between efficiency and chilling temperature resulted from changing the speed ratio. The authors also showed implications to compressor speed, cooling cycle flow, chilling temperature, and

thermal COP as power cycle flow was modulated. Inferior selection of off the shelf components for the prototype resulted in a COP of 0.18 and a system incapable of producing a continuous chilling load.

To date, there are no experimental organic Rankine vapor compression chiller investigations which could be used to develop an accurate and relevant off-design, thermo-economic model for a technology suited for the proposed application. None of the technologies operated at a relevant scale for district cooling and only the systems from Biancardi et al. and Demierre et al. operated at relevant boundary conditions (driving source representative of reciprocating engine waste heat streams and standard, liquid coupled heat rejection and chilling stream temperatures). No investigation implemented multiple methods of heat recuperation nor low global warming potential refrigerants. Some authors presented off-design performance data but did not show clear performance trends over a wide range of conditions required to validate or tune a comprehensive off-design performance model. Furthermore, only two studies considered compact heat exchanger technologies.

2.5. Focus of Current Investigation

There are significant research needs for organic Rankine vapor compression chillers. One need is to understand the capital costing characteristics of the technology with multiple methods of heat recuperation and compact heat exchanger technologies through a thermo-economic design optimization study. Another need is to understand the performance characteristics of the same system over the entire range of conditions it is expected to operate at over its lifecycle through a comprehensive off-design performance study. Both studies could assess the technology with low global warming potential working fluids and at boundary conditions optimized for district cooling applications when the system is driven by waste heat from a reciprocating engine prime mover. The results of these analysis would enable an objective economic assessment of organic Rankine vapor compression chillers as one sustainable solution to the growing challenges of globalization and climate change. However, the development of such models

requires a comprehensive set of organic Rankine vapor compression chiller performance data to verify their methods produce accurate results, which is not yet available in literature.

The focus of this research effort is to create a comprehensive set of organic Rankine vapor compression chiller performance data through the design, fabrication, and experimentation of a novel prototype to guide future analytical investigations into the technology. The prototype is differentiated from all previous experimental investigations using low global warming potential refrigerants as working fluids, implementing three heat recuperation methods (recuperator, economizer, and suction line heat exchanger), and selecting boundary conditions and a scale which are relevant for reciprocating engine waste heat driven district cooling applications. Experimental methods are also differentiated by following performance rating standards for commercial chilling technologies to accurately quantify both the baseline performance of the technology and its performance trends at deviating boundary conditions. The subsequent chapter details the analytical model used to set a baseline performance target for the prototype and the considerations for the selection/design of critical system components.

Chapter 3 System Simulation and Critical Component Selection

To accurately assess the viability of organic Rankine vapor compression chilling through thermo-economic design optimization and off-design performance modeling, a comprehensive set of experimental data is needed to validate results. The prototype designed, fabricated, and experimented in this research effort fills this need and addresses the limitations of previous experimental investigations. This chapter presents a model used to simulate the baseline performance of the prototype. The boundary conditions and technical considerations which shaped the model were informed through literature and collaboration with manufacturing partners. Modeling methodology was adapted from a previous analytical investigation into organic Rankine vapor compression systems [82]. Results were used to select or design critical components for the system and to provide a comparison to experimental test results in Chapter 5. A complete sample calculation for the model is presented in Appendix A.

3.1. System Simulation

The simulation of the prototype followed the process flow diagram presented in Figure 3-1. The numbering convention was held constant throughout the remainder of this investigation for consistency. As shown, all heat exchangers were simulated and operated in counter flow orientation to maximize system performance.

First, a high-pressure, vapor refrigerant is expanded through a high-speed radial turbine in the organic Rankine power cycle. The expansion of the vapor to a lower pressure generates mechanical energy which is sent directly to a centrifugal compressor via a common shaft. A directly coupled, high-speed turbo-compressor was selected over positive displacement machinery to minimize power transfer losses and improve the operational flexibility of the prototype. A single working fluid was considered for both the power and cooling sub cycles of the organic Rankine vapor compression chiller as the scale of the prototype and, thus, torque placed on the turbo-compressor shaft prevented the use of the hermetic

magnetic coupling technology investigated in the experiment by Garland et al. [84]. Once expanded, the vapor refrigerant leaving the turbine exchanges heat with the liquid refrigerant exiting the power cycle pump in the recuperative heat exchanger. This simultaneously reduces the heat rejection load of the power cycle condenser and increases the apparent heat input to the system. Both actions improve the thermal efficiency of the power cycle. After the rejection of its sensible heat in the recuperator, the vapor refrigerant is fully condensed into a liquid in the power cycle condenser. Once liquified, the refrigerant is pressurized in the power cycle pump to the level at which it initially entered the turbine. The liquid is preheated by the recuperator and economizer before it enters the generator. The generator fully vaporizes the refrigerant. Vapor leaving the generator enters the turbine to complete the cycle.

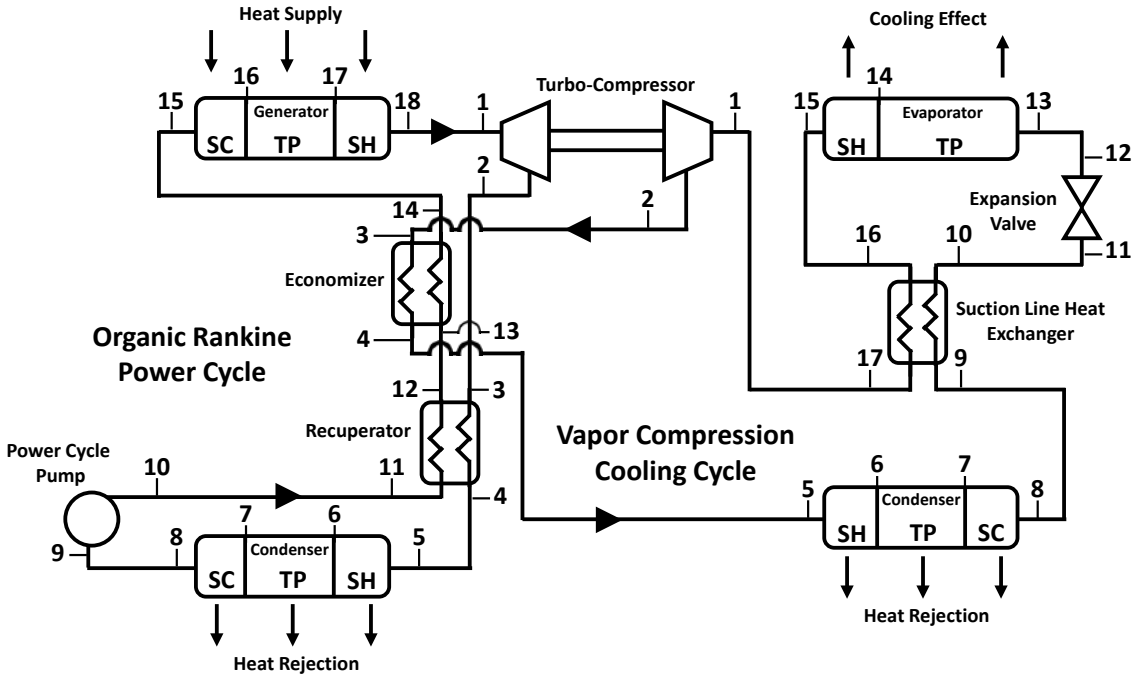

Figure 3-1 Prototype organic Rankine vapor compression cycle diagram

On the vapor compression cycle, a vapor-phase refrigerant is pressurized by the compressor using the mechanical energy generated by the turbine. The vapor refrigerant at the compressor discharge exchanges heat with the liquid refrigerant exiting the recuperator in the economizer. The heat from the economizer is added to the power cycle liquid after the recuperator as it had a greater thermal quality

(temperature) than the turbine vapor discharge. The economizer simultaneously reduces the heat rejection load of the cooling cycle condenser and increases the apparent heat input to the system. These actions improve the thermal efficiency of the cooling and power cycle, respectively. After the rejection of its sensible heat in the economizer, the vapor refrigerant is fully condensed into a liquid in the cooling cycle condenser. Separate condensers were implemented into the prototype despite the use of a common refrigerant in each sub cycle. This strategy, also implemented in the experimental investigations by Biancardi et al. and Demierre et al., was investigated to simplify prototype troubleshooting [175,176]. Once liquified, the refrigerant leaving the cooling cycle condenser heats the vapor leaving the evaporator in the suction line heat exchanger. The liquid leaving the suction line heat exchanger is then throttled to a lower pressure to produce a two-phase, liquid-vapor mixture of refrigerant with a lower thermal quality. The throttled refrigerant enters the evaporator where it is fully vaporized to produce the desired cooling effect. As previously detailed, the vapor leaving the evaporator exchanges energy with the liquid leaving the cooling cycle condenser. Cooling the liquid at the cooling cycle condenser outlet through the suction line heat exchanger decreases the vapor mass quality of the two-phase refrigerant mixture entering the evaporator, which directly increases the chilling capacity of the cooling cycle. Heating the vapor at the evaporator outlet through the suction line heat exchanger reduces the risk of droplet formation in the compressor. It also considerably increases the thermal quality of the compressor discharge, which improves the utility of the economizer. The vapor leaving the suction line heat exchanger enters the compressor to complete the cycle.

3.1.1. Boundary Conditions and Technical Assumptions

As the most prolific district cooling technology [16], standard operating conditions for electrically driven, centrifugal, water-cooled chillers were selected as boundary conditions for the prototype organic Rankine vapor compression chiller. These conditions were taken from a performance rating standard which requires electric chillers to cool water from 12°C to 7°C with condenser water entering the system

at 30°C and leaving at 35°C [44]. While water was used in the evaporator, a 50% by volume mixture of ethylene glycol and water was used in both condensers for heat rejection. The use of a glycol mixture in the condensers was required to prevent the risk of frozen pipes when the system was nonfunctioning. As previously mentioned, district cooling chillers are implemented with cooling duties ranging between 210 and 35,170 kW [45]. For the prototype, a chilling duty of 300 kW was set to yield a relevant operational scale. Future studies following a thermo-economic design optimization analysis of the prototype could determine the optimal chilling duty using well-established, process engineering scaling methodologies.

The energy source for the prototype was selected to be a 50% by volume mixture of ethylene glycol and water with a supply temperature of 91°C and a temperature difference of 5°C to match the alternative streams. This driving source is representative of those required for the commercial state of the art alternative thermally driven chilling technology [76] and reciprocating engine coolant waste heat [46,178]. Coolant (generally a glycol mixture) typically exits a reciprocating engine between 87°C and 110°C while the temperature difference is limited to 8.3°C to avoid placing thermal stresses on the device. Exhaust waste heat (which has temperatures between 380°C to 540°C [46]) could also be used as a waste heat source but was not considered in this investigation to simplify the analysis. The exhaust heat would either be added to the coolant stream (before the generator after leaving the engine) to increase the inlet temperature to and temperature difference across the generator, or directly to the refrigerant after the coolant heat. Either configuration would require an additional heat exchanger.

Working fluids for the prototype were down selected with several criteria. As a primary focus of the research effort, refrigerants were first filtered if their hundred-year global warming potential value was above 100. At a global warming potential value of 100, the release of one kilogram of refrigerant causes the same greenhouse effect as releasing 100 kilograms of carbon dioxide. From here, fluids with a safety classification outside of A1 or A2L from American Society of Heating, Refrigerating and Air-Conditioning Engineers were filtered to avoid flammability and toxicity concerns [179,180]. Further

excluded from this subset of working fluids were zeotropic mixtures to avoid challenges related to two-phase temperature glide [181], azeotropic mixtures with constituents controlled under the Kigali Amendment to the Montreal Protocol [142], fluids with critical temperatures below that of the driving source (91°C) for increased energy savings potential [145], fluids with working pressures anywhere in the cycle below two atmospheres (202.65 kPa) to reduce the impact of frictional pressure loss and prevent contamination from air leakages [89], and so-called "wet" fluids that, when expanded isentropically, could yield liquid droplets within the turbine which present a risk to the integrity of the device [144]. Two fluids, R1234ZE(E) and R1234yf, met the specified criteria. Preliminary modeling efforts found R1234yf could yield higher thermal COPs, but R1234ZE(E) was selected as the prototype working fluid as it required less pumping power, smaller heat exchangers, and was less costly per unit mass.

With the cycle layout, boundary conditions, chilling duty, and working fluid selected for the prototype, technical assumptions for each of the components were required to simulate the performance of the technology. The finalized assumptions used in the simulation effort are outlined in Table 3-1. These assumptions were iteratively refined with project partners and equipment suppliers to simultaneously ensure the prototype was highly efficient and practical to construct.

The pinch temperatures in the generator, evaporator, and condensers were several of the specified inputs to the performance simulation. As previously detailed, reducing pinch temperatures in phase change heat exchangers improves their thermal performance but increases their physical size. The pinch location for the evaporator is at the refrigerant inlet (cooling cycle state point 13). For the power and cooling cycle condensers, the pinch location is the superheated vapor to two-phase transition point (cooling cycle state point 6 and power cycle state point 6). The generator pinch temperature is at the subcooled liquid to two-phase transition point (power cycle state point 16). The pinch locations for the prototype are shown on a temperature to entropy diagram with representative state points overlaid against a refrigerant saturation curve and the temperature profiles for the external streams in Figure 3-2.

Table 3-1 Prototype performance simulation boundary conditions and technical assumptions

Modeling Input Parameter	*Value*	*Modeling Input Parameter*	*Value*
Radial Turbine Isentropic Efficiency	83.1%	Evaporator Superheating	0.6°C
Centrifugal Compressor Isentropic Efficiency	82.0%	Evaporator Pinch Temperature	0.4°C
Turbo-Compressor Shaft Efficiency	94.3%	Evaporator Refrigerant Pressure Loss	4.0 kPa
Power Cycle Pump Isentropic Efficiency	30.0%	Economizer Effectiveness	84.5%
Generator Superheated Vapor Regime Effectiveness	98.5%	Economizer Vapor Pressure Loss	5.6 kPa
Generator Pinch Temperature	2.3°C	Economizer Liquid Pressure Loss	6.6 kPa
Generator Refrigerant Pressure Loss	11 kPa	Recuperator Effectiveness	84.4%
Power Cycle Condenser Subcooling	1.0°C	Recuperator Vapor Pressure Loss	5.0 kPa
Power Cycle Condenser Pinch Temperature	1.2°C	Recuperator Liquid Pressure Loss	4.6 kPa
Power Cycle Condenser Refrigerant Pressure Loss	5.0 kPa	Suction Line Heat Exchanger Effectiveness	88.4%
Cooling Cycle Condenser Subcooling	1.0°C	Suction Line Heat Exchanger Vapor Pressure Loss	4.5 kPa
Cooling Cycle Condenser Pinch Temperature	1.1°C	Suction Line Heat Exchanger Liquid Pressure Loss	3.5 kPa
Cooling Cycle Condenser Refrigerant Pressure Loss	5.0 kPa	-	-

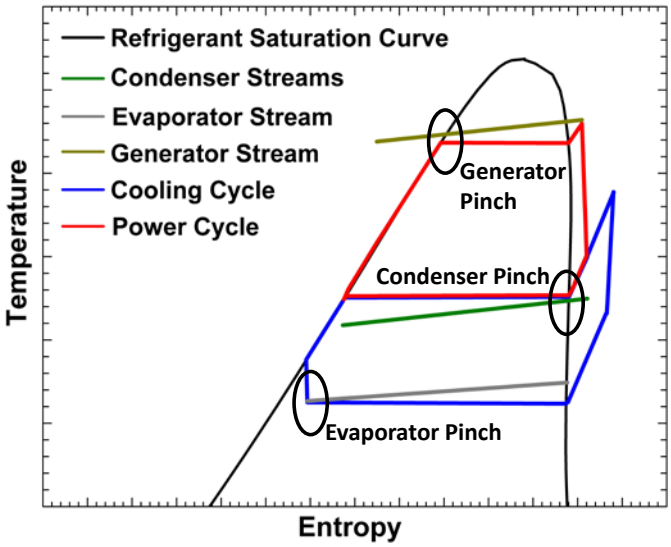

Figure 3-2 Representative prototype heat exchanger pinch temperature locations

Additional constraints for the phase changing heat exchangers were their degree of superheating or subcooling. The benefits of increasing generator superheating were recognized through maximizing the effectiveness value (Equation (3.1) and Equation (3.2)) of the generator superheated flow regime with the consideration that doing so would increase the physical size of the device. The effectiveness value (ε) is

the ratio of the actual heat duty ($\dot{Q}$) to the maximum possible heat duty ($\dot{Q}_{\max}$). The maximum possible heat duty is calculated using the minimum product of mass flow ($\dot{m}$) and average specific heat (CP_{avg}) of the two streams interacting in the heat exchanger (hot and cold) and the temperature difference between the higher temperature stream inlet ($T_{hot,in}$) and the lower temperature stream inlet ($T_{cold,in}$).

$$\varepsilon = \frac{\dot{Q}}{\dot{Q}_{max}} \tag{3.1}$$

$$\dot{Q}_{max} = MIN((\dot{m} \cdot Cp_{avg})_{hot}, (\dot{m} \cdot Cp_{avg})_{cold}) \cdot (T_{hot,in} - T_{cold,in}) \tag{3.2}$$

The subcooling from both condensers was equated to simulate prototype performance as if a single condenser were used. As previously mentioned, increasing the degree of condenser subcooling yields considerable performance benefits to the cooling cycle but inhibits the performance of the power cycle. Since a suction line heat exchanger was incorporated into this system architecture (which increases the effective subcooling at the outlet of the cooling cycle condenser), the amount of subcooling was minimized in both condensers. The minimum value of condenser subcooling was set to ensure power cycle pump cavitation was avoided. Lastly, the evaporator superheating was minimized to increase the utility of the suction line heat exchanger. Other assumptions for the heat exchangers include the effectiveness values of the recuperative units and the pressure losses through each device.

Technical assumptions for the turbo-compressor and power cycle pump included isentropic and power transfer efficiencies. As a custom turbo-compressor was required for this effort, the turbine, compressor, and power transfer (from the turbine to the compressor) efficiency values were maximized to limitations suggested by the manufacturer. The only technical assumption for the power cycle pump was its isentropic efficiency. A greater value for power cycle pump isentropic efficiency could have been possible through the development of a custom unit. However, it was found through simulation efforts that the pump isentropic efficiency directly affected electrical energy consumption but had a small impact

on thermal performance. Thus, a commercial unit with a lower efficiency value was selected for this development effort to reduce project risk.

3.1.2. Methodology

With the system boundary conditions and component level technical assumptions outlined, a performance model was created in Engineering Equations Solver using the values as inputs [182]. Hand calculations verifying the validity of the model are presented in Appendix A. Modeling methodology was adapted from a design and optimization study by Young et al. [82]. The analysis assumed the system was operating at steady state with well-insulated piping to prevent any heat losses. In addition, the expansion valve on the vapor compression cycle was isenthalpic. Pressure loss between each component was assumed to be the averaged value of the manufacturer estimated heat exchanger pressure losses (5.48 kPa). Refrigerant pressure losses through heat exchangers with phase change were first assumed to be equally distributed amongst flow regimes. Once the model was developed, pressure loss through heat exchangers with phase changes were altered to be proportional to the heat duty in each region. Potential gravitational effects on system pressure were ignored. The vapor qualities (mass fraction of vapor to liquid) were set to zero at two-phase fluid to subcooled liquid transition points and set to unity at two-phase fluid to superheated vapor transition points. Unspecified effectiveness values were constrained between zero and unity to satisfy the second law of thermodynamics. The first law of thermodynamics was defined with Equation (3.3) (scaled by 100 to yield a percentage) which was an energy balance variable (*EB*) adapted from the performance rating standard used to inform experimentation efforts [44]. The energy input (E_{in}) term was the sum of the generator heat duty in kW, the evaporator heat duty in kW, and the pump work in kW, while the rate of energy output (E_{out}) was the sum of the two condenser heat duties in kW.

$$EB = 200 \cdot \frac{\dot{E}_{\text{in}} - \dot{E}_{\text{out}}}{\dot{E}_{\text{in}} + \dot{E}_{\text{out}}} \tag{3.3}$$

The first step in this modeling effort was to determine the mass flowrate of the external evaporator stream ($\dot{m}_{\mathrm{evap,w}}$) using the desired chilling load ($\dot{Q}_{\mathrm{evap}}$), the selected temperature difference (($T_{\mathrm{evap,w,in}} - T_{\mathrm{evap,w,out}}$)), and the average specific heat of the fluid between the inlet and outlet ($Cp_{\mathrm{evap,w,avg}}$) as shown in Equation (3.4). Specific heat was determined for water using internal functions to the modeling software with the respective fluid, average temperature, and assumed pressure as inputs. The pressure assumed for the water stream was 101 kPa to return liquid properties.

$$\dot{Q}_{\mathrm{evap}} = \dot{m}_{\mathrm{evap,w}} \cdot Cp_{\mathrm{evap,w,avg}} \cdot (T_{\mathrm{evap,w,in}} - T_{\mathrm{evap,w,out}}) \tag{3.4}$$

The evaporator refrigerant inlet state point was then fixed assuming an arbitrary vapor quality between zero and unity, and a temperature equal to the evaporator water outlet temperature less the assumed pinch temperature. This allowed the determination of the state point pressure using internal functions to the modeling software for saturation pressure with the temperature as an input. With this pressure determined, the pressures at points 1 and 12-17 in the vapor compression cycle were set using the assumed component and pipe run pressure losses. Setting the quality at the evaporator two-phase fluid to superheated vapor transition to unity also fixed the transition point thermodynamic properties using internal functions to the modeling software for saturation temperature with the pressure as an input and, subsequently, the outlet state point assuming the prescribed superheating. Using the pressure and temperature (or quality) at each state point within the evaporator, enthalpy (h) and entropy were determined with internal functions to the modeling software. These properties were used to determine the evaporator external stream temperature at the transition point, the evaporator section effectiveness values, and the vapor compression cycle refrigerant flowrate using Equation (3.5) to Equation (3.7) for both the two-phase fluid and superheated vapor sections. The enthalpy difference for the streams external to the system, in this case the hot stream, were simply determined by scaling the temperature difference of the section with the specific heat capacity of the section determined using the average

temperature and assumed pressure. The specific heat capacity for the refrigerant (required to determine effectiveness values) was determined using the average temperature and pressure of the section. In analyzing a two-phase heat exchanger section, the specific heat capacity for the refrigerant is indeterminate and Equation (3.7) always uses the external stream mass flow and specific heat capacity to determine effectiveness.

$$\dot{Q} = \dot{m}_{\text{cold}} \cdot (h_{\text{cold,out}} - h_{\text{cold,in}}) \tag{3.5}$$

$$\dot{Q} = \dot{m}_{\text{hot}} \cdot (h_{\text{hot,in}} - h_{\text{hot,out}}) \tag{3.6}$$

$$\dot{Q} = \varepsilon \cdot MIN((\dot{m} \cdot Cp_{\text{avg}})_{\text{hot}}, (\dot{m} \cdot Cp_{\text{avg}})_{\text{cold}}) \cdot (T_{\text{hot,in}} - T_{\text{cold,in}}) \tag{3.7}$$

With a vapor compression cycle mass flow determined, the cooling cycle condenser glycol superheated vapor to two-phase fluid transition temperature had to be assumed as a value between the inlet and outlet condition to continue. This was used to determine the transition point refrigerant temperature by adding the assumed pinch temperature. The transition point was then fixed assuming a vapor quality of unity and a pressure determined with internal functions to the modeling software for saturation pressure. This fixed the remaining vapor compression cycle pressures assuming the component and pipe run pressure losses. It also fixed the state points for the refrigerant two-phase fluid to subcooled liquid transition assuming a vapor quality of zero and the outlet using the assumed condenser subcooling. Equation (3.5) to Equation (3.7) were once again used for the vapor compression cycle condenser regions to determine the glycol mass flow rate, the two-phase fluid to subcooled liquid glycol transition temperature, the condenser refrigerant inlet enthalpy (and thus temperature) and the three effectiveness values for the unit. Instead of pressure being used as an input for the specific heat capacities for the specified glycol mixture, internal functions to the modeling software required only the average temperature and a prescribed concentration of 50% as it always returns liquid properties.

The high and low-pressure regimes of the vapor compression cycle were then ready to be coupled by constraining the performance of the suction line heat exchanger. The inlet enthalpy for the liquid side was assumed to equal the condenser discharge enthalpy and the vapor side inlet enthalpy was assumed to equal the evaporator discharge enthalpy from the heat loss in pipe runs assumption. Using the pressures and enthalpies for the inlet conditions, the inlet temperatures were found using internal functions to the modeling software. Assuming the suction line heat exchanger effectiveness value, the outlet enthalpy values for the device (and thus temperatures) were determined using Equation (3.5) to Equation (3.7). This also fixed the inlet conditions to the expansion valve and compressor with the pipe run heat loss assumption.

With the inlet condition to the expansion valve determined, the outlet condition can be properly fixed assuming an isenthalpic process, removing the previously assumed evaporator inlet quality constraint, equating the enthalpy at the outlet to the value at the evaporator inlet, and determining the temperatures at each state point using internal functions to the modeling software.

The compressor performance can then be modeled by first determining the isentropic outlet enthalpy using internal functions to the modeling software and the outlet pressure and inlet entropy as inputs. Then, using Equation (3.8) for compressor efficiency (η_{comp}), the compressor outlet condition becomes fixed and its required work input ($\dot{W}_{\text{comp}}$) is determined using Equation (3.9).

$$\eta_{\text{comp}} = \frac{h_{\text{out,s}} - h_{in}}{h_{\text{out}} - h_{\text{in}}} \tag{3.8}$$

$$\dot{W}_{\text{comp}} = \dot{m} \cdot (h_{\text{out}} - h_{\text{in}}) \tag{3.9}$$

This completely fixes the cooling cycle state points with the pipe run heat loss assumption to determine the inlet and outlet cross-cycle economizer vapor conditions and its heat duty using Equation (3.6). The economizer effectiveness cannot be used to remove the condenser glycol superheated vapor

to two-phase fluid transition temperature assumption until a portion of the organic Rankine cycle is modeled.

Modeling of the organic Rankine cycle begins with the generator. The first refrigerant temperature determined is the generator subcooled liquid to two-phase fluid transition point by assuming a glycol transition temperature between the specified inlet and outlet condition and subtracting the specified pinch temperature. This point is fully constrained assuming a vapor quality of zero and a pressure determined using internal functions to the modeling software for saturation pressure. With this pressure determined, the pressures at state points 1 and 10-18 in the organic Rankine cycle are set assuming the component and pipe run pressure losses. This allows the determination of the generator two-phase fluid to superheated vapor transition state point assuming a vapor quality of unity. This then allows the determination of the generator glycol mass flow rate, the refrigerant inlet and outlet state points, the glycol two-phase fluid to superheated vapor transition temperature, and the subcooled and two-phase region effectiveness values by applying Equation (3.5) to Equation (3.7) for each regime while assuming the generator inlet and outlet glycol temperatures, the superheated region effectiveness value, and an arbitrary organic Rankine cycle refrigerant mass flow rate.

The determination of the actual organic Rankine cycle refrigerant mass flow rate first requires the determination of the turbine outlet pressure. To determine this pressure, and the remaining organic Rankine cycle pressures assuming the component and pipe run pressure losses, the power cycle condenser refrigerant superheated vapor to two-phase fluid transition state point is determined. This requires a separate condenser glycol superheated vapor to two-phase fluid transition temperature assumption for the organic Rankine cycle to determine the state point refrigerant temperature using the assumed pinch temperature. This temperature, and the assumed vapor quality of unity, fixes the state point through determining the saturation pressure using internal functions to the modeling software. The condenser refrigerant two-phase fluid to subcooled liquid transition and outlet state point can also be

determined at this time assuming a transition point vapor quality of zero and the prescribed condenser subcooling. These points will subsequently fix the pump inlet state point using the pipe run heat loss assumption. With the turbine outlet pressure determined, the inlet state point is fixed using the pipe run heat loss assumption and the turbine isentropic outlet enthalpy is determined using internal functions to the modeling software and the outlet pressure and inlet entropy as inputs. Using Equation (3.10) for turbine efficiency (η_{turb}), Equation (3.11) for turbine work ($\dot{W}_{\text{turb}}$), and Equation (3.12) for turbo-compressor shaft transfer efficiency (η_{shaft}), while removing the previously assumed organic Rankine cycle mass flow constraint, allows for the proper determination of the cycle mass flow, fixes the state point at the turbine outlet, and determines the required turbine work to produce the desired chilling load.

$$\eta_{\text{turb}} = \frac{h_{\text{in}} - h_{out}}{h_{\text{in}} - h_{\text{out,s}}} \tag{3.10}$$

$$\dot{W}_{\text{turb}} = \dot{m} \cdot (h_{\text{in}} - h_{\text{out}}) \tag{3.11}$$

$$\eta_{\text{shaft}} = \frac{\dot{W}_{\text{comp}}}{\dot{W}_{\text{turb}}} \tag{3.12}$$

With the state points regarding the turbine and generator fixed, as well as fixing the organic Rankine cycle mass flowrate to the appropriate value, attention is turned back to the economizer. Using the pipe run heat loss assumption fixes the economizer liquid outlet state point while the inlet state point is fixed using Equation (3.5) and the previously determined economizer heat duty. At this point, Equation (3.7) can be used with the prescribed economizer effectiveness value to remove the previously assumed vapor compression cycle condenser glycol superheated vapor to two-phase fluid transition temperature constraint. The recuperator liquid outlet and vapor inlet conditions can now be fixed using the pipe run heat loss assumption at this time. However, before the recuperator performance can be modeled, the organic Rankine cycle pump state points must be fixed. With the inlet condition previously fixed, the outlet

condition can be fixed using the assumed pump efficiency (η_{pump}) with Equation (3.13) and its work ($\dot{W}_{\text{pump}}$) can be determined using Equation (3.14).

$$\eta_{\text{pump}} = \frac{h_{\text{out,s}} - h_{in}}{h_{\text{out}} - h_{\text{in}}} \tag{3.13}$$

$$\dot{W}_{\text{pump}} = \dot{m} \cdot (h_{\text{out}} - h_{\text{in}}) \tag{3.14}$$

With the pump outlet state point set, the recuperator liquid inlet state point can be determined using the pipe run heat loss assumption. Equation (3.5) to Equation (3.7) can now be used to determine the recuperator vapor discharge state point using the prescribed effectiveness value while removing the generator subcooled liquid to two-phase fluid transition temperature constraint.

At this point, the refrigerant state points for both the organic Rankine cycle and vapor compression cycle are fully constrained. However, the model is not complete until Equation (3.5) to Equation (3.7) are also applied to the organic Rankine cycle condenser flow regimes. Doing so determines the heat duties and effectiveness values of each section. Also determined are the external stream mass flow rate and two transition temperatures when removing the final constraint placed on the condenser glycol superheated vapor to two-phase fluid transition temperature.

With the model complete, pressure loss assumptions are changed from equal distribution to distribution based upon heat duty, and a number of system level performance metrics are calculated. The first is the thermal COP using Equation (3.15). The electrical equivalent COP (COP_{EC}) is then determined using Equation (3.16) which assumes a perfect conversion of electricity to pump work. The performance of the individual cycles are determined using Equation (3.17) and Equation (3.18) for the power (η_{ORC}) and cooling cycle (COP_{VC}), respectively. These formulations require the determination of the total generator and evaporator heat duties which are simply the sum of the heat duties of the individual sections. The

total heat duties of the condensers are also required to assess the energy balance. The final value calculated is the second law efficiency with the formulations presented in the previous chapter.

$$COP_{TH} = \frac{\dot{Q}_{evap}}{\dot{Q}_{gen}} \tag{3.15}$$

$$COP_{EC} = \frac{\dot{Q}_{evap}}{\dot{W}_{pump}} \tag{3.16}$$

$$\eta_{ORC} = \frac{\dot{W}_{turb} - \dot{W}_{pump}}{\dot{Q}_{gen}} \tag{3.17}$$

$$COP_{VC} = \frac{\dot{Q}_{evap}}{\dot{W}_{comp}} \tag{3.18}$$

3.1.3. State Points and Performance Metrics

The complete performance model was assessed to simulate the operation of the prototype at its baseline conditions. Table 3-2 presents the thermodynamic state points of the organic Rankine vapor compression system determined through the simulation effort while Table 3-3 presents state points for the liquid streams external to the prototype. Power cycle state points 6 and 17 and cooling cycle state points 6 and 14 are representative of saturated vapor refrigerant. Power cycle state points 7 and 16 and cooling cycle state point 7 are representative of saturated liquid refrigerant. The vapor mass quality at cooling cycle state point 12 is 8.54% and 8.95% at cooling cycle state point 13.

Using the state points internal and external to the system with the formulations of the previous section allowed the determination of key system level performance characteristics outlined in Table 3-4. First, through the unconstrained heat exchanger effectiveness values and energy balance, it was determined that the first and second law of thermodynamics were satisfied. The slight deviation of the energy balance from zero is a result of assuming averaged values for specific heat capacities. The

simulated second law efficiency shows the prototype is highly competitive with commercial solutions whose second law efficiencies were presented in the previous chapter. This performance is possible using the recuperative heat exchangers which collectively transfer 97.72 kW of energy throughout the sub cycles. The performance is also a result of the ambitious technical assumptions used in the simulation which were carefully selected to represent the components selected or custom designed for implementation into the prototype.

Table 3-2 Simulated prototype refrigerant thermodynamic state points

Organic Rankine Cycle					***Vapor Compression Cycle***				
	Mass Flow Rate [kg s^{-1}]			2.791		Mass Flow Rate [kg s^{-1}]			1.827
State Point	Temperature [°C]	Pressure [kPa]	Enthalpy [kJ kg^{-1}]	Quality [-]	State Point	Temperature [°C]	Pressure [kPa]	Enthalpy [kJ kg^{-1}]	Quality [-]
1	89.80	2,236	437.4	Superheat	1	31.06	256.8	411.9	Superheat
2	47.21	705.1	419.4	Superheat	2	65.04	699.6	437.9	Superheat
3	47.11	699.6	419.4	Superheat	3	64.96	694.1	437.9	Superheat
4	39.41	694.6	411.4	Superheat	4	46.83	688.5	419.3	Superheat
5	39.29	689.1	411.1	Superheat	5	46.73	683.1	419.3	Superheat
6	36.08	689.0	407.6	1	6	35.75	682.7	407.4	1
7	35.83	684.1	249.7	0	7	35.51	678.1	249.2	0
8	34.83	684.1	248.2	Subcool	8	34.51	678.1	247.8	Subcool
9	34.83	678.6	248.2	Subcool	9	34.51	672.6	247.8	Subcool
10	38.10	2,281	252.9	Subcool	10	18.32	669.1	225.0	Subcool
11	38.10	2,275	252.9	Subcool	11	18.32	663.6	225.0	Subcool
12	43.61	2,270	260.9	Subcool	12	7.169	281.7	225.0	0.0854
13	43.61	2,265	260.9	Subcool	13	6.600	276.2	225.0	0.0895
14	51.90	2,258	273.0	Subcool	14	6.181	272.2	388.4	1
15	51.90	2,253	273.0	Subcool	15	6.781	272.2	389.2	Superheat
16	85.37	2,249	327.8	0	16	6.636	266.7	389.2	Superheat
17	85.23	2,243	428.1	1	17	31.16	262.2	411.9	Superheat
18	89.90	2,242	437.4	Superheat	-	-	-	-	-

Table 3-3 Simulated prototype external stream thermodynamic state points

Heat Exchanger	*Inlet Temperature*	*Outlet Temperature*	*TPSH/TPSC Temperature*	*Mass Flow Rate [kg s^{-1}]*
Generator	91.0°C	86.0°C	90.72°C / 87.67°C	25.41
Power Cycle Condenser	30.0°C	35.0°C	34.88°C / 30.04°C	26.99
Cooling Cycle Condenser	30.0°C	35.0°C	34.65°C / 30.04°C	18.57
Evaporator	12.0°C	7.00°C	11.98°C / -	14.30

Table 3-4 Simulated prototype performance metrics

Performance Metric	*Value*	*Performance Metric*	*Value*
Thermal COP	0.6539	Generator SC/TP ε Values	0.9523/0.5701
Electrical Equivalent COP	22.79	Power Cycle Condenser Heat Duty	455.6 kW
Second Law Efficiency	32.05%	Power Cycle Condenser SC/TP/SH ε Values	0.1715/0.8013/0.8303
Organic Rankine Cycle Efficiency	8.102%	Cooling Cycle Condenser Heat Duty	313.5 kW
Vapor Compression COP	6.320	Cooling Cycle Condenser SC/TP/SH ε Values	0.1814/0.8074/0.9466
Energy Balance	0.3723%	Evaporator TP/SH ε Values	0.9256/0.1409
Turbine Work	50.34 kW	Recuperator Heat Duty	22.12 kW
Compressor Work	47.47 kW	Economizer Heat Duty	33.99 kW
Pump Work	13.16 kW	Suction Line Heat Exchanger Heat Duty	41.61 kW
Generator Heat Duty	458.8 kW	-	-

3.2. System Component Selection

The organic Rankine vapor compression performance simulation results were presented to manufacturing partners and equipment suppliers as specifications for critical components required for the prototype development effort. The critical components include the heat exchangers, turbo-compressor, power cycle pump, and cooling cycle expansion valve. This section details the critical components selected for the prototype and computational methods used to verify their adequacy.

3.2.1. Heat Exchangers

The prototype organic Rankine vapor compression system uses seven heat exchangers for its base operation and to fully recuperate heat across the prototype: generator, evaporator, power cycle condenser, cooling cycle condenser, recuperator, economizer, and suction line heat exchanger. Highly effective, low cost, aluminum brazed technologies were proposed for all organic Rankine vapor compression prototype system heat exchangers. Modine Manufacturing was partnered with to design, fabricate, and deliver these devices due to their success in developing such technologies on a large platform for a previous experimental organic Rankine vapor compression facility [84]. However, to reduce timeframe and budgetary risks, it was decided to custom manufacture only the generator and recuperative heat exchangers while sourcing commercial off the shelf options for the evaporator and two condensers for the first prototype iteration. The commercial off the shelf devices were sized and sourced by Modine Manufacturing through one of their equipment suppliers, Provides, who manufactures shell and tube technologies for commercial chilling systems.

The evaporator selected for the organic Rankine vapor compression system is shown in Figure 3-3. This heat exchanger is a four pass, spray evaporator which vaporizes the two-phase refrigerant mixture leaving the cooling cycle expansion valve. The two-phase refrigerant mixture enters the shell side of the device on the bottom of the heat exchanger. The refrigerant is then routed through spray nozzles which distribute it over tube passes containing the evaporator loop fluid to vaporize it. Any liquid remaining floods tube passes at the bottom of the device which fully vaporizes it. The vapor refrigerant exits the shell side on the top of the device to be sent to the suction line heat exchanger. The evaporator water enters one side of the heat exchanger where it passes back and forth through the shell via the tubes four times in a cross-counterflow configuration.

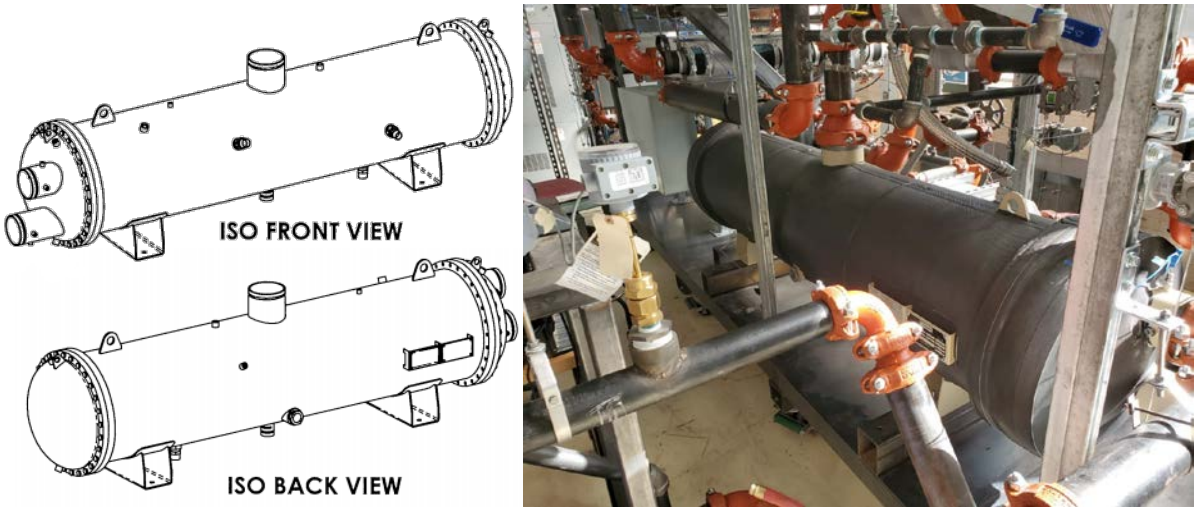

Figure 3-3 Evaporator engineering drawings (Left) and installed unit (Right)

The power and cooling cycle condensers selected for the organic Rankine vapor compression system are shown in Figure 3-4. These heat exchangers are standard, four pass, shell and tube condensers which liquify the vapor refrigerant leaving the economizer and the vapor refrigerant leaving the recuperator in parallel. The units were coupled in parallel to simulate operation as if a single unit were used. However, provisions were made to isolate each condenser to simplify troubleshooting. Vapor enters the shell side of each device through connections on the top of the heat exchangers to condense on the tube passes. The condensate collects at the bottom of the devices where it exits the shell side to be sent to the suction-line heat exchanger or power cycle pump. The ethylene glycol mixture enters one side of each heat exchanger where it passes back and forth through the shell via the tubes four times in a cross-counterflow configuration. While the condensers share an identical external geometry, the internal geometry of the heat exchangers is different to accommodate the differing cycle flow rates.

The final phase changing heat exchanger for the organic Rankine vapor compression system is the generator, shown in Figure 3-5. This heat exchanger is a custom manufactured, compact, aluminum brazed, plate fin, cross-counterflow evaporator which vaporizes the liquid refrigerant leaving the economizer. The refrigerant enters the device on one side of the heat exchanger. It then serpentines

through the device to preheat, vaporize, and superheat. The resulting vapor exits at the opposite end of the device. The ethylene glycol mixture enters one side of the heat exchanger where it flows against the serpentine refrigerant flow in a cross-counterflow configuration. Unlike the shell and tube devices, the complete generator consists of three cores in parallel instead of a single device. The parallel cores reduced pressure loss, improved heat transfer, and mitigated technical risk.

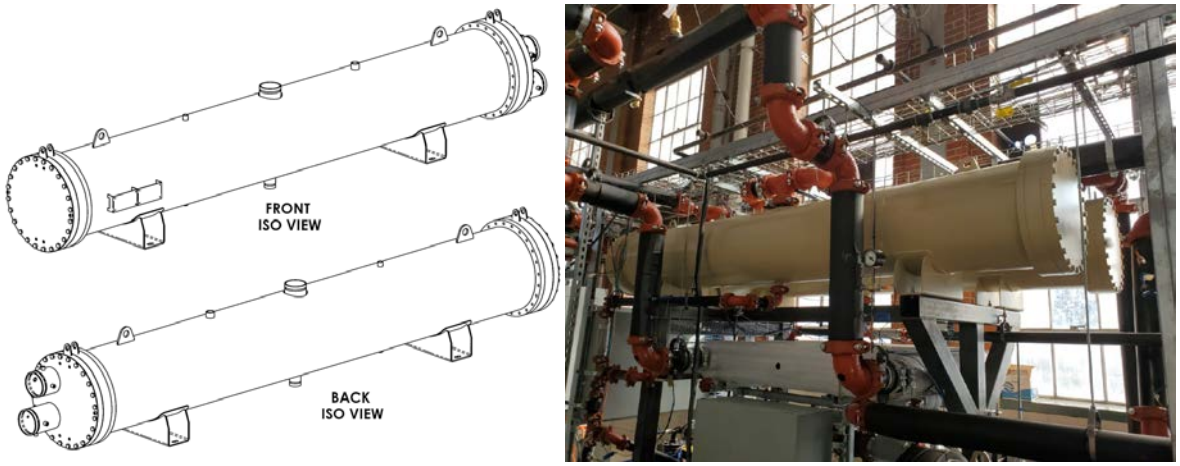

Figure 3-4 Condenser engineering drawings (Left) and installed units (Right)

Figure 3-5 Prototype organic Rankine vapor compression generator

The three recuperative heat exchangers for the organic Rankine vapor compression system are shown in Figure 3-6. Each of these devices were custom manufactured, single-phase, compact, aluminum brazed, plate fin, counterflow heat exchangers. Both the recuperator and suction line heat exchanger consist of two parallel heat exchangers while the economizer only required a single device. Table 3-5 shows the performance capabilities of each heat exchanger as predicted by the manufacturer.

Figure 3-6 Prototype recuperator, economizer, and suction line heat exchanger (Left to Right)

Table 3-5 Manufacturer estimated heat exchanger performance capabilities

	Heat Duty [kW]	***Working Fluid***	***Flowrate [kg s^{-1}]***	***Pressures [kPa]***		***Temperatures [°C]***	
				Inlet	***Differential***	***Inlet***	***Outlet***
Evaporator	305.3	R1234ZE(E)	1.93	276.2	4.0	6.6	6.8
		Water	18.8	-	53	12.0	7.0
Cooling Cycle Condenser	319.9	R1234ZE(E)	1.93	718.6	5.0	50.0	36.4
		50% EG/H_2O	11.8	-	46	29.0	37.0
Power Cycle Condenser	489.0	R1234ZE(E)	3.06	718.6	5.0	50.0	36.4
		50% EG/H_2O	18.1	-	48	29.0	37.0
Generator	499.4	R1234ZE(E)	3.06	2,189	11	55.3	90.9
		50% EG/H_2O	21.0	-	8.0	91.0	84.4
Recuperator	40.8	R1234ZE(E)	3.06	725.0	5.0	52.5	39.4
				2,180	4.6	37.4	46.8
Economizer	36.5		1.93	720.0	5.6	68.2	49.0
			3.06	2,173	6.6	46.6	54.8
Suction Line Heat Exchanger	47.2		1.93	270.0	4.5	6.4	33.9
				713.0	3.5	36.3	18.1

To ensure adequate performance, the thermal conductance of each prototype heat exchanger was calculated from the manufacturer performance estimations. These values were then compared to those needed to satisfy the technical assumptions in the performance simulation. Thermal conductance is commonly used as a proxy for the physical size (and, thus, cost or performance) of the unit [170]. The log mean temperature difference (*LMTD*) for each heat exchanger section (Equation (3.19)) must be determined prior to the thermal conductance values (*UA*) (Equation (3.20)). The log mean temperature difference method for determination of heat exchanger thermal conductance assuming standard counterflow heat exchange was selected for its simplicity over other methods [183]. The total heat exchanger thermal conductance for a device with multiple flow regimes is simply the sum of the individual values.

$$LMTD = \frac{(T_{\text{hot,in}} - T_{\text{cold,out}}) - (T_{\text{hot,out}} - T_{\text{cold,in}})}{\ln\left(\frac{T_{\text{hot,in}} - T_{\text{cold,out}}}{T_{\text{hot,out}} - T_{\text{cold,in}}}\right)} \tag{3.19}$$

$$UA = \frac{\dot{Q}}{LMTD} \tag{3.20}$$

Table 3-6 shows the thermal conductance values of each heat exchanger from the manufacturer performance estimations and the simulation effort. For the manufacturer estimations, pressure losses were assumed to be equally distributed amongst flow regimes in phase change heat exchangers to extrapolate refrigerant transitional temperatures. The inlet vapor mass quality to the evaporated was assumed to be 12.4%, which matched the value given by the component supplier. Finally, constant specific heats were assumed to extrapolate external stream transitional temperatures for the manufacturer estimated heat exchangers. For each heat exchanger, the thermal conductance estimated from the manufacturer values surpass the value required to achieve the results of the performance simulation. This was an indication that the heat exchangers were appropriately sized for the prototype investigation.

Table 3-6 Heat exchanger thermal conductance comparison

Thermal Conductance Values	*Simulation Effort*	*Manufacturer Estimation*
Generator	98.81 kW K^{-1}	115.9 kW K^{-1}
Power Cycle Condenser	156.4 kW K^{-1}	171.6 kW K^{-1}
Cooling Cycle Condenser	111.5 kW K^{-1}	112.2 kW K^{-1}
Evaporator	148.2 kW K^{-1}	154.6 kW K^{-1}
Recuperator	9.931 kW K^{-1}	11.55 kW K^{-1}
Economizer	4.833 kW K^{-1}	5.707 kW K^{-1}
Suction Line Heat Exchanger	6.239 kW K^{-1}	8.040 kW K^{-1}
Total	535.9 kW K^{-1}	579.6 kW K^{-1}

3.2.2. Turbo-Compressor

In addition to the high-performance heat exchangers, the custom fabricated turbo-compressor was a key enabling technology for the prototype development effort. The turbo-compressor was manufactured by Barber Nichols Inc., who was partnered with due to their recent success in developing a similar prototype turbo-compressor for a previous experimental organic Rankine vapor compression demonstration [84]. The design of the turbo-compressor for this effort and its performance characteristics as predicted by the manufacturer are shown in Figure 3-7.

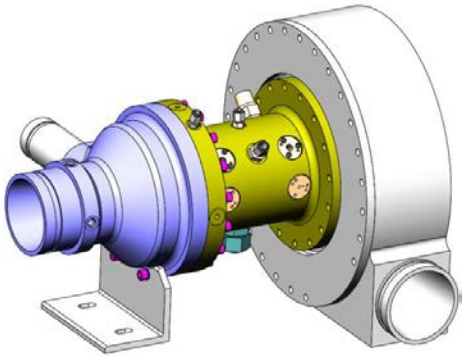

Parameter	*Value*
Working Fluid	R1234ZE(E)
Shaft Speed	30,000 RPM
Turbine Inlet Conditions	90.88 °C, 2,152 kPa, 3.06 kg s^{-1}
Compressor Inlet Conditions	33.84 °C, 267.7 kPa, 1.93 kg s^{-1}
Turbine Performance	2.97 Total to Static Pressure Ratio 52.5 kW Power Generation 83.1% Total to Total Efficiency 0.0911 Meter Blade
Compressor Performance	2.71 Total to Total Pressure Ratio 49.5 kW Power Consumption 82.0% Total to Total Efficiency 0.124 Meter Blade
Transfer Efficiency	94.3%

Figure 3-7 Turbo-compressor design and performance estimation

The design directly coupled a radial turbine with a diameter of 0.0911 m to a centrifugal compressor with a diameter of 0.124 m. The designated operational speed of the two devices was 30 kRPM. As previously mentioned, the efficiency of the turbine and compressor are dependent on both their physical construction and operational parameters [143]. Cordier maps were investigated for both devices to assess the accuracy of the manufacturer performance predictions and the validity of the technical assumptions in the simulation effort. The maps used to investigate the turbine and compressor are shown in Figure 3-8 and Figure 3-9, respectively. The specific speeds (*Ns*) (Equation (3.21)) and specific diameters (*Ds*) (Equation (3.22)) outlined on both maps are representative of the simulation state points presented in Table 3-2, the diameter (*D*) of each device, and the speed (ω) designated by the manufacturer. The units for the diameter, adiabatic enthalpy change (*Had*), volumetric flow rate ($\dot{V}$), and speed must be adjusted to the units specified by the Cordier maps. The inlet volumetric flow rate is used for the determination of compressor specific speed and diameter, but the turbine uses its discharge volumetric flow rate. The specific speed for the turbine was 63.8 while it was 88.7 for the compressor. The specific diameter for the turbine was 1.65 while it was 1.63 for the compressor. For both the turbine and compressor, the calculated specific speed and diameter show an efficiency surpassing 80% is achievable using the device fabricated by Barber Nichols Inc. at the conditions from the performance simulation. Thus, the technical assumptions for the performance simulation regarding the performance of the turbo-compressor are justified. The turbo-compressor installed into the organic Rankine vapor compression cycle is shown in Figure 3-10. In addition to the main fluid inlet and discharge ports, several ancillary connections are shown. Two of the connections drain refrigerant from the central cavity of the device while it is operational. One drain is designated for vapor refrigerant while the other is designated for liquid. Vapor refrigerant enters the central cavity through the shaft seals on the turbine and compressor. Liquid refrigerant is fed to the shaft bearings for lubrication and to the central cavity for cooling. However, the liquid refrigerant cannot enter the flow field of either the compressor or turbine as it could severely

damage either device. Other process connections shown in Figure 3-7 and Figure 3-10 are for instrumentation.

$$Ns = \frac{\omega_{adj} \cdot \sqrt{\dot{V}_{adj}}}{Had_{adj}^{0.75}} \tag{3.21}$$

$$Ds = \frac{D_{adj} \cdot Had_{adj}^{0.25}}{\sqrt{\dot{V}_{adj}}} \tag{3.22}$$

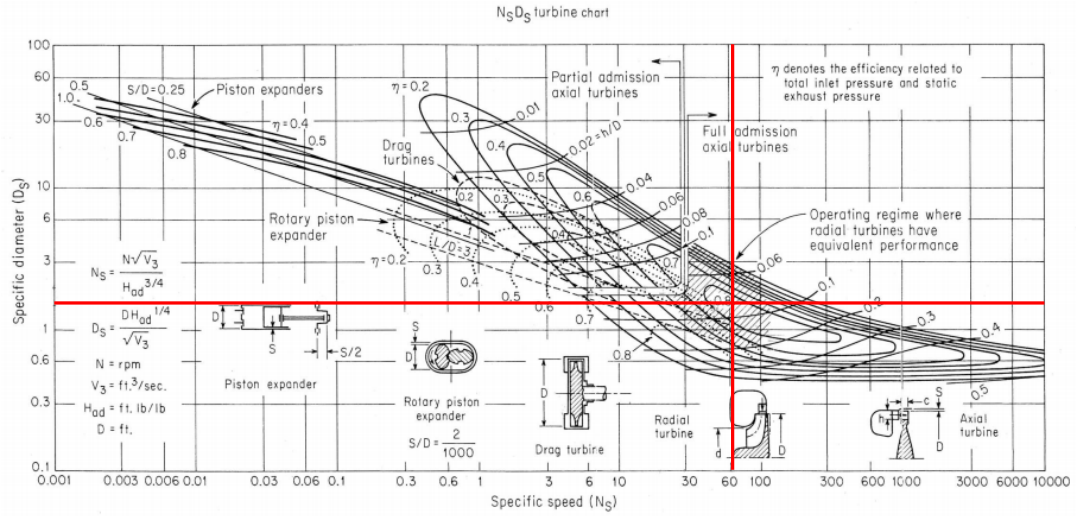

Figure 3-8 Empirical Cordier performance map for expansion devices (Adapted from [143])

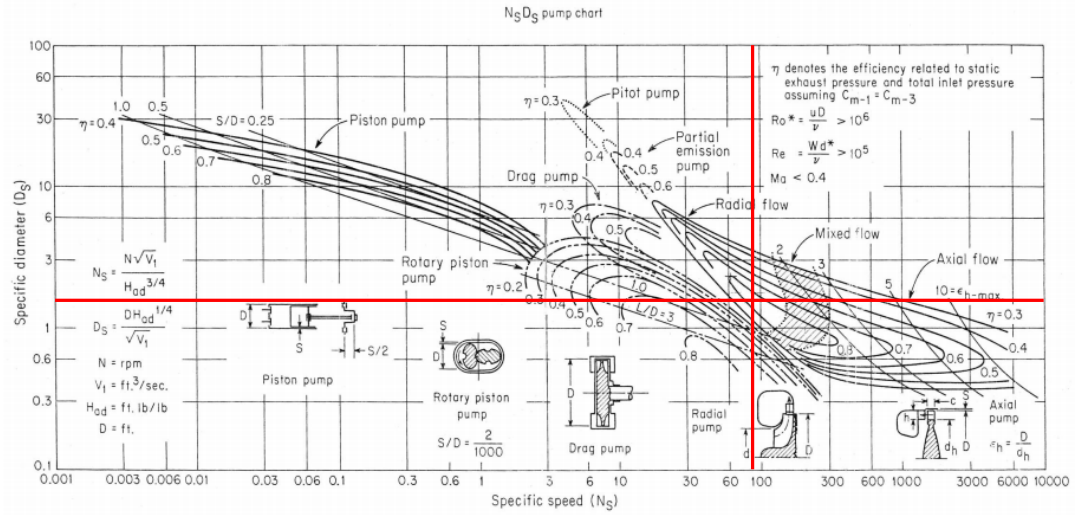

Figure 3-9 Empirical Cordier performance map for compression devices (Adapted from [143])

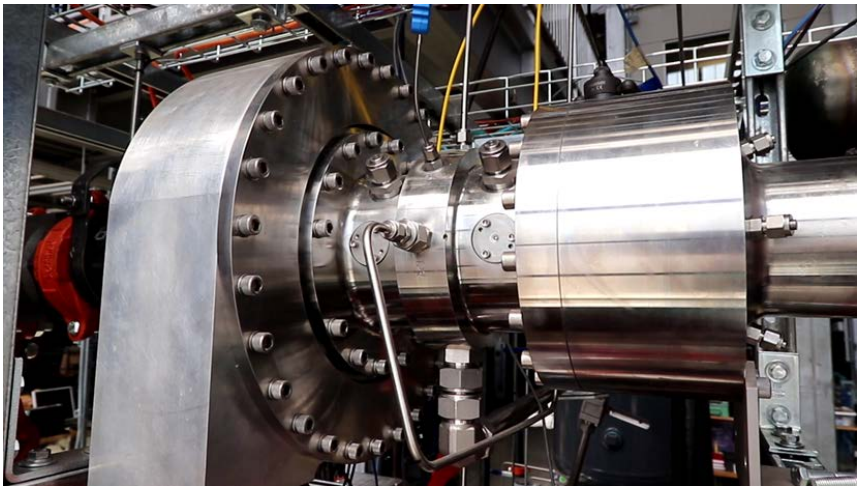

Figure 3-10 Custom fabricated turbo-compressor for the prototype development effort

3.2.3. Power Cycle Pump and Cooling Cycle Expansion Valve

A commercial off the shelf pumping technology was selected for the prototype development effort. Considering the state points presented in Table 3-2, the pump head requirement was 1,602 kPa (from inlet to outlet) with a flow requirement of 8.90 m^3 hr^{-1} (using the inlet density). Figure 3-11 shows the power cycle pump and its full speed operational curve as published by the manufacturer [184]. The required head and flow in units appropriate for the manufacturer performance curve are 535.9 ft-H_2O and 39.18 GPM, respectively. The power cycle pump was grossly oversized for the application to ensure there would not be flow or pressure limitations. A variable frequency drive was selected to modulate the speed of the pump motor to achieve the desired flow rate.

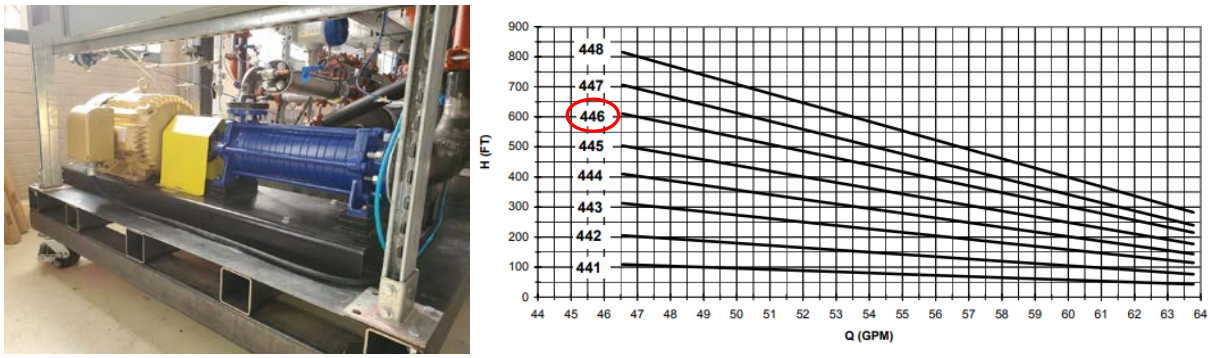

Figure 3-11 Power cycle pump and full speed performance curve (Adapted from [184])

In addition to satisfying the flow and head requirements, the power cycle pump was selected for its low net positive suction head requirements. As a pump draws in fluid, zones of negative relative pressure form before and on the suction side of the pump blades. In some circumstances, this drop in pressure will partially vaporize the fluid being pumped. As a fluid with entrained vapor is pressurized within a pump, the vapor bubbles can collapse (or implode) at supersonic velocities creating shock waves and liquid jets. This process is called cavitation and can be detected qualitatively through the noise it creates or quantitatively via a reduced flow and pressure delivery. When cavitation occurs near the pump housing or blades, the force and vibrations of the shock waves and liquid jets can severely damage the device. If vaporization from suction is severe enough, the pump housing will entirely fill with vapor reducing both the flow and pressure delivery of the pump to zero in a phenomenon called vapor lock. To avoid vapor lock and cavitation, a minimum net positive suction head must be applied to the device during operation. This required net positive suction head (or net positive suction head required) is determined empirically by manufacturers and is specified on data sheets for each device. The full speed net positive suction head requirements for the power cycle pump are shown in Figure 3-12 [184]. To surpass the requirement, net positive suction head (*NPSH*) must be built through increasing the inlet pressure (P) relative to the saturation pressure (P_{sat}) (through subcooling the fluid), increasing its inlet velocity ($\vec{V}$), and/or physically lowering the device a distance (H) relative to the fluid source to create a fluid column which artificially inflates the pressure at the device inlet as shown in Equation (3.23) [185]. Fluid velocity is determined using Equation (3.24) with mass flow, flow area (A), and density (ρ). The universal gravitational constant (g) is also used in the derivation of net positive suction head.

$$NPSH = \frac{1{,}000 \cdot (P - P_{sat})}{\rho \cdot g} + \frac{\vec{V}^2}{2g} + H \tag{3.23}$$

$$\vec{V} = \frac{\dot{m}}{\rho \cdot A} \tag{3.24}$$

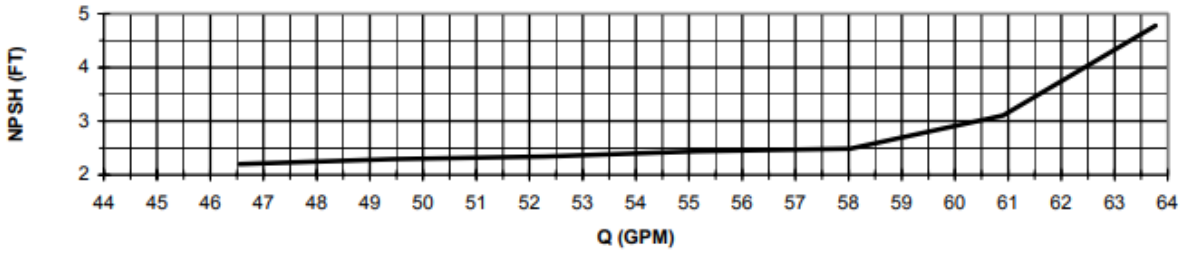

Figure 3-12 Power cycle pump net positive suction head required curve (Adapted from [184])

The net positive suction head available was determined for the power cycle pump using the results of the performance simulation. For modeling purposes, it was assumed that there was no fluid column supplied to the pump to build net positive suction head (*H=0*), the gravitational constant was 9.81 m s^{-2}, and a flow area of 4.768 × 10^{-3} m^2 to represent the diameter of the prototype power cycle pump suction flange. The net positive suction head available with these considerations was 1.22 m (or 4.00 ft). Thus, there is sufficient net positive suction head available for the prototype pump without a fluid column to avoid cavitation and vapor lock during operation.

The only challenge with the selection of the power cycle pump was that the manufacturer did not provide isentropic efficiency estimations for its operation. Thus, the technical assumption of 30% pump isentropic efficiency in the performance simulation carries no merit. A sensitivity analysis was performed with the performance simulation to assess the effect of varying pump efficiency. Holding all other boundary conditions and technical assumptions at their baseline values, the pump isentropic efficiency was varied parametrically from 10% to 100% in increments of 10%. The results of this investigation are listed in Table 3-7.

It is shown that pump isentropic efficiency marginally impacts the thermal efficiency of an organic Rankine vapor compression system, but directly impacts the electrical equivalent efficiency. Thus, the isentropic efficiency of the power cycle pump is not critical for the experimental demonstration but must be considered in future investigations to maximize the energy savings potential of the technology. An

interesting observation from the pump isentropic efficiency sensitivity simulation is that the thermal efficiency of the system improves with a deteriorating pump efficiency. As the pump efficiency deteriorates, the outlet temperature of the pump increases. An increase in pump outlet temperature effectively reduces the heat duty of the generator, which overall improves the thermal efficiency of the system.

Table 3-7 Simulation sensitivity analysis on pump isentropic efficiency

Isentropic Pump Efficiency	***Thermal COP***	***Electrical Equivalent COP***	***Isentropic Pump Efficiency***	***Thermal COP***	***Electrical Equivalent COP***
10%	0.6658	7.639	60%	0.6509	45.52
20%	0.6568	15.22	70%	0.6505	53.10
30%	0.6539	22.79	80%	0.6502	60.68
40%	0.6524	30.37	90%	0.6500	68.25
50%	0.6515	37.95	100%	0.6498	75.83

The final critical component of the organic Rankine vapor compression prototype is the expansion valve, which is shown in Figure 3-13. This component was challenging to size with modeling techniques as an unknown portion of the throttling process is complete by the spray nozzles on the evaporator. A simple, manual globe valve was found to adequately throttle and maintain refrigerant flow for this research effort, but an automated replacement would be required for autonomous, transient system operation.

Figure 3-13 Cooling cycle expansion valve

Chapter 4 Experimental Setup and Methodology

The previous chapter detailed a thermodynamic performance model for an enhanced organic Rankine vapor compression chiller designed to deliver 300 kW of chilled water at boundary conditions representative of thermally driven district cooling systems powered by coolant waste heat from reciprocating engines. The model was used to simulate the baseline performance of the chiller using verified technical assumptions from the manufacturers and suppliers of the turbo-compressor, heat exchangers, and power cycle pump selected to construct a full-scale prototype. This chapter presents the architecture of the organic Rankine vapor compression prototype and the methods used to quantify its operational characteristics during experimentation. Additional design considerations for the prototype are outlined in Appendix B. Appendix C and Appendix D present the operational and maintenance procedures for the prototype, respectively. Appendix E presents the methods used to calibrate system instrumentation. The complete prototype is shown in Figure 4-1 integrated with three auxiliary systems to support its operation: an evaporator loop, a generator loop, and a condenser loop. The complete test facility was constructed on the main level of Room 131 in the Colorado State University Powerhouse Energy Institute.

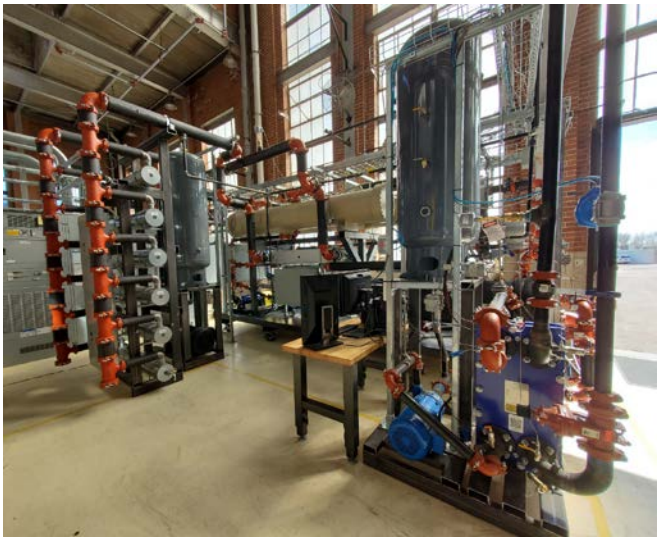

Figure 4-1 Complete experimental organic Rankine vapor compression chiller test facility

4.1. Prototype Layout

A detailed layout of the organic Rankine vapor compression prototype and supporting systems is shown in the piping and instrumentation diagram in Figure 4-2. The architecture of the power and cooling cycle follows the process flow diagram presented in the previous chapter but includes additional equipment outside of the critical components to aid in system operation. The generator loop supplies simulated waste heat to the prototype. The chilling duty of the prototype is rejected to the evaporator loop which simulates a district cooling network. The condenser loop rejects energy that cannot be utilized to the environment using a cooling tower. A detailed list of system components is presented in Table 4-1.

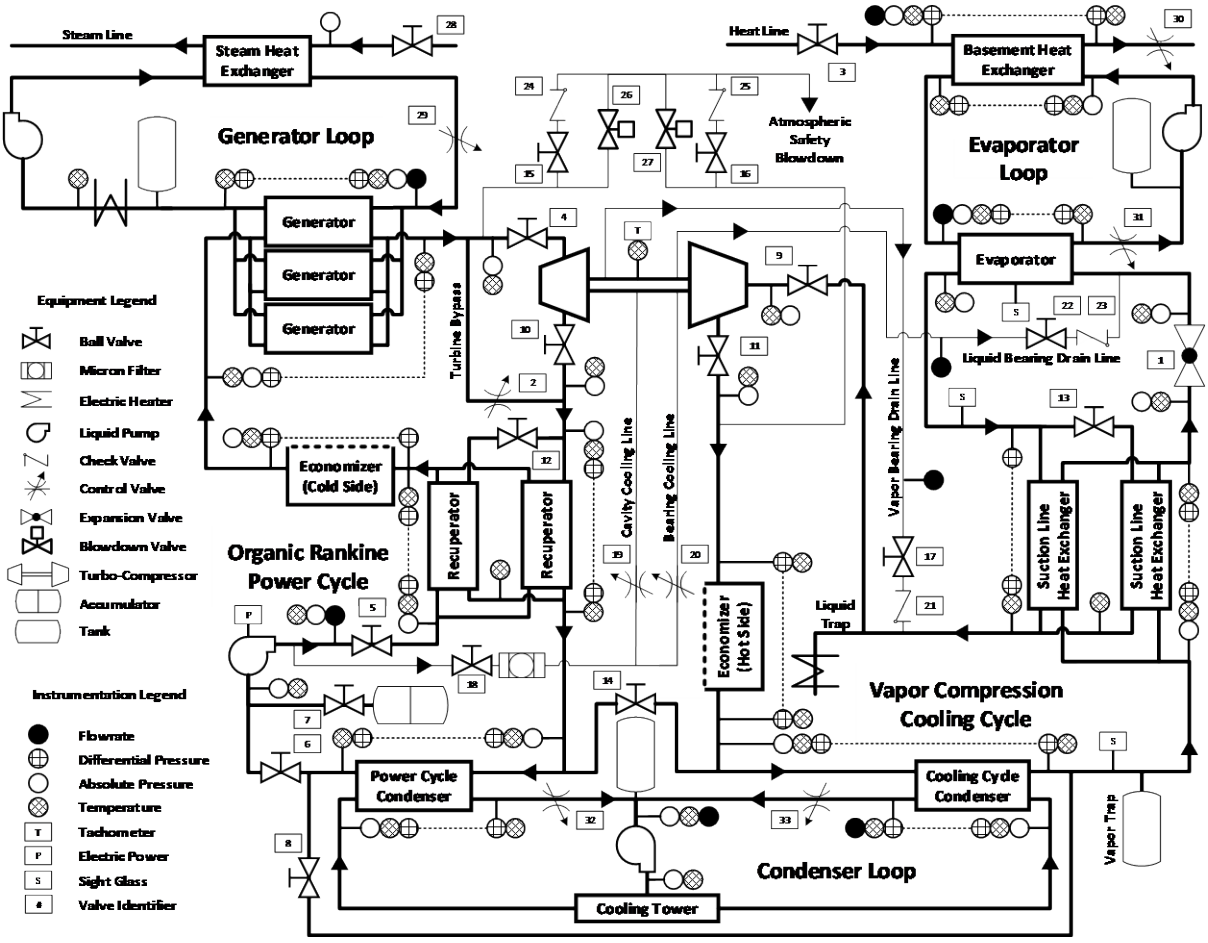

Figure 4-2 Organic Rankine vapor compression prototype piping and instrumentation diagram

Table 4-1 List of organic Rankine vapor compression prototype components

Component	*Supplier*	*Part Number*
Turbo-Compressor	Barber Nichols Inc.	BNTC008-000
Generators	Modine Manufacturing	PR0452300400
Evaporator	Provides	ESWN.5021168-4P
Power Cycle Condenser	Provides	CB.4531250-4P.M
Cooling Cycle Condenser	Provides	CB.4531166-4P.M
Recuperators	Modine Manufacturing	PR0452300200
Economizer	Modine Manufacturing	PR0452300100
Suction Line Heat Exchangers	Modine Manufacturing	PR0452300300
Power Cycle Pump	Sero Pump Systems	SRZS 446 US W X G12E-HK.60
Power Cycle Pump Motor	Baldor	EM41O3T
Power Cycle Pump Variable Frequency Drive	Yaskawa	PW4A0044
Valve 1 & 2	McMaster	4737K58
Valves 3 – 8	Gruvlok	GL7542N
Valves 9 – 14	Gruvlok	GL7542R
Valves 15 – 18	Swagelok	SS-43GS4
Valve 19 & 20	Swagelok	SS-4GUF4
Valve 21	Swagelok	SS-4C-1
Valve 22	Swagelok	SS-T65MS16
Valve 23	Swagelok	SS-16C2-1
Valve 24 & 25	Swagelok	SS-4CPA2-350
Valve 26 & 27	McMaster	4749K154749K15
Valve 28	McMaster	3639T581
Valve 29	McMaster	49265K14
Valve 30 and 31	AVK	45-080-GGN
Valve 30	McMaster	2709N13
Valve 32 and 33	AVK	45-100-GGN
Accumulator	Parker	A9K2310D3KUZ
Liquid Trap Heater	McMaster	3656K13
Liquid Trap Heater Relay	McMaster	70255K342
Liquid Trap Heater Switch	McMaster	48255K26
Micron Filter	Swagelok	SS-4F-05

Component	*Supplier*	*Part Number*
Sight Glasses	McMaster	1079K17
External Loop Surge Tanks	McMaster	4376K18
Steam Line Heat Source	Vapor Power	HS2-4617-SHJ
Steam Heat Exchanger	Armstrong	WSD-4H-102-2E4
Generator Loop Pump	Peerless Pump	C1230A
Generator Loop Pump Motor	Baldor	EJMM2334T
Generator Loop Circulation Heaters	McMaster	35705K162
Basement Heat Exchanger	Alfa-Laval	T8-MFG
Heat Line Heat Source	Mighty Therm	MT2H2000NACK1CJN
Evaporator Loop Pump	Peerless Pump	C620A
Evaporator Loop Pump Motor	Baldor	EJMM3713T
Cooling Tower	Cool Water Technologies	RTCC-150
Cooling Tower Fan Variable Frequency Drive	ABB Inc.	ACH550-PDR-038A-4
Condenser Loop Pump	Paco Pumps	10-25707-140008-2881P
Condenser Loop Pump Motor	Baldor	EJMM4108T

As previously detailed, liquid refrigerant is supplied to the turbo-compressor to lubricate its bearings and provide a cooling effect. The liquid is supplied from the power cycle pump discharge where the system pressure is at its greatest value. The liquid is filtered before it diverts to either lubricate the shaft bearings or provide a cooling effect to the central cavity. The turbo-compressor vapor drain line terminates at the vapor outlet of the suction line heat exchanger where system pressure is at its minimum value. However, the liquid drain line terminates at the refrigerant inlet to the evaporator, so liquid is not drawn into the compressor. An additional feature relating to the turbo-compressor is the turbine bypass loop. This, along with the isolation valves around the device, allowed refrigerant to bypass the turbine during startup and shutdown to avoid the possibility of sending liquid into the device.

Two tanks were integrated into the prototype organic Rankine vapor compression cycle design. The accumulator allowed the addition or removal of refrigerant from the system by simply pressurizing or

depressurizing the non-process side of the device. Once the system charge was optimized, the accumulator also acted as a buffer tank for the power cycle pump to avoid the possibility of vapor lock and cavitation. The second tank was the vapor trap. This device was installed at the highest point within the system to capture non-condensable gasses which have the possibility of entering the system as it is being charged or through the accumulator seal during its pressurization. Opposed to the vapor trap, a liquid trap was placed to capture any liquid refrigerant before it could enter the compressor. The liquid trap consisted of an electric immersion heater which was triggered by a level sensor wired to a relay.

Another feature incorporated into the prototype system design was an atmospheric safety blowdown system. Much of the prototype was hydrostatically pressure rated following Underwriters Laboratory 1995: Heating and Cooling Equipment, Second Edition, with 1999 Revisions [186]. Components which did not conform to this standard were the power cycle pump, turbine, and generators. To prevent an over pressurization of these components, a pressure shutoff switch was used on the power cycle pump to disrupt its power at (or beyond) a critical pressure. The atmospheric safety blowdown system was a backup to the pressure switch. The system used pressure relief valves and pressure safety valves to vent the power and/or cooling cycle refrigerant charge to the atmosphere to avoid an over-pressurization event.

4.2. Subsystems Layout

Three auxiliary systems were required to support experimentation of the prototype organic Rankine vapor compression system: a generator loop, an evaporator loop, and a condenser loop. The generator loop provides a continuous supply of simulated reciprocating engine coolant waste heat (via a hot ethylene glycol-water stream) to the organic Rankine vapor compression system generators. The glycol-water stream is circulated using a high temperature pump and the flowrate through the generator loop is modulated with a control valve. A surge tank was installed into the generator loop to allow the

fluid to expand and contract while its temperature changed without straining the piping network. While not shown on the piping and instrumentation diagram, the primary heat source for this loop is a natural gas fired steam generator. Steam from the steam generator is condensed in the steam heat exchanger to heat the glycol-water stream. The condensed steam is recycled back to the steam generator in a closed loop. It was found that the steam generator provided inadequate energy to power the prototype. Thus, six electric circulation heaters were also integrated into the generator loop. Each heater could be individually powered or disconnected to satisfy the heat demand of the prototype. Figure 4-3 shows the steam generator, steam heat exchanger, and circulation heaters.

Figure 4-3 Generator loop steam source and heat exchanger (Left) and circulation heaters (Right)

The evaporator loop supplies a continuous cooling demand for the organic Rankine vapor compression system to fulfill during experimentation. A pump circulates water within the evaporator loop to be cooled in the evaporator and reheated through the basement heat exchanger. While not shown on the piping and instrumentation diagram, heat is supplied to the basement heat exchanger via a circulated propylene glycol-water loop heated to a fixed temperature through a natural gas fired circulation heater. Flowrate through the basement heat exchanger on the heat line side is modulated with a control valve.

The control valve, whose position is set with a proportional–integral–derivative controller, effectively controls the heat input to the evaporator loop. Similar to the generator loop, the evaporator loop flowrate is modulated with a control valve and the fluid within the loop can expand or contract in a surge tank as its temperature changes. The natural gas fired circulation heater and the skid supporting the evaporator loop equipment is shown in Figure 4-4.

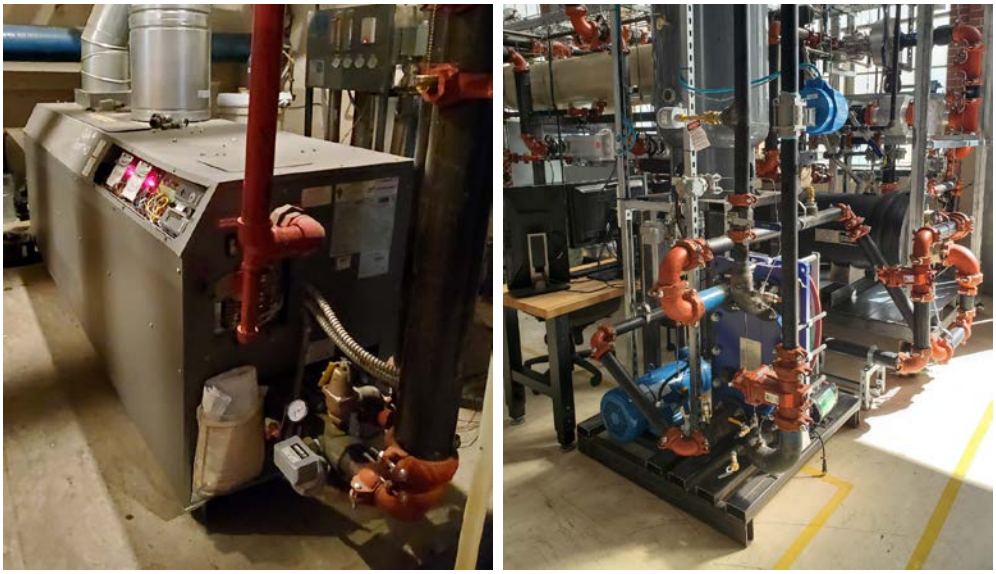

Figure 4-4 Heat line circulation heater (Left) and evaporator loop equipment skid (Right)

The final auxiliary system, the condenser loop, rejects the unusable thermal energy from the prototype to the environment. Heat is transferred from the prototype to the condenser loop through the two condensers. A pump circulates a glycol-water mixture through the condensers to carry the heat to a hybrid evaporative cooling tower shown in Figure 4-5. The cooling tower sprays water over a tube coil containing the glycol-water mixture to cool it. The heated water is than evaporatively cooled with a fan powered by a variable frequency drive. The variable frequency drive on the fan is set by a proportional–integral–derivative controller to effectively control the heat duty of the condenser loop. Like the other auxiliary loops, the condenser loop flowrate is modulated with control valves and the fluid within the loop can expand or contract in a surge tank as its temperature changes.

Figure 4-5 Condenser loop cooling tower

With the equipment and configuration of the prototype and auxiliary systems determined, a system solid model was created to guide the construction of the test facility. The solid model was generated using SolidWorks 2018 by Dassault Systems [187]. The complete solid model is shown in Figure 4-6. All critical prototype components are identified apart from the recuperators, which are located out of view beneath the generators.

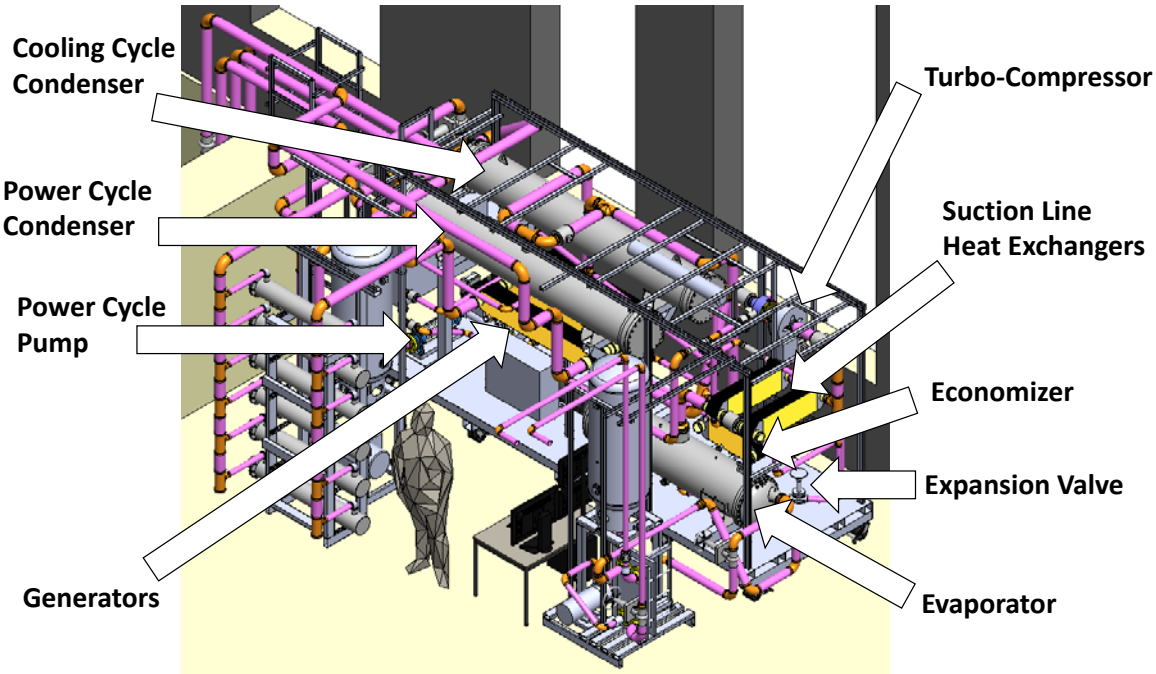

Figure 4-6 Test facility solid model with critical prototype components labeled

4.3. Instrumentation

The experimental test facility was fitted with instrumentation to monitor the system during testing and record the data required to analyze system performance. The placement of instruments is shown in the piping and instrumentation diagram in Figure 4-1. Signals from instrumentation were sent to a data acquisition system where they were transmitted through ethernet to a virtual interface for processing and collection. The virtual interface was developed in LabVIEW 2018 [188]. Table 4-2 lists the critical data acquisition system components and their functionality.

Table 4-2 List of test facility data acquisition components

Part Number	***Description***	***Function***
cRIO-9066	Data acquisition controller	Communicates signals from modules to virtual interface
cRIO-9149	Data acquisition controller expansion chassis	Increases controller module capacity
NI-9266	Current output module	Sets variable frequency drives and actuating valve positions
NI-9476	Voltage output module	Trips variable frequency drives
NI-9205	Voltage input module	Registers voltage signals from instrumentation
NI-9213	Temperature input module	Registers voltage signals from thermocouples

Instrumentation to monitor system performance was selected considering the operating conditions of the experimental facility, the capabilities of the selected data acquisition hardware, and the requirements of the commercial chiller performance rating standards used to guide experimentation. System pressure and temperature instrumentation was calibrated to increase accuracy over the factory values following the standard error of linear regression method from the 2018 American Society of Mechanical Engineers Performance Test Code 19.1 [189]. Table 4-3 lists the bias error, range, and part number of each instrument. System pressure transmitters where sourced from ifm Effector and measured gauge pressure. Each reading was scaled by the reading of an ambient pressure transmitter to convert the gauge readings to absolute readings. Bias errors for system pressure transmitters in Table 4-3 are adjusted to include the compounded error of the absolute transmitter. The absolute pressure transmitter was also sourced from ifm Effector. Differential pressure transmitters were sourced from Dwyer Instruments while thermocouples were sourced from TC Direct. Four types of flow meters were used throughout the

prototype. The volumetric flow meters in the auxiliary systems were sourced from Badger. The remaining volumetric flow meters were sourced from Omega Engineering and the power cycle mass flow meter was sourced from Krohne. Turbo-compressor shaft speed was measured with a proximity sensor and driver sourced from Metrix. The power consumption of the power cycle pump was measured with a current transducer from Johnson Controls assuming a three-phase voltage of 460 VAC, which was measured with a multimeter at the pump variable frequency drive power terminals.

Table 4-3 List of test facility instrumentation

Pressure Transmitter	***Error ± kPa***	***Upper Limit kPa***	***Part Number***
Generator Refrigerant Inlet	4.126	3,547	PX3223
Turbine Inlet	4.251	-	-
Power Cycle Pump Outlet	3.986	-	-
Recuperator Liquid Inlet	4.361	-	-
Economizer Liquid Outlet	4.142	-	-
Turbine Outlet	1.349	1,134	PX3244
Power Cycle Condenser Refrigerant Inlet	1.272	-	-
Power Cycle Pump Inlet	1.477	-	-
Compressor Outlet/Economizer Vapor Inlet	1.303	-	-
Cooling Cycle Condenser Refrigerant Inlet	1.392	-	-
Expansion Valve Inlet	1.320	-	-
Recuperator Vapor Inlet	1.495	-	-
Suction Line Heat Exchanger Liquid Inlet	1.343	-	-
Compressor Inlet	1.063	789	PX3224
Expansion Valve Outlet	0.984	-	-
Evaporator Refrigerant Outlet/ Suction Line Heat Exchanger Vapor Inlet	0.994	-	-
Generator Glycol Inlet	0.987	-	-
Power Cycle Condenser Glycol Inlet	1.100	-	-
Cooling Cycle Condenser Glycol Inlet	0.961	-	-
Condenser Loop Pump Inlet	0.962	-	-
Condenser Loop Pump Outlet	0.946	-	-
Evaporator Water Inlet	0.980	-	-
Basement Heat Exchanger Water Inlet	1.020	-	-
Basement Heat Exchanger Glycol Inlet	0.988	-	-
Ambient Pressure	0.5	100	PT0507
Differential Pressure Transmitter	***Error ± kPa***	***Upper Limit kPa***	***Part Number***
Power Cycle Condenser Glycol	0.6065	186.6	3100D-4-FM-1-1
Evaporator Water	-	-	-
Cooling Cycle Condenser Glycol	-	-	-
Basement Heat Exchanger Water	-	-	-
Power Cycle Condenser Refrigerant	0.1213	37.33	3100D-3-FM-1-1

Differential Pressure Transmitter	*Error ± kPa*	*Upper Limit kPa*	*Part Number*
Economizer Vapor	0.1213	37.33	3100D-3-FM-1-1
Cooling Cycle Condenser Refrigerant	-	-	-
Generator Glycol	-	-	-
Recuperator Liquid	-	-	-
Evaporator Refrigerant	-	-	-
Suction Line Heat Exchanger Liquid	-	-	-
Recuperator Vapor	-	-	-
Generator Refrigerant	-	-	-
Economizer Liquid	-	-	-
Suction Line Heat Exchanger Vapor	-	-	-
Basement Heat Exchanger Glycol	-	-	-

Thermocouple	*Error ± °C*	*Range °C*	*Part Number*
Generator Glycol Inlet	0.0652	40-120	205-615
Generator Glycol Outlet/Generator Loop Heater Inlet	0.0746	-	-
Generator Loop Heater Outlet	0.0583	-	-
Evaporator Water Inlet	0.0354	2.2-32.2	-
Evaporator Water Outlet	0.0265	-	-
Basement Heat Exchanger Water Inlet	0.0194	-	-
Basement Heat Exchanger Water Outlet	0.0220	-	-
Power Cycle Condenser Glycol Inlet	0.0587	12.8-45.6	-
Power Cycle Condenser Glycol Outlet	0.0596	-	-
Cooling Cycle Condenser Glycol Outlet	0.0391	-	-
Cooling Cycle Condenser Glycol Inlet	0.0491	-	-
Condenser Loop Pump Inlet	0.0610	-	-
Condenser Loop Pump Outlet	0.0427	-	-
Expansion Valve Inlet	0.0623	0.5-95	-
Expansion Valve Outlet	0.0950	-	-
Evaporator Refrigerant Outlet/ Suction Line Heat Exchanger Vapor Inlet	0.0695	-	-
Basement Heat Exchanger Glycol Inlet	0.0852	-	-
Basement Heat Exchanger Glycol Outlet	0.0931	-	-
Cooling Cycle Condenser Refrigerant Outlet	0.0657	-	-
Turbo-Compressor Cavity	0.0647	-	-
Recuperator Vapor Balance	0.0671	-	-
Recuperator Vapor Inlet	0.0716	-	-
Recuperator Vapor Outlet	0.0698	-	-
Recuperator Liquid Inlet	0.0602	-	-
Economizer Vapor Outlet	0.0508	-	-
Economizer Liquid Outlet	0.0642	-	-
Recuperator Liquid Outlet/Economizer Liquid Inlet	0.0541	-	-
Economizer Vapor Inlet	0.0493	-	-
Generator Refrigerant Inlet	0.0873	-	
Generator Refrigerant Outlet	0.0823	-	-
Turbine Inlet	0.0789	-	-
Turbine Outlet	0.0630	-	-
Power Cycle Condenser Refrigerant Inlet	0.0636	-	-
Power Cycle Condenser Refrigerant Outlet	0.0710	-	-

Thermocouple	*Error ± °C*	*Range °C*	*Part Number*
Power Cycle Pump Inlet	0.0635	40-120	205-615
Power Cycle Pump Outlet	0.0659	-	-
Compressor Inlet	0.0587	-	-
Compressor Outlet	0.0706	-	-
Cooling Cycle Condenser Refrigerant Inlet	0.0634	-	-
Suction Line Heat Exchanger Vapor Outlet	0.0618	-	-
Suction Line Heat Exchanger Vapor Balance	0.0570	-	-
Suction Line Heat Exchanger Liquid Inlet	0.0565	-	-
Suction Line Heat Exchanger Liquid Outlet	0.1305	-	-
Volumetric Flow Meter	***Error ± % Reading***	***Range $m^3\ hr^{-1}$***	***Part Number***
Cooling Condenser Loop Glycol	1%	9-180	SDI1D1N10-0200
Full Condenser Loop Glycol	-	-	-
Generator Loop Glycol	-	-	-
Evaporator Loop Water	-	3-68	-
Turbo-Compressor Liquid Drain	-	0.23-0.45	FLMH-1002SS-MA
Turbo-Compressor Vapor Drain	-	0-0.12	FMA2808
Mass Flow Meter	***Error ± % Reading + kg s^{-1}***	***Range kg s^{-1}***	***Part Number***
Power Cycle	0.1% + 0.00061	0-4.056	VE234S0ME0G 010000003000
Tachometer	***Error ± % Reading***	***Range kRPM***	***Part Number***
Turbo-Compressor Speed	<1%	0.01-100	MX2033 and 10026-925-10-02
Power Meter	***Error ± % Reading***	***Range kW***	***Part Number***
Power Cycle Pump Power	2%	4.988-49.88	CTD-C1G00-1

4.4. Test Schedule

The experiments performed on the prototype followed rating standards of commercial chilling technologies to accurately verify system performance characteristics over a wide range of operating conditions. The primary standard referenced was Air-conditioning, Heating, and Refrigeration Institute Standard 551/591, 2018 Standard for Performance Rating of Water-chilling and Heat Pump Water-heating Packages Using the Vapor Compression Cycle [44]. This is the same standard from which the organic Rankine vapor compression chiller boundary conditions were taken to ensure the relevance of the prototype for district cooling applications. Standard 560 from the Air-conditioning, Heating, and

Refrigeration Institute, 2000 Standard for Absorption Water Chilling and Water Heating Packages [190], was also used to guide experimentation considering Standard 551/591 does not explicitly encompass performance rating methods for thermally driven cooling systems. Both referenced standards require three sets of tests to be performed on a chiller to fully rate its performance. The system does not have to operate continuously for rating purposes, meaning startup and shutdown between each testing condition is allowed. Refrigerant charge should not vary for a series of test points. Thermodynamic properties for fluids can be determined using presented empirical formulas in either standard or National Instruments REFPROP software version 9.1 or later to assess performance.

The first system experiment quantifies the full-load performance of the technology. The boundary conditions at which the system must operate at for the full-load test are outlined in Table 4-4. The prototype was designed to deliver a full-load chilling duty of 300 kW at its standard operating conditions. Considering the chilling duty, the target volumetric flow rate in the evaporator loop is 51.44 m^3 hr^{-1}. The heat duty of both condensers and the generator at this chilling duty are dependent upon the efficiency of the prototype. Thus, the experiment to quantify full-load performance must be completed iteratively to determine and set the flowrates of the generator and condenser loop. Further iteration is required if the evaporator heat duty is different from the target value. For a full-load experiment to be valid, the evaporator load must fall within ±5.166%, the external loop flowrates must fall within ±5.000%, the condenser and evaporator temperatures must fall within ±0.28°C, and the generator temperature must not deviate beyond ±3.0°C of the specified values. Each of the values are to be taken as the average of the experimental dataset. The dataset must span >900 seconds with a minimum of 30 data points collected at uniform time intervals. Data points may also be time averaged over periods not exceeding 1/60 the test interval. Furthermore, the sample standard deviation of the evaporator outlet and condenser inlet temperature measurements cannot exceed 0.10°C, the ratio of the standard deviation to the average

value of the external loop flowrates cannot exceed 0.750%, and the absolute value of the energy balance cannot exceed 3.69%.

Table 4-4 Full-load test conditions for prototype experimentation (Adapted from [44,190])

Boundary Condition	***Temperature [°C]***	***Flow Rate [m^3 hr^{-1} kW^{-1}]***	***Fouling Parameter [m^2 K^{-1} kW^{-1}]***
Evaporator Water Outlet	7.00	0.1715	0.018
Condenser Glycol Inlet	30.00	0.2016	0.044
Generator Glycol Inlet	91.00	0.1955	0.018

With a successful full-load, standard operating condition experiment complete, another full-load experiment must be performed at altered operating conditions to determine the effect heat exchanger fouling will have on system performance. This inherent degradation to the thermal performance of heat exchangers occurs to a new system after it is installed and operated in-field. Altering the leaving evaporator water, entering condenser glycol, and entering generator glycol temperatures of the organic Rankine vapor compression system by their corresponding adjusted temperatures demonstrates how a new system would operate after fouling occurs. Equation (4.1) to Equation (4.7) show how the specified fouling parameters in Table 4-4 are used to determine an adjusted temperature (T_{adj}) for each external loop heat exchanger. These formulations require the inlet and outlet temperatures of the external loop streams (T_{ext}), the saturation temperature of the refrigerant internal to the system ($T_{sat,r}$), the heat duty of the heat exchanger as measured with the external stream instrumentation ($\dot{Q}_{\mathrm{ext}}$), the external heat transfer area of the heat exchanger (A_{ext}), and the specified fouling parameter from the test standards (*FP*). The adjusted temperature is added to the condenser glycol inlet temperature, subtracted from the evaporator water leaving temperature, and subtracted from the generator glycol inlet temperature to appropriately alter the standard testing conditions for fouling.

$$T_{\text{range}} = \left| T_{\text{out,ext}} - T_{\text{in,ext}} \right| \tag{4.1}$$

$$T_{small} = \left| T_{sat,r} - T_{out,ext} \right| \tag{4.2}$$

$$T_{LMTD} = \frac{T_{range}}{\ln\left(1 + \frac{T_{range}}{T_{small}}\right)} \tag{4.3}$$

$$T_{ILMTD} = FP \frac{\dot{Q}_{ext}}{A_{ext}} \tag{4.4}$$

$$FC = \frac{T_{range}}{T_{LMTD} - T_{ILMTD}} \tag{4.5}$$

$$T_{clean} = \frac{T_{range}}{e^{FC} - 1} \tag{4.6}$$

$$T_{adj} = T_{small} - T_{clean} \tag{4.7}$$

The second set of tests performed on the device demonstrates the ability of the technology to operate at conditions, or applications, outside of the standard at full load. Table 4-5 shows a summary of these off-design operating conditions, which do not have to be corrected for fouling.

Table 4-5 Off-design test conditions for prototype experimentation (Adapted from [44,190])

Boundary Condition	***Temperature [°C]***	***Flow Rate [$m^3\ hr^{-1}\ kW^{-1}$]***
Evaporator Water Outlet	2.20 to 21.10	0.0858 to 0.3430
Condenser Glycol Inlet	12.80 to 40.60	0.1008 to 0.4032
Generator Glycol Inlet	82.00 to 204.0	0.0978 to 0.3910

The system is to be tested over the specified range of off-design test points to the limitations of the technology. There are no accuracy criteria for the evaporator heat duty in these tests as the system efficiency is expected to change as a function of the varying conditions. However, the heat input to the system must remain within 5.000% of the full-load test value. All other test criteria related to timing,

temperature, flowrate, and energy balance are identical to those of the full-load test. Only one variable is to be altered from the standard value during any given test. The maximum increment for varying temperatures is 2.0°C for the evaporator, 3.0°C for the condenser, and 5.0°C for the generator. The flowrates are to be altered such that the temperature difference across each heat exchanger is approximately halved at the highest flowrate and doubled at the lowest flowrate. Additional off-design tests at flowrates between the standard and both the lowest and highest testing conditions shall also be complete. Thus, each external loop shall have four off-design experimental data points to correlate to the full-load standard.

The final set of tests assess the part-load operating characteristics of the technology using the Integrated Part-Load Value methodology. Integrated Part-Load Value is a weighted efficiency based upon the ability of a chilling technology to provide 100%, 75%, 50%, and 25% chilling loads at conditions representative of blended climate data. Weighting factors for the Part-Load Value (*PLV*) are shown in Equation (4.8). As previously detailed, a chiller is only expected to operate at its standard, full-load condition 1% of its useful lifecycle. Thus, the weighting factor applied to the 100% load COP value is 0.01.

$$PLV = 0.01 \cdot COP_{100\%} + 0.42 \cdot COP_{75\%} + 0.45 \cdot COP_{50\%} + 0.12 \cdot COP_{25\%} \tag{4.8}$$

The altered operating conditions for part-load experimentation are outlined in Table 4-6. All external loop flowrates are held at their full-load values. Neither the evaporator water leaving temperature, nor the generator glycol inlet temperature vary from the baseline test aside from their correction for fouling. The evaporator heat duty quantified through experimentation at turn-down must fall within 2% of the full load value from the target. If the targeted loads cannot be tested within 2% of the full load value, linear interpolation is allowed on data points above and below the targeted load. If a system being rated is unable to perform at or below a part load condition, the targeted efficiency for the part load condition is adjusted using Equation (4.9) with the data for the closest approaching loading

condition tested. Test criteria related to timing, temperature, and flowrate are identical to those of the full-load test. The energy balance criteria vary for each test point (±3.69% at 100% load, ±5.31% at 75% load, ±7.33% at 50% load, and ±10.94% at 25% load).

$$COP_{adj} = \frac{COP_{test}}{\left(-0.13\frac{Load_{adj}}{Load_{test}}\right)+1.13} \tag{4.9}$$

Table 4-6 Part-load test conditions for prototype experimentation (Adapted from [44,190])

Boundary Condition	***Temperature [°C]***	***Fouling Parameter [m^2 K^{-1} kW^{-1}]***
Evaporator Water Outlet	7.00	0.018
Condenser Glycol Inlet		
100% Load	30.00	
75% Load	24.50	0.044
50% Load	19.00	
25% Load	19.00	
Generator Glycol Inlet	91.00	0.018

4.5. Data Analysis

A data reduction model was developed to verify the quality of data collected against the rating criteria and assess its implications regarding prototype performance. Engineering Equations Solver and Microsoft Excel with a REFPROP 10.0 software package were used to create the reduction model [182,191]. A hand calculation for model verification is presented in Appendix F using the dataset collected to assess the full-load, standard operation of the prototype.

The reduction model simply requires raw data from the data acquisition system to be pasted into the model to function. The data from the data acquisition system contains the calibrated readouts of each module channel and several control variables such as variable frequency drive setpoints and timestamps for each datapoint. The timestamp is used to pull the relevant portion of the data from the data acquisition

master file. Once pasted into the reduction model, variables from the dataset are reduced to their average value ($\bar{z}$), standard deviation (s), random error (E_R), and total error (E_T) using Equation (4.10) to Equation (4.13), respectively [189]. The average, standard deviation, and random error require the total number of data points (N), the random error requires the Student T coverage factor for a 95% confidence two-tailed distribution (k), and the total error requires the bias error of the instrument (E_B).

$$\overline{z} = \frac{\sum_{i=1}^{n} z_i}{N} \tag{4.10}$$

$$s = \sqrt{\frac{\sum_{i=1}^{n} (z_i - \overline{z})^2}{N}} \tag{4.11}$$

$$E_R = \frac{k \cdot s}{\sqrt{N}} \tag{4.12}$$

$$E_T = \sqrt{E_R^2 + E_B^2} \tag{4.13}$$

With averaged data values determined, state points for the refrigerant within the prototype are populated into tables for the power cycle and cooling cycle. Temperatures at the inlets and outlets of each system component are documented as their true value and converted to Kelvin for use with internal functions to REFPROP. Temperatures at state points within two-phase heat exchangers are determined using REFPROP temperature functions assuming the saturated quality (whether vapor or liquid) and the pressure at the state point. Pressures are documented as their true value where recorded and converted to megapascals for use with REFPROP functions. Where a pressure transmitter is installed upstream of a component with a differential pressure transmitter across the component, the outlet pressure is determined by subtracting the differential reading from the inlet reading without scaling the value for frictional or gravitational discrepancies. The reverse is true where a pressure transmitter is installed

downstream of a component with a differential pressure transmitter across the component. Pressure loss through multi-phase heat exchangers is assumed to be equally distributed amongst the flow regimes to determine pressure state points. Pressure within the evaporator is assumed constant from the outlet pressure transmitter reading as no differential transmitter could be installed due to the working principle of the spray nozzles.

The pressure and temperature state points are then used as inputs to REFPROP functions to determine enthalpy at each state point. Enthalpy at saturated conditions is determined assuming the respective quality and pressure at the state point. Enthalpy across the expansion valve and into the evaporator inlet is assumed constant. In some instances, the enthalpy will be incorrectly determined due to precision limitations of the instrumentation or unique operating conditions. For example, when there is excessive subcooling in the power cycle condenser, the recuperator can begin to condense the vapor flowing through it causing the reading at the recuperator vapor outlet and/or power cycle condenser vapor inlet to assume it is at a liquid state. This could also occur at the generator outlet when pinch limitations are met, and the fluid is unable to fully vaporize and superheat. Similarly, the evaporator outlet can assume a liquid state due to the working principle of the spray evaporator which discharges a nearly saturated vapor. Alternatively, when there is insufficient cooling in the condensers, the measurements can predict that the refrigerant exists as a superheated vapor or subcooled liquid when it could exist as a two-phase fluid.

When an incorrect enthalpy reading is produced for the recuperator, and/or generator, the incorrectly determined enthalpy values are instead determined by performing an energy balance on the device as shown in Equation (4.14). The energy balance uses the mass flow rate ($\dot{m}$) and the enthalpy (h) difference across both the hot and cold process sides of a heat exchanger to determine the unknown variable. When an incorrect enthalpy reading at the generator outlet translates to an incorrect reading at the turbine inlet, the turbine inlet value is corrected to equal the generator outlet condition whether the

experimental or corrected value. Similarly, when an incorrect enthalpy reading at the recuperator vapor outlet translates to an incorrect reading at the power cycle condenser inlet, the condenser inlet value is corrected to equal the recuperator vapor outlet condition whether the experimental or corrected value. When an incorrect reading is produced for the evaporator outlet, a saturated vapor condition is assumed at the outlet and suction line heat exchanger vapor inlet as the absence of liquid in the vapor stream is qualitatively verified using the sight glass at the evaporator discharge port. Data correction is not required to the power cycle condenser discharge or pump inlet state points if the fluid is not fully condensed. This is because operation at this condition is not possible considering the pump would vapor lock from zero net positive suction head. However, when the cooling cycle condenser failed to fully condense refrigerant, the corrected, high-temperature, suction line heat exchanger inlet enthalpy was determined using an energy balance on the suction line heat exchanger. When this correction was required, the same resulting enthalpy value was also assumed at the cooling cycle condenser outlet and the two-phase to liquid transition state point was removed from the dataset. With the enthalpies for each state point properly characterized, the entropies at each state point are determined using REFPROP functions with state point enthalpy and pressure as inputs. All parameters determined using REFPROP functions for refrigerant were determined assuming equations of state presented by Akasaka for R1234ZE(E) [192].

$$\dot{m}_{\text{hot}} \cdot (h_{\text{hot,in}} - h_{\text{hot,out}}) = \dot{m}_{\text{cold}} \cdot (h_{\text{cold,out}} - h_{\text{cold,in}}) \tag{4.14}$$

The only external loop state points which required quantification were the temperatures and pressures which were taken as averaged values from the raw data files. Similar to the state points internal to the prototype, where a pressure transmitter is installed upstream of a component with a differential pressure transmitter across the component, the outlet pressure is determined by subtracting the differential reading from the inlet reading without scaling the value for frictional or gravitational discrepancies and vice versa. This has inconsequential implications for performance rating as other

external loop fluid properties used for rating purposes, such as specific heat and density, are uninfluenced by liquid pressure.

The power cycle mass flow is determined experimentally with the Coriolis mass flow meter while the cooling cycle mass flow had to be determined using an energy balance across the economizer (Equation (4.14)). Mass flow for external loops (except for the power cycle condenser) were determined by scaling the measured volumetric flowrates by the fluid density at the measurement point. Power cycle condenser glycol mixture mass flowrate was determined by deducting the cooling cycle condenser glycol mixture mass flowrate from the total condenser loop glycol mixture mass flowrate which was measured at the condenser loop pump inlet. Density for water was determined using REFPROP functions with temperature and pressure at the measurement point as the input variables. Pressure is only required as an input for water calculations to verify the fluid is in a liquid state. Density (ρ) for 50% ethylene glycol-water was determined using a second order polynomial with temperature (T) at the measurement point as the independent variable as shown in Equation (4.15). Specific heats for water and refrigerant (for heat duty calculations) were determined using REFPROP functions with averaged temperature and pressure across the heat exchanger (section or whole device) as the input variables. Specific heat (Cp) for 50% ethylene glycol-water was determined using a second order polynomial with averaged temperature (T_{avg}) across the component as the independent variable as shown in Equation (4.16). Second order polynomials for 50% ethylene glycol-water properties were derived from data presented in the technical data sheet for the specific glycol implemented in the test loops [193].

$$\rho = -0.001519 \cdot T^2 - 0.4901 \cdot T + 1,097 \tag{4.15}$$

$$Cp = -3.428 \cdot (10^{-8}) \cdot T_{avg}^2 + 0.003957 \cdot T_{avg} + 3.170 \tag{4.16}$$

With state points, flow rates, and other thermophysical properties determined, several system wide performance calculations are performed. These calculations closely followed the methods presented

in Chapter 3 with a few exceptions. First, considering discrepancies in data from random, bias, and systematic error, heat duties for each heat exchanger were determined for both processes (hot and cold) except for devices where an energy balance was performed to assess a corrected enthalpy value or a mass flow. Following the performance rating standards, thermal COP, electrical equivalent COP, organic Rankine cycle efficiency, vapor compression cycle COP, and energy balance were assessed using the heat duties of the generator, evaporator, and condensers in addition to the turbine, compressor, and pump work. Performance characteristics presented in this work used the heat duty of the external streams for the generator, evaporator, and condensers following the rating methods. The external heat duties are preferable to the internal heat duties as no data correction was required on the external streams and performance calculations are independent of pressure measurements. Electrical equivalent COP and organic Rankine cycle efficiency used measured power cycle pump power consumption instead of the thermodynamic work calculated using the measured mass flow and enthalpy difference across the device. However, thermodynamic pump work was used in the energy balance as the parasitic losses of the variable frequency drive and pump motor do not contribute to energy transfer to or from the system. The turbine and pump work (as well as their efficiencies) were determined using the associated enthalpies and flowrate measurements. Alternatively, compressor work and efficiency were determined using total enthalpies (h_o) instead of the measured static values (h) to account for changes in fluid kinetic energy during compression following Equation (4.17). Velocity ($\vec{V}$) for the total enthalpy calculation was determined with the respective mass flow, density (calculated using REFPROP density functions with pressure and temperature (or inlet entropy for an isentropic process) as inputs), and the flow area at the measurement point.

$$h_o = h + \frac{\vec{V}^2}{2{,}000} \tag{4.17}$$

The calculation of total properties was only required for the compressor as other devices with a considerable density change (generator, condensers, evaporator, and power cycle pump) minimized kinetic energy change by varying the outlet flow area of the component relative to the inlet.

In addition to fluid machinery work and efficiency, pinch temperatures and adjusted temperatures for fouled testing were determined for each external loop heat exchanger at each test condition following the methods presented in the previous section. A number of plots were also generated to visualize system operation and stability including: turbine and compressor performance maps, real time flowrates for the power cycle refrigerant, cooling cycle refrigerant (through an economizer energy balance), and external loop fluids, inlet and outlet temperatures and heat duties for each of the external loop heat exchangers, and both temperature to entropy and pressure to enthalpy state point diagrams against respective refrigerant saturation curves. Finally, a complete error assessment was performed on each calculation to provide further confidence in the results. The methods used to plot turbine and compressor performance data were informed by the device manufacturer [194,195]. The methods used to propagate experimental error were taken from the 2018 American Society of Mechanical Engineers Performance Test Code 19.1 [189]. Turbo-compressor performance mapping and experimental error propagation methods are detailed in the subsequent sections.

4.5.1. Turbo-Compressor Performance Mapping

As a standard for the creation of turbomachinery performance maps, the manufacturer generated the turbo-compressor performance maps assuming fixed inlet conditions (temperature and pressure) while varying flow and rotational speed to estimate the resulting pressure ratios, efficiencies, and enthalpy changes. Thus, the first step in mapping turbine and compressor performance data is to select an appropriate reference condition for each device to transform (or correct) the experimental values to

dynamically similar conditions such that they can be plotted on the same map. The reference conditions selected are outlined in Table 4-7 and shown highlighted on the performance maps in Figure 4-7.

Table 4-7 Turbine and compressor reference conditions for mapping

Reference Parameter	*Units*	*Turbine*	*Compressor*
Speed	kRPM	30.00	
Mass Flow	kg s^{-1}	3.045	2.000
Inlet Pressure	kPa	2,152	267.7
Inlet Temperature	°C	90.88	33.84
Compressibility Factor	-	0.6762	0.9415
Ratio of Specific Heats	-	1.426	1.115
Gas Constant	J kg^{-1} K^{-1}	72.91	
Simulated Pressure Ratio	-	3.122 Total to Static	2.589 Total to Total

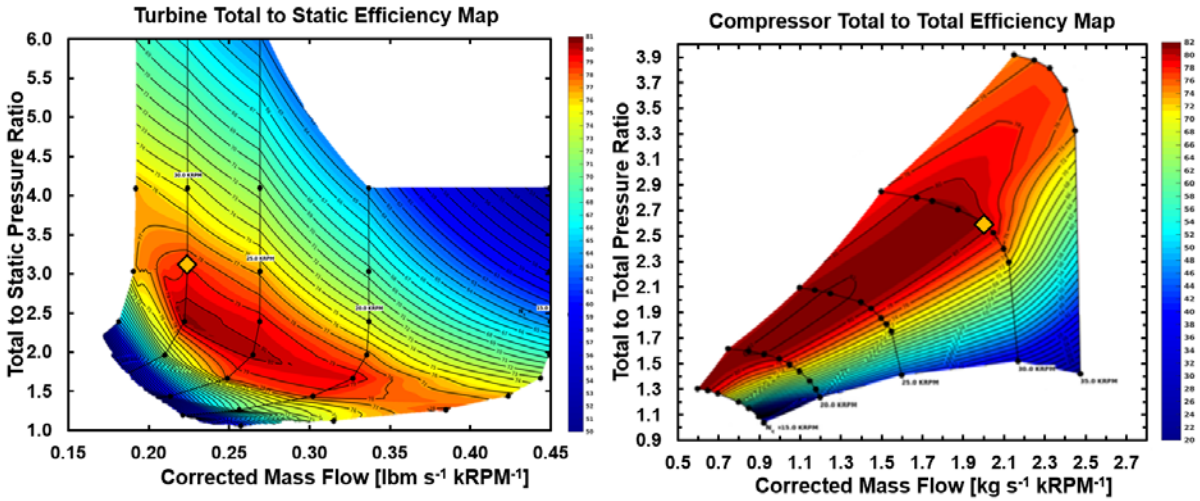

Figure 4-7 Turbine (Left) and compressor (Right) performance maps with reference conditions

For the compressor, the total-to-total pressure ratio and efficiency were plotted against a corrected mass flow while total-to-static pressure ratio and efficiency were plotted against corrected mass flow for the turbine. As mentioned in the previous section, static properties relate to a fluid which is at rest while total properties account for the influence of fluid kinetic energy. Total pressure (P_o) is calculated using Equation (4.18) with the static pressure (P) the fluid density (ρ) and the fluid velocity ($\vec{V}$). Total

temperature (T_o) is calculated using Equation (4.19) with the static temperature (T), fluid velocity, and fluid specific heat value (Cp).

$$P_o = P + \frac{\rho \cdot \vec{V}^2}{2{,}000} \tag{4.18}$$

$$T_o = T + \frac{\vec{V}^2}{2{,}000 \cdot Cp} \tag{4.19}$$

With the total to static pressure ratio determined for the turbine (inlet to outlet), the next step in mapping device performance is to determine the corrected mass flow rate for the operating condition. The corrected mass flow ($\dot{m}_{\mathrm{cor}}$) is a function of the actual mass flow ($\dot{m}_{\mathrm{test}}$) (adjusted to units of pound mass per second to correlate to the manufacturer map), the corrected rotational speed of the device, and four parameters used to correct the value to a dynamically similar condition to the reference as shown in Equation (4.20). The parameters for corrected mass flow rate are determined following Equation (4.21) through Equation (4.25).

$$\dot{m}_{\mathrm{cor,turb}} = \frac{\dot{m}_{\mathrm{turb,test,adj}} \cdot \psi \cdot \sqrt{\theta}}{\delta \cdot \omega_{\mathrm{cor}}} \tag{4.20}$$

$$\psi = \frac{\gamma_{\mathrm{ref}} \left(\frac{2}{\gamma_{\mathrm{ref}} + 1} \right)^{\frac{\gamma_{\mathrm{ref}}}{\gamma_{\mathrm{ref}} - 1}}}{\gamma_{\mathrm{test}} \left(\frac{2}{\gamma_{\mathrm{test}} + 1} \right)^{\frac{\gamma_{\mathrm{test}}}{\gamma_{\mathrm{test}} - 1}}} \tag{4.21}$$

$$\theta = \left(\frac{\vec{V}_{\mathrm{cr,in,test}}}{\vec{V}_{\mathrm{cr,in,ref}}} \right)^2 \tag{4.22}$$

$$\vec{V}_{\mathrm{cr}} = \sqrt{\frac{2 \cdot \gamma}{\gamma + 1} G \cdot Z \cdot R \cdot TA_o} \tag{4.23}$$

$$\delta = \frac{P_{o,in,test}}{P_{o,in,ref}} \tag{4.24}$$

$$\omega_{cor} = \frac{\omega_{test}}{\sqrt{\theta}} \tag{4.25}$$

The ratio of specific heats (γ) and compressibility factor (Z) for the reference (ref) and test (test) points are determined using REFPROP functions with the total inlet temperature and total inlet pressure of the device as input variables. For critical velocity ($\vec{V}_{cr}$), the gravitational correction constant (G) is assumed to be 9.81 $m^2\ s^{-2}$, the fluid gas constant (R) is the ideal gas constant (8.3145 $J\ K^{-1}\ mol^{-1}$) divided by the fluid molecular weight as determined using REFPROP functions (0.11404 $kg\ mol^{-1}$), and the temperature (TA_o) is the total, absolute, inlet value. The gravitational correction constant in the critical velocity calculation is canceled in the derivation of the velocity mapping coefficient. Also cancelled is the fluid gas constant when the same fluid is tested as the reference. The corrected rotational speed of the device (ω_{cor}) is calculated using the tested rotational speed (ω_{test}) and the device velocity parameter (θ).

Plotting turbine corrected mass flow against its total to static pressure ratio not only shows how the operational point compares to the reference but also what its total to static efficiency and speed should be given map efficiency contours. The total to static efficiency for the turbine is calculated similarly to the turbine isentropic efficiency as presented in Chapter 3 but uses the total enthalpy for the inlet value as shown in Equation (4.26).

$$\eta_{turb,ts} = \frac{h_{o,in} - h_{out}}{h_{o,in} - h_{out,s}} \tag{4.26}$$

Compressor mapping uses nearly the same methods as those presented for the turbine with a few discrepancies. First, the manufacturer generated performance maps for this device based on total-to-total pressure ratio and efficiency. Also, standard units were used in the generation of the compressor

map (so the adjustment of experimental mass flow to units of pound mass per second is not required) and the corrected mass flow derivation for the compressor negates the use of shaft speed as shown in Equation (4.27).

$$\dot{m}_{\text{cor,comp}} = \frac{\dot{m}_{\text{comp,test}} \cdot \psi \cdot \sqrt{\theta}}{\delta} \tag{4.27}$$

The scaling of the turbine corrected mass flow by device shaft speed is required to separate the vertical speed lines which otherwise collapse on themselves. This is a result of the ability of the device to operate over a range of pressure ratios (and thus enthalpy differences and efficiencies) when the flow is choked. Unlike the turbine, a unique operating condition (speed) exists for each compressor mass flow and pressure ratio within the stall boundary. This boundary, estimated by the manufacturer at each speed as the point on the performance map with the lowest corrected flowrate, is where flow begins to separate from compressor blades. Flow separation impairs performance (both efficiency and flow), and, if severe enough, can result in surge where flow pulsates or reverses entirely. Both stall and surge, in addition to sending liquid into either the compressor or turbine, pose a significant threat to device integrity and are to be avoided during experimentation.

4.5.2. Error Assessment

The final component of the data reduction model fully assesses the quality of the data collected against the specified testing criteria. As each of the instruments were selected or calibrated to surpass Air-Conditioning, Heating and Refrigeration Institute bias limits, confirming the data point conforms to testing criteria is sufficient justification to validate the accuracy of performance results for commercial chilling systems. Even so, an uncertainty analysis following the procedures in the 2018 American Society of Mechanical Engineers Performance Test Code 19.1 was complete on the full-load, baseline experimental data point to provide further confidence in the performance data. The methods presented

in the test code allow for the determination of uncertainty for each performance calculation using the standard method of error propagation. This method determines the uncertainty (U_o) of a calculation by taking the square root of the sum of the product of the squared total error of each variable and the squared partial derivative of the calculation with respect to the same variable using Equation (4.28). Here, the partial derivative of *a* with respect to *b* relates to a hypothetical performance calculation where *a* is the dependent variable and *b* is one of *n* independent variables used in the calculation.

$$U_a = \sqrt{\sum_{i=1}^{n} \left(\frac{\partial a}{\partial b_i} \right)^2 E_{T,b_i}^2} \tag{4.28}$$

Due to the amount of data analyzed in the data reduction model and the inability to propagate error in Excel, a separate uncertainty model was created in Engineering Equations Solver (using the same formulations as the reduction model) to propagate error using the internal uncertainty solver of the software [182]. Data is input to the uncertainty model in arrays (total experimental error and averaged measurement values for temperatures, pressures, differential pressures, and flow rates) which are generated in the reduction model for each data set. Agreement between these two models was used to confirm the fidelity of error calculations considering the data analysis model was previously verified through hand calculations.

Chapter 5 Experimental Results and Discussion

The previous chapter outlined the architecture of the organic Rankine vapor compression prototype and supporting test facilities, as well as the experimental methods used to collect and assess experimental performance data. This chapter presents the results drawn from the experimental data and a discussion of the prototype performance characteristics. Experimentation began with characterizing the full-load, standard performance of the organic Rankine vapor compression system. The off-design operation of the prototype was then tested, and the results were normalized to the baseline to identify operational trends at differing boundary conditions. Finally, the Integrated Part-Load Value efficiency of the prototype was quantified. All data sets were collected at a frequency of 2 Hz over a 900 second interval to conform to the testing criteria.

5.1. Full-Load Experimentation

The prototype was brought to the full-load, standard operating conditions and held at steady state to collect the first datapoint. Table 5-1 shows the temperatures, flow rates, inlet pressures, and differential pressures of the external stream heat exchangers over the test period. For each measured variable, the total uncertainty was <1% greater than the respective bias errors due to low systematic uncertainties. In reference to the simulation effort and specifications, the generator inlet and outlet temperatures were 91°C and 86°C, the condenser inlet and outlet temperatures were 30°C and 35°C, and the evaporator inlet and outlet temperatures were 12°C and 7°C, respectively. The heat duties for the simulation effort were 458.8 kW, 455.6 kW, 313.5 kW, and 300 kW for the generator, power condenser, cooling condenser, and evaporator, respectively. The temperature differences and heat duties yielded simulated liquid mass flow rates of 25.41 kg s^{-1}, 26.99 kg s^{-1}, 18.57 kg s^{-1}, and 14.30 kg s^{-1} for the generator glycol, power condenser glycol, cooling condenser glycol, and evaporator water, respectively. Inlet and differential pressures were neither simulated nor specified in the performance rating standards.

Table 5-1 Generator, condenser, and evaporator loop state points measured during testing at baseline operating conditions

External Loop Heat Exchanger	*Inlet Temperature [°C]*	*Outlet Temperature [°C]*	*Inlet Pressure [kPa]*	*Differential Pressure [kPa]*	*Flow [kg s^{-1}]*
Generator	91.18 ± 0.07	86.24 ± 0.07	350.8 ± 0.99	33.13 ± 0.12	27.23 ± 0.27
Power Condenser	29.91 ± 0.06	36.58 ± 0.06	320.9 ± 1.10	62.05 ± 0.61	19.78 ± 0.35
Cooling Condenser	30.05 ± 0.05	36.82 ± 0.04	317.9 ± 0.96	62.55 ± 0.61	13.05 ± 0.13
Evaporator	12.12 ± 0.04	6.996 ± 0.027	526.4 ± 0.98	34.64 ± 0.61	12.27 ± 0.12

The targeted evaporator duty could not be tested within ±5.166% of the targeted value (300 kW), so the operating conditions were altered to represent the achievable cooling duty. Flow and temperature stability and precision for the external test facility loops conformed to the criteria presented in the previous chapter (to yield a 5°C temperature difference across each device), except for the condenser glycol flow rates. The total flow rate for both condensers was 25.6% below the target value (the cutoff was ±5%), yet the flow rate did meet the stability criteria for ratio of standard deviation to mean value. The condenser loop pump could not overcome the prohibitive frictional pressure losses in the cooling tower supply and return lines. The flow rate limitation affected system performance but could not be easily corrected without a major test facility overhaul. Table 5-2 shows the average state points of the refrigerant at the baseline operating condition. These state points are overlayed against the simulated values from Chapter 3 in the subsequent sections.

Corrections were made to the state points at the evaporator outlet, suction line heat exchanger inlets, and cooling cycle condenser outlet following the methods outlined in the previous chapter. The temperature measurement at the evaporator outlet was too close to the saturation line and erroneously returned subcooled liquid properties when using REFPROP. The sole presence of vapor was visually confirmed using a sight glass at the evaporator outlet. The refrigerant exiting the cooling cycle condenser

was two-phase, and, thus, the transition from two-phase to saturated liquid (cooling cycle state point 7) occurred in the suction line heat exchanger. The two-phase condition at the outlet of the condenser was visually confirmed in a sight glass. The power cycle pump did not cavitate or vapor lock which suggests the condenser refrigerant discharges were not well mixed. Overall performance metrics with associated uncertainties were calculated with the refrigerant state points and auxiliary loop state points as shown in Table 5-3.

Table 5-2 Refrigerant state points measured during testing at baseline operating conditions

	Power Cycle				***Cooling Cycle***			
State Point	***Temperature [°C]***	***Pressure [kPa]***	***Enthalpy [kJ kg^{-1}]***	***Quality [-]***	***Temperature [°C]***	***Pressure [kPa]***	***Enthalpy [kJ kg^{-1}]***	***Quality [-]***
1	90.22	2,241	437.9	Superheat	35.69	244.6	416.5	Superheat
2	50.45	743.3	422.0	Superheat	73.29	759.5	445.6	Superheat
3	50.49	743.0	422.1	Superheat	73.20	759.5	445.5	Superheat
4	39.28	731.3	410.5	Superheat	47.40	745.8	418.8	Superheat
5	39.08	731.4	410.3	Superheat	47.26	722.8	419.1	Superheat
6	37.97	725.2	409.2	1	37.56	717.0	409.0	1
7	37.66	718.9	252.3	0	-	-	-	-
8	35.26	712.7	248.8	Subcool	36.84	705.4	261.1	0.0621
9	35.36	724.6	249.0	Subcool	36.62	708.0	261.1	0.0609
10	38.34	2,459	253.3	Subcool	24.14	701.8	233.1	0
11	38.42	2,364	253.4	Subcool	24.14	710.7	233.1	0
12	46.15	2,355	264.6	Subcool	21.74	463.9	233.1	0.0127
13	46.15	2,302	264.6	Subcool	6.031	269.0	233.1	0.1383
14	56.09	2,294	279.3	Subcool	6.031	269.0	388.5	1
15	56.06	2,299	279.3	Subcool	5.722	269.0	388.5	Superheat
16	86.17	2,287	329.2	0	5.722	269.0	388.5	Superheat
17	85.92	2,275	429.8	1	35.85	250.3	416.5	Superheat
18	90.83	2,263	438.3	Superheat	-	-	-	-

Table 5-3 System performance metrics at baseline operating conditions

Performance Parameter	*Experimental Value*	*Previously Simulated Value*
Generator Heat Duty [kW]	473.0 ± 10.6	458.8
Power Condenser Heat Duty [kW]	435.7 ± 9.5	455.6
Cooling Condenser Heat Duty [kW]	291.8 ± 4.0	313.5
Evaporator Heat Duty [kW]	263.8 ± 3.5	300
Power Cycle Mass Flow [kg s^{-1}]	3.145 ± 0.004	2.791
Cooling Cycle Mass Flow [kg s^{-1}]	1.737 ± 0.016	1.827
Turbine Work [kW]	50.07 ± 0.57	50.34
Compressor Work [kW]	50.24 ± 0.48	47.47
Transfer Efficiency [%]	100.3 ± 1.5	94.3
Turbine Efficiency [%]	76.7 ± 0.90	83.1
Compressor Efficiency [%]	84.8 ± 0.54	82.0
Pump Work [kW]	13.53 ± 0.41	13.16
Pump Efficiency [%]	35.6 ± 1.1	30.0
Pump Power Consumption [kW]	13.62 ± 0.27	13.16
Turbo-Compressor Speed [kRPM]	31.5 ± 0.30	30.0
Thermal COP [-]	0.5577 ± 0.015	0.6539
Electrical Equivalent COP [-]	19.37 ± 0.46	22.79
Energy Balance [%]	3.08 ± 2.0	0.37
Organic Rankine Cycle Efficiency [%]	7.71 ± 0.22	8.10
Vapor Compression Cycle COP [-]	5.25 ± 0.09	6.32

The data verified that the energy balance (3.08%) met the cutoff criteria of the referenced standards (±3.69%). The 3.08% energy loss in this experiment was likely due to natural convection from the hot surfaces of the heat exchangers. The heat input in the generator was 473 kW ± 10.6 kW and the

cooling duty in the evaporator was 263.8 kW ± 3.5 kW which yielded an overall thermal COP of 0.56 ± 0.01. The target evaporator heat duty of 300 kW required a higher heat input than what was achievable at the standard operating conditions due to test facility challenges. The turbine and compressor operated at 31.5 kPRM ± 0.3 kRPM, with a power transfer efficiency of 100.3% ± 1.5%. The power transfer efficiency between turbine and compressor was quite high, which was likely due to the very low windage and bearing losses from the careful design of the shaft bearings and integrated cooling system. The differences between the experimental results and the thermodynamic modeling will be explained in detail in the following sections.

5.1.1. Discussion of Power Cycle Operation

The experimental state points of the power cycle are shown in Figure 5-1 on a temperature to entropy diagram with the external temperature streams overlaid. The generator phase change pinch point temperature was lower than the design (1.6°C experimental versus 2.3°C model) and the condenser phase change pinch points were very close to the design (1.3°C experimental versus 1.2°C model for the power cycle condenser). While unrelated to the operation of the generator itself, the lower generator pinch temperature is indicative of the reduced cooling duty of the prototype relative to the targeted design point. During testing, further increases to the power cycle pump speed (required to increase the system cooling duty) yielded greater generator saturation pressures instead of increased mass flowrate. This suggests the flow was choked either in the nozzle array or the rotor itself which could be a contributing factor to the reduced isentropic efficiency (76.7% versus 83.1%, respectively) [173]. As further increases to pump setting (and thus saturation pressure) presented a risk of sending liquid droplets to the turbine, this data point represented the maximum achievable cooling duty considering all other variables. While choked turbine flow prevented increased flowrates in the power cycle at this test condition, it is noted that the experimental flowrate (3.15 kg s^{-1}) is substantially greater than the model predicted flowrate (2.79 kg s^{-1}). The turbine required a greater flowrate to overcome test limitations including the reduced

turbine efficiency. Other limitations which contributed to the increased flowrate include the reduced condenser loop flowrate (which decreased turbine and increased compressor pressure ratio) and greater than anticipated system piping pressure losses. The pressure ratio of the turbine was 3.02 compared to the modeled pressure ratio of 3.12. Figure 5-2 shows the experimental turbine operational point plotted on the turbine map.

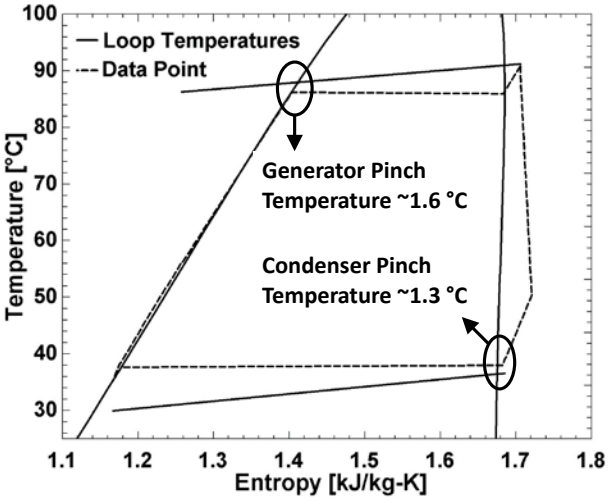

Figure 5-1 Measured power cycle temperature and entropy state points at baseline test conditions

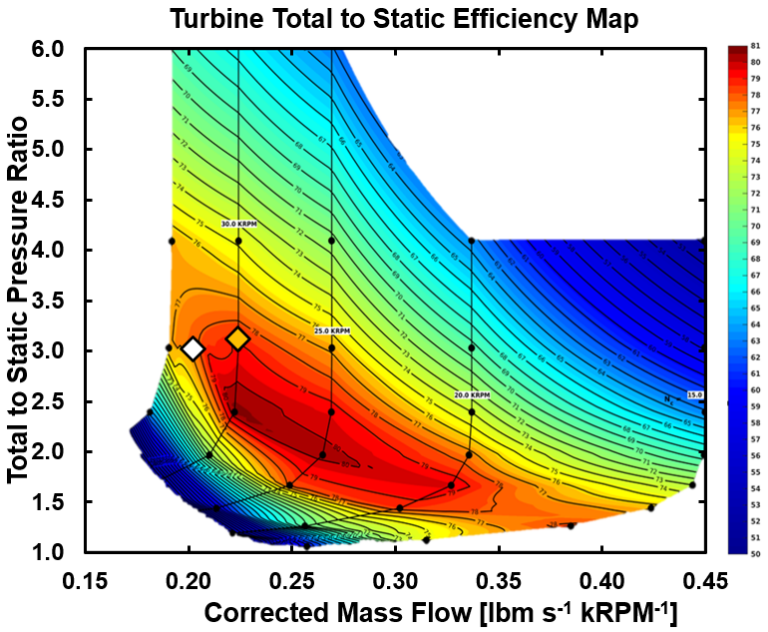

Figure 5-2 Turbine performance mapping at baseline testing conditions

For the baseline operating condition, the turbine performance map shows good agreement between the experimental total to static efficiency and that estimated by the contours (76.8% versus ~77.5%). Furthermore, the mapping shows the turbine is operating with choked flow considering the operating point is between two vertical speed lines. The power cycle pump consumed 13.53 kW ± 0.41 kW to pressurize the refrigerant with an isentropic efficiency of 35.64% ± 1.10%. The efficiency of the power cycle pump was greater than that assumed in the modeling effort (30%). The heat input in the generator was 473 kW ± 10.6 kW and the power output of the turbine was 50.07 kW ± 0.57 kW. Accounting for the power cycle pump energy consumption resulted in an organic Rankine cycle efficiency of 7.71% ± 0.22%, which was slightly lower than the modeled value of 8.1%.

Figure 5-3 shows a comparison between the temperature, pressure, enthalpy, and entropy state points of the organic Rankine power cycle against R1234ZE(E) refrigerant saturation curves, where the experimental data is plotted as a dashed line and the previously simulated conditions is plotted as a solid line.

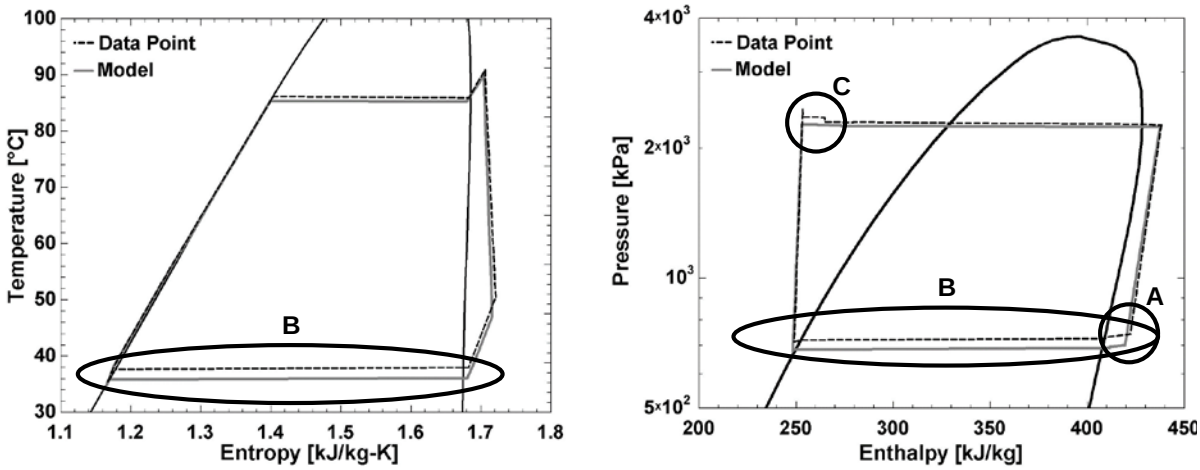

Figure 5-3 Comparison of power cycle state points with discrepancies between the experiment and simulation highlighted (A) Decreased drop in enthalpy across turbine, (B) increased condenser saturation pressure and temperature, and (C) increased line pressure losses between the pump discharge and economizer liquid inlet connection ports

The turbine had a reduced enthalpy drop over what was modeled (15.9 kJ kg^{-1} experimental versus 18.0 kJ kg^{-1} model) due to the reduced isentropic efficiency and pressure ratio. The reduced enthalpy drop is represented by Item A in Figure 5-3 which increased the power cycle mass flow required to generate the turbine power needed by the cooling cycle. The lower-than-design flow rate in the glycol lines of the condenser was the primary cause of the increased low side saturation pressure (and temperature) in the power cycle condenser (item B in Figure 5-3). There were also more significant pressure losses in the power cycle compared to the modeling prediction (item C in Figure 5-3). The pressure loss in the refrigerant lines from the power cycle pump to the recuperator and from the recuperator to the economizer were much larger than anticipated. These values were 95.5 kPa, and 53.1 kPa, respectively, compared to the modeled value of 5.48 kPa. The additional pressure drop was likely due to the much higher experimental flow rate (3.15 kg s^{-1}) than the model (2.79 kg s^{-1}). In addition, some of the added pressure drop in the power cycle pump to recuperator piping was due to the Krohne Coriolis mass flow meter.

The economizer was located right after the recuperator on the power cycle and at the discharge of the compressor on the cooling cycle. The high temperature compressor discharge (73.3°C) preheated the power cycle fluid after the recuperator (46.2°C). The refrigerant enthalpy in the power cycle rose from 264.6 kJ kg^{-1} to 279.3 kJ kg^{-1} through the economizer at a mass flow rate of 3.15 kg s^{-1}, which yielded a heat input from the economizer of 46.3 kW to the power cycle fluid just before the generator cores. If the economizer were not included in the system, 46.3 kW of additional heat energy would have to be input to the system to operate at the same conditions. Thus, the heat input of 473 kW would have been increased to 519.3 kW and the thermal efficiency of the power cycle would have decreased from 7.7% to 7.0%. The overall thermal COP of the system would decrease from 0.56 to 0.51.

5.1.2. Discussion of Cooling Cycle Operation

Figure 5-4 a comparison between the temperature, pressure, enthalpy, and entropy state points of the vapor compression cycle against R1234ZE(E) refrigerant saturation curves, where the experimental data is plotted as a dashed line and the previously simulated conditions is plotted as a solid line. The condensing saturation pressure (and temperature) was higher than the model predicted value (item A in Figure 5-4) due to the less than expected flowrate in the condenser loop. In contrast to the turbine, the elevated condenser pressure increased the pressure ratio across the compressor (3.10 experimental versus 2.73 model), which increases the enthalpy rise relative to the baseline (29.1 kJ kg^{-1} experimental versus 26.0 kJ kg^{-1} model). The increased compressor pressure ratio (and, thus, enthalpy rise) was also a result of increased pressure loss (18.7 kPa experimental versus 4.50 kPa model) in the vapor side of the suction line heat exchanger (item B in Figure 5-4) and a higher-than-expected pressure loss (22.9 kPa experimental versus 5.48 kPa model) in the piping between the economizer vapor outlet and cooling cycle condenser inlet (item C in Figure 5-4). The higher compressor enthalpy rise decreased the flow rate delivered by the device (1.74 kg s^{-1} experimental versus 1.83 kg s^{-1} model), which had a negative impact on the amount of chilling provided in the evaporator. While not noticeable on the phase diagrams, the improved compressor and shaft efficiencies over the baseline prediction helped to counteract some of these challenges. The compressor efficiency was 84.8% in experimental testing compared to 82.0% in the modeling design point. The shaft efficiency was 100.3% in the experiment compared to 94.30% in the simulations. The compressor consumed 50.41 kW ± 0.48 kW of power, which was higher than the turbine power provided, but within measurement error.

Compressor performance is better illustrated by mapping the operation of the device during the baseline test against the reference condition shown in Figure 5-5. While the experimental total to total efficiency is not well represented by the map contours (84.8% versus ~79.0%) there are some valuable conclusions that can be drawn from the map. First, the high efficiency of the device and the shaft

transmission from the turbine allows a considerable corrected flow rate through the device (1.92 kg s^{-1}) despite the elevated pressure ratio. However, as the compressor pressure ratio and/or flow increase, the compressor speed must also increase. The increased compressor speed translates to the turbine (as they are directly coupled) which shifts the turbine performance away from its best efficiency point. Furthermore, increasing the pressure ratio of the compressor shifts its operation closer to the manufacturer predicted stall line. A shift in the baseline operating point towards the compressor stall line suggests that the compressor operation will be increasingly limited at off-design operation where there is either an increase in compressor pressure ratio and/or a decrease in compressor flowrate.

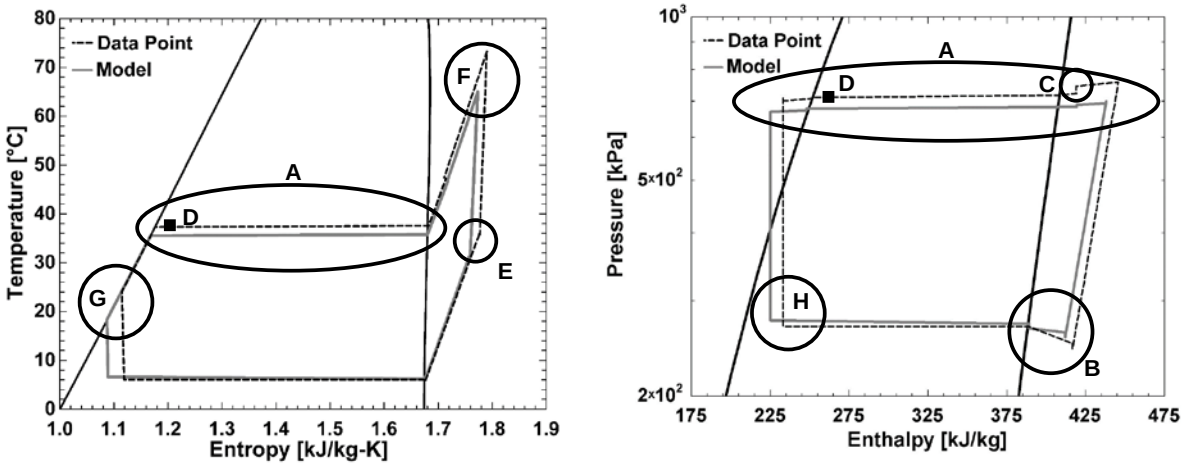

Figure 5-4 Comparison of cooling cycle state points with discrepancies between the experiment and simulation highlighted (A) increased condenser saturation pressure and temperature, (B) increased suction line heat exchanger vapor pressure loss, (C) increased line pressure loss between the economizer vapor outlet and cooling cycle condenser inlet, (D) multi-phase condenser discharge, (E) increased compressor inlet temperature, (F) increased compressor outlet temperature, (G) decreased condenser subcooling, and (H) decreased evaporator enthalpy difference

Opposite the compressor on the cooling cycle, the refrigerant leaving the cooling condenser (item D in Figure 5-4) was a two-phase mixture and not fully subcooled, which further degraded the performance of the cooling cycle. Since the suction line heat exchanger was in a counter flow orientation, the two-phase fluid entering the high temperature side of the device increased the average temperature difference for energy exchange over the design point value. The higher temperature difference and

elevated condenser saturation temperature increased the suction line heat exchanger vapor discharge temperature over the baseline (35.85°C experimental versus 31.16°C model) as shown in item E in Figure 5-4. Higher vapor outlet temperature from the suction line heat exchanger and higher compressor discharge pressure from the condenser saturation temperature elevated the compressor discharge temperature over the baseline value (73.3°C experimental versus 65.0°C model). The higher discharge temperature and pressure (item F in Figure 5-4) increased the heat duty of the economizer (46.4 kW versus 34.0 kW). Since the condenser glycol pump could not deliver the design point flow rate, the higher temperature of the condenser outlet reduced subcooling in the suction line heat exchanger (item G in Figure 5-4) and increased the vapor mass quality entering the evaporator (13.8% versus 9.0%). As there was no evaporator superheated vapor energy exchange, the 4.8% decrease in evaporator refrigerant latent heat directly decreased the prototype chilling duty 4.8%. The enthalpy change across the evaporator during experimentation was 155.5 kJ kg^{-1} experimental versus 164.2 kJ kg^{-1} during modeling. The decrease in evaporator enthalpy change is shown in item H in Figure 5-4. Item H in Figure 5-4 also shows that the evaporator refrigerant inlet saturation pressure (and, thus, temperature) were less than the design. The inlet temperature to the evaporator was 6.03°C versus 6.60°C, which resulted in a greater evaporator pinch temperature (0.97°C versus 0.4°C). However, the elevated pinch temperature is not an indication of reduced evaporator performance, but a result of assuming there was no evaporator pressure loss. Pressure loss across the evaporator could not be measured due to the working principle of the spray evaporator.

Despite the challenges with the cooling cycle condenser, the suction line heat exchanger increases the amount of subcooling prior to the expansion valve inlet to increase the evaporator heat duty. Through the suction line heat exchanger, the enthalpy of the liquid stream decreases from 261.1 kJ kg^{-1} to 233.1 kJ kg^{-1}. With a mass flow of 1.74 kg s^{-1}, this yields a 48.7 kW increase in evaporator cooling capacity. Without the suction line heat exchanger, the cooling capacity from the evaporator would have been 215.1 kW, an

18.5% decrease from the 263.8 kW experimental chilling capacity. The overall COP of the organic Rankine vapor compression prototype would then decrease from 0.56 to 0.45. The suction line heat exchanger also increases the inlet temperature of the compressor (and, thus, outlet temperature), which would typically increase the load of the condenser. In this prototype, this phenomenon is avoided by integrating an economizing heat exchanger that captured the additional sensible energy at compressor discharge and transferred it to the power cycle. Thus, the utility of the suction line heat exchanger and economizer are paramount to increasing the efficiency of an organic Rankine vapor compression system. With these enhancements, the vapor compression cycle COP was 5.23 ± 0.09, which was competitive with state-of-the-art vapor compression chillers [141]. Considering the system was powered by heat (which in practice would be otherwise wasted), the electrical equivalent COP of the cooling cycle was 19.37 ± 0.46.

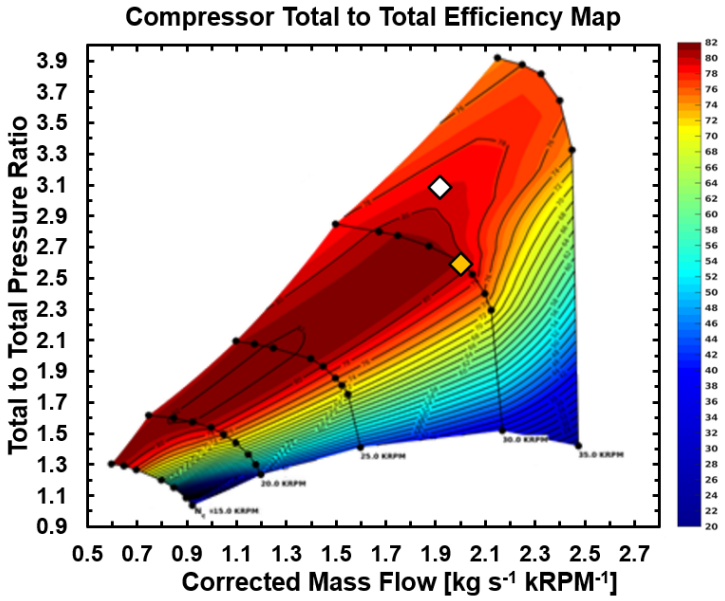

Figure 5-5 Compressor performance mapping at baseline testing conditions

5.1.3. Evaluation of Results to Improve System Performance

The overall COP of the prototype organic Rankine vapor compression system was 0.56 ± 0.01, which was lower than the model predicted value of 0.65. Furthermore, the evaporator cooling duty was 263.8 kW, which was less than the targeted value of 300 kW. As discussed in the previous section, the

increased evaporator inlet vapor quality from the inability of the cooling cycle condenser to fully liquify and sub cool the refrigerant directly reduced the amount of cooling duty by 4.8%. The factors discussed above (lower than design condenser glycol flow rate, choked flow in the turbine, and higher than design pressure losses) further contributed to the lowered COP and chilling duty of the system. To analyze the impact of individual inputs on overall system performance, a scenario analysis was conducted on the baseline thermodynamic performance model from Chapter 3 as shown in Figure 5-6. The variables included in the study were the condenser glycol flow rate, turbine, compressor and shaft efficiencies, and pressure losses. For each scenario analysis, a single input was updated in the model (from the initial assumption for the simulation to the value determined through experimentation), with all other inputs remaining the same as previously modeled, and the impact on full system performance was quantified.

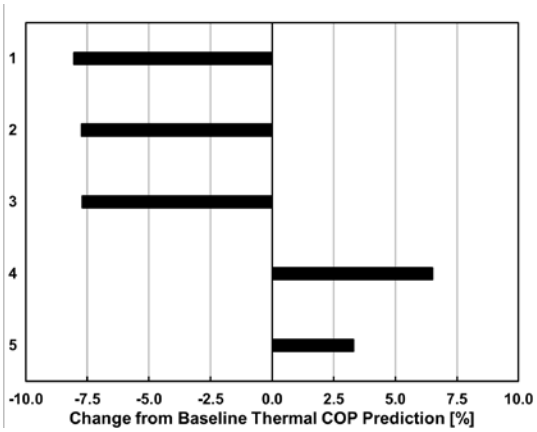

Scenario Analysis	*Values*	*COP*
Baseline Modeling Prediction	***-***	***0.65***
(1) Increased condenser outlet temperature	35.0°C to 36.7°C	0.60
(2) Turbine efficiency	83.1% to 76.7%	0.60
(3) System Pressure Losses	All in text	0.60
(4) Turbo-compressor shaft efficiency	94.3% to 100%	0.70
(5) Compressor efficiency	82.0% to 84.8%	0.67

Figure 5-6 Scenario analysis of prototype component limitations

Since the condenser glycol pump could not deliver the design point flow rate, the outlet temperature of the glycol mixture from the condensers was higher in the experimental testing than the design point simulations. The average condenser glycol mixture outlet temperature was 36.7°C instead of the target value of 35.0°C, which detrimentally reduced the performance of the full system. When the thermodynamic model was updated to have a 36.7°C condenser outlet temperature, the saturation

pressure of the refrigerant in the condenser increased. The increased saturation pressure caused an increase in the enthalpy rise across the compressor (27.3 kJ kg^{-1} compared to 26.0 kJ kg^{-1}). The higher compressor pressure ratio increased the power requirement from the turbine (from 47.47 kW to 50.08 kW) since the chilling duty was a fixed input to the model. The turbine enthalpy drop decreased due to the higher saturation pressure in the condenser (18.0 kJ kg^{-1} to 17.3 kJ kg^{-1}). As a result, the power cycle mass flow was higher to satisfy the greater power demand (from 2.79 kg s^{-1} to 3.07 kg s^{-1}), which was similar to mass flow rate experienced during testing. Additionally, the compressor inlet temperature and outlet temperature increased to 32.5°C and 68.0°C relative to the baseline values of 31.1°C and 65.0°C, respectively. The cumulative impacts of reduced condenser flow rate results in an 8.1% decrease in thermal COP, as shown in Figure 5-6.

The experimental differences in turbine, compressor, and shaft efficiencies had considerable impact on the system performance. When the turbine efficiency was reduced from the modeled value of 83.1% to the experimental value of 76.7% in the baseline simulation, the power cycle mass flow increased to 3.02 kg s^{-1} to maintain cooling duty, while the thermal COP decreased by 7.7%. The higher flow rate maintained the power output of the turbine despite the decreased efficiency. When the compressor efficiency was increased to the experimental value of 84.8% (from 82.0%), thermal COP was increased by 3.3%. The power transfer efficiency was more impactful on full system performance than the compressor efficiency. Although the measurements were within experimental error, a near-perfect shaft efficiency was measured in the experiments (100.3% ± 1.5%), which suggested the manufacturer overestimated the losses of the turbo-compressor. Assuming a shaft efficiency of 100% in the baseline model (where the original prediction was 94.3%) increased thermal COP by 6.5%.

Figure 5-6 shows the cumulative effects of the following experimental refrigerant pressure drops: suction line heat exchanger vapor side, cooling cycle economizer to condenser inlet piping, power cycle pump outlet to recuperator liquid inlet piping, and power cycle recuperator liquid outlet to power cycle

economizer liquid inlet piping. The increased pressure drops were input to the baseline simulation individually and the decrease in thermal COP was documented. The suction line vapor pressure drop was measured at 18.7 kPa, which was considerably higher than the 4.50 kPa pressure drop in the simulation. When the vapor pressure drop was increased in the simulation, the thermal COP decreased by 5.7% which was the largest individual impact of the pressure drops. Any pressure loss in the suction line heat exchanger vapor side must be immediately overcome by the compressor, which directly increases the power requirement. The suction line heat exchanger vapor pressure drop had such a large individual impact because the absolute pressure is <300 kPa. Thus, the pressure drop of 18.7 kPa represents a 7% loss in operating pressure. In comparison, 7% loss in operating pressure on the high side of the power cycle would be 171 kPa. It is very important to carefully design the heat exchangers on the low-pressure parts of the cycle because very small pressure drop can have considerable ramifications. The experimentally measured pressure drop from the cooling cycle economizer to the cooling cycle condenser inlet was 22.9 kPa, compared to the simulation value of 5.48 kPa. The higher pressure drop in this line decreased the thermal COP by 2.3%.

The piping run from the power cycle pump outlet to the liquid recuperator inlet had an experimental pressure drop of 95.5 kPa, which was almost 20 times higher than the modeled value of 5.48 kPa. Although this pressure drop was so much higher than expected, it only caused a 0.5% decrease in the thermal COP. The small impact on thermal COP is likely because 95.5 kPa pressure drop is a much smaller fraction of the absolute pressure (2,459 kPa) compared to the pressure drop and absolute pressure in the suction line heat exchanger vapor line, and pump work requirement does not impact thermal COP. The final line loss that was examined in the sensitivity analysis was the pressure drop in the power cycle from the recuperator liquid outlet to the economizer liquid inlet. In the piping from the recuperator to the economizer, the pressure drop was 53.1 kPa, compared to the modeled value of 5.48. When the additional pressure drop was incorporated into the simulation, the thermal COP decreased by 0.3%.

The liquid pressure losses in the lines between the pump and economizer on the power cycle marginally affect thermal performance. The vapor pressure loss through the suction line heat exchanger is twice as impactful as the pressure loss from the economizer to cooling condenser connection although both values should be addressed to improve thermal performance. When all four increased pressure drops were included in the simulation, the thermal COP decreased by 7.7%, which was the second most impactful variable in the scenario study.

The scenario analysis showed there was considerable opportunity to improve the performance characteristics of the prototype over the experimental values determined in this effort if certain components could be improved. The flow rate limitation in the condenser loop should be addressed by selecting and implementing an improved circulation pump and reducing the frictional pressure losses in the condenser piping networks. Pressure losses throughout the system could be improved by increasing the diameter of piping networks to reduce frictional losses. The pressure loss of the vapor through the suction line heat exchanger could also be corrected by updating and optimizing the internal geometry to decrease the pressure drop. Alternatively, a third suction line heat exchanger core could be installed with the two units currently in parallel. In addition, the size of the cooling cycle condenser should be increased to ensure there is sufficient refrigerant subcooling at the outlet on the cooling cycle which would help increase the enthalpy change across the evaporator. Alternatively, an individual, properly sized condensing heat exchanger could be selected to replace the parallel units.

Finally, the baseline performance model was updated to determine the efficiency and cooling duty achievable with the prototype using the current turbo-compressor design, but with original estimates for pressure drop and condenser saturation temperatures. Updating the turbine, compressor, and shaft efficiencies to 76.7%, 84.8%, and 100% in the baseline model showed 300 kW of cooling was produced with a thermal COP of 0.66. The power cycle mass flow at this operating condition was 2.76 kg s^{-1}, suggesting the cooling duty would not be limited by flow choking in the turbine. Moving away from choked

flow could increase the turbine efficiency and further improve the COP of the organic Rankine vapor compression system. The electrical equivalent COP at this set of conditions is 23.08. This is a 19.2% improvement over the experimental value.

5.2. Off-Design Experimentation

With the baseline performance of the organic Rankine vapor compression prototype thoroughly characterized, the test facility was operated over a wide range of off-design conditions at full-load to assess implications to system performance. Considering the flow limitation in the condenser loop (and the scenario analysis for the baseline data point showing the implications of the limitation) the prototype performance was not assessed at off-design condenser loop flowrates. Furthermore, the generator pinch limitation prevented experimentation at reduced generator glycol loop flow rates and supply temperatures while meaningful generator glycol flow rates above the design value could not be achieved due to limitations of the generator loop circulation pump. The off-design flow rate targets for the condenser loop were updated to address the limitations of the circulation pump. Thus, condenser loop flow rate was required to remain within ±5% of the value during baseline experimentation (32.83 kg s^{-1}). The baseline test heat duties for the generator and evaporator (473.0 kW and 263.8 kW, respectively) yield flowrate targets of 26.87 kg s^{-1} and 12.57 kg s^{-1} for the generator loop and evaporator loop at the design temperature difference specification of 5°C, respectively.

For each experiment where external loop flowrates were held at their baseline values, the flowrates were held within 5% of the specified value. Flowrates were also held within 5% of the values specified for experiments where the flowrate was altered to assess performance trends. The evaporator and condenser loops met flowrate stability criteria of 0.75% for all off-design tests. The heat duty of the generator was held within 5% of the design case value for each test. Generator inlet temperature was maintained within ± 3°C the target value for each test through connecting/disconnecting generator loop

heaters to match thermal demand. Several test points did not meet energy balance criteria, the worst energy balance value for full load application rating was 4.21% compared to the cutoff criteria of ± 3.69%. This variance in energy balance was determined acceptable considering the system was not insulated and heat loss from the prototype contributed to the magnitude of this value.

At high chilling duties and chilled water delivery temperatures, the standard deviation criterion for chilled water delivery (<0.1°C) was not met. The worst standard deviation for the chilled water delivery during experimentation was 0.14°C which was a result of an undersized basement heat exchanger and thermal cycling of the heat line energy source. The circulation heater supplying energy to the basement heat exchanger cycled on and off during experimentation to maintain a thermal setpoint. At low heat line temperatures and high chilled water delivery temperatures, there was insufficient driving potential given the size of the basement heat exchanger to reject the produced cooling load. The chilled water delivery temperature would thus decrease until the circulation heater cycled which caused a period of unavoidable oscillations in the chilled water delivery temperature considering the use of a proportional–integral–derivative controller on the heat line control valve. The temperature of the heat line supply and chilled water delivery over the course of the data point with the worst chilled water temperature stability is shown in Figure 5-7. At this point, full load performance of the organic Rankine vapor compression system with a chilled water delivery temperature of 13.1°C was tested.

Furthermore, several test points did not meet condenser inlet temperature stability given erratic ambient conditions during experimentation. Figure 5-8 shows the average condenser glycol inlet temperature and the speed of the cooling tower fans over the course of the data point with the worst condenser inlet temperature stability. The stability at this point was 0.16°C considering testing was complete during a rainstorm where cooling tower fan speed had to be varied manually between 42% and 100% its capacity to account for gusting winds. At this point, full load performance of the prototype with a chilled water delivery temperature of 5.1°C was tested.

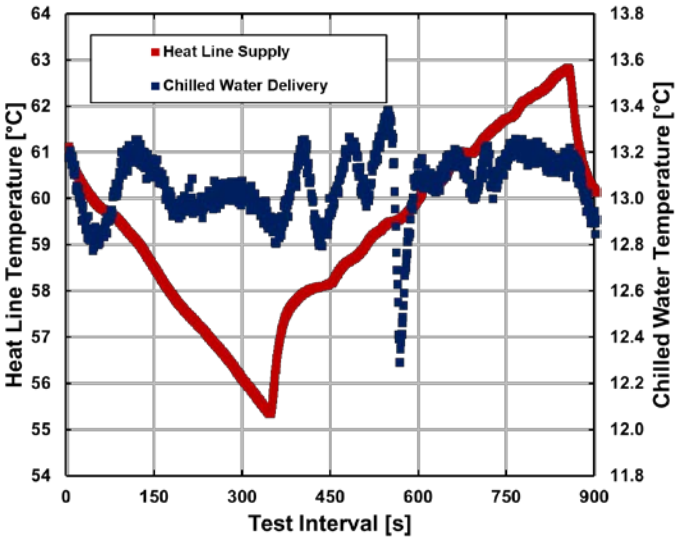

Figure 5-7 Chilled water delivery temperature instabilities during experimentation

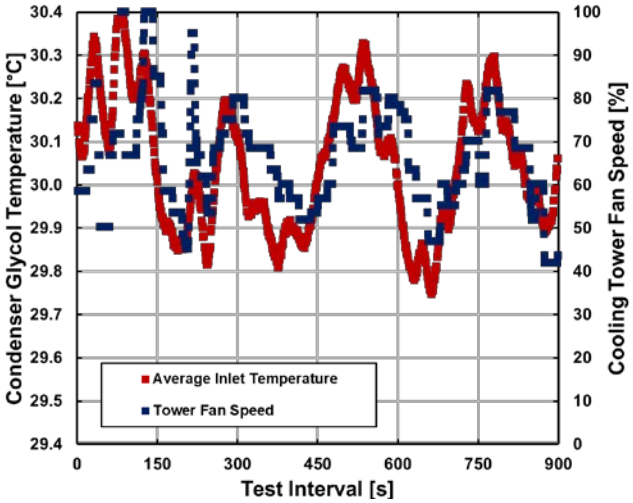

Figure 5-8 Condenser glycol supply temperature instabilities during experimentation

The data points which failed to meet temperature or energy balance criteria during performance rating were not retested for improvement as the dynamic shaft seal on the power cycle pump began leaking, which halted further experimentation. However, the failure of select data points to meet all criteria did not taint observable performance trends for each range of tested conditions. Therefore, these data points are simply called out in text with the criteria which was not met, and the respective value quantified during experimentation.

5.2.1. Off-Design Evaporator Experimentation

The prototype was first experimented at full-load with off-design evaporator water discharge temperatures. For these experiments, the system was able to be operated between 2.1°C and 13.1°C. Testing at higher delivery temperatures was not possible due to evaporator loop instabilities. Compressor stall was not detected at the lowest chilled water delivery temperatures, but the efficiency of the device reduced suggesting an operational limitation was being approached. If testing at chilled water delivery temperatures below 2.1°C were desired, it is likely the condenser glycol inlet temperature would have to be reduced to avoid stall. Furthermore, it is suggested that the evaporator loop fluid be changed to a glycol mixture to prevent freezing. Test points which did not meet evaporator temperature stability included the test points at 13.1°C and 11.1°C with standard deviations of 0.14°C and 0.12°C, respectively. Test points which did not meet condenser temperature stability included the test points at 5.1°C, 3.1°C, and 2.1°C with standard deviations of 0.16°C, 0.14°C, and 0.16°C, respectively. Figure 5-9 shows key performance parameters at off-design chilled water delivery temperatures normalized to the respective values at the baseline operating condition (7°C chilled water delivery).

Power cycle operation is largely unaffected by changes to chilled water delivery temperature over the entire set of test conditions. In varying the chilled water delivery boundary condition, the operation of the power cycle can be affected in two ways. First, the altered compressor conditions could change the speed of the turbine which could shift the turbine efficiency. Second, there could be a change in economizer heat duty which would change the power cycle flowrate needed to maintain the generator heat duty. Plotting turbine and compressor performance on their respective maps shows how the relationship between the two devices changes with chilled water delivery temperature (Figure 5-10). At the lowest chilled water delivery temperature, the compressor speed is at its highest value. Thus, the turbine equivalent mass flow is at its minimum value. As the speed of the compressor rises with increasing evaporator chilled water delivery temperature, the turbine operating point crosses several efficiency

contours pushing the device towards its best efficiency point. However, a representative increase in turbine efficiency is not observed in the experimental performance data, which suggests the turbine map is not fully accurate. Indeed, turbine total to static efficiency is at its minimum value (75.32%) at the minimum chilled water delivery temperature. However, the experimental total to static efficiency first increases (to 77.29% at a chilled water delivery temperature of 7.1°C) then decreases (to 76.49% at a chilled water delivery temperature of 13.1°C) as the chilled water delivery temperature increases. The less than 1% increase in turbine efficiency over the testing conditions marginally effects the performance of the organic Rankine cycle.

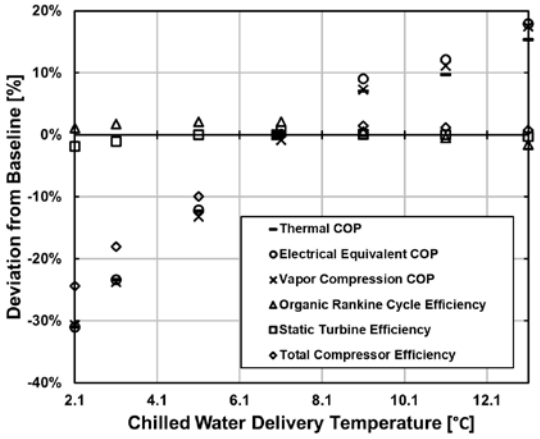

	2.1 °C	*7 °C*	*13.1 °C*
COP_{TH}	0.3845	0.5577	0.6430
COP_{EC}	13.35	19.37	22.83
COP_{VC}	3.638	5.250	6.169
η_{ORC}	7.791%	7.706%	7.586%
η_{turb}	75.25%	76.70%	76.49%
η_{comp}	64.08%	84.75%	85.38%

Figure 5-9 Performance trends at full load with off-design chilled water delivery temperatures

The compressor pressure ratio increases with decreasing chilled water delivery temperature. This is a result of the evaporator requiring a lower saturation temperature (and thus pressure) to deliver chilled water at lower temperatures. The compressor, with a largely consistent power transferred from the turbine, can provide less mass flow as its pressure ratio increases. Alternatively, greater compressor mass flows are achievable at lower compressor pressure ratios. While there is an overall increase in cooling cycle mass flow (from 1.163 kg s^{-1} at 2.1°C chilled water delivery to 2.148 kg s^{-1} at 13.1°C chilled water delivery), there is a reduction in equivalent mass flow rate at chilled water delivery temperatures greater

than the design (7°C). This is a result of altering fluid properties as the chilled water delivery temperature increases. At 7°C chilled water delivery, the refrigerant density at the compressor inlet is 11.46 kg m^{-3} which translates to a volumetric flow of 545.6 m^3 hr^{-1}. At the greatest chilled water delivery temperature, the compressor inlet density is 14.42 kg m^{-3} which translates to a slightly lesser volumetric flow of 536.1 m^3 hr^{-1}. The decrease in equivalent compressor mass flow as compressor pressure ratio decreases causes the reduction in device speed (from 33.6 kRPM at 2.1°C to 29.2 kRPM at 13.1°C) which affected turbine equivalent mass flow. The combination of these effects (low compressor pressure ratio, high turbine load, and low shaft speed) resulted in improved compressor efficiencies. The greatest compressor efficiency documented during experimentation was at a chilled water delivery temperature of 9.1°C with a value of 85.97%.

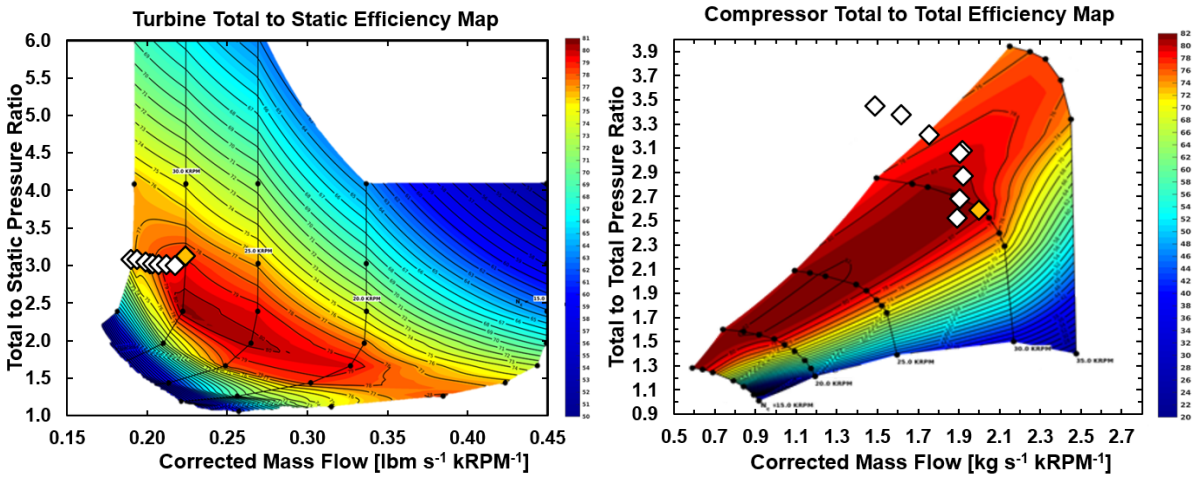

Figure 5-10 Chilled water delivery temperature testing turbo-compressor performance mapping

To further visualize prototype performance at off-design chilled water delivery temperatures, the temperature to entropy refrigerant state points for the maximum chilled water delivery test (13.1°C) and the minimum (2.1°C) were plotted against the baseline operating condition state points as shown in Figure 5-11.

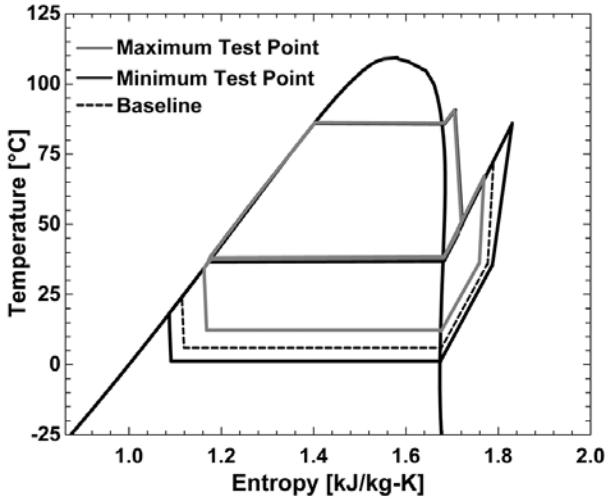

Figure 5-11 Experimental comparison of chilled water delivery temperature testing state points

The maximum, minimum, and baseline state points for the power cycle completely overlap further showing the consistent operation of the organic Rankine cycle irrespective of chilled water delivery temperature. This is true even considering an increased compressor discharge temperature at lower chilled water delivery temperatures (85.96°C at the minimum versus 67.09°C at the maximum). An increase in compressor discharge temperature would typically increase the economizer heat duty. However, the effective heat input to the power cycle from the economizer varies little with this change, from 47.22 kW at 2.1°C to 42.43 kW at 13.1°C. The economizer heat duty is largely consistent as an increase in compressor discharge temperature is balanced by a reduction in cooling cycle mass flow as chilled water delivery temperatures decrease. Thus, as shown in Figure 5-9, the system efficiency largely follows the efficiency of the compressor. The only other performance implication at differing chilled water delivery temperatures is that of the suction line heat exchanger. As there is an increase in chilled water delivery temperature, there exists a decreased driving potential for energy exchange in the suction line heat exchanger. This is shown in the suction line heat exchanger vapor enthalpy change (changing from 31.18 kJ kg^{-1} at 2.1°C to 22.80 kJ kg^{-1} at 13.1°C). As less heat is transferred to the suction line heat exchanger vapor at increased chilled water delivery temperatures, the subcooling of the refrigerant

entering the cooling cycle expansion valve is reduced. As previously detailed, an increase in vapor mass quality entering the evaporator (from decreased levels of refrigerant subcooling in the suction line heat exchanger) directly impacts the chilling duty of the organic Rankine vapor compression system.

In addition to testing the prototype at differing chilled water delivery temperatures, the organic Rankine vapor compression system was experimented at differing chilled water delivery flow rates. The circulation pump in the evaporator loop could produce a maximum flowrate of 17.64 kg s^{-1}. Thus, the four test points for off-design evaporator loop flow rate testing were 17.64 kg s^{-1}, 15.11 kg s^{-1}, 10.04 kg s^{-1}, and 7.50 kg s^{-1} considering the baseline evaporator loop flowrate of 12.57 kg s^{-1}. All testing criteria were met for this range of experiments aside from energy balances. In the order of presented flowrates, the respective energy balances were 3.77%, 3.86%, 4.14%, and 4.21% compared to the cutoff criteria of 3.69%. Figure 5-12 shows key performance parameters at off-design evaporator loop flow rates normalized to the respective values at the baseline operating condition.

The first observation in comparing off-design evaporator loop flow test points is that the resulting performance trends do not well align with the baseline value. The power cycle performance is improved over the baseline and the cooling cycle performance is impaired. This is indicative of a loss of fluid charge in the system where the condenser subcooling is decreased. Indeed, shortly after this experiment was performed, it was found that there was a leak across the power cycle pump shaft seal with a handheld refrigerant leak detector. To account for this leak in the remaining experiments, the power cycle accumulator was slightly pressurized to effectively increase system charge without physically adding refrigerant to the system. Condenser subcooling at full-load, baseline operating conditions was used as a proxy to set the accumulator charge value for future tests.

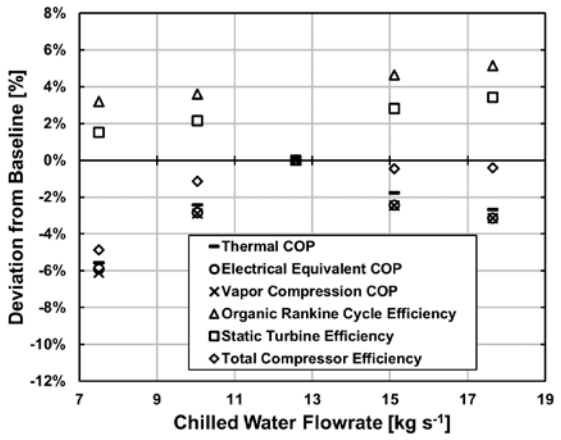

	7.51 [kg s^{-1}]	***12.58 [kg s^{-1}]***	***17.64 [kg s^{-1}]***
COP_{TH}	0.5266	0.5577	0.5427
COP_{EC}	18.22	19.37	18.76
COP_{VC}	4.904	5.223	5.059
η_{ORC}	7.952%	7.706%	8.102%
η_{turb}	77.87%	76.70%	79.33%
η_{comp}	80.63%	84.75%	84.40%

Figure 5-12 Performance trends at full load with off-design chilled water delivery flow rates

Further investigation into this range of experimental datapoints shows reducing system-wide performance characteristics at both lower and higher evaporator loop flowrates. Lower thermal performance is expected at elevated evaporator loop flowrates because the elevated flowrate will reduce the inlet temperature relative to the baseline (considering the chilled water delivery temperature is fixed). With a lesser inlet water temperature, there is less driving potential for heat exchange which could result in lesser refrigerant saturation temperatures (and, thus, pressures) within the evaporator to vaporize the refrigerant. This would increase the load of the compressor considering the fixed boundary conditions of the condensers. However, the saturation temperature at the maximum evaporator loop flowrate (17.64 kg s^{-1}) is greater than that of the baseline (6.13°C versus 6.03°C) suggesting the increased flowrate promotes heat transfer more than the decreased temperature differential impairs it. This assertion is further supported considering the performance of the prototype is also impaired at decreased evaporator loop flowrates. Here, performance improvements should be recognized considering increases to evaporator water inlet temperature and, thus, driving potential for heat exchange. However, this is not recognized considering the saturation temperature at the lowest flowrate tested was 5.64°C. This

decreased saturation temperature resulted in a slightly lesser cooling cycle mass flowrate to overcome the increased pressure differential of the compressor.

While there are clear performance trends relating to an altered flow rate of water through the evaporator at full-load operation, the implications to system performance are marginal compared to the effect of varying chilled water delivery temperature. This is shown both in the turbo-compressor maps in Figure 5-13 and in Figure 5-14 where the refrigerant state points for the maximum, minimum, and baseline evaporator loop flowrate datapoints (17.64 kg s^{-1}, 7.50 kg s^{-1}, and 12.57 kg s^{-1}, respectively) are plotted against each other on a temperature to entropy diagram.

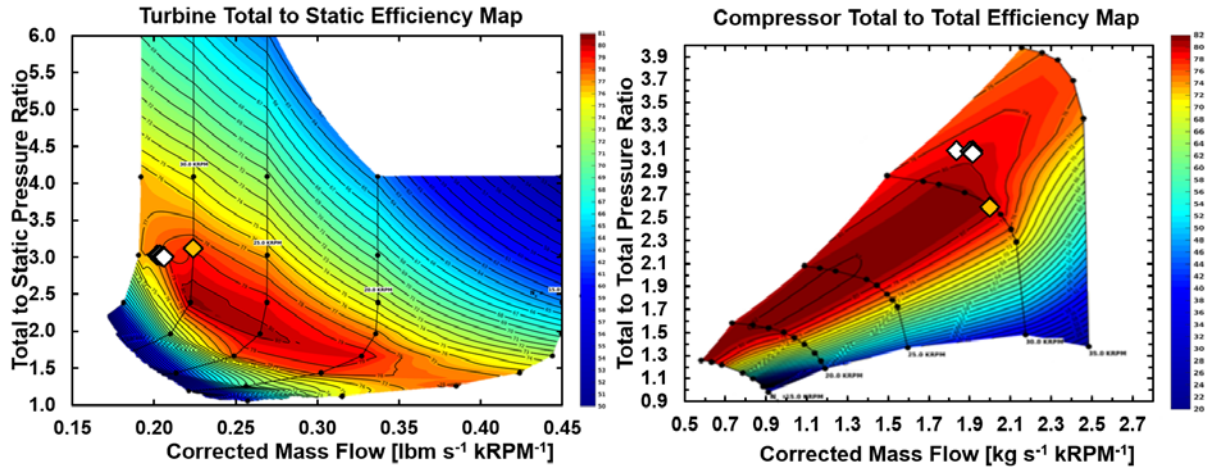

Figure 5-13 Chilled water delivery flow rate testing turbo-compressor performance mapping

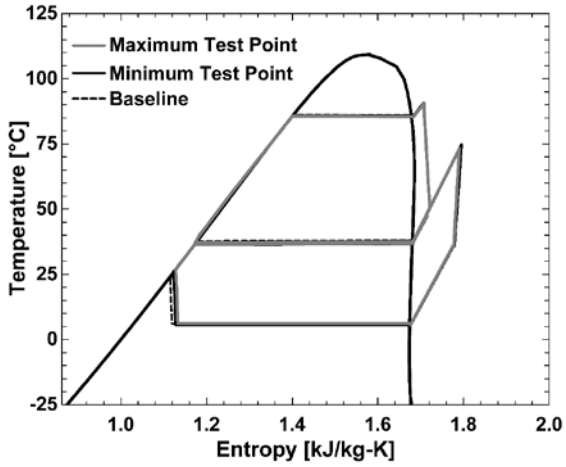

Figure 5-14 Experimental comparison of chilled water delivery flow rate testing state points

The only discernable discrepancy between the datasets is the liquid refrigerant subcooling in the suction line heat exchanger. The lesser subcooling at the minimum and maximum evaporator loop flowrates is a result of the lesser refrigerant charge during this series of testing conditions. If the correct charge would have been implemented, it is speculated that the data sets would overlap entirely.

5.2.2. Off-Design Condenser Experimentation

The next series of full-load tests performed on the prototype characterized its performance at varying condenser glycol mixture inlet temperatures. Performance implications regarding varying condenser loop flowrates were not assessed through experimentation considering the limitations of the test facility and the discussion of these limitations through the baseline scenario analysis. For this series, the prototype system was operated with condenser glycol mixture inlet temperatures varying between 16.6°C and 32.6°C. Testing at higher condenser inlet temperatures was not possible as the compressor would stall causing instabilities to system operation and risk to prototype integrity. Testing at lower condenser inlet temperatures was not possible considering the ambient temperatures during experimentation. All test points conformed to rating criteria except for the energy balances of the 32.6°C and 28.6°C test points. The energy balances of these conditions were 3.69% (rounded down) and 4.04% compared to the cutoff of 3.69%. Figure 5-15 shows key performance parameters at off-design condenser glycol mixture inlet temperatures normalized to the respective values at the baseline operating condition.

Altering the condenser glycol mixture inlet temperature had significant implications to performance regarding the operation of both sub cycles. For the organic Rankine cycle, the reduction in condenser glycol mixture inlet temperature increases the overall pressure ratio across the turbine (3.86 total-to-static at 16.6°C versus 3.03 at the baseline) as shown in the turbo-compressor maps in Figure 5-16. This significantly increases the turbine work (57.71 kW at 16.6°C versus 50.07 kW at the baseline) considering there are marginal changes to turbine efficiency over the range of test conditions.

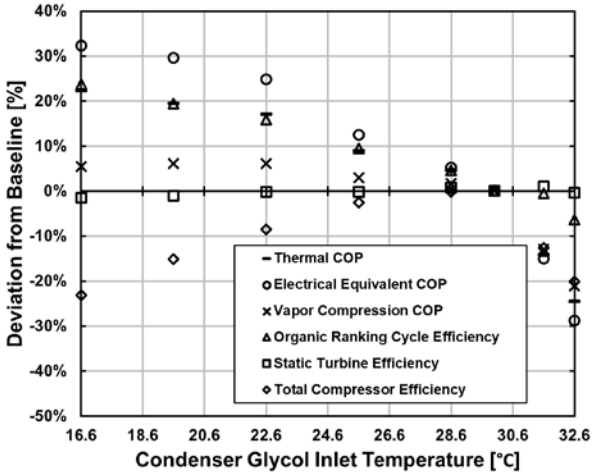

	16.6 °C	*30 °C*	*32.6 °C*
COP_{TH}	0.6816	0.5577	0.4211
COP_{EC}	25.63	19.37	13.80
COP_{VC}	5.539	5.250	4.145
η_{ORC}	9.541%	7.706%	7.218%
η_{turb}	75.54%	76.70%	76.37%
η_{comp}	65.12%	84.75%	67.72%

Figure 5-15 Performance trends at full load with off-design condenser glycol supply temperatures

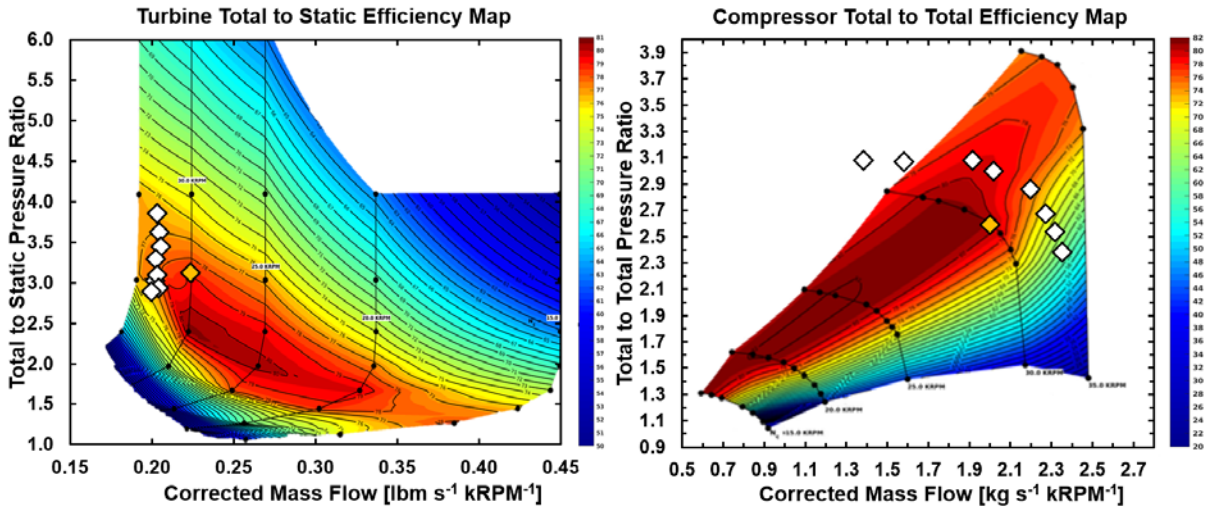

Figure 5-16 Condenser glycol supply temperature testing turbo-compressor performance mapping

Alternatively, the compressor pressure ratio decreases at decreasing condenser glycol inlet temperatures (3.38 total-to-total at 16.6°C versus 3.08 at the baseline). The pressure ratio changes to both the turbine and compressor at decreasing condenser glycol inlet temperature should increase the flow rate through the cooling cycle which would improve the chilling capacity of the prototype and the thermal COP considering the fixed generator heat duty. However, the flow rate through the compressor increases at a decreasing rate as the compressor efficiency is sharply reduced at decreased condenser glycol inlet temperatures (from 84.75% at the baseline to 65.12% at 16.6°C). The compressor efficiency at

reduced condenser glycol supply temperatures is reduced more than at increased chilled water delivery temperatures because the compressor refrigerant inlet density does not change. Thus, there is no decrease in compressor speed, and compressor equivalent mass flow increases with decreasing condenser glycol supply temperature. Compressor efficiency is also severely reduced with increasing condenser glycol mixture inlet temperatures as the device quickly enters the stall regime (from 74.05% at 31.6°C to 67.72% at 32.6°C). Stall is more prevalent at increased condenser glycol supply temperatures than at decreased chilled water delivery temperatures because the turbine work also decreases with increasing condenser glycol supply temperature from a lesser pressure ratio (from 50.07 kW at the baseline to 47.73 kW at 32.6°C). The implications to compressor efficiency are also observed in plotting refrigerant temperature to entropy state points (regarding the slope of the compression process) for the maximum (32.6°C) and minimum (16.6°C) condenser glycol inlet temperature test points against the baseline (30.0°C) state points in Figure 5-17.

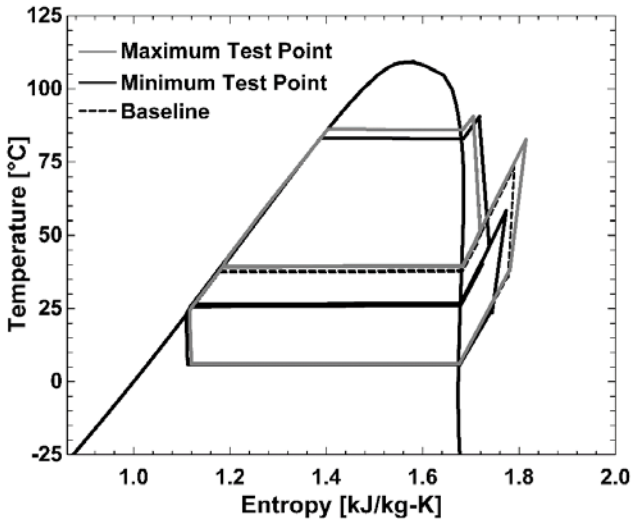

Figure 5-17 Experimental comparison of condenser glycol supply temperature testing state points

The refrigerant state point plots also show that there is an increased pinch temperature in the generator at the minimum test point over the baseline (4.43°C versus 1.62°C). As the condenser glycol inlet temperature is reduced, the generator subcooled regime heat duty increases (from 157.2 kW at the

baseline to 166.2 kW at 16.6°C considering refrigerant enthalpies and flow rates) from a reducing condenser saturation temperature and economizer heat duty (from 46.38 kW at the baseline to 37.25 kW at 16.6°C). Thus, to avoid increases to the generator heat duty above the cutoff criteria of ± 5%, the power cycle mass flow had to be slightly decreased from the baseline (from 3.145 kg s^{-1} to 2.910 kg s^{-1}).

5.2.3. Off-Design Generator Experimentation

The final series of full-load tests performed on the prototype characterized its performance at varying generator glycol mixture inlet temperatures. Performance implications regarding varying generator loop flowrates were not assessed through experimentation considering the generator pinch limitation and the inability of the generator loop circulation pump to produce a meaningful flow rate greater than the baseline value. While assessing performance at differing generator glycol supply temperatures, the system was operated between the baseline (91°C) and 120°C. Testing at higher supply temperatures could have caused damage to system components with limited temperature ratings. Testing at lesser supply temperatures was not possible at full load considering the generator pinch temperature limitation detailed in the discussion of the baseline system experimental results. Datasets at varied generator glycol supply temperatures met or surpassed all rating criteria. Figure 5-18 shows key performance parameters at off-design generator glycol supply temperatures normalized to the respective values at the baseline operating condition.

It is shown that there is a substantial improvement to organic Rankine cycle efficiency as generator glycol mixture inlet temperature increases. This is a result of the increased superheating that occurred in the generator (from 4.91°C at the baseline to 30.4°C at a glycol mixture inlet temperature of 120°C). Superheating increased in the generator as the generator glycol supply temperature increased as the generator refrigerant outlet temperature converged to the generator glycol mixture supply temperature under all test conditions and an attempt was made to maintain the generator refrigerant

saturation pressure. The increased superheating increased the isentropic enthalpy change across the turbine (from 20.76 kJ kg^{-1} at the baseline to 25.77 kJ kg^{-1} at a glycol mixture inlet temperature of 120°C) which greatly increased its work output (from 50.07 kW to 62.89 kW) considering the turbine isentropic efficiency was largely consistent across the range of testing conditions (varying between 76.70% at the baseline to a maximum of 78.44% at 120°C). The increased turbine power increased the efficiency of the power cycle considering the generator heat duty was fixed and there was little change to pump work.

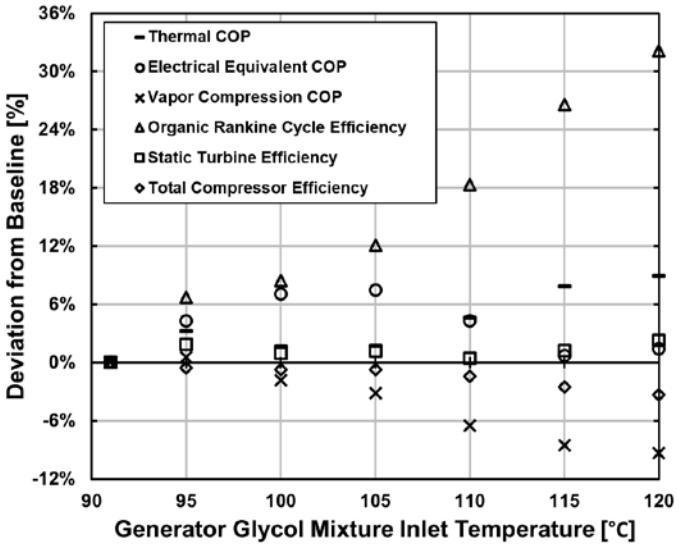

	91 °C	*120 °C*
COP_{TH}	0.5577	0.6075
COP_{EC}	19.37	19.64
COP_{VC}	5.250	4.761
η_{ORC}	7.706%	10.18%
η_{turb}	76.70%	78.44%
η_{comp}	84.75%	81.90%

Figure 5-18 Performance trends at full load with off-design generator glycol supply temperatures

Pump work was largely consistent through testing considering the attempt to maintain generator refrigerant saturation pressure. It was desired to maintain the refrigerant saturation pressure in the generator during testing to only assess how varying the generator glycol mixture inlet temperature affected performance, not refrigerant saturation pressure. However, this was challenging considering the changing generator heat transfer regimes at increased glycol mixture inlet temperatures and the requirement to maintain the overall heat duty within 5% of the baseline value. Plotting the turbo-compressor operating points on the respective performance maps in Figure 5-19 shows the turbine pressure ratio (and thus generator saturation pressure) closely matched the baseline value (lowest

equivalent mass flow) up to a generator glycol mixture inlet temperature of 105°C. The pressure ratio was then slightly increased over the next two data points (110°C and 115°C) which resulted in slight decreases to equivalent mass flow. The last two tests (115°C and 120°C) had similar pressure ratios which allow a representative increase to equivalent mass flow that was observed at the lower temperature testing conditions.

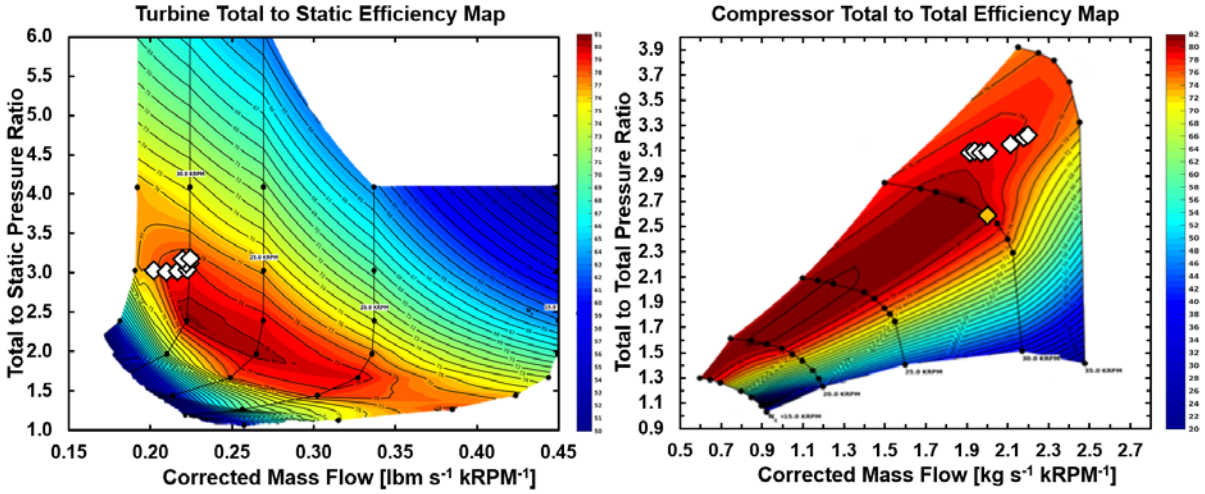

Figure 5-19 Generator glycol supply temperature testing turbo-compressor performance mapping

The changes to generator refrigerant saturation pressure were the primary cause of the inconsistent trends observed for electrical equivalent COP and thermal COP in Figure 5-18. First, the electrical equivalent COP increases while the thermal COP remains largely unchanged. Then, the thermal COP increases but the electrical equivalent COP decreases back near the baseline value. This tradeoff suggests greater electrical equivalent COP values are achievable with increased turbine superheat at the expense of saturation pressure while greater thermal COP values are achievable with increased generator saturation pressure at the expense of superheating and pump power consumption.

Also observed in the turbo-compressor performance mapping for this dataset is that increased turbine power at elevated generator glycol mixture inlet temperatures resulted in increases to compressor mass flow. The compressor pressure ratio was largely fixed considering the boundary

conditions at the condensers and evaporator were consistent during testing. However, slight increases to compressor pressure ratio are observed in mapping as the flow rate increases. This is a result of increasing frictional pressure losses in the heat exchangers and pipe runs adjacent to the compressor (from increasing volumetric flows) which limit performance as previously detailed in the scenario analysis for the baseline experimental test point. While the compressor equivalent mass flow increases, its efficiency is not as severely reduced as it was at reduced condenser glycol mixture inlet temperature considering the representative increase to pressure ratio across the device.

To further analyze implications of generator glycol mixture supply temperature on prototype operation, the baseline experimental temperature to entropy state points were plotted against those at the maximum generator glycol mixture supply temperature (120°C) in Figure 5-20. The first observation in this comparison is the slightly elevated generator saturation temperature and the substantiated degree of generator superheating at the maximum test condition. At the maximum test condition, the increased generator superheating results in a turbine discharge temperature (81.51°C) which surpasses the compressor discharge temperature (76.24°C). Thus, the order in which the recuperator and economizer transfer energy to the liquid leaving the power cycle pump is undesirable for this operating condition. However, the economizer still transfers 20.2 kW to the power cycle at the maximum generator glycol supply temperature test point despite the recuperator transferring 132.4 kW. The baseline heat duty for these two devices were 46.4 kW and 35.7 kW, respectively. The reason the economizer is still able to transfer heat to the power cycle, despite the turbine discharge having a greater thermal quality than that of the compressor, is that the power cycle liquid leaving the pump has a much higher specific heat capacity than the vapor in the recuperator and economizer. The increased heat capacity of the liquid results in it being heated a lesser degree than the vapor which is heating it is cooled. If the generator glycol mixture supply temperature were to be further increased, it is possible that energy could be transferred from the liquid at the recuperator liquid outlet to the vapor entering the economizer from the compressor, which

would impair prototype performance. An interesting option to mitigate this challenge would be to match the turbine and compressor discharge temperatures and combine the recuperator and economizer into a single heat exchanger which transfers heat to the liquid refrigerant leaving the power cycle pump.

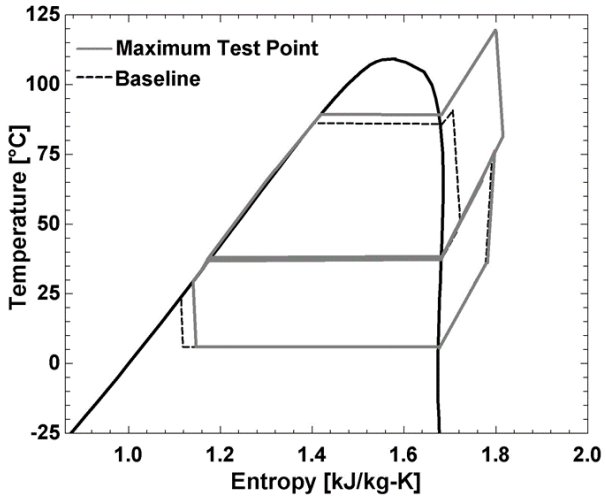

Figure 5-20 Experimental comparison of generator glycol supply temperature testing state points

Also shown in plotting refrigerant temperature to entropy state points is a reduced degree of cooling cycle subcooling at the high temperature suction line heat exchanger outlet at the maximum generator glycol supply temperature. This reduction in subcooling results in the decreases to vapor compression cycle COP with increasing generator glycol mixture supply temperature shown in Figure 5-18. The cause of this change relates to the reduced heat duty of the economizer and the performance limitations of the cooling cycle condenser. As the economizer heat duty is decreased, the cooling cycle condenser heat duty is increased. As the cooling cycle condenser is already limited in its performance, the vapor quality entering the high temperature suction line heat exchanger connection port increases as generator glycol mixture supply temperature increases (from ~6.09% at the baseline to ~11.4% at the maximum test condition). This increases the refrigerant inlet vapor quality to the evaporator (18.20% versus 13.83%) which directly decreases the cooling duty of the prototype as previously detailed in the discussion of the baseline experimental datapoint.

5.3. Integrated Part-Load Value Experimentation

The final set of experiments performed on the organic Rankine vapor compression system were used to quantify the Integrated Part-Load Value efficiency of the prototype. This first required an assessment of the full-load baseline operating condition dataset to determine the adjusted temperatures for the external stream heat exchangers under the 100% part-load operating condition. The adjusted temperatures calculated from the baseline experimental data were 0.05°C, 0.29°C, and 0.19°C for the generator glycol inlet, the average condenser glycol inlet, and the evaporator water outlet, respectively. Thus, the updated boundary conditions for simulated fouling testing at 100% load were a generator glycol inlet temperature of 90.95°C, average condenser glycol inlet temperature of 30.29°C, and evaporator water outlet temperature of 6.81°C. The respective temperatures at the baseline operating condition quantified through experimentation were 91.18°C, 29.98°C, and 7.00°C. Thus, the only baseline test temperature which did not already conform to the rating criteria (considering fouling) was the average condenser glycol mixture inlet temperature which missed the precision criteria (±0.28°C) by 0.03°C. Therefore, another full-load test was performed at the specified fouling conditions at the baseline flowrates (26.87 kg s^{-1} generator loop, 32.83 kg s^{-1} condenser loop, and 12.57 kg s^{-1} evaporator loop) to better represent operation with fouled heat exchangers as specified by the Integrated Part-Load Value methodology. The resulting temperatures at this experimental operating condition were a generator glycol inlet of 91.01°C, average condenser glycol inlet of 30.29°C, and evaporator water outlet of 6.81°C.

In addition to the fouled full-load test, three tests at the remaining part load conditions were complete (75%, 50%, and 25%) at the external loop temperature targets presented in Table 4-6. It was found that the adjusted temperature for each heat exchanger reduced at lower loading conditions, and, thus, the three remaining tests did not have to be repeated with fouling considerations as the clean datapoints already met fouling temperature target cutoff criteria. In fact, all testing criteria were met for the part-load data points during experimentation, including chilling duty targets. At each part load

condition, chilling duties were tested within 2% the full load value (±5.276 kW) without requiring correction or interpolation of data. Figure 5-21 shows key performance parameters at part-load operation normalized to the respective values at the baseline operating condition. With these values, the Integrated Part-Load Value for the prototype was determined to be 0.682 for thermal COP and 60.3 for electrical equivalent COP. These are 122% and 311% the baseline values, respectively.

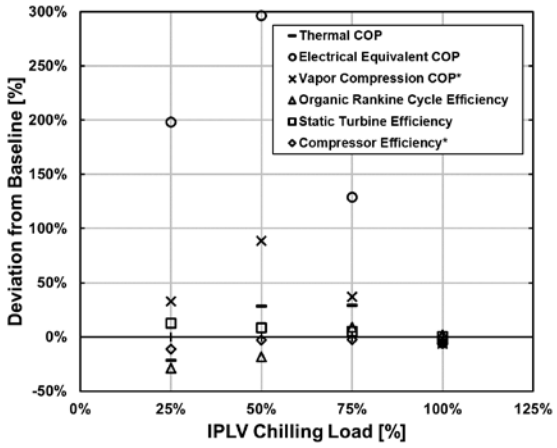

	Baseline	*100%*	*75%*	*50%*	*25%*
COP_{TH}	0.5577	0.5260	0.7199	0.7155	0.4361
COP_{EC}	19.37	18.25	44.36	76.78	57.76
COP_{VC}	5.250	4.919	7.196*	9.916*	6.984*
η_{ORC}	7.706%	7.845%	8.382%	6.284%	5.490%
η_{turb}	76.70%	77.09%	80.50%	83.12%	86.50%
η_{comp}	84.75%	80.07%	82.84%*	82.35%*	75.39%*

Figure 5-21 Performance trends at part load considering heat exchanger fouling

As denoted by asterisks in Figure 5-21, the vapor compression cycle COP values presented for 75%, 50%, and 25% part-load operation are calculated using the static turbine work production in place of the total compressor power consumption. Turbine work (which equals compressor power consumption given a perfect transfer efficiency) had to be used at these conditions considering an energy balance on the economizer was unable to accurately predict cooling cycle mass flow. This prevented the plotting of compressor performance at 75%, 50%, and 25% load on the turbo-compressor maps in Figure 5-22 which required an accurate compressor flow measurement to quantify total properties. Considering total compressor properties could not be determined for the 75%, 50%, and 25% loading conditions, the efficiencies presented for the device in Figure 5-21 are the static values (also denoted by asterisks).

An energy balance could not be used on the economizer to determine cooling cycle mass flow rate at turndown. The economizer had a significantly lower heat duty at 75% load (4.3 kW versus 46.3 kW at 100% load adjusted for fouling), which increased the uncertainty in the derivation. At 50% load, the heat duty of the economizer was reversed, which inhibited system performance. At 25% load, the economizer transferred energy from the cooling cycle to the power cycle, but the power cycle refrigerant in the economizer was a two-phase mixture of liquid and vapor. The change in utility of the economizer at part-load is a result of reducing saturation pressures in the generator and condensers.

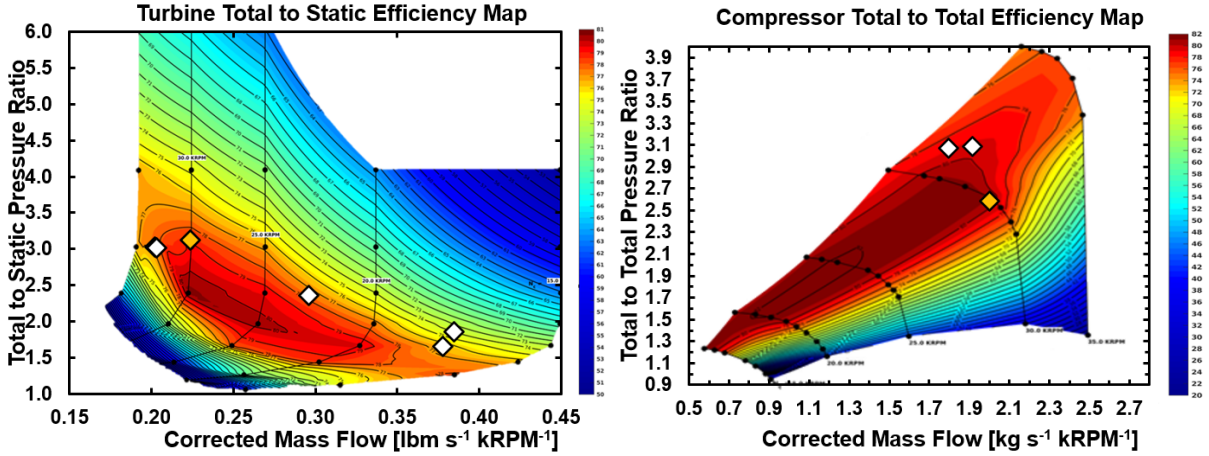

Figure 5-22 Part load testing turbo-compressor performance mapping

At part-load, the condenser glycol inlet temperature is reduced, which lowers the condenser saturation pressure. The condenser saturation pressure is also reduced at part load from a reduction in system pressure losses at lower flowrates. Thus, there was a decrease in compressor discharge temperature from the reduced condenser saturation pressures. As mentioned earlier, the power cycle mass flow and generator refrigerant saturation pressure are interdependent. To decrease the evaporator chilling load, the power cycle pump speed was decreased to reduce the turbine power input to the cooling cycle. A byproduct of decreasing the pump speed was also a decrease in the generator refrigerant saturation pressure. Similar to experimenting at elevated generator temperatures, this increased the superheating at the turbine inlet and outlet. The combination of increased turbine superheating and

reduced compressor discharge temperature minimized the economizer utility at 75% load. At 50% load, the economizer heat transfer was reversed as the compressor discharge was heated ~5.6°C from the pump discharge (which was cooled ~0.9°C). However, at 25% load, the saturation pressure in the generator had reduced to a value which the economizer was able to transfer energy from the compressor discharge to the power cycle as the power cycle refrigerant was two-phase. The high-pressure saturation temperature in the power cycle at 25% load was ~41.7°C where the compressor discharge temperature was 44.9°C. Figure 5-23 shows the refrigerant temperature to entropy state points at part-load experimentation to visualize the changes to saturation pressure and economizer utility.

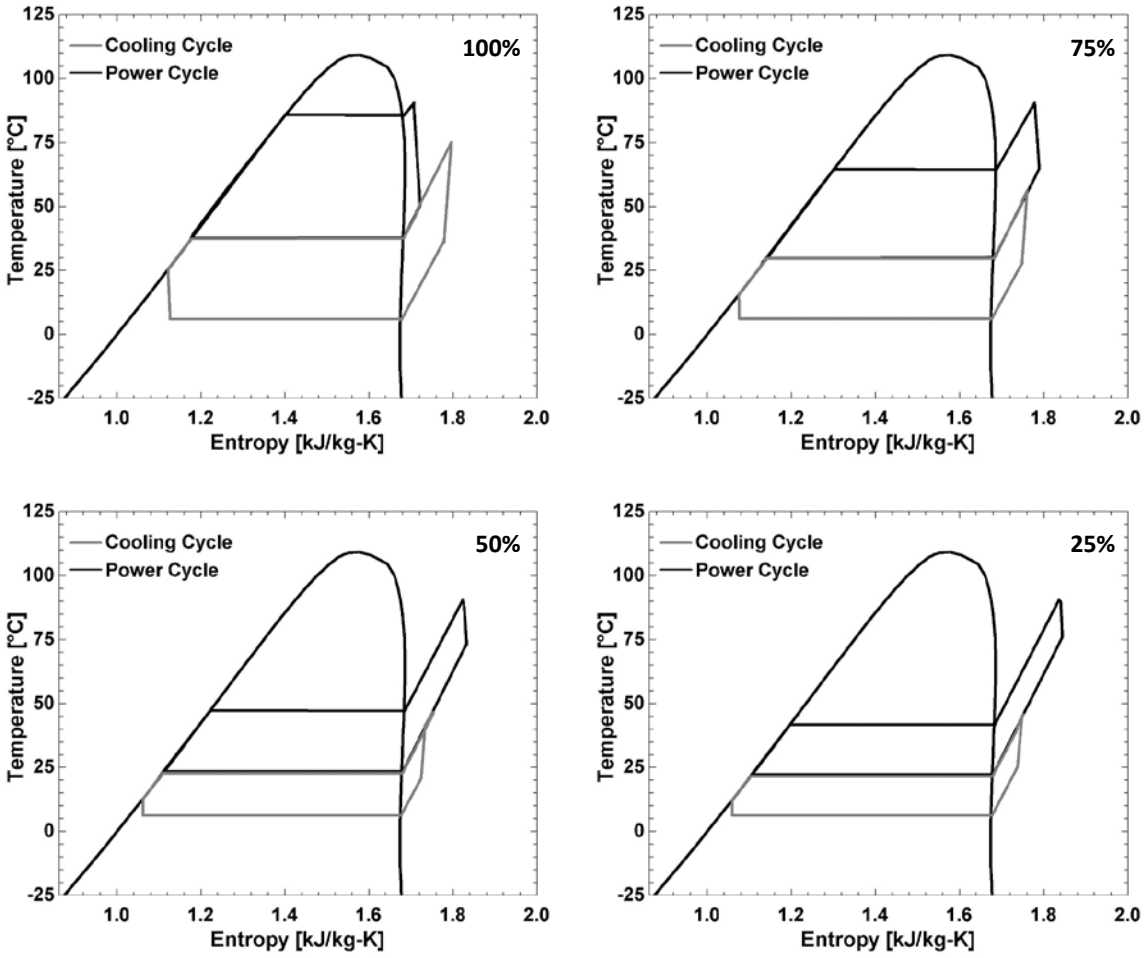

Figure 5-23 Experimental comparison of part load testing state points

Another performance trend observed at reduced evaporator loads for Integrated Part-Load Value testing was that there were significant improvements to the turbine efficiency. The maximum turbine efficiency quantified during all experiments was 86.50% at the lowest evaporator loading condition of 25%. As shown in mapping turbine performance at part load, turbine efficiency improvements were recognized as pressure ratio is decreased, shaft speed is decreased, and, as a result, equivalent mass flow is increased. An additional component which saw performance improvements at part-load operation was the cooling cycle condenser. At part-load, the condenser glycol flow rates were held at their baseline values. With the full-load condenser loop flowrate and reduced heat duties, the cooling cycle condenser was better able to condense the cooling cycle refrigerant. During the baseline experiment, the refrigerant left the cooling cycle condenser at a vapor mass quality of 6.2% (and 7.7% considering fouling). The vapor mass quality at the cooling cycle condenser outlet was reduced to 0.8% at 75% load, and the fluid was fully subcooled at 50% and 25% load.

The changes to system saturation pressures and flow rates also affected the operation of the compressor at part-load operation. The reduction in compressor pressure ratio at part-load was not significant enough in comparison to the reduction in compressor mass flow to avoid stalling at 50% and 25% loading conditions. While experimentation was complete to quantify Integrated Part-Load Value, it is not recommended the compressor be further operated at these conditions without creating provisions within the test facility to mitigate risk of damage to the device. Compressor stall at 50% and 25% load results in reducing compressor efficiency which reduces the vapor compression cycle efficiency and impairs the overall thermal performance of the prototype.

Despite the challenges with compressor stall and economizer utility, the organic Rankine vapor compression cycle was able to achieve Integrated Part-Load Value efficiencies surpassing the baseline values. The electrical equivalent COP improved more than any other performance metric at part-load as shown in Figure 5-21. As detailed in the discussion of off-design generator glycol inlet temperature testing,

there exists a performance trade-off with generator refrigerant saturation pressure. As generator refrigerant saturation pressure increases, there is a decrease in electrical equivalent COP but, generally, an improvement to thermal COP. However, as the prototype is operated at part-load, the saturation pressures in the condensers are also reduced from a representative reduction in condenser glycol mixture supply temperature and reduced system pressure loss. The combination of reduced saturation pressures in the generator and condensers maintains the turbine pressure ratio at a sufficient value, which results in a simultaneous improvement to thermal COP and electrical equivalent COP at 75% and 50% loading conditions. At 25% loading, the condenser glycol inlet temperature is held at the same value as the 50% test, which, considering the reduced compressor efficiency from stalling and further reduced generator refrigerant saturation pressure, results in a decrease to both electrical equivalent COP and thermal COP.

Chapter 6 Conclusions

This research effort presented the motivation, simulation, design, and experimentation of an advanced organic Rankine vapor compression chiller prototype. The baseline performance of the prototype was simulated in Chapter 3 using a thermodynamic model. The model boundary conditions and technical assumptions were set to allow the system to deliver sustainable district cooling loads using coolant waste heat from reciprocating engines for centralized power delivery. This assessment predicted a well-designed prototype could deliver 300 kW of chilled water at 7°C at a thermal COP of 0.65. To achieve this operation, 458.8 kW of heat in the form of 91°C coolant is required to power the technology with heat rejection to a separate liquid coolant loop at 30°C. The chilled water, heat supply coolant, and heat rejection coolant were all assumed to have temperature differentials of 5°C across their respective heat exchanger. The system would require 13.16 kW of electrical energy to circulate refrigerant through the organic Rankine cycle of the prototype. Thus, the electrical equivalent COP of the prototype was simulated to be 22.8. Considering the technologies suspected to fill growing global cooling demands have COPs around 4 [1], the prototype organic Rankine vapor compression system could significantly reduce the electrical generation increases required to support demand. Furthermore, the prototype uses an environmentally benign working fluid (R1234ZE(E)), which, with reduced electrical generation emissions, could help to combat climate change.

To test the results of the simulation effort, a prototype organic Rankine vapor compression chiller and supporting systems for experimentation were designed and constructed. The selection of critical system components and calculations used to determine their adequacy were outlined in Chapter 3. Chapter 4 presented the piping and instrumentation diagram of the entire test facility and discussed key features. A solid model of the system was also presented showing the system format. The resulting prototype (not including auxiliary equipment) was 5.28 m in length, 1.75 m in width, and 2.84 m in height with a mass just under 7,000 kg fully charged (water, glycol mixtures, and refrigerant). Considering the

design cooling duty of the prototype, this yields specific sizing characteristics of 30.8 m^2 MW^{-1}, 87.5 m^3 MW^{-1}, and 23.3 kg kW^{-1} for footprint, volume, and mass, respectively. While these values are already comparable to those of commercial alternatives [52,60,196,197], there is significant opportunity for their minimization through further design optimization. The final sections in Chapter 4 presented the instrumentation and methods used to test and rate the performance of the prototype, as well as the architecture of a data reduction model used to assess performance data. Experimental methods were informed from commercial performance rating standards for vapor compression and absorption chillers [44,190].

Chapter 5 presented the experimental results of each performance rating test as well as a discussion on the implications of the data. Performance rating tests included a full-load, baseline test, off-design tests with differing chilled water delivery temperatures, chilled water delivery flowrates, condenser glycol supply temperatures, and generator glycol supply temperatures, and part-load tests to determine the Integrated Part-Load Value performance. The baseline experimentation of the test facility showed the prototype was unable to produce its design chilling duty and thermal COP within the commercial specification. The thermal COP and chilling duty of the prototype in practice was limited by several system components which failed to meet the specification from their manufacturer. A major limitation was the flowrate of glycol through the condenser loop (25.6% below the target value) which prevented the baseline dataset from meeting the accuracy criteria for condenser glycol flow rate.

At the baseline operating condition, the inlet and outlet temperatures to the generator were 91.18°C and 86.24°C on the external process connections, respectively. The average inlet and outlet temperatures of the condensers on the external process connections were 29.98°C and 36.70°C, respectively. The inlet and outlet temperatures of the evaporator on the external process connections were 12.12°C and 7.00°C, respectively. At these conditions, 263.8 kW of chilled water was produced at a thermal COP of 0.56 The primary challenges relating to the loss in efficiency over the modeling predictions

were the reduced flowrate through the external condenser process connections, the inability of the cooling cycle condenser to liquify and sub cool its refrigerant, a reduced turbine efficiency, and underpredicted pressure losses. These challenges require more energy to be supplied to the system to achieve the target cooling duty. Slight increases to the heat duty over the design (473.0 kW versus 458.8 kW) were obtainable through increasing the power sent to the power cycle pump and supplied by the generator loop circulation heaters. However, increasing the flow through the power cycle quickly resulted in choked turbine flow which increased its back pressure and, thus, the saturation pressure in the generator. Considering the fixed boundary conditions on the external process connections to the generator, this resulted in a pinch limitation which prevented the system from achieving 300 kW of cooling. However, it is noted that the compressor and turbo-compressor shaft transfer efficiencies were greater in experimentation than the original predictions from the manufacturer of the device.

With the baseline operational data assessed, a scenario analysis was performed using the baseline thermodynamic model from Chapter 3 and experimentally determined component performances as new modeling input variables. It was found that the prototype would be able to achieve its design case cooling duty without flow choking in the turbine at a thermal COP surpassing the original prediction (0.66 versus 0.65) while using the current turbo-compressor design. However, this would require test facility modifications to improve the external flowrate through the condensers, reduce the performance inhibiting pressure losses throughout the system, and replace the malfunctioning cooling cycle condenser with a properly functioning unit.

Further experimentation was complete following this analysis to determine the response of the prototype to differing boundary and loading conditions. The majority of datapoints conformed to all rating criteria with a few exceptions. It is noted that all tests were steady state over a fifteen-minute interval with data collected at 2 Hz. All test points were related back to the baseline operating condition to identify performance trends. The identification of system-wide organic Rankine vapor compression performance

trends at off-design system operation is critical to the future development of validated thermo-economic design optimization studies to assess the true economic viability of the technology. The first set of off-design tests were performed at differing chilled water delivery temperatures at full-load operation. It was found that the prototype could operate at chilled water delivery temperatures between 2.1°C (the minimum temperature required by performance rating standards) and 13.1°C. Operation at higher chilled water delivery temperatures at full load was not possible due to an undersized basement heat exchanger and an oscillating heat source for the heat line. System performance was found to improve with increasing chilled water delivery temperature up to a maximum thermal COP of 0.7043. The greatest compressor efficiency quantified during experimentation (88.07%) was obtained during these tests at a chilled water delivery temperature of 13.1°C. Efficiency of the prototype at lower chilled water delivery temperature followed the efficiency of the compressor, which reduced as it approached stall.

Another test was performed at full load assessing the response of the system to differing chilled water flowrates at a fixed chilled water delivery temperature. It was found performance is impaired at both decreasing and increasing chilled water flowrates suggesting the water flow plays a larger role in evaporator heat transfer than the temperature difference between the two process fluids. It was found that the performance trends of these test points did not align with the baseline operating condition and indicated a loss of refrigerant in the system. Thus, the prototype was inspected and a leak across the power cycle pump shaft seal was located. Experimentation continued with the accumulator slightly pressurized following this discovery to effectively bring the system charge back to its baseline value.

Prototype operation was also assessed at variable condenser glycol mixture inlet temperatures at full load. Operation at full load with differing condenser glycol mixture flowrates was not tested considering the effects were previously assessed through the scenario analysis and the limitations of the test facility. It was found that the prototype could operate at condenser glycol mixture inlet temperatures between 16.6°C and 32.6°C at full load. Operation at lower temperatures was not possible considering

the ambient temperatures during experimentation. Operation at higher temperatures was not possible as the compressor began stalling placing the health of the turbo-compressor at risk. System performance was found to improve with decreasing condenser glycol mixture supply temperature through increasing the performance of both the cooling cycle and power cycle. However, performance improvements were not as drastic as those at varying chilled water delivery temperature (maximum thermal COP of 0.6816 at condenser glycol mixture inlet temperature of 16.6°C). This was because the compressor efficiency drastically decreased with decreasing condenser glycol inlet temperatures where the compressor flowrate increased (from an increasing power output of the power cycle) and the compressor pressure ratio decreased (from a decreasing condenser refrigerant saturation pressure). In fact, the efficiency of the compressor at a condenser glycol mixture supply temperature of 16.6°C (65.12%) was less than it was at 32.6°C (67.72%) where the unit was stalling, which was an unanticipated result.

The final full-load application rating conditions investigated experimentally related to the glycol mixture inlet temperature of the generators. Experimentation at off-design generator glycol flow rates was not possible considering the pinch limitation in the generator and the generator loop circulation pump was unable to provide meaningful increases to flowrate over the baseline value. It was found that the prototype could operate at generator glycol mixture inlet temperatures between 91.0°C and 120.0°C at full load. Operation at lower temperatures was not possible considering the pinch limitation in the generator. Operation at greater temperatures was not possible considering the temperature ratings of system components. Thermal performance of the prototype increases with increasing generator glycol mixture inlet temperature considering significant improvements to the organic Rankine cycle efficiency (>30%) over the baseline. However, the improved performance of the power cycle is challenged by a decrease in performance in the cooling cycle. As the generator glycol mixture inlet temperature increases, the turbine discharge temperature increases. This increases the heat duty of the recuperator but decreases the heat duty of the economizer. As the cooling cycle condenser is already limited in its

performance, a reduction in economizer heat duty increases the vapor mass quality at the discharge of the cooling cycle condenser which reduces the achievable cooling duty in the evaporator. This set of tests also uncovered a performance trade-off between thermal COP and electrical COP. Electrical COP decreases with increasing generator saturation temperature, but the thermal COP increases.

The final set of experiments assessed the part-load operation of the prototype following the Integrated Part-Load Value methodology. First, the system was operated at full load with external loop temperatures adjusted for fouling. Specifically, the generator glycol mixture inlet temperature was decreased 0.23°C, the average condenser glycol mixture inlet temperature was increased 0.31°C, and the chilled water delivery temperature was decreased 0.19°C from the baseline test. These small changes resulted in a significant reduction in thermal performance (from 0.56 thermal COP to 0.53). However, it is noted that, to meet the testing criteria for commercial water chilling technologies, the condenser water temperature only had to be increased 0.03°C from the baseline value. The generator glycol mixture inlet temperature and chilled water delivery temperature were already within the tolerances for the full-load operating condition considering heat exchanger fouling. This shows that manufacturers of commercial systems can inflate the published performance capabilities of their technologies if operated close to the boundaries of the criteria cutoffs. Performing the remaining experiments at 75%, 50%, and 25% load showed the Integrated Part-Load thermal COP of the system was 0.68 while the electrical equivalent value was 60.3. These were 122% and 311% the baseline values, respectively. The greatest turbine efficiency quantified during experimentation (86.50%) was obtained during these tests at a loading condition of 25%.

Several operational challenges occurred during part-load testing. First, the compressor stalled at 50% and 25% load. Although these points were able to be tested, it is not recommended they be operated at again until provisions are incorporated to prevent compressor stall to mitigate risk to the turbo-compressor. Also, the economizer has limited utility at turndown. From 100% load to 75% load, the

economizer heat duty decreases an order of magnitude due to an increasing turbine discharge temperature and a decreasing compressor discharge temperature. An increasing turbine discharge temperature is a result of a decreasing generator refrigerant saturation pressure (due to a lower power cycle mass flowrate) while a decreasing compressor discharge temperature is a result of a decreasing condenser refrigerant saturation pressure (due to a reduced condenser glycol mixture inlet temperature and reduced system pressure losses). At 50% load, the economizer heat duty is reversed, and heat is transferred from the fluid leaving the high-pressure recuperator port to the vapor leaving the compressor. The reversal of economizer heat transfer increases the heat duty of the cooling cycle condenser and the generator. This, however, does not greatly inhibit cooling cycle performance as the cooling cycle condenser is better able to liquify and sub cool its refrigerant at part-load operating conditions. Finally, at 25% load, the economizer functions properly once more considering the refrigerant saturation temperature in the generator is now lower than the compressor discharge temperature. Thus, sensible energy at the compressor discharge is translated to latent energy in the generator.

6.1. Recommendations for Future Research

This study presented baseline experimental performance data and operational trends over varying conditions for an advanced organic Rankine vapor compression chiller prototype. Continuation of this research should include:

- Addressing the primary limitations of the test facility through another iteration of design and construction. The flow limitations in the condenser loop should be addressed through increasing the diameter of the loop piping and selecting a more appropriate circulation pump. The pressure loss limitations in the system should be addressed through redesigning the suction line heat exchanger for minimal vapor pressure loss and increasing the routing diameter of the piping network from the evaporator discharge port to the cooling cycle

condenser refrigerant inlet port. Alternatively, a third suction line heat exchanger core could be placed in parallel with the two cores currently implemented in the system to reduce the pressure loss of the heat exchanger. The piping pressure losses from the power cycle pump discharge to the power cycle economizer inlet could be improved through increasing piping diameters to increase electrical equivalent COP. The two-phase discharge limitations of the cooling cycle condenser should be addressed through replacing the parallel power and cooling cycle condensers with an individual, properly sized unit. The loss of refrigerant through the power cycle pump shaft seal should be addressed through implementing a hermetic unit with a magnetic coupling. This unit could be custom fabricated to improve its isentropic efficiency, which would greatly improve the electrical equivalent COP of the system. The oscillating temperatures in the evaporator loop should be addressed through increasing the number of plates on the basement heat exchanger and tailoring the operation of the heat line circulation heater to the test facility during experimentation. Lastly, the compressor stalling limitations should be addressed through investigating hot gas bypass and variable inlet compressor guide vanes. Other novel methods could also be investigated to reduce the pressure ratio and/or increase the flowrate through the unit at the onset of stall.

- Creating a comprehensive thermo-economic, off-design performance model for organic Rankine vapor compression technology which is validated against the experimental data from this research effort. The thermo-economic model should include component level performance calculations to determine the energy savings potential of the prototype over the complete range of conditions a waste heat driven district cooling chiller would operate at. The model could then be used with component level cost calculations to optimize system design variables to determine the commercial viability of organic Rankine vapor compression chilling.

- Expanding the range of off-design performance tests performed on the prototype. Except for the part-load tests, only one design variable was altered from the baseline at a time during experimentation. Extending the off-design experimentation methods to part-load conditions would produce a more robust dataset for model validation. Furthermore, additional datapoints are needed to develop turbo-compressor maps with accurate efficiency contours. Other tests which could be performed on the prototype include transient system testing (quantifying the dynamic system response to a change in operating conditions) and the demonstration of advanced control algorithms to further improve system energy savings potential.

References

[1] International Energy Agency (IEA), 2018, *The Future of Cooling*, Paris.

[2] EIA, 2020, *Monthly Energy Review - April 2020*.

[3] Shah, N., Letschert, V., and Phadke, A., 2015, *Benefits of Leapfrogging to Superefficiency and Low Global Warming Potential Refrigerants in Room Air Conditioning*.

[4] Oak Ridge National Laboratory, 1997, *Energy and Global Warming Impacts of HFC Refrigerants and Emerging Technologies*.

[5] Goetzler, W., Guernsey, M., Young, J., Fuhrman, J., and Abdelaziz, O., 2016, "The Future of Air Conditioning for Buildings," Dep. Energy Off. Energy Effic. Renew. Energy Build. Technol. Off.

[6] UNEP, 2016, "The Kigali Amendment to the Montreal Protocol: HFC Phase-Down," OzonAction Fact Sheet.

[7] "Global Cooling Prize" [Online]. Available: https://globalcoolingprize.org/. [Accessed: 23-Sep-2020].

[8] "Million Cool Roofs Challenge" [Online]. Available: https://www.coolroofschallenge.org/. [Accessed: 23-Sep-2020].

[9] "Chill Challenge" [Online]. Available: https://www.ewb-usa.org/chill-challenge/. [Accessed: 23-Sep-2020].

[10] "Cool Cities Award" [Online]. Available: https://ashden.org/news/ashden-cool-cities-award-can-we-protect-the-most-vulnerable/#:~:text=The Ashden Cool Cities Award%2C supported by K-CEP%2C,for people most at risk. [Accessed: 23-Sep-2020].

[11] "Off-Grid Cold Chain Competition" [Online]. Available: https://efficiencyforaccess.org/global-leap-ogccc. [Accessed: 23-Sep-2020].

[12] SEforALL, 2018, *Chilling Prospects: Providing Sustainable Cooling for All*.

[13] Eveloy, V., and Ayou, D. S., 2019, "Sustainable District Cooling Systems: Status, Challenges, and Future Opportunities, with Emphasis on Cooling-Dominated Regions," Energies.

[14] Butters, C., Nordin, A., and Khai, D. T. H., 2018, "District Cooling: A Key Solution for Hot Climate Cities," *Designing Cooler Cities*.

[15] Inayat, A., and Raza, M., 2019, "District Cooling System via Renewable Energy Sources: A Review," Renew. Sustain. Energy Rev.

[16] ASHRAE, 2019, *District Cooling Guide*, Atlanta, GA.

[17] International District Energy Association, 2008, *District Cooling Best Practices Guide*, Westborough, Massachusetts.

[18] Werner, S., 2017, "International Review of District Heating and Cooling," Energy.

[19] Khir, R., and Haouari, M., 2015, "Optimization Models for a Single-Plant District Cooling System," Eur. J. Oper. Res.

[20] Penman, J., Gytarsky, M., Hiraishi, T., Irving, W., and Krug, T., 2006, *2006 IPCC - Guidelines for National Greenhouse Gas Inventories*.

[21] Gang, W., Wang, S., Xiao, F., and Gao, D. C., 2016, "District Cooling Systems: Technology Integration, System Optimization, Challenges and Opportunities for Applications," Renew. Sustain. Energy Rev.

[22] Lake, A., Rezaie, B., and Beyerlein, S., 2017, "Review of District Heating and Cooling Systems for a Sustainable Future," Renew. Sustain. Energy Rev.

[23] United Nations Environment Programme, 2015, *District Energy in Cities: Unlocking the Potential of Energy Efficiency and Renewable Energy*, Paris, France.

[24] Booten, C., Nicholson, S., Mann, M., and Abdelaziz, O., 2020, *Refrigerants: Market Trends and Supply Chain Assessment*.

[25] Looney, C. M., and Oney, S. K., 2007, "Seawater District Cooling and Lake Source District Cooling," Energy Eng. J. Assoc. Energy Eng.

[26] Hawaii Department of Business, Economic Development, and Tourism (DBEDT) Energy, Resources, and T. D., 2002, *Sea Water District Cooling Feasibility Analysis for the State of Hawaii*, Honolulu.

[27] Deng, J., Wang, R. Z., and Han, G. Y., 2011, "A Review of Thermally Activated Cooling Technologies for Combined Cooling, Heating and Power Systems," Prog. Energy Combust. Sci.

[28] Al Moussawi, H., Fardoun, F., and Louahlia-Gualous, H., 2016, "Review of Tri-Generation Technologies: Design Evaluation, Optimization, Decision-Making, and Selection Approach," Energy Convers. Manag.

[29] Jradi, M., and Riffat, S., 2014, "Tri-Generation Systems: Energy Policies, Prime Movers, Cooling Technologies, Configurations and Operation Strategies," Renew. Sustain. Energy Rev.

[30] Liu, M., Shi, Y., and Fang, F., 2014, "Combined Cooling, Heating and Power Systems: A Survey," Renew. Sustain. Energy Rev.

[31] Dincer, I., and Acar, C., 2015, "A Review on Clean Energy Solutions for Better Sustainability," Int. J. Energy Res.

[32] International Energy Agency (IEA), 2019, *Energy Policies of IEA Countries: United States 2019 Review*.

[33] International Energy Agency (IEA), 2016, *Energy Policies of IEA Countries: Japan 2016 Review*.

[34] International Energy Agency (IEA), 2020, *Energy Policy Review: India 2020*.

[35] International Energy Agency (IEA), 2014, *Energy Policies Beyond IEA Countries: Russia 2014*.

[36] International Energy Agency (IEA), 2017, *Energy Policies Beyond IEA Countries: Mexico 2017*.

[37] International Energy Agency (IEA), 2020, *Energy Policy Review: European Union 2020*.

[38] Lawrence Livermore National Laboratory, 2019, "Energy Flow Charts" [Online]. Available: https://flowcharts.llnl.gov/commodities/energy. [Accessed: 19-Sep-2021].

[39] Labus, J. M., Bruno, C. C., and Coronas, A., 2013, "Review on Absorption Technology with Emphasis

on Small Capacity Absorption Machines," Therm. Sci.

[40] U.S. Department of Energy, 2021, "U.S. DOE Combined Heat and Power Installation Database" [Online]. Available: https://doe.icfwebservices.com/chpdb/. [Accessed: 21-Sep-2021].

[41] U.S. Department of Energy Better Buildings Initiative, 2021, "Combined Heat and Power (CHP) Project Profiles Database" [Online]. Available: https://betterbuildingssolutioncenter.energy.gov/chp/chp-project-profiles-database. [Accessed: 21-Sep-2021].

[42] U.S. Department of Energy Office of Energy Efficiency and Renewable Energy, and TIAX LLC, 2004, *Distributed Energy Program Report: Review of Thermally Activated Technologies*.

[43] Wu, D. W., and Wang, R. Z., 2006, "Combined Cooling, Heating and Power: A Review," Prog. Energy Combust. Sci.

[44] Air-Conditioning Heating and Refrigeration Institute, 2018, "AHRI Standard 551-591 (SI) with Errata: 2018 Standard for Performance Rating of Water-Chilling and Heat Pump Water-Heating Packages Using the Vapor Compression Cycle."

[45] Calderoni, M., Babu Sreekumar, B., Dourlens-Quaranta, S., Lennard, Z., Rama, M., Klobut, K., Wang, Z., Duan, X., Zhang, Y., Nilsson, J., and Hargo, L., 2019, *Sustainable District Cooling Guidelines. IEA DHC/CHP Report*.

[46] Darrow, K., Tidball, R., Wang, J., and Hampson, A., 2017, *Catalog of CHP Technologies*.

[47] Srikhirin, P., Aphornratana, S., and Chungpaibulpatana, S., 2000, "A Review of Absorption Refrigeration Technologies," Renew. Sustain. Energy Rev.

[48] Wu, W., Wang, B., Shi, W., and Li, X., 2014, "An Overview of Ammonia-Based Absorption Chillers and Heat Pumps," Renew. Sustain. Energy Rev., **31**.

[49] Garousi Farshi, L., Seyed Mahmoudi, S. M., Rosen, M. A., and Yari, M., 2012, "A Comparative Study of the Performance Characteristics of Double-Effect Absorption Refrigeration Systems," Int. J. Energy Res.

[50] Gebreslassie, B. H., Medrano, M., and Boer, D., 2010, "Exergy Analysis of Multi-Effect Water-LiBr Absorption Systems: From Half to Triple Effect," Renew. Energy.

[51] Maryami, R., and Dehghan, A. A., 2017, "An Exergy Based Comparative Study between LiBr/Water Absorption Refrigeration Systems from Half Effect to Triple Effect," Appl. Therm. Eng.

[52] Bryair, "Adsorption Chillers" [Online]. Available: https://www.bryair.com/products-solutions/adsorption-chillers/. [Accessed: 28-Apr-2021].

[53] Wang, R. Z., and Oliveira, R. G., 2006, "Adsorption Refrigeration-An Efficient Way to Make Good Use of Waste Heat and Solar Energy," Prog. Energy Combust. Sci., **32**(4).

[54] Lu, Z., Wang, R., Xia, Z., and Gong, L., 2013, "Experimental Investigation Adsorption Chillers Using Micro-Porous Silica Gel-Water and Compound Adsorbent-Methanol," Energy Convers. Manag., **65**.

[55] Lu, Z. S., Wang, L. W., and Wang, R. Z., 2012, "Experimental Analysis of an Adsorption Refrigerator with Mass and Heat-Pipe Heat Recovery Process," Energy Convers. Manag., **53**(1).

[56] Akahira, A., Alam, K. C. A., Hamamoto, Y., Akisawa, A., and Kashiwagi, T., 2004, "Mass Recovery

Adsorption Refrigeration Cycle - Improving Cooling Capicity," *International Journal of Refrigeration*.

[57] Wang, R. Z., 2001, "Performance Improvement of Adsorption Cooling by Heat and Mass Recovery Operation," Int. J. Refrig., **24**(7).

[58] Saha, B. B., Koyama, S., Lee, J. B., Kuwahara, K., Alam, K. C. A., Hamamoto, Y., Akisawa, A., and Kashiwagi, T., 2003, "Performance Evaluation of a Low-Temperature Waste Heat Driven Multi-Bed Adsorption Chiller," Int. J. Multiph. Flow, **29**(8).

[59] Spanswick, I., 2003, "Advances in Steam Cooling," Natl. Eng., **107**(5).

[60] Johnson Controls, 2008, "Model YST Steam-Turbine Drive Centrifugal Liquid Chillers Design Level F" [Online]. Available: https://www.johnsoncontrols.com/en_ca/-/media/jci/be/united-states/hvac-equipment/chillers/files/be_yst_spec_engineeringguide.pdf. [Accessed: 05-Feb-2021].

[61] Dixit, R., 2018, "Insights into Advanced Steam Turbine Centrifugal Chiller Technology," Process Heat.

[62] Özdemir Küçük, E., and Kiliç, M., 2021, "Comparative Performance Analysis of ORC–VCRC Combined Systems Based on Refrigerant Selection," Sci. Technol. Built Environ., **27**(1).

[63] Bao, J., Zhang, L., Song, C., Zhang, N., Zhang, X., and He, G., 2020, "Comparative Study of Combined Organic Rankine Cycle and Vapor Compression Cycle for Refrigeration: Single Fluid or Dual Fluid?," Sustain. Energy Technol. Assessments, **37**.

[64] Sleiti, A. K., Al-Ammari, W. A., and Al-Khawaja, M., 2020, "Review of Innovative Approaches of Thermo-Mechanical Refrigeration Systems Using Low Grade Heat," Int. J. Energy Res., **44**(13).

[65] Chunnanond, K., and Aphornratana, S., 2004, "Ejectors: Applications in Refrigeration Technology," Renew. Sustain. Energy Rev.

[66] Chen, J., Havtun, H., and Palm, B., 2015, "Conventional and Advanced Exergy Analysis of an Ejector Refrigeration System," Appl. Energy, **144**.

[67] Noeres, P., Holder, D., and Althaus, W., 2000, "A Combined District Heating and Cooling Network in City of Gera (Germany) Using Steam-Jet Ejector Technology," Stroj. Vestnik-Journal Mech. Eng., **46**(8).

[68] Aidoun, Z., Ameur, K., Falsafioon, M., and Badache, M., 2019, "Current Advances in Ejector Modeling, Experimentation and Applications for Refrigeration and Heat Pumps. Part 2: Two-Phase Ejectors," Inventions, **4**(1).

[69] Aidoun, Z., Ameur, K., Falsafioon, M., and Badache, M., 2019, "Current Advances in Ejector Modeling, Experimentation and Applications for Refrigeration and Heat Pumps. Part 1: Single-Phase Ejectors," Inventions, **4**(1).

[70] Alexis, G. K., 2005, "Exergy Analysis of Ejector-Refrigeration Cycle Using Water as Working Fluid," Int. J. Energy Res., **29**(2).

[71] Sahlot, M., and Riffat, S. B., 2016, "Desiccant Cooling Systems: A Review," Int. J. Low-Carbon Technol., **11**(4).

[72] Enteria, N., and Mizutani, K., 2011, "The Role of the Thermally Activated Desiccant Cooling Technologies in the Issue of Energy and Environment," Renew. Sustain. Energy Rev., **15**(4).

[73] Alexander, M., 2018, "India Cooling Action Plan," Minist. Environ. For. Clim. Chang. Gov. India.

[74] Short, W., Packey, D. J., and Holt, T., 1995, *A Manual for the Economic Evaluation of Energy Efficiency and Renewable Energy Technologies*.

[75] UNEP Technical Options Committee, 2019, *2018 Report of the Refrigeration, Air Conditioning and Heat Pumps Technical Options Committee*.

[76] U.S. Department of Energy, 2017, *Absorption Chillers for CHP Systems*.

[77] Hansen, T., Ringler, E., and Chatterton, W., 2013, *Demonstration of a Solar Thermal Combined Heating, Cooling and Hot Water System Utilizing an Adsorption Chiller for DoD Installations*.

[78] Cochrane, B., and Chiarotto, E., 2018, "Application of Steam Turbine Driven Chillers in CHP/DES System," *IDEA Annual Conference*, Vancouver.

[79] Resource Dynamics Corporation, 2003, *Cooling, Heating, and Power for Industry: A Market Assessment.*

[80] 2020, "Chemical Engineering Magazine Plant Cost Index," Chem. Eng. Mag.

[81] Steven Brown, J., and Domanski, P. A., 2014, "Review of Alternative Cooling Technologies," Appl. Therm. Eng.

[82] Young, D., Gibson, S. C., and Bandhauer, T. M., 2018, "Working Fluid Selection and Technoeconomic Optimization of a Turbocompression Cooling System," J. Therm. Sci. Eng. Appl., **10**(6).

[83] Molés, F., Navarro-Esbrí, J., Peris, B., Mota-Babiloni, A., and Kontomaris, K., 2015, "Thermodynamic Analysis of a Combined Organic Rankine Cycle and Vapor Compression Cycle System Activated with Low Temperature Heat Sources Using Low GWP Fluids," Appl. Therm. Eng., **87**.

[84] Garland, S. D., Noall, J., and Bandhauer, T. M., 2018, "Experimentally Validated Modeling of a Turbo-Compression Cooling System for Power Plant Waste Heat Recovery," Energy.

[85] Kaynakli, O., and Kilic, M., 2007, "Theoretical Study on the Effect of Operating Conditions on Performance of Absorption Refrigeration System," Energy Convers. Manag.

[86] Samanta, S., and Basu, D. N., 2016, "Energy and Entropy-Based Optimization of a Single-Stage Water-Lithium Bromide Absorption Refrigeration System," Heat Transf. Eng.

[87] Jawahar, C. P., and Saravanan, R., 2010, "Generator Absorber Heat Exchange Based Absorption Cycle-A Review," Renew. Sustain. Energy Rev.

[88] Khamooshi, M., Parham, K., and Atikol, U., 2013, "Overview of Ionic Liquids Used as Working Fluids in Absorption Cycles," Adv. Mech. Eng.

[89] Coker, A. K., 2010, *Ludwig's Applied Process Design for Chemical and Petrochemical Plants: Fourth Edition*.

[90] Papadopoulos, A. I., Gkouletsos, D., Champilomatis, V., Giannakakis, A., Kousidis, V., Hassan, I., and Seferlis, P., 2020, "Systematic Assessment of Working Fluid Mixtures for Absorption Refrigeration

Based on Techno-Economic, Environmental, Health and Safety Performance," Energy Convers. Manag.

[91] Bellos, E., Tzivanidis, C., and Antonopoulos, K. A., 2016, "Exergetic and Energetic Comparison of LiCl-H2O and LiBr-H2O Working Pairs in a Solar Absorption Cooling System," Energy Convers. Manag.

[92] Patel, J., Pandya, B., and Mudgal, A., 2017, "Exergy Based Analysis of LiCl-H2O Absorption Cooling System," *Energy Procedia*.

[93] Parham, K., Atikol, U., Yari, M., and Agboola, O. P., 2013, "Evaluation and Optimization of Single Stage Absorption Chiller Using (LiCl + H2O) as the Working Pair," Adv. Mech. Eng.

[94] Ren, J., Qian, Z., Yao, Z., Gan, N., and Zhang, Y., 2019, "Thermodynamic Evaluation of LiCl-H2O and LiBr-H2O Absorption Refrigeration Systems Based on a Novel Model and Algorithm," Energies.

[95] Saravanan, R., and Maiya, M. P., 1998, "Thermodynamic Comparison of Water-Based Working Fluid Combinations for a Vapour Absorption Refrigeration System," Appl. Therm. Eng.

[96] Papadopoulos, A. I., Kyriakides, A. S., Seferlis, P., and Hassan, I., 2019, "Absorption Refrigeration Processes with Organic Working Fluid Mixtures- a Review," Renew. Sustain. Energy Rev.

[97] Liu, X., Ye, Z., Bai, L., and He, M., 2019, "Performance Comparison of Two Absorption-Compression Hybrid Refrigeration Systems Using R1234yf/Ionic Liquid as Working Pair," Energy Convers. Manag.

[98] Sujatha, I., and Venkatarathnam, G., 2018, "Comparison of Performance of a Vapor Absorption Refrigeration System Operating with Some Hydrofluorocarbons and Hydrofluoroolefins as Refrigerants along with Ionic Liquid [Hmim][TF2N] as the Absorbent," Int. J. Refrig.

[99] Liu, X., Bai, L., Liu, S., and He, M., 2016, "Vapor–liquid Equilibrium of R1234yf/[HMIM][Tf2N] and R1234ze(E)/ [HMIM][Tf2N] Working Pairs for the Absorption Refrigeration Cycle," J. Chem. Eng. Data.

[100] Wang, K., Abdelaziz, O., Kisari, P., and Vineyard, E. A., 2011, "State-of-the-Art Review on Crystallization Control Technologies for Water/LiBr Absorption Heat Pumps," *International Journal of Refrigeration*.

[101] Rivera, W., Romero, R. J., Cardoso, M. J., Aguillón, J., and Best, R., 2002, "Theoretical and Experimental Comparison of the Performance of a Single-Stage Heat Transformer Operating with Water/Lithium Bromide and Water/Carrol ™," Int. J. Energy Res.

[102] Florides, G. A., Kalogirou, S. A., Tassou, S. A., and Wrobel, L. C., 2003, "Design and Construction of a LiBr-Water Absorption Machine," Energy Convers. Manag.

[103] Davis, D., 2018, "Modern Absorption Titanium Tubes the 'New Normal' in District Energy Systems," *IDEA Capmus Energy 2018*, Baltimore, MD.

[104] Ventas, R., Lecuona, A., Zacarías, A., and Venegas, M., 2010, "Ammonia-Lithium Nitrate Absorption Chiller with an Integrated Low-Pressure Compression Booster Cycle for Low Driving Temperatures," Appl. Therm. Eng.

[105] Nikbakhti, R., Wang, X., Hussein, A. K., and Iranmanesh, A., 2020, "Absorption Cooling Systems – Review of Various Techniques for Energy Performance Enhancement," Alexandria Eng. J.

[106] Xu, Z. Y., and Wang, R. Z., 2016, “Absorption Refrigeration Cycles: Categorized Based on the Cycle Construction,” Int. J. Refrig.

[107] Razmi, A., Soltani, M., M. Kashkooli, F., and Garousi Farshi, L., 2018, “Energy and Exergy Analysis of an Environmentally-Friendly Hybrid Absorption/Recompression Refrigeration System,” Energy Convers. Manag.

[108] Sun, D. W., Eames, I. W., and Aphornratana, S., 1996, “Evaluation of a Novel Combined Ejector - Absorption Refrigeration Cycle - I: Computer Simulation,” Int. J. Refrig.

[109] Aphornratana, S., and Eames, I. W., 1998, “Experimental Investigation of a Combined Ejector-Absorption Refrigerator,” Int. J. Energy Res.

[110] Vereda, C., Ventas, R., Lecuona, A., and Venegas, M., 2012, “Study of an Ejector-Absorption Refrigeration Cycle with an Adaptable Ejector Nozzle for Different Working Conditions,” Appl. Energy.

[111] Abed, A. M., Alghoul, M. A., Sopian, K., Majdi, H. S., Al-Shamani, A. N., and Muftah, A. F., 2017, “Enhancement Aspects of Single Stage Absorption Cooling Cycle: A Detailed Review,” Renew. Sustain. Energy Rev.

[112] Al-Sulaiman, F. A., Dincer, I., and Hamdullahpur, F., 2010, “Exergy Analysis of an Integrated Solid Oxide Fuel Cell and Organic Rankine Cycle for Cooling, Heating and Power Production,” J. Power Sources.

[113] Mehrpooya, M., Sayyad, S., and Zonouz, M. J., 2017, “Energy, Exergy and Sensitivity Analyses of a Hybrid Combined Cooling, Heating and Power (CCHP) Plant with Molten Carbonate Fuel Cell (MCFC) and Stirling Engine,” J. Clean. Prod.

[114] Mehrpooya, M., Dehghani, H., and Ali Moosavian, S. M., 2016, “Optimal Design of Solid Oxide Fuel Cell, Ammonia-Water Single Effect Absorption Cycle and Rankine Steam Cycle Hybrid System,” J. Power Sources.

[115] Wu, W., Wang, B., Shi, W., and Li, X., 2014, “Absorption Heating Technologies: A Review and Perspective,” Appl. Energy.

[116] Xu, Z., and Wang, R., 2017, “Absorption Heat Pump for Waste Heat Reuse: Current States and Future Development,” Front. Energy.

[117] Ibarra-Bahena, J., Raman, S., Galindo-Luna, Y. R., Rodríguez-Martínez, A., and Rivera, W., 2020, “Role of Membrane Technology in Absorption Heat Pumps: A Comprehensive Review,” Membranes (Basel).

[118] Rivera, W., Best, R., Cardoso, M. J., and Romero, R. J., 2015, “A Review of Absorption Heat Transformers,” Appl. Therm. Eng.

[119] Goetzler, W., Zogg, R., Young, J., and Johnson, C., 2014, *Energy Savings Potential and RD&D Opportunities for Non-Vapor-Compression HVAC Technologies*.

[120] Choudhury, B., Saha, B. B., Chatterjee, P. K., and Sarkar, J. P., 2013, “An Overview of Developments in Adsorption Refrigeration Systems towards a Sustainable Way of Cooling,” Appl. Energy.

[121] Wang, L. W., Wang, R. Z., and Oliveira, R. G., 2009, “A Review on Adsorption Working Pairs for Refrigeration,” Renew. Sustain. Energy Rev., **13**(3).

[122] Younes, M. M., El-Sharkawy, I. I., Kabeel, A. E., and Saha, B. B., 2017, "A Review on Adsorbent-Adsorbate Pairs for Cooling Applications," Appl. Therm. Eng., **114**.

[123] AL-Dadah, R., Mahmoud, S., Elsayed, E., Youssef, P., and Al-Mousawi, F., 2020, "Metal-Organic Framework Materials for Adsorption Heat Pumps," Energy, **190**.

[124] Yuan, Y., Zhang, H., Yang, F., Zhang, N., and Cao, X., 2016, "Inorganic Composite Sorbents for Water Vapor Sorption: A Research Progress," Renew. Sustain. Energy Rev., **54**.

[125] Boman, D. B., Hoysall, D. C., Pahinkar, D. G., Ponkala, M. J., and Garimella, S., 2017, "Screening of Working Pairs for Adsorption Heat Pumps Based on Thermodynamic and Transport Characteristics," Appl. Therm. Eng., **123**.

[126] Sarbu, I., and Sebarchievici, C., 2015, "General Review of Solar-Powered Closed Sorption Refrigeration Systems," Energy Convers. Manag., **105**.

[127] Freni, A., Maggio, G., Sapienza, A., Frazzica, A., Restuccia, G., and Vasta, S., 2016, "Comparative Analysis of Promising Adsorbent/Adsorbate Pairs for Adsorptive Heat Pumping, Air Conditioning and Refrigeration," Appl. Therm. Eng., **104**.

[128] Cabeza, L. F., Solé, A., and Barreneche, C., 2017, "Review on Sorption Materials and Technologies for Heat Pumps and Thermal Energy Storage," Renew. Energy, **110**.

[129] Li, X. H., Hou, X. H., Zhang, X., and Yuan, Z. X., 2015, "A Review on Development of Adsorption Cooling - Novel Beds and Advanced Cycles," Energy Convers. Manag., **94**.

[130] Demir, H., Mobedi, M., and Ülkü, S., 2010, "The Use of Metal Piece Additives to Enhance Heat Transfer Rate through an Unconsolidated Adsorbent Bed," Int. J. Refrig., **33**(4).

[131] Askalany, A. A., Henninger, S. K., Ghazy, M., and Saha, B. B., 2017, "Effect of Improving Thermal Conductivity of the Adsorbent on Performance of Adsorption Cooling System," Appl. Therm. Eng., **110**.

[132] Vivekh, P., Kumja, M., Bui, D. T., and Chua, K. J., 2018, "Recent Developments in Solid Desiccant Coated Heat Exchangers – A Review," Appl. Energy, **229**.

[133] Alahmer, A., Ajib, S., and Wang, X., 2019, "Comprehensive Strategies for Performance Improvement of Adsorption Air Conditioning Systems: A Review," Renew. Sustain. Energy Rev., **99**.

[134] Taylan, O., Baker, D. K., and Kaftanoğlu, B., 2012, "COP Trends for Ideal Thermal Wave Adsorption Cooling Cycles with Enhancements," Int. J. Refrig., **35**(3).

[135] Kilic, M., and Anjrini, M., 2020, "Comparative Performance Analysis of a Combined Cooling System with Mechanical and Adsorption Cycles," Energy Convers. Manag., **221**.

[136] Banker, N. D., Dutta, P., Prasad, M., and Srinivasan, K., 2008, "Performance Studies on Mechanical + Adsorption Hybrid Compression Refrigeration Cycles with HFC 134a," Int. J. Refrig., **31**(8).

[137] Dai, Y. J., Wang, R. Z., and Xu, Y. X., 2002, "Study of a Solar Powered Solid Adsorption - Desiccant Cooling System Used for Grain Storage," Renew. Energy, **25**(3).

[138] Li, C. H., Wang, R. Z., and Lu, Y. Z., 2002, "Investigation of a Novel Combined Cycle of Solar Powered Adsorption-Ejection Refrigeration System," Renew. Energy, **26**(4).

[139] Zhang, X. J., and Wang, R. Z., 2002, "A New Combined Adsorption-Ejector Refrigeration and Heating

Hybrid System Powered by Solar Energy," Appl. Therm. Eng., **22**(11).

[140] Gordon, J. M., Ng, K. C., Chua, H. T., and Chakraborty, A., 2002, "The Electro-Adsorption Chiller: A Miniaturized Cooling Cycle with Applications to Micro-Electronics," Int. J. Refrig., **25**(8).

[141] U.S. Energy Information Administration, 2018, *Updated Buildings Sector Appliance and Equipment Costs and Efficiencies*.

[142] UNEP, and OzonAction - UNEP, 2016, *The Kigali Amendment to the Montreal Protocol: HFC Phase-Down*.

[143] Keneth, E., and Nichols, P. E., 2010, "How to Select Turbomachinery For Your Application How to Select Turbomachinery For Your Application," Barber-Nichols Inc.

[144] Bao, J., and Zhao, L., 2013, "A Review of Working Fluid and Expander Selections for Organic Rankine Cycle," Renew. Sustain. Energy Rev.

[145] Quoilin, S., Broek, M. Van Den, Declaye, S., Dewallef, P., and Lemort, V., 2013, "Techno-Economic Survey of Organic Rankine Cycle (ORC) Systems," Renew. Sustain. Energy Rev.

[146] Rackley, S., 2017, *Carbon Capture and Storage*, Butterworth-Heinemann.

[147] Copeland, C. C., 2019, "Improving the Performance of Steam Turbine Chiller Plants," ASHRAE J., **61**(8).

[148] Vankeirsbilck, I., Vanslambrouck, B., Gusev, S., and De Paepe, M., 2011, "Organic Rankine Cycle as Efficient Alternative to Steam Cycle for Small Scale Power Generation," 8th Int. Conf. Heat Transf. Fluid Mech. Thermodyn., (July).

[149] Jouhara, H., Khordehgah, N., Almahmoud, S., Delpech, B., Chauhan, A., and Tassou, S. A., 2018, "Waste Heat Recovery Technologies and Applications," Therm. Sci. Eng. Prog., **6**.

[150] He, C., Liu, C., Gao, H., Xie, H., Li, Y., Wu, S., and Xu, J., 2012, "The Optimal Evaporation Temperature and Working Fluids for Subcritical Organic Rankine Cycle," Energy.

[151] Bundela, P. S., and Chawla, V., 2010, "Sustainable Development through Waste Heat Recovery," Am. J. Environ. Sci., **6**(1).

[152] Stijepovic, M. Z., Linke, P., Papadopoulos, A. I., and Grujic, A. S., 2012, "On the Role of Working Fluid Properties in Organic Rankine Cycle Performance," Appl. Therm. Eng.

[153] Rahbar, K., Mahmoud, S., Al-Dadah, R. K., Moazami, N., and Mirhadizadeh, S. A., 2017, "Review of Organic Rankine Cycle for Small-Scale Applications," Energy Convers. Manag.

[154] Nasir, M. T., and Kim, K. C., 2016, "Working Fluids Selection and Parametric Optimization of an Organic Rankine Cycle Coupled Vapor Compression Cycle (ORC-VCC) for Air Conditioning Using Low Grade Heat," Energy Build., **129**.

[155] Jeong, J., and Kang, Y. T., 2004, "Cycle of a Refrigeration Cycle Driven by Refrigerant Steam Turbine," Int. J. Refrig., **27**(1).

[156] Wang, H., Peterson, R., and Herron, T., 2011, "Design Study of Configurations on System COP for a Combined ORC (Organic Rankine Cycle) and VCC (Vapor Compression Cycle)," Energy.

[157] Christensen, R. N., and Santoso, M., 1990, "An Evaluation of a Rankine Cycle Driven Heat Pump,"

Heat Recover. Syst. CHP, **10**(2).

[158] Wang, H., and Peterson, R. B., 2011, "Performance Enhancement of a Thermally Activated Cooling System Using Microchannel Heat Exchangers," Appl. Therm. Eng., **31**(14–15).

[159] Wang, H., Peterson, R., Harada, K., Miller, E., Ingram-Goble, R., Fisher, L., Yih, J., and Ward, C., 2011, "Performance of a Combined Organic Rankine Cycle and Vapor Compression Cycle for Heat Activated Cooling," Energy, **36**(1).

[160] Yih, J., and Wang, H., 2020, "Experimental Characterization of Thermal-Hydraulic Performance of a Microchannel Heat Exchanger for Waste Heat Recovery," Energy Convers. Manag., **204**.

[161] Li, T., Jia, Y., Wang, J., Meng, N., Liu, Q., and Qin, H., 2020, "Energy, Economic and Environmental Evaluation of a Novel Combined Cooling and Power System Characterized by Temperature and Humidity Independent Control," Energy Convers. Manag., **215**.

[162] Bounefour, O., and Ouadha, A., 2017, "Performance Improvement of Combined Organic Rankine-Vapor Compression Cycle Using Serial Cascade Evaporation in the Organic Cycle," *Energy Procedia*.

[163] Yilmaz, A., 2015, "Transcritical Organic Rankine Vapor Compression Refrigeration System for Intercity Bus Air-Conditioning Using Engine Exhaust Heat," Energy, **82**.

[164] Ashwni, Sherwani, A. F., and Tiwari, D., 2020, "Thermodynamic Analysis of Simple and Modified Organic Rankine Cycle and Vapor Compression Refrigeration (ORC–VCR) Systems," Environ. Prog. Sustain. Energy.

[165] Zheng, N., Wei, J., and Zhao, L., 2018, "Analysis of a Solar Rankine Cycle Powered Refrigerator with Zeotropic Mixtures," Sol. Energy, **162**.

[166] Salim, M. S., and Kim, M. H., 2019, "Multi-Objective Thermo-Economic Optimization of a Combined Organic Rankine Cycle and Vapour Compression Refrigeration Cycle," Energy Convers. Manag., **199**.

[167] Zeyghami, M., Goswami, D. Y., and Stefanakos, E., 2015, "A Review of Solar Thermo-Mechanical Refrigeration and Cooling Methods," Renew. Sustain. Energy Rev., **51**.

[168] Saleh, B., 2018, "Energy and Exergy Analysis of an Integrated Organic Rankine Cycle-Vapor Compression Refrigeration System," Appl. Therm. Eng., **141**.

[169] Li, H., Bu, X., Wang, L., Long, Z., and Lian, Y., 2013, "Hydrocarbon Working Fluids for a Rankine Cycle Powered Vapor Compression Refrigeration System Using Low-Grade Thermal Energy," Energy Build., **65**.

[170] Nasir, M. T., Ali, M. A., Khan, T. S., Al-Hajri, E., Kadri, M. B., and Kim, K. C., 2019, "Performance Assessment and Multi Objective Optimization of an Organic Rankine Cycle Driven Cooling Air Conditioning System," Energy Build., **191**.

[171] Kim, K. H., and Perez-Blanco, H., 2015, "Performance Analysis of a Combined Organic Rankine Cycle and Vapor Compression Cycle for Power and Refrigeration Cogeneration," Appl. Therm. Eng., **91**.

[172] Mounier, V., Mendoza, L. C., and Schiffmann, J., 2017, "Thermo-Economic Optimization of an ORC Driven Heat Pump Based on Small Scale Turbomachinery and Comparison with Absorption Heat Pumps," Int. J. Refrig., **81**.

[173] Demierre, J., Rubino, A., and Schiffmann, J., 2015, “Modeling and Experimental Investigation of an Oil-Free Microcompressor-Turbine Unit for an Organic Rankine Cycle Driven Heat Pump,” J. Eng. Gas Turbines Power, **137**(3).

[174] Prigmore, D., Barber, R., Co, B. E., and Ave, W., 1975, “Cooling with the Sun’s Heat,” J. Sol. Energy.

[175] Biancardi, F. R., Sitler, J. W., and Melikian, G., 1982, “Development and Test of Solar Rankine Cycle Heating and Cooling Systems,” Int. J. Refrig., **5**(6).

[176] Demierre, J., Favrat, D., Schiffmann, J., and Wegele, J., 2014, “Experimental Investigation of a Thermally Driven Heat Pump Based on a Double Organic Rankine Cycle and an Oil-Free Compressor-Turbine Unit,” Int. J. Refrig., **44**.

[177] Liang, Y., Mckeown, A., Yu, Z., and Alshammari, S. F. K., 2021, “Experimental Study on a Heat Driven Refrigeration System Based on Combined Organic Rankine and Vapour Compression Cycles,” Energy Convers. Manag., **234**.

[178] United States Nuclear Regulatory Commission, 2019, “Engine Cooling Systems,” *Diesel Generators as Emergancy Power Sources*.

[179] 2019, “Designation and Safety Classification of Refrigerants,” ASHRAE Stand., **34**.

[180] The Heating, Refrigeration, and A.-C. I. of C., 2019, “HRAI List of Refrigerants” [Online]. Available: https://www.hrai.ca/refrigerant-landscape-resources. [Accessed: 10-May-2021].

[181] Rajapaksha, L., 2007, “Influence of Special Attributes of Zeotropic Refrigerant Mixtures on Design and Operation of Vapour Compression Refrigeration and Heat Pump Systems,” Energy Convers. Manag., **48**(2).

[182] Klein, S. A., 2019, “Engineering Equations Solver.”

[183] Incropera, F. P., DeWitt, D. P., Bergman, T. L., and Lavine, A. S., 2013, *Principles of Heat and Mass Transfer*.

[184] SERO Pump Systems, 2014, “SRZS 440 Data Sheet No. 15.49. 02/05. US.Z” [Online]. Available: https://seropumps.com/wp-content/uploads/2014/09/SRZS4401750RPMCurves.pdf. [Accessed: 12-May-2021].

[185] Wright, T., and Gerhart, P., 2009, *Fluid Machinery: Application, Selection, and Design, Second Edition*.

[186] Underwriters Laboratories Inc., 1999, “UL 1995: Heating and Cooling Equipment.”

[187] Dassault Systems, 2018, “SolidWorks 2018.”

[188] National Instruments, 2018, “LabVIEW.”

[189] American Society of Mechanical Engineers, 2019, *ASME PTC 19.1-2018. Test Uncertainty*.

[190] Air-Conditioning Heating and Refrigeration Institute, 2000, “AHRI Standard 560-2000: 2000 Standard for Absorption Water Chilling and Water Heating Packages.”

[191] Lemmon, E. W., Bell, I. H., Huber, M. L., and McLinden, M. O., 2018, “NIST Reference Fluid Thermodynamic and Transport Properties Database (REFPROP), Version 10.0; Standard Reference Data; National Institute of Standards and Technology: Gaithersburg, MD.,” NIST Stand. Ref.

Databasev23.

[192] Akasaka, R., 2011, “New Fundamental Equations of State with a Common Functional Form for 2,3,3,3-Tetrafluoropropene (R-1234yf) and Trans-1,3,3,3-Tetrafluoropropene (R-1234ze(E)),” Int. J. Thermophys., **32**(6).

[193] DOW Chemical Company, *DOWTHERM 4000 Technical Data Sheet - Form 180-01313-0417*.

[194] Glassman, A. J., 1994, *Turbine Design And Application*.

[195] Mattingly, J. D., 1996, *Elements of Gas Turbine Propulsion*, McGraw-Hill Inc.

[196] LG, 2015, “LG HVAC Solution Absorption Chiller” [Online]. Available: https://www.lg.com/global/business/download/resources/sac/Catalogue_Absorption Chillers_ENG_F.pdf. [Accessed: 28-Apr-2021].

[197] Colibri-bv, “Colibri Ammonia Absorption Refrigeration” [Online]. Available: https://colibris.home.xs4all.nl/. [Accessed: 28-Apr-2021].

[198] Coleman, H. W., and Steele, G. W., 1989, *Experimentation and Uncertainty Analysis for Engineers*, Wiley, New York, New York.

Appendix A Sample Calculations for Performance Modeling

This appendix presents sample calculations used to validate the performance model investigated in Chapter 3 for predicting the baseline performance of the manufactured prototype system. The validated model was also investigated in Chapter 5 to assess state point discrepancies between the performance simulation and prototype experimentation. All hand calculations were performed assuming the modeling inputs in Table A-1.

Table A-1 Input parameters for performance simulation hand calculation

	External Stream Temperatures Inlet to Outlet [°C]	***Pinch Temperature [°C]***	***Superheating or Subcooling [°C]***	***Effectiveness Value [-]***
Generator	91.00 to 84.50	2.0	-	0.95
Power Cycle Condenser	29.40 to 37.40	0.5	1.0	-
Cooling Cycle Condenser	29.40 to 37.40	0.5	1.0	-
Evaporator	12.22 to 6.670	0.5	1.0	-
Recuperator	-	-	-	0.95
Economizer	-	-	-	0.95
Suction Line Heat Exchanger	-	-	-	0.95

The cooling duty of the system was set at 300 kW. The generator effectiveness value applied only to the superheated flow regime. Superheating was assumed for the evaporator outlet while subcooling was assumed for the condenser outlets. The generator and condensers used a 50% by volume mixture of ethylene glycol and water as the external process fluid, while the evaporator used pure water. The organic Rankine power cycle and vapor compression cooling cycle both used R1234ZE(E) as their working fluid. Pressure losses (pipe and heat exchanger) of 10 kPa were assumed throughout the cycles, and pressure loss through multi-phase heat exchangers was assumed to be equally distributed amongst the flow regimes. Potential gravitational effects on pressure, heat loss, and heat leakage were neglected. Thus, the enthalpy values between component state points were equated. The cooling cycle expansion process was

assumed to be isenthalpic. The isentropic efficiency values assumed for the turbine, compressor, and pump were 0.8, 0.8, and 0.3, respectively. The turbo-compressor power transfer efficiency was assumed to be 0.97.

Assessing the performance model detailed in Chapter 3 with the presented parameters as inputs allowed the determination of the thermodynamic state points presented in Table A-2. The basic thermodynamic and heat transfer formulations from which the model was built were reassessed by hand using these values to compare to the solutions generated by the model. The numbering convention for the state points matches that presented throughout the text.

Table A-2 State point predictions for use as hand calculation input variables

	Power Cycle			***Mass Flow [kg s^{-1}]***	***3.699***
State Point	***Temperature [°C]***	***Pressure [kPa]***	***Enthalpy [kJ kg^{1}]***	***Entropy [kJ kg^{1} K^{1}]***	***Quality [-]***
1	89.44	2,188	438.1	1.708	-
2	50.71	755.1	422.0	1.720	-
3	50.52	745.1	422.0	1.721	-
4	40.14	735.1	411.3	1.688	-
5	39.93	725.1	411.3	1.689	-
6	37.77	721.8	408.6	1.680	1
7	37.60	718.5	252.2	1.177	0
8	36.60	715.1	250.8	1.173	-
9	36.60	705.1	250.8	1.173	-
10	39.80	2,258	255.4	1.183	-
11	39.80	2,248	255.4	1.183	-
12	47.20	2,238	266.1	1.217	-
13	47.20	2,228	266.1	1.217	-
14	56.08	2,218	279.3	1.258	-
15	56.07	2,208	279.3	1.258	-
16	84.42	2,205	326.1	1.394	0
17	84.35	2,202	428.0	1.679	1
18	89.62	2,198	438.1	1.707	-

		Cooling Cycle		*Mass Flow [kg s^{1}]*	*1.816*
State Point	***Temperature [°C]***	***Pressure [kPa]***	***Enthalpy [kJ kg^{1}]***	***Entropy [kJ kg^{1} K^{1}]***	***Quality [-]***
1	34.26	232.1	415.3	1.777	-
2	74.63	746.8	447.1	1.795	-
3	74.49	736.8	447.1	1.796	-
4	48.44	726.8	420.2	1.717	-
5	48.25	716.8	420.2	1.718	-
6	37.34	713.5	408.3	1.680	1
7	37.18	710.2	251.6	1.176	0
8	36.18	706.8	250.1	1.171	-
9	36.18	696.8	250.1	1.171	-
10	17.65	686.8	224.1	1.084	-
11	17.65	676.8	224.1	1.084	-
12	7.213	282.1	224.1	1.086	0.0800
13	6.170	272.1	224.1	1.086	0.0875
14	5.638	267.1	388	1.674	1
15	6.638	262.1	389.3	1.680	-
16	6.374	252.1	389.3	1.682	-
17	34.45	242.1	415.3	1.774	-

External Streams	***Inlet Temperature***	***Outlet Temperature***	***Superheated Transition Temperature***	***Subcooled Transition Temperature***	***Mass Flow [kg s^{-1}]***
Generator	91.00°C	84.50°C	90.59°C	86.42°C	25.05
Power Cycle Condenser	29.40°C	37.40°C	37.27°C	29.47°C	21.96
Cooling Cycle Condenser	29.40°C	37.40°C	36.84°C	29.47°C	11.42
Evaporator	12.22°C	6.670°C	12.18°C	-	12.88

The results of this assessment, presented in Table A-3, show only slight variations between modeling predictions and hand calculations due to rounding error. This confirms the validity of the model and the results presented in the text which were informed by it. Isentropic process variables used for hand calculations in Table A-3 were assessed using internal functions to Engineering Equations Solver for enthalpy using the respective outlet pressure and inlet entropy to the device being investigated. Entropy

was also assessed using functions internal to Engineering Equations Solver using the respective inlet temperature and pressure to the device being investigated. Specific heat capacities were assessed for the refrigerant using the average refrigerant pressure and temperature of the heat exchanger section being investigated. Specific heat capacities for the external streams were assessed for water or the ethylene glycol-water mixture using the average temperature of the heat exchanger section being investigated and an assumed pressure of 101 kPa or a concentration of 50%, respectively. Formulations used to determine pressures via pressure loss were not included in this investigation, nor were formulations for isenthalpic processes or pinch temperatures, as the results shown in Table A-2 agree with the modeling input specifications. The gravitational constant used in the determination of net positive suction head variables was assumed to be 9.81 m s^{-2}. Fluid velocity was determined using an assumed area of 4.768 x 10^{-3} m^2 to represent the flow area of the power cycle pump inlet. Specific speed and specific diameter formulations used conversion factors of 35.315, 334.6 and 3.281 to convert volumetric flow from m^3 s^{-1} to ft^3 s^{-1}, adiabatic enthalpy change from kJ kg^{-1} to ft lbf lbm^{-1}, and blade diameter from m to ft, respectively. A speed of 30 kRPM was used in the formulation for device specific speed and a diameter of 0.1 m was used in the formulation for device specific diameter. Density was assessed using internal functions to the modeling software using the respective pressure and temperature as input variables.

Table A-3 Hand calculations verifying accuracy of performance simulations

Calculation	*Formulation*	*Hand Calculation*	*Model Result*	*Hand Value*	*Units*
Evaporator Water Mass Flow	$\dot{Q}_{\text{evap}} = \dot{m}_{\text{evap,w}}\, Cp_{\text{evap,w,avg}}\, (T_{\text{evap,w,in}} - T_{\text{evap,w,out}})$	$300 = \dot{m}_{\text{evap,w}}\, 4.196\, (12.22 - 6.67)$	12.88	12.88	kg s^{-1}
	$\dot{Q}_{\text{evap,tp,hot}} = \dot{m}_{\text{evap,w}}\, Cp_{\text{evap,tp,w,avg}}\, (T_{\text{evap,w, tpsh}} - T_{\text{evap,w,out}})$	$\dot{Q}_{\text{evap,tp,hot}} = 12.88\, 4.196\, (12.18 - 6.67)$		297.8	
Evaporator Two-Phase Heat Transfer	$\dot{Q}_{\text{evap,tp,cold}} = \dot{m}_{\text{cc}}\, (\text{h}_{\text{cc,14}} - \text{h}_{\text{cc,13}})$	$\dot{Q}_{\text{evap,tp,cold}} = 1.816\, (388.0 - 224.1)$	297.8	297.6	kW
	$\dot{Q}_{\text{evap,tp}} = \varepsilon_{\text{evap,tp}}\, \dot{m}_{\text{evap,w}}\, Cp_{\text{evap,tp,w,avg}}\, (T_{\text{evap,w, tpsh}} - T_{\text{cc,13}})$	$\dot{Q}_{\text{evap,tp}} = 0.9168\, 12.88\, 4.196(12.18 - 6.17)$		297.8	
Evaporator Two-Phase Log Mean Temperature Difference	$LMTD_{\text{evap,tp}} = \dfrac{(T_{\text{evap,w, tpsh}} - T_{\text{cc,14}}) - (T_{\text{evap,w, out}} - T_{\text{cc,13}})}{ln\left((T_{\text{evap,w, tpsh}} - T_{\text{cc,14}})/(T_{\text{evap,w, out}} - T_{\text{cc,13}})\right)}$	$LMTD_{\text{evap,tp}} = \dfrac{(12.18 - 5.638) - (6.67 - 6.170)}{ln\left((12.18 - 5.638)/(6.67 - 6.170)\right)}$	2.349	2.350	K
Evaporator Two-Phase Thermal Conductance	$UA_{\text{evap,tp}} = \dfrac{\dot{Q}_{\text{evap,tp}}}{LMTD_{\text{evap,tp}}}$	$UA_{\text{evap,tp}} = \dfrac{297.8}{2.349}$	126.7	126.8	kW K^{-1}
Evaporator Superheated Heat Transfer	$\dot{Q}_{\text{evap,sh,hot}} = \dot{m}_{\text{evap,w}}\, Cp_{\text{evap,sh,w,avg}}\, (T_{\text{evap,w, in}} - T_{\text{evap,w,tpsh}})$	$\dot{Q}_{\text{evap,sh,hot}} = 12.88\, 4.192\, (12.22 - 12.18)$	2.245	2.160	kW

Calculation	*Formulation*	*Hand Calculation*	*Model Result*	*Hand Value*	*Units*
	$\dot{Q}_{\text{evap,sh,cold}} = \dot{m}_{\text{cc}}\ (\text{h}_{\text{cc,15}} - \text{h}_{\text{cc,14}})$	$\dot{Q}_{\text{evap,sh,cold}} = 1.816\ (389.3 - 388.0)$		2.361	
	$\dot{Q}_{\text{evap,sh}} = \varepsilon_{\text{evap,sh}} \min\left(\dot{m}_{\text{evap,w}}\ Cp_{\text{evap,sh,w,avg}}, \dot{m}_{\text{cc}}\ Cp_{\text{evap,sh,r,avg}}\right)(T_{\text{evap,w, in}} - T_{\text{cc,14}})$	$\dot{Q}_{\text{evap,sh}} = 0.2052 \min(12.88\ 4.192,\ 1.816\ 0.9153)\ (12.22 - 5.638)$		2.245	
Evaporator Superheated Log Mean Temperature Difference	$LMTD_{\text{evap,sh}} = \frac{\left(T_{\text{evap,w, in}} - T_{\text{cc,15}}\right) - \left(T_{\text{evap,w, tpsh}} - T_{\text{cc,14}}\right)}{ln\left(\left(T_{\text{evap,w, in}} - T_{\text{cc,15}}\right)/\left(T_{\text{evap,w, tpsh}} - T_{\text{cc,14}}\right)\right)}$	$LMTD_{\text{evap,sh}} = \frac{(12.22 - 6.638) - (12.18 - 5.638)}{ln\left((12.22 - 6.638)/(12.18 - 5.638)\right)}$	6.049	6.049	K
Evaporator Superheated Thermal Conductance	$UA_{\text{evap,sh}} = \frac{\dot{Q}_{\text{evap,sh}}}{LMTD_{\text{evap,sh}}}$	$UA_{\text{evap,sh}} = \frac{2.245}{6.049}$	0.3712	0.3711	$kW\ K^{-1}$
	$\dot{Q}_{\text{ccond,sc,cold}} = \dot{m}_{\text{ccond,eg}}\ Cp_{\text{ccond,sc,eg,avg}}\ (T_{\text{ccond,eg,tpsc}} - T_{\text{ccond,eg,in}})$	$\dot{Q}_{\text{ccond,sc,cold}} = 11.42\ 3.361\ (29.47 - 29.40)$		2.69	
Vapor Compression Condenser Subcooled Heat Transfer	$\dot{Q}_{\text{ccond,sc,hot}} = \dot{m}_{\text{cc}}\ (\text{h}_{\text{cc,7}} - \text{h}_{\text{cc,8}})$	$\dot{Q}_{\text{ccond,sc,hot}} = 1.816\ (251.6 - 250.1)$	2.62	2.72	kW
	$\dot{Q}_{\text{ccond,sc}} = \varepsilon_{\text{ccond,sc}} \min\left(\dot{m}_{\text{ccond,eg}}\ Cp_{\text{ccond,sc,eg,avg}}, \dot{m}_{\text{cc}} Cp_{\text{ccond,sc,r,avg}}\right)(T_{\text{cc,7}} - T_{\text{ccond,eg,in}})$	$\dot{Q}_{\text{ccond,sc}} = 0.1286 \min(11.42\ 3.361,\ 1.816\ 1.443)\ (37.18 - 29.40)$		2.62	

Calculation	*Formulation*	*Hand Calculation*	*Model Result*	*Hand Value*	*Units*
Vapor Compression Condenser Subcooled Log Mean Temperature Difference	$LMTD_{\mathrm{ccond,sc}} = \frac{\left(T_{\mathrm{cc,7}} - T_{\mathrm{ccond,eg,tpsc}}\right) - \left(T_{\mathrm{cc,8}} - T_{\mathrm{ccond,eg,in}}\right)}{ln\left(\left(T_{\mathrm{cc,7}} - T_{\mathrm{ccond,eg,tpsc}}\right)/\left(T_{\mathrm{cc,8}} - T_{\mathrm{ccond,eg,in}}\right)\right)}$	$LMTD_{\mathrm{ccond,sc}} = \frac{(37.18 - 29.47) - (36.18 - 29.40)}{ln\left((37.18 - 29.47)/(36.18 - 29.40)\right)}$	7.231	7.235	K
Vapor Compression Condenser Subcooled Thermal Conductance	$UA_{\mathrm{ccond,sc}} = \frac{\dot{Q}_{\mathrm{ccond,sc}}}{LMTD_{\mathrm{ccond,sc}}}$	$UA_{\mathrm{ccond,sc}} = \frac{2.62}{7.231}$	0.3624	0.3623	$kW\ K^{-1}$
	$\dot{Q}_{\mathrm{ccond,tp,cold}} = \dot{m}_{\mathrm{ccond,eg}}\ Cp_{\mathrm{ccond,tp,eg,avg}}\ (T_{\mathrm{ccond,eg,\ tpsh}} - T_{\mathrm{ccond,eg,tpsc}})$	$\dot{Q}_{\mathrm{ccond,tp,cold}} = 11.42\ 3.379\ (36.84 - 29.47)$		284.4	
Vapor Compression Condenser Two-Phase Heat Transfer	$\dot{Q}_{\mathrm{ccond,tp,hot}} = \dot{m}_{\mathrm{cc}}\ (\mathrm{h}_{\mathrm{cc,6}} - \mathrm{h}_{\mathrm{cc,7}})$	$\dot{Q}_{\mathrm{ccond,tp,hot}} = 1.816\ (408.3 - 251.6)$	284.7	284.6	kW
	$\dot{Q}_{\mathrm{ccond,tp}} = \varepsilon_{\mathrm{ccond,tp}}\ \dot{m}_{\mathrm{ccond,eg}}\ Cp_{\mathrm{ccond,tp,eg,avg}}(T_{\mathrm{cc,6}} - T_{\mathrm{ccond,eg,tpsc}})$	$\dot{Q}_{\mathrm{ccond,tp}} = 0.9365\ 11.42\ 3.379\ (37.34 - 29.47)$		284.4	
Vapor Compression Condenser Two-Phase Log Mean Temperature Difference	$LMTD_{\mathrm{ccond,tp}} = \frac{\left(T_{\mathrm{cc,6}} - T_{\mathrm{ccond,eg,tpsh}}\right) - \left(T_{\mathrm{cc,7}} - T_{\mathrm{ccond,eg,tpsc}}\right)}{ln\left(\left(T_{\mathrm{cc,6}} - T_{\mathrm{ccond,eg,tpsh}}\right)/\left(T_{\mathrm{cc,7}} - T_{\mathrm{ccond,eg,tpsc}}\right)\right)}$	$LMTD_{\mathrm{ccond,tp}} = \frac{(37.34 - 36.84) - (37.18 - 29.47)}{ln\left((37.34 - 36.84)/(37.18 - 29.47)\right)}$	2.635	2.636	K

Calculation	*Formulation*	*Hand Calculation*	*Model Result*	*Hand Value*	*Units*
Vapor Compression Condenser Two-Phase Thermal Conductance	$UA_{\mathrm{ccond,tp}} = \frac{\dot{Q}_{\mathrm{ccond,tp}}}{LMTD_{\mathrm{ccond,tp}}}$	$UA_{\mathrm{ccond,tp}} = \frac{284.7}{2.635}$	108.0	108.0	kW K^{-1}
	$\dot{Q}_{\mathrm{ccond,sh,cold}} = \dot{m}_{\mathrm{ccond,eg}}\, Cp_{\mathrm{ccond,sh,eg,avg}}\, (T_{\mathrm{ccond,eg,out}} - T_{\mathrm{ccond,eg,tpsh}})$	$\dot{Q}_{\mathrm{ccond,sh,cold}} = 11.42\ 3.399\ (37.40 - 36.84)$		21.74	
Vapor Compression Condenser Superheated Heat Transfer	$\dot{Q}_{\mathrm{ccond,sh,hot}} = \dot{m}_{\mathrm{cc}}\ (\mathrm{h}_{\mathrm{cc},5} - \mathrm{h}_{\mathrm{cc},6})$	$\dot{Q}_{\mathrm{ccond,sh,hot}} = 1.816\ (420.2 - 408.3)$	21.55	21.61	kW
	$\dot{Q}_{\mathrm{ccond,sh}} = \varepsilon_{\mathrm{ccond,sh}} \min\left(\dot{m}_{\mathrm{ccond,eg}}\, Cp_{\mathrm{ccond,sh,eg,avg}}, \dot{m}_{\mathrm{cc}}\, Cp_{\mathrm{ccond,sh,r,avg}}\right)(T_{\mathrm{cc},5} - T_{\mathrm{ccond,eg,tpsh}})$	$\dot{Q}_{\mathrm{ccond,sh}} = 0.9918 \min(11.42\ 3.399,\ 1.816\ 1.049)\ (48.25 - 36.84)$		21.56	
Vapor Compression Condenser Superheated Log Mean Temperature Difference	$LMTD_{\mathrm{ccond,sh}} = \frac{(T_{\mathrm{cc},5} - T_{\mathrm{ccond,eg,out}}) - (T_{\mathrm{cc},6} - T_{\mathrm{ccond,eg,tpsh}})}{ln\left((T_{\mathrm{cc},5} - T_{\mathrm{ccond,eg,out}})/(T_{\mathrm{cc},6} - T_{\mathrm{ccond,eg,tpsh}})\right)}$	$LMTD_{\mathrm{ccond,sh}} = \frac{(48.25 - 37.40) - (37.34 - 36.84)}{ln\left((48.25 - 37.40)/(37.34 - 36.84)\right)}$	3.363	3.363	K
Vapor Compression Condenser Superheated Thermal Conductance	$UA_{\mathrm{ccond,sh}} = \frac{\dot{Q}_{\mathrm{ccond,sh}}}{LMTD_{\mathrm{ccond,sh}}}$	$UA_{\mathrm{ccond,sh}} = \frac{21.55}{3.363}$	6.408	6.408	kW K^{-1}
Suction Line Heat Exchanger Heat Transfer	$\dot{Q}_{\mathrm{slhx,cold}} = \dot{m}_{\mathrm{cc}}\ (\mathrm{h}_{\mathrm{cc},17} - \mathrm{h}_{\mathrm{cc},16})$	$\dot{Q}_{\mathrm{slhx,cold}} = 1.816\ (415.3 - 389.3)$	47.37	47.22	kW

Calculation	*Formulation*	*Hand Calculation*	*Model Result*	*Hand Value*	*Units*
	$\dot{Q}_{\text{slhx,hot}} = \dot{m}_{\text{cc}}\,(\text{h}_{\text{cc,9}} - \text{h}_{\text{cc,10}})$	$\dot{Q}_{\text{slhx,hot}} = 1.816\,(250.1 - 224.1)$		47.22	
	$\dot{Q}_{\text{slhx}} = \varepsilon_{\text{slhx}}\,\dot{m}_{\text{cc}}\,\min\,(Cp_{\text{slhx,r,hot,avg}}, Cp_{\text{slhx,r,cold,avg}})(T_{\text{cc,9}} - T_{\text{cc,16}})$	$\dot{Q}_{\text{slhx}} = 0.9500\ 1.816\ \min\,(1.407,\ 0.9213)\ (36.18 - 6.374)$		47.37	
Suction Line Heat Exchanger Log Mean Temperature Difference	$LMTD_{\text{slhx}} = \frac{(T_{\text{cc,9}} - T_{\text{cc,17}}) - (T_{\text{cc,10}} - T_{\text{cc,16}})}{ln\left((T_{\text{cc,9}} - T_{\text{cc,17}})/(T_{\text{cc,10}} - T_{\text{cc,16}})\right)}$	$LMTD_{\text{slhx}} = \frac{(36.18 - 34.45) - (17.65 - 6.374)}{ln\left((36.18 - 34.45)/(17.65 - 6.374)\right)}$	5.090	5.092	K
Suction Line Heat Exchanger Thermal Conductance	$UA_{\text{slhx}} = \frac{\dot{Q}_{\text{slhx}}}{LMTD_{\text{slhx}}}$	$UA_{\text{slhx}} = \frac{47.37}{5.090}$	9.306	9.306	$kW\ K^{-1}$
Compressor Efficiency	$\eta_{\text{comp}} = \frac{\text{h}_{\text{cc,s,2}} - \text{h}_{\text{cc,1}}}{\text{h}_{\text{cc,2}} - \text{h}_{\text{cc,1}}}$	$\eta_{\text{comp}} = \frac{440.8 - 415.3}{447.1 - 415.3}$	0.8000	0.8019	-
Compressor Work	$\dot{W}_{\text{comp}} = \dot{m}_{\text{cc}}(\text{h}_{\text{cc,2}} - \text{h}_{\text{cc,1}})$	$\dot{W}_{\text{comp}} = 1.816\ \ (447.1 - 415.3)$	57.71	57.75	kW
Economizer Heat Transfer	$\dot{Q}_{\text{econ,cold}} = \dot{m}_{\text{pc}}\,(\text{h}_{\text{pc,14}} - \text{h}_{\text{pc,13}})$	$\dot{Q}_{\text{econ,cold}} = 3.699\,(279.3 - 266.1)$	48.87	48.83	kW
	$\dot{Q}_{\text{econ,hot}} = \dot{m}_{\text{cc}}\,(\text{h}_{\text{cc,3}} - \text{h}_{\text{cc,4}})$	$\dot{Q}_{\text{econ,hot}} = 1.816\,(447.1 - 420.2)$		48.85	

Calculation	*Formulation*	*Hand Calculation*	*Model Result*	*Hand Value*	*Units*
	$\dot{Q}_{\text{econ}} = \varepsilon_{\text{econ}} \min(\dot{m}_{\text{cc}} Cp_{\text{econ,r,hot,avg}}, \dot{m}_{\text{pc}} Cp_{\text{econ,r,cold,avg}})(T_{\text{cc,3}} - T_{\text{pc,13}})$	$\dot{Q}_{\text{econ}} = 0.9500 \min(1.816\ 1.038,\ 3.699\ 1.488)\ (74.49 - 47.20)$		48.87	
Economizer Log Mean Temperature Difference	$LMTD_{\text{econ}} = \frac{(T_{\text{cc,3}} - T_{\text{pc,14}}) - (T_{\text{cc,4}} - T_{\text{pc,13}})}{ln\left((T_{\text{cc,3}} - T_{\text{pc,14}})/(T_{\text{cc,4}} - T_{\text{pc,13}})\right)}$	$LMTD_{\text{econ}} = \frac{(74.49 - 56.08) - (48.44 - 47.20)}{ln((74.49 - 56.08)/(48.44 - 47.20))}$	6.363	6.364	K
Economizer Thermal Conductance	$UA_{\text{econ}} = \frac{\dot{Q}_{\text{econ}}}{LMTD_{\text{econ}}}$	$UA_{\text{econ}} = \frac{48.87}{6.363}$	7.681	7.680	kW K^{-1}
	$\dot{Q}_{\text{gen,sh,hot}} = \dot{m}_{\text{gen,eg}} Cp_{\text{gen,sh,eg,avg}} (T_{\text{gen,eg, in}} - T_{\text{gen,eg,tpsh}})$	$\dot{Q}_{\text{gen,sh,hot}} = 25.05\ 3.618\ (91.00 - 90.59)$		37.16	
Generator Superheated Heat Transfer	$\dot{Q}_{\text{gen,sh,cold}} = \dot{m}_{\text{pc}} (\text{h}_{\text{pc,18}} - \text{h}_{\text{pc,17}})$	$\dot{Q}_{\text{gen,sh,cold}} = 3.699\ (438.1 - 428.0)$	37.29	37.36	kW
	$\dot{Q}_{\text{gen,sh}} = \varepsilon_{\text{gen,sh}} \min(\dot{m}_{\text{gen,eg}} Cp_{\text{gen,sh,eg,avg}}, \dot{m}_{\text{pc}} Cp_{\text{gen,sh,r,avg}})(T_{\text{gen,eg, in}} - T_{\text{pc,17}})$	$\dot{Q}_{\text{gen,sh}} = 0.9500 \min(25.05\ 3.618,\ 3.699\ 1.595)\ (91.00 - 84.35)$		37.27	
Generator Superheated Log Mean Temperature Difference	$LMTD_{\text{gen,sh}} = \frac{(T_{\text{gen,eg, in}} - T_{\text{pc,18}}) - (T_{\text{gen,eg,tpsh}} - T_{\text{pc,17}})}{ln\left((T_{\text{gen,eg, in}} - T_{\text{pc,18}})/(T_{\text{gen,eg,tpsh}} - T_{\text{pc,17}})\right)}$	$LMTD_{\text{gen,sh}} = \frac{(91.00 - 89.62) - (90.59 - 84.35)}{ln((91.00 - 89.62)/(90.59 - 84.35))}$	3.224	3.221	K

Calculation	*Formulation*	*Hand Calculation*	*Model Result*	*Hand Value*	*Units*
Generator Superheated Thermal Conductance	$UA_{\text{gen,sh}} = \frac{\dot{Q}_{\text{gen,sh}}}{LMTD_{\text{gen,sh}}}$	$UA_{\text{gen,sh}} = \frac{37.29}{3.224}$	11.57	11.57	kW K^{-1}
	$\dot{Q}_{\text{gen,tp,hot}} = \dot{m}_{\text{gen,eg}}\, Cp_{\text{gen,tp,eg,avg}}(T_{\text{gen,eg,tpsh}} - T_{\text{gen,eg,tpsc}})$	$\dot{Q}_{\text{gen,tp,hot}} = 25.05\ 3.611\ (90.59 - 86.42)$		377.2	
Generator Two-Phase Heat Transfer	$\dot{Q}_{\text{gen,tp,cold}} = \dot{m}_{\text{pc}}\ (\text{h}_{\text{pc,17}} - \text{h}_{\text{pc,16}})$	$\dot{Q}_{\text{gen,tp,cold}} = 3.699\ (428.0 - 326.1)$	377.2	376.9	kW
	$\dot{Q}_{\text{gen,tp}} = \varepsilon_{\text{gen,tp}}\, \dot{m}_{\text{gen,eg}}\, Cp_{\text{gen,tp,eg,avg}}\ (T_{\text{gen,eg,tpsh}} - T_{\text{pc,16}})$	$\dot{Q}_{\text{gen,tp}} = 0.6759\ 25.05\ 3.611\ (90.59 - 84.42)$		377.2	
Generator Two-Phase Log Mean Temperature Difference	$LMTD_{\text{gen,tp}} = \frac{(T_{\text{gen,eg,tpsh}} - T_{\text{pc,17}}) - (T_{\text{gen,eg,tpsc}} - T_{\text{pc,16}})}{ln\left((T_{\text{gen,eg,tpsh}} - T_{\text{pc,17}})/(T_{\text{gen,eg,tpsc}} - T_{\text{pc,16}})\right)}$	$LMTD_{\text{gen,tp}} = \frac{(90.59 - 84.35) - (86.42 - 84.42)}{ln((90.59 - 84.35)/(86.42 - 84.42))}$	3.727	3.726	K
Generator Two-Phase Thermal Conductance	$UA_{\text{gen,tp}} = \frac{\dot{Q}_{\text{gen,tp}}}{LMTD_{\text{gen,tp}}}$	$UA_{\text{gen,tp}} = \frac{377.2}{3.727}$	101.2	101.2	kW K^{-1}
	$\dot{Q}_{\text{gen,sc,hot}} = \dot{m}_{\text{gen,eg}}\, Cp_{\text{gen,sc,eg,avg}}\ (T_{\text{gen,eg,tpsc}} - T_{\text{gen,eg,out}})$	$\dot{Q}_{\text{gen,sc,hot}} = 25.05\ 3.601\ (86.42 - 84.50)$		173.2	
Generator Subcooled Heat Transfer			173		kW
	$\dot{Q}_{\text{gen,sc,cold}} = \dot{m}_{\text{pc}}\ (\text{h}_{\text{pc,16}} - \text{h}_{\text{pc,15}})$	$\dot{Q}_{\text{gen,sc,cold}} = 3.699\ (326.1 - 279.3)$		173.1	

Calculation	*Formulation*	*Hand Calculation*	*Model Result*	*Hand Value*	*Units*
	$\dot{Q}_{\text{gen,sc}} = \varepsilon_{\text{gen,sc}} \min(\dot{m}_{\text{gen,eg}} Cp_{\text{gen,sc,eg,avg}}, \dot{m}_{\text{pc}} Cp_{\text{gen,sc,r,avg}})(T_{\text{gen,eg, tpsc}} - T_{\text{pc,15}})$	$\dot{Q}_{\text{gen,sc}} = 0.9476 \min(25.05\ 3.601,\ 3.699\ 1.626)\ (86.42 - 56.07)$		173.0	
Generator Subcooled Log Mean Temperature Difference	$LMTD_{\text{gen,sc}} = \frac{(T_{\text{gen,eg, tpsc}} - T_{\text{pc,16}}) - (T_{\text{gen,eg,out}} - T_{\text{pc,15}})}{ln\left((T_{\text{gen,eg, tpsc}} - T_{\text{pc,16}})/(T_{\text{gen,eg,out}} - T_{\text{pc,15}})\right)}$	$LMTD_{\text{gen,sc}} = \frac{(86.42 - 84.42) - (84.50 - 56.07)}{ln((86.42 - 84.42)/(84.50 - 56.07))}$	9.956	9.957	K
Generator Subcooled Thermal Conductance	$UA_{\text{gen,sc}} = \frac{\dot{Q}_{\text{gen,sc}}}{LMTD_{\text{gen,sc}}}$	$UA_{\text{gen,sc}} = \frac{173.0}{9.956}$	17.37	17.38	kW K^{-1}
	$\dot{Q}_{\text{pcond,sc,cold}} = \dot{m}_{\text{pcond,eg}} Cp_{\text{pcond,sc,eg,avg}} (T_{\text{pcond,eg,tpsc}} - T_{\text{pcond,eg,in}})$	$\dot{Q}_{\text{pcond,sc,cold}} = 21.96\ 3.361\ (29.47 - 29.40)$		5.167	
Organic Rankine Condenser Subcooled Heat Transfer	$\dot{Q}_{\text{pcond,sc,hot}} = \dot{m}_{\text{pc}} (\text{h}_{\text{pc,7}} - \text{h}_{\text{pc,8}})$	$\dot{Q}_{\text{pcond,sc,hot}} = 3.699\ (252.2 - 250.8)$	5.343	5.179	kW
	$\dot{Q}_{\text{pcond,sc}} = \varepsilon_{\text{pcond,sc}} \min(\dot{m}_{\text{pcond,eg}} Cp_{\text{pcond,sc,eg,avg}}, \dot{m}_{\text{pc}} Cp_{\text{pcond,sc,r,avg}})(T_{\text{pc,7}} - T_{\text{pcond,eg,in}})$	$\dot{Q}_{\text{pcond,sc}} = 0.1220 \min(21.96\ 3.361,\ 3.699\ 1.445)\ (37.60 - 29.40)$		5.347	
Organic Rankine Condenser Subcooled Log Mean Temperature Difference	$LMTD_{\text{pcond,sc}} = \frac{(T_{\text{pc,7}} - T_{\text{pcond,eg,tpsc}}) - (T_{\text{pc,8}} - T_{\text{pcond,eg,in}})}{ln\left((T_{\text{pc,7}} - T_{\text{pcond,eg,tpsc}})/(T_{\text{pc,8}} - T_{\text{pcond,eg,in}})\right)}$	$LMTD_{\text{pcond,sc}} = \frac{(37.60 - 29.47) - (36.60 - 29.40)}{ln((37.60 - 29.47)/(36.60 - 29.40))}$	7.652	7.656	K

Calculation	*Formulation*	*Hand Calculation*	*Model Result*	*Hand Value*	*Units*
Organic Rankine Condenser Subcooled Thermal Conductance	$UA_{\text{pcond,sc}} = \frac{\dot{Q}_{\text{pcond,sc}}}{LMTD_{\text{pcond,sc}}}$	$UA_{\text{pcond,sc}} = \frac{5.343}{7.652}$	.6983	0.6983	$\frac{\text{kW}}{\text{K}^{-1}}$
	$\dot{Q}_{\text{pcond,tp,cold}} = \dot{m}_{\text{pcond,eg}}\, Cp_{\text{pcond,tp,eg,avg}}\, (T_{\text{pcond,eg, tpsh}} - T_{\text{pcond,eg,tpsc}})$	$\dot{Q}_{\text{pcond,tp,cold}} = 21.96\ 3.380\ (37.27 - 29.47)$		579.0	
Organic Rankine Condenser Two-Phase Heat Transfer	$\dot{Q}_{\text{pcond,tp,hot}} = \dot{m}_{\text{pc}}\ (\text{h}_{\text{pc,6}} - \text{h}_{\text{pc,7}})$	$\dot{Q}_{\text{pcond,tp,hot}} = 3.699\ (408.6 - 252.2)$	578.5	578.5	kW
	$\dot{Q}_{\text{pcond,tp}} = \varepsilon_{\text{pcond,tp}}\, \dot{m}_{\text{pcond,eg}}\, Cp_{\text{pcond,tp,eg,avg}}(T_{\text{pc,6}} - T_{\text{pcond,eg,tpsc}})$	$\dot{Q}_{\text{pcond,tp}} = 0.9397\ 21.96\ 3.380\ (37.77 - 29.47)$		578.9	
Organic Rankine Condenser Two-Phase Log Mean Temperature Difference	$LMTD_{\text{pcond,tp}} = \frac{(T_{\text{pc,6}} - T_{\text{pcond,eg,tpsh}}) - (T_{\text{pc,7}} - T_{\text{pcond,eg,tpsc}})}{ln\left((T_{\text{pc,6}} - T_{\text{pcond,eg,tpsh}})/(T_{\text{pc,7}} - T_{\text{pcond,eg,tpsc}})\right)}$	$LMTD_{\text{pcond,tp}} = \frac{(37.77 - 37.27) - (37.60 - 29.47)}{ln\left((37.77 - 37.27)/(37.60 - 29.47)\right)}$	2.735	2.736	K
Organic Rankine Condenser Two-Phase Thermal Conductance	$UA_{\text{pcond,tp}} = \frac{\dot{Q}_{\text{pcond,tp}}}{LMTD_{\text{pcond,tp}}}$	$UA_{\text{pcond,tp}} = \frac{578.5}{2.735}$	211.5	211.5	$\frac{\text{kW}}{\text{K}^{-}}$
Organic Rankine Condenser Superheated Heat Transfer	$\dot{Q}_{\text{pcond,sh,cold}} = \dot{m}_{\text{pcond,eg}}\, Cp_{\text{pcond,sh,eg,avg}}\, (T_{\text{pcond,eg,out}} - T_{\text{pcond,eg,tpsh}})$	$\dot{Q}_{\text{pcond,sh,cold}} = 21.96\ 3.400\ (37.40 - 37.27)$	10.02	9.71	kW

Calculation	*Formulation*	*Hand Calculation*	*Model Result*	*Hand Value*	*Units*
	$\dot{Q}_{\mathrm{pcond,sh,hot}} = \dot{m}_{\mathrm{pc}}\,(\mathrm{h}_{\mathrm{pc,5}} - \mathrm{h}_{\mathrm{pc,6}})$	$\dot{Q}_{\mathrm{pcond,sh,hot}} = 3.699\,(411.3 - 408.6)$		9.99	
	$\dot{Q}_{\mathrm{pcond,sh}} = \varepsilon_{\mathrm{pcond,sh}} \min(\dot{m}_{\mathrm{pcond,eg}}\, Cp_{\mathrm{pcond,sh,eg,avg}}, \dot{m}_{\mathrm{pc}}\, Cp_{\mathrm{pcond,sh,r,avg}})(T_{\mathrm{pc,5}} - T_{\mathrm{pcond,eg,tpsh}})$	$\dot{Q}_{\mathrm{pcond,sh}} = 0.9599 \min(21.96\ 3.400,\ 3.699\ 1.061)\,(39.93 - 37.27)$		10.02	
Organic Rankine Condenser Superheated Log Mean Temperature Difference	$LMTD_{\mathrm{pcond,sh}} = \frac{(T_{\mathrm{pc,5}} - T_{\mathrm{pcond,eg,out}}) - (T_{\mathrm{pc,6}} - T_{\mathrm{pcond,eg,tpsh}})}{ln\left((T_{\mathrm{pc,5}} - T_{\mathrm{pcond,eg,out}})/(T_{\mathrm{pc,6}} - T_{\mathrm{pcond,eg,tpsh}})\right)}$	$LMTD_{\mathrm{pcond,sh}} = \frac{(39.93 - 37.40) - (37.77 - 37.27)}{ln((39.93 - 37.40)/(37.77 - 37.27))}$	1.251	1.252	K
Organic Rankine Condenser Superheated Thermal Conductance	$UA_{\mathrm{pcond,sh}} = \frac{\dot{Q}_{\mathrm{pcond,sh}}}{LMTD_{\mathrm{pcond,sh}}}$	$UA_{\mathrm{pcond,sh}} = \frac{10.02}{1.251}$	8.013	8.010	$kW\ K^{-1}$
	$\dot{Q}_{\mathrm{recup,cold}} = \dot{m}_{\mathrm{pc}}\,(\mathrm{h}_{\mathrm{pc,12}} - \mathrm{h}_{\mathrm{pc,11}})$	$\dot{Q}_{\mathrm{recup,cold}} = 3.699\,(266.1 - 255.4)$		39.58	
Recuperator Heat Transfer	$\dot{Q}_{\mathrm{recup,hot}} = \dot{m}_{\mathrm{pc}}\,(\mathrm{h}_{\mathrm{pc,3}} - \mathrm{h}_{\mathrm{pc,4}})$	$\dot{Q}_{\mathrm{recup,hot}} = 3.699\,(422.0 - 411.3)$	39.71	39.58	kW
	$\dot{Q}_{\mathrm{recup}} = \varepsilon_{\mathrm{recup}}\, \dot{m}_{\mathrm{pc}} \min(Cp_{\mathrm{recup,r,hot,avg}}, Cp_{\mathrm{recup,r,cold,avg}})(T_{\mathrm{pc,3}} - T_{\mathrm{pc,11}})$	$\dot{Q}_{\mathrm{recup}} = 0.9500\ 3.699 \min(1.053,1.450)\,(50.52 - 39.80)$		39.68	

Calculation	*Formulation*	*Hand Calculation*	*Model Result*	*Hand Value*	*Units*
Recuperator Log Mean Temperature Difference	$LMTD_{\text{recup}} = \frac{(T_{\text{pc,3}} - T_{\text{pc,12}}) - (T_{\text{pc,4}} - T_{\text{pc,11}})}{ln\left((T_{\text{pc,3}} - T_{\text{pc,12}})/(T_{\text{pc,4}} - T_{\text{pc,11}})\right)}$	$LMTD_{\text{recup}} = \frac{(50.52 - 47.20) - (40.14 - 39.80)}{ln((50.52 - 47.20)/(40.14 - 39.80))}$	1.314	1.308	K
Recuperator Thermal Conductance	$UA_{\text{recup}} = \frac{\dot{Q}_{\text{recup}}}{LMTD_{\text{recup}}}$	$UA_{\text{recup}} = \frac{39.71}{1.314}$	30.21	30.22	$kW\ K^{-1}$
Turbine Efficiency	$\eta_{\text{turb}} = \frac{h_{\text{pc,1}} - h_{\text{pc,2}}}{h_{\text{pc,1}} - h_{\text{pc,s,2}}}$	$\eta_{\text{turb}} = \frac{438.1 - 422.0}{438.1 - 418.0}$	0.8000	0.8010	-
Turbine Work	$\dot{W}_{\text{turb}} = \dot{m}_{\text{pc}}(h_{\text{pc,1}} - h_{\text{pc,2}})$	$\dot{W}_{\text{turb}} = 3.699\ \ (438.1 - 422.0)$	59.49	59.55	kW
Shaft Efficiency	$\eta_{\text{shaft}} = \frac{\dot{W}_{\text{comp}}}{\dot{W}_{\text{turb}}}$	$\eta_{\text{shaft}} = \frac{57.71}{59.49}$	0.9700	0.9701	-
Pump Efficiency	$\eta_{\text{pump}} = \frac{h_{\text{pc,s,10}} - h_{\text{pc,9}}}{h_{\text{pc,10}} - h_{\text{pc,9}}}$	$\eta_{\text{pump}} = \frac{252.1 - 250.8}{255.4 - 250.8}$	0.30	0.2826	-
Pump Work	$\dot{W}_{\text{pump}} = \dot{m}_{\text{pc}}(h_{\text{pc,10}} - h_{\text{pc,9}})$	$\dot{W}_{\text{pump}} = 3.699\ \ (255.4 - 250.8)$	17.00	17.02	kW
Thermal COP	$COP_{\text{TH}} = \frac{\dot{Q}_{\text{evap}}}{\dot{Q}_{\text{gen,sc}} + \dot{Q}_{\text{gen,tp}} + \dot{Q}_{\text{gen,sh}}}$	$COP_{\text{TH}} = \frac{300}{173.0 + 377.2 + 37.29}$	0.5107	0.5106	-

Calculation	*Formulation*	*Hand Calculation*	*Model Result*	*Hand Value*	*Units*
Electrical Equivalent COP	$COP_{\mathrm{EC}} = \frac{\dot{Q}_{\mathrm{evap}}}{\dot{W}_{\mathrm{pump}}}$	$COP_{\mathrm{EC}} = \frac{300}{17.00}$	17.64	17.65	-
Total Thermal Conductance	$UA_{\mathrm{tot}} = \sum UA$	$UA_{\mathrm{tot}} = 30.21 + 8.013 + 211.5 + 0.6983 + 17.37 + 101.2 + 11.57 + 7.681 + 9.306 + 6.408 + 108.0 + 0.3624 + 0.3712 + 126.7$	639.5	639.4	kW K^{-1}
Pressure Net Positive Suction Head	$NPSH_{\mathrm{P}} = \frac{1000}{\rho_{\mathrm{pc,9}}\, g}\,(P_{\mathrm{pc,9}} - P_{\mathrm{sat,pc,9}})$	$NPSH_{\mathrm{P}} = \frac{1000}{1123\ 9.81}\,(705.1 - 698.9)$	0.5672	0.5628	m
Pump Inlet Velocity	$\vec{V}_{\mathrm{pc,9}} = \frac{\dot{m}_{\mathrm{pc}}}{\rho_{\mathrm{pc,9}}\ 0.004768}$	$\vec{V}_{\mathrm{pc,9}} = \frac{3.699}{1123\ 0.004768}$	0.6909	0.6908	m s^{-1}
Velocity Net Positive Suction Head	$NPSH_{\mathrm{V}} = \frac{\vec{V}_{\mathrm{pc,9}}^{2}}{2\ g}$	$NPSH_{\mathrm{V}} = \frac{0.6909^{2}}{2\ 9.81}$	0.0243	0.0243	m
Turbine Specific Speed	$Ns_{\mathrm{turb}} = \frac{1000\ \omega_{\mathrm{turb}}\ \sqrt{35.315\frac{\dot{m}_{\mathrm{pc}}}{\rho_{\mathrm{pc,2}}}}}{(334.6\ (\mathrm{h}_{\mathrm{pc,1}} - \mathrm{h}_{\mathrm{pc,s,2}}))^{0.75}}$	$Ns_{\mathrm{turb}} = \frac{1000\ 30\sqrt{35.315\frac{3.699}{37.51}}}{(334.6\ (438.1 - 418.0))^{0.75}}$	75.37	75.38	-
Turbine Specific Diameter	$Ds_{\mathrm{turb}} = \frac{3.281\ D_{\mathrm{turb}}(334.6\ (\mathrm{h}_{\mathrm{pc,1}} - \mathrm{h}_{\mathrm{pc,s,2}}))^{0.25}}{\sqrt{35.315\frac{\dot{m}_{\mathrm{pc}}}{\rho_{\mathrm{pc,2}}}}}$	$Ds_{\mathrm{turb}} = \frac{3.281\ 0.1(334.6\ (438.1 - 418.0))^{0.25}}{\sqrt{35.315\frac{3.699}{37.51}}}$	1.592	1.592	-

Calculation	*Formulation*	*Hand Calculation*	*Model Result*	*Hand Value*	*Units*
Compressor Specific Speed	$Ns_{\text{comp}} = \frac{1000\ \omega_{\text{comp}} \sqrt{35.315 \frac{\dot{m}_{\text{cc}}}{\rho_{\text{cc,1}}}}}{(334.6\ (\text{h}_{\text{cc,s,2}} - \text{h}_{\text{cc,1}}))^{0.75}}$	$Ns_{\text{comp}} = \frac{1000\ 30 \sqrt{35.315 \frac{1.816}{10.90}}}{(334.6\ (440.8 - 415.3))^{0.75}}$	82.17	82.97	-
Compressor Specific Diameter	$Ds_{\text{comp}} = \frac{3.281\ D_{\text{comp}} (334.6\ (\text{h}_{\text{cc,s,2}} - \text{h}_{\text{cc,1}}))^{0.25}}{\sqrt{35.315 \frac{\dot{m}_{\text{cc}}}{\rho_{\text{cc,1}}}}}$	$Ds_{\text{turb}} = \frac{3.281\ 0.1 (334.6\ (440.8 - 415.3))^{0.25}}{\sqrt{35.315 \frac{1.816}{10.90}}}$	1.299	1.300	-

Appendix B Test Facility Design Considerations

This appendix lists prototype design considerations beyond those presented in Chapters 3 and 4, which were excluded for simplification. The layout of a fluid management subsystem integrated with the organic Rankine vapor compression prototype is shown in Figure B-1. This subsystem was incorporated into the experimental design to aid in operational and maintenance tasks. The system could be used to add or remove refrigerant from the prototype, effectively add or remove refrigerant from the prototype by modulating the pressure within the accumulator, or transfer refrigerant from one cycle to the other. Transferring refrigerant from one cycle to another was useful at startup or during system operation when the condensers were isolated from one another. When operating with isolated condensers, refrigerant would leak from the power cycle to the cooling cycle through the turbo-compressor coolant lines and turbine shaft seal. The fluid management subsystem connected to the prototype at 6 points as shown in Figure B-1: (1) at the non-refrigerant process connection of the accumulator, (2) between Valve 18 and the micron filter in the turbo-compressor coolant supply line, (3) at the inlet to the power cycle condenser, (4) at the inlet to the cooling cycle condenser, (5) at the liquid outlet of the suction line heat exchanger, and (6) at the liquid inlet to the suction line heat exchanger.

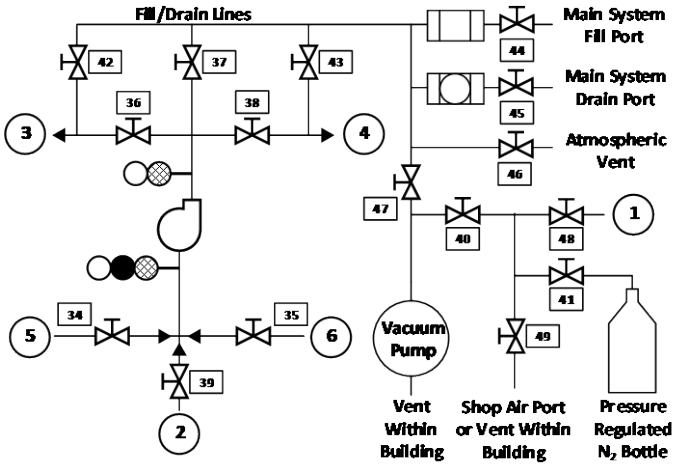

Figure B-1 Prototype fluid management piping and instrumentation diagram

The equipment in the fluid management subsystem is as follows. The fluid management pump was Liquiflo part number M6S6PEE10020B with a NEMA Premium motor part number 00218ET3ER145TC-W22. The pump was driven by a Schneider Electric variable frequency drive ATV312HU15N4. Valves 34 to 49 were: McMaster 4749K154749K15 (34 and 35), Swagelok SS-43GS4 (36 to 41), Swagelok SS-43GS4-A (42 to 47), and Swagelok SS-43GF4 (48 and 49). The micron filter was part number SS-4F-05 from Swagelok to protect the compressor used for refrigerant recovery. The fill port was equipped with a filter dryer (Emerson BFK-084) to purify refrigerant charge of water and particulate. The vacuum pump was from McMaster (McMaster 4396K45). The fluid management pump, its variable frequency drive, and the enclosure housing the fill/drain station is shown in Figure B-2. The power cycle pump variable frequency drive is also shown in Figure B-2 as the two shared an enclosure on the prototype skid.

Figure B-2 (Left to Right) Fluid management pump, variable frequency drives, and fill/drain station

Figure B-3 to Figure B-6 show the turbine bypass line, organic Rankine vapor compression tanks, compressor inlet liquid trap, and safety blowdown subsystem, respectively. These considerations were detailed in Chapter 4. Figure B-7 shows the electrical panelboards used to power the system. A 120 VAC line outlet was extended from existing infrastructure to the panel board shown on the left-hand side of Figure B-7. The 120 VAC outlet powered the data acquisition system, lab computer, liquid trap safety heater, turbo-compressor vapor drain line flow meter, heat line control valve, and enclosure fans to cool

the variable frequency drives. The 120 VAC outlet is shown next to four 460 VAC outlets which are powered from the panelboard above the outlets. These four outlets serve as the supplies for the condensing loop pump, power cycle pump variable frequency drive, fluid transfer pump variable frequency drive, and evaporator loop pump. The respective breakers to feed these outlets within the enclosure (Siemens BQD style) have capacities of 40, 40, 30, and 25 amps. The 120 VAC outlet is fed from two breakers in a separate panel board serving adjacent lab spaces with a combined capacity of 45 amps. The 250-amp, 460 VAC board for the pumps (Siemens P1E42MC250AT) is supplied from the building electrical switchgears with an 800-amp switchboard via a 400-amp breaker (Eaton KDC-100K) set to 250-amps using an adjustable trip unit (Eaton KES3250LS). SOOW cords were used to transmit power from the outlets to their respective components and were routed up through the piping support holding the panel board and over to the test facility in wire trays (also supporting instrument and signal wires) to maintain a clear walkway. The other 460 VAC panel board serving the test facility (Siemens P1E42MC400AT) is affixed to the generator loop heater skid. This board has 400 amps of capacity and has six 60-amp breakers (also Siemens BQD style) each serving a single generator loop electrical heater.

Figure B-3 Test facility turbine bypass loop

Figure B-4 Test facility accumulator (Left) and liquid receiver (Right)

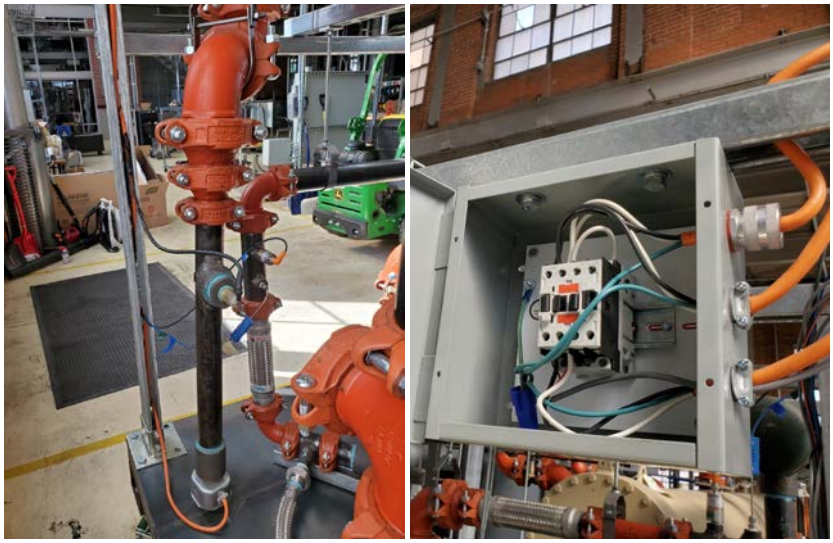

Figure B-5 Test facility liquid trap with heater and float switch (Left) and relay enclosure (Right)

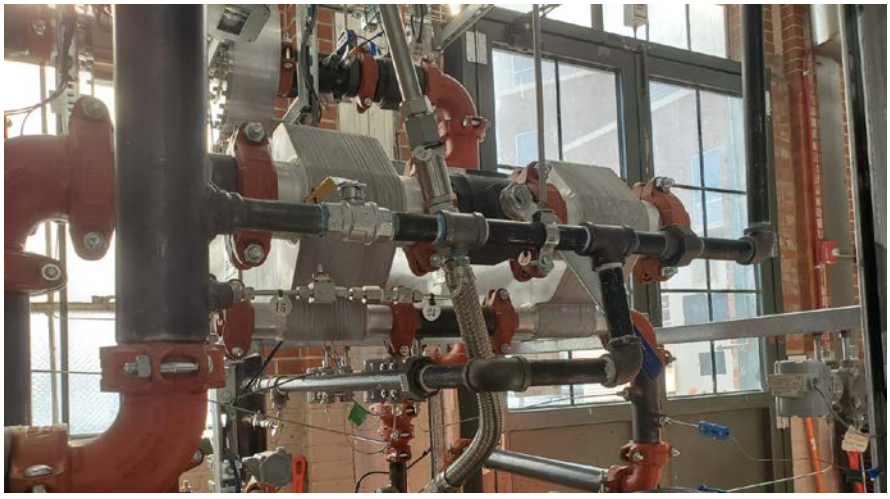

Figure B-6 Test facility atmospheric safety blowdown subsystem

Figure B-7 Test facility electrical supplies

A complete test facility solid model was previously shown in Chapter 4. The same model is shown in various orientations in Figure B-8 to Figure B-12. Figure B-8 shows the overall constraints which bounded the format of the prototype. The length, width, and height constraints for the prototype were set to 5.79 m, 2.11 m, and 3.18 m respectively. However, the prototype was optimized to slightly surpass these constraints with a final length, width, and height of 5.28 m, 1.75 m, and 2.84 m, respectively. The length constraint was derived from the length of the available workspace less that of a 0.91 m walkway to allow for a fire escape behind the north end of the test facility. The walkway was also required in front of building switchgears for their accessibility. The width and height were constrained to allow the transportation of the completed unit into/out of the building through the east doors. This allowed for the partial construction of the prototype outside of the building. Partial construction was complete outside of the building where a lift truck could be utilized to place shell and tube heat exchangers and the power

cycle pump. This was required as the floor of the available workspace could not support a lift truck, nor could the structural beams support an adequate crane. Thus, heavy duty casters were selected to support the prototype skid to transport and position the system.

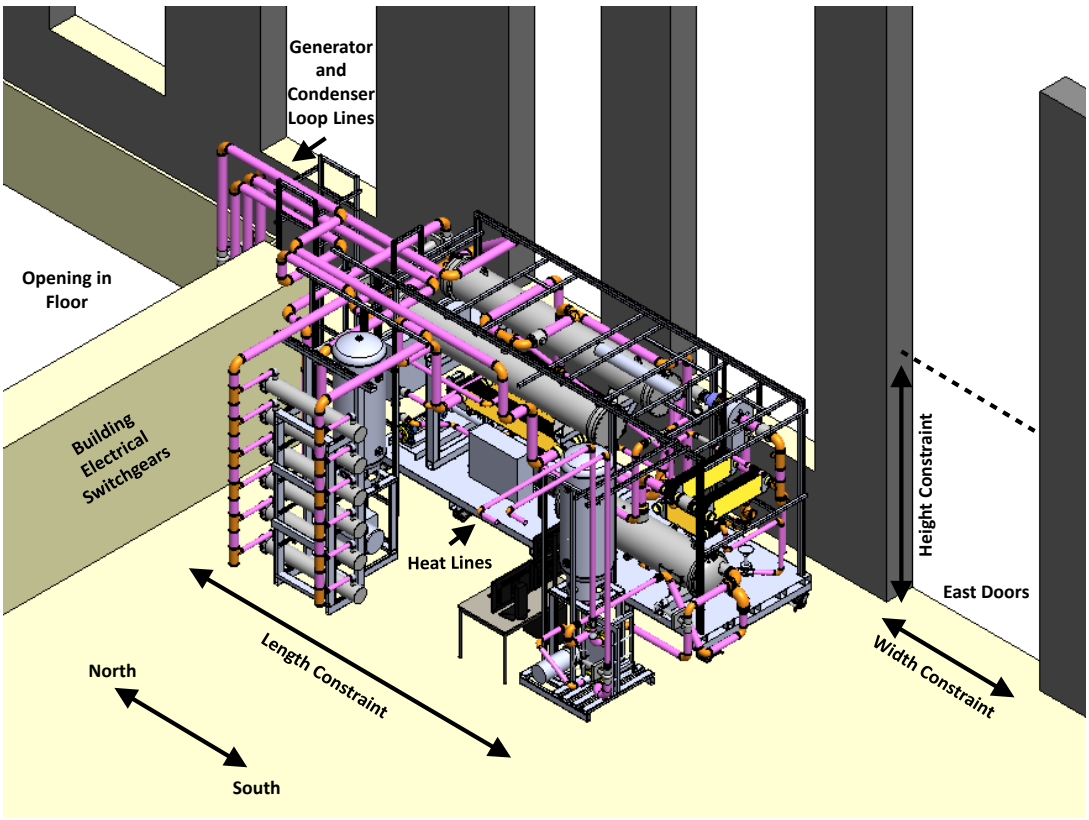

Figure B-8 Solid modeling constraints of the test bed workspace

In addition to the geometric constraints, system design was further constrained by the locations of the cooling tower, steam line heat source, and heat line heat source. The lab space one floor above and directly to the south of the available workspace was already fitted with heat line connections to the building circulation heater. Thus, the existing supply and return lines were branched and routed to the available workspace for connection to the basement heat exchanger. This constrained the evaporator loop skid and evaporator to the southmost portion of the available workspace. The prototype cooling tower was required to be placed at the northeast corner of the building in the utility yard where electric and water connections were already present. Condenser loop piping connected to the unit through

preexisting ports drilled through the foundation of the building in the basement level of Room 131. Thus, the condensers and condenser loop skid were constrained to the northmost portion of the available workspace to allow the loop piping to directly enter the basement through the opening in the floor. Lastly, the generator loop lines had to connect with the generator loop pump and steam heat exchanger which are both collocated with the building steam generator in the northwest corner of the basement level of Room 131. Thus, the generator loop lines can also be seen entering the basement through the opening in the floor with the condenser loop lines. Despite the routing of the generator loop, the generators were constrained to the side of the prototype to attach to the circulation heaters. The generator loop circulation heaters were located close to the building electric switchgears to minimize installation costs. The component labels for Figure B-9 to Figure B-12 are as follows: (A) power cycle condenser, (B) generators, (C) evaporator, (D) turbo-compressor, (E) power cycle pump, (F) suction line heat exchangers, (G) liquid trap enclosure, (H) variable frequency drive enclosure, (I) power cycle mass flow meter, (J) accumulator, (K) vapor trap, (L) data acquisition enclosure, (M) liquid trap, (N) expansion valve, (O) cooling cycle condenser, (P) fill/drain station enclosure, (Q) recuperators, (R) economizer, and (S) turbine bypass loop.

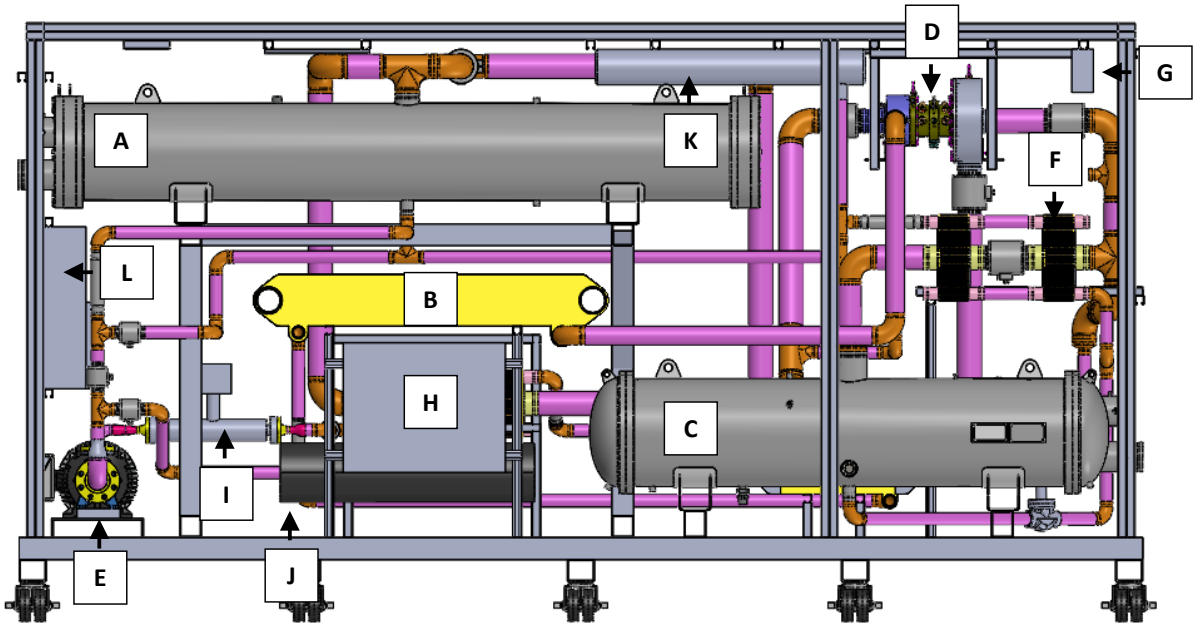

Figure B-9 Labeled front view of the prototype solid model

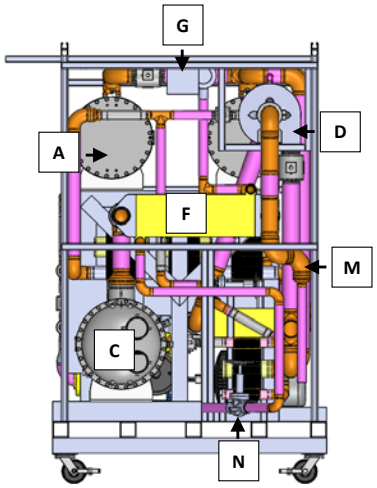

Figure B-10 Labeled right view of the prototype solid model

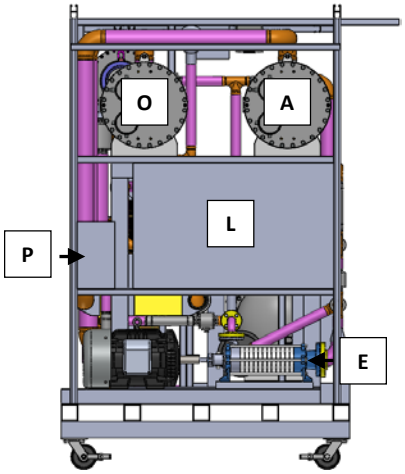

Figure B-11 Labeled left view of the prototype solid model

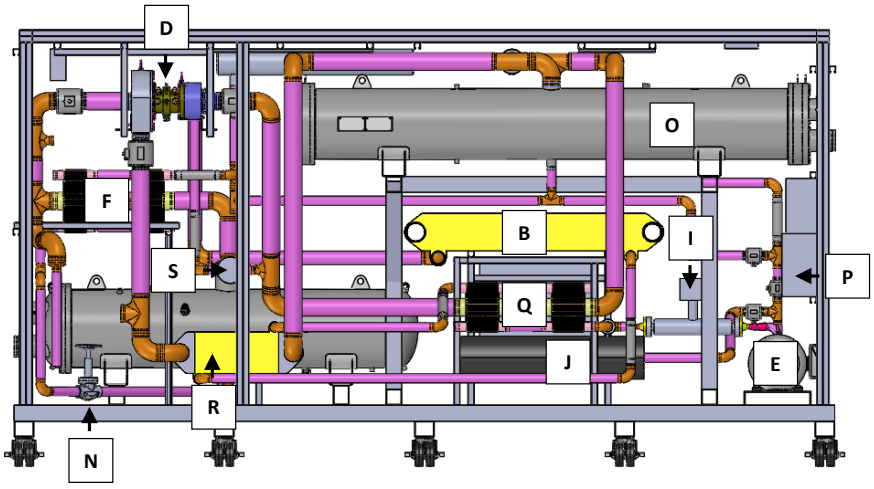

Figure B-12 Labeled back view of the prototype solid model

Additional modeling efforts were complete by manufacturing partners for the turbo-compressor and custom heat exchangers. Labeled cutaway views of the turbo-compressor are shown in Figure B-13 to show the inner workings of the device.

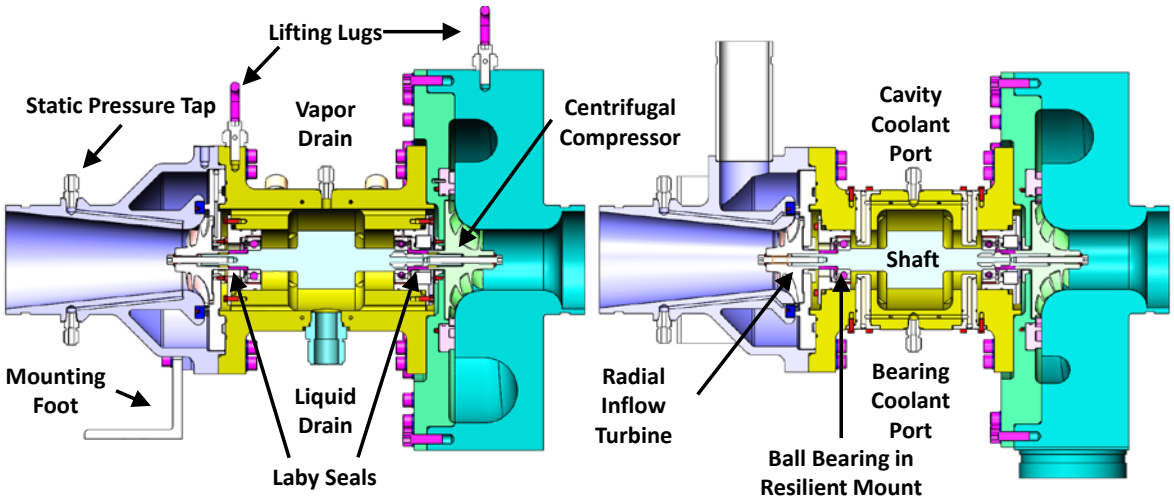

Figure B-13 Labeled cut-away schematic of the custom fabricated turbo-compressor

Computational fluid dynamic analysis was also performed on both the turbine and compressor in its design and in the development of the performance maps. Figure B-14 shows one of the fluid simulations complete for both devices. Computational fluid dynamic analysis was required to estimate the performance of the unit as the working fluid had a low compressibility factor at the specified working conditions. Furthermore, the structural integrity of the turbo-compressor was assessed with finite element analysis. Figure B-15 shows a finite element analysis complete on the turbo-compressor housings to determine their maximum working pressure.

For the heat exchangers, a number of simulations were performed to assess performance and integrity. Figure B-16 shows finite element analysis and computational fluid dynamic assessment performed on the custom heat exchangers. These simulations helped to optimize the strength of the custom devices. Pressure loss simulations of the recuperative heat exchangers showed that vapor flow favored the parallel unit furthest from the vapor inlet. Thus, valves were placed between the parallel

recuperator and suction line heat exchanger vapor inlet connections to balance flow. These valves are numbers 12 and 13 in the piping and instrumentation diagram presented in Chapter 4, respectively.

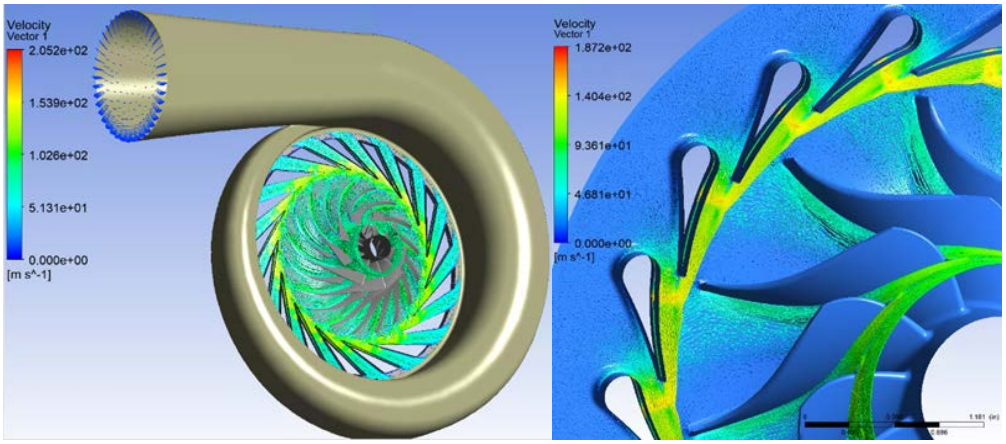

Figure B-14 Compressor (Left) and turbine (Right) computational fluid dynamic analysis

Figure B-15 Turbine (Left) and compressor (Right) finite element analysis strength assessment

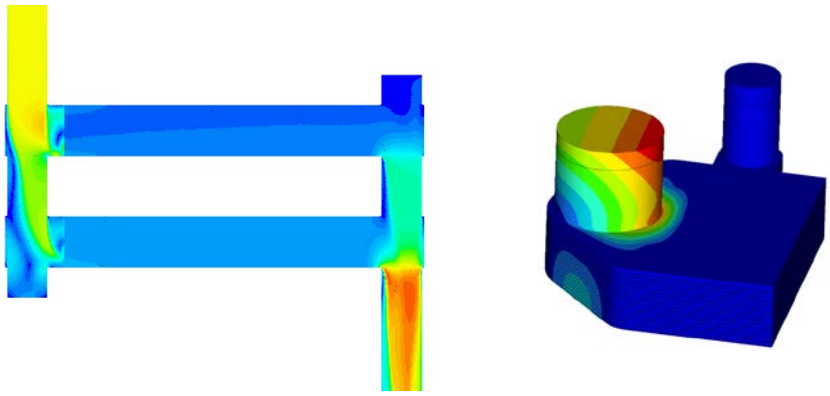

Figure B-16 Heat exchanger computational fluid dynamic (Left) and finite element (Right) analysis

Additional considerations for system design included the selection of pipes, fittings, and structural members for use in fabrication. American Society for Testing and Materials International A53 Schedule 40 black coated carbon steel pipe was selected for much of the prototype and auxiliary loop piping due to its sufficient pressure rating and its ability to be welded, threaded, and grooved. Flexible two-inch grooved end hoses were incorporated into the main system design to account for misalignment and absorb vibration. Four-inch hoses were used on auxiliary loop piping but had an insufficient pressure rating for the prototype power and cooling cycles. Thus, misalignment for the four-inch prototype networks was tolerated using flexible grooved connections implemented throughout the entire test facility. Class 300 American National Standards Institute flanges were selected where required on the prototype while Class 150 flanges were used where required on auxiliary loops. Schedule 40 pipe fittings were used with these flanges to transition from welded connections to threaded or grooved connections. Unistrut fixturing was selected to support piping networks and lightweight components while structural steel was selected to support larger components. Unistrut allowed for iterative design work and easily supported piping networks using rod mounted loop hangers or strut mounted clamps. The only unique supports were two floor mounted units which were used to secure the accumulator. 4x5x0.188 rectangular steel tube was selected for the base of the prototype skid and to support the evaporator due to its accommodating width for the casters and appropriate height for the saddles on the evaporator. 4x0.188 square steel tubing was selected for the remainder of the prototype skid and to hold the condensers. The prototype skid was covered with 12 gauge hot rolled steel sheet to create a solid working surface. 2x4x0.188 rectangular steel tubing was used for the auxiliary loop skids.

The test facility was fabricated following the completion of the solid model and the delivery of materials. Sheered sheet metal and skid members cut with a bandsaw or chop saw were welded together with a metal inert gas welder with carbon steel wire and 25% carbon dioxide – 75% argon shielding gas. A magnetic base drill press and a hand drill were used to create the mounting holes required throughout

the system. The Unistrut skeleton of the main skid was cut with a chop saw and assembled using Unistrut fittings, clamps, and standard Grade 5 hardware tightened to specification. Figure B-17 shows the preliminary assembly of the prototype, the evaporator loop skid, and the condenser loop skid.

Figure B-17 Preliminary assembly of test facility skids

Piping sections were cut with a bandsaw and fitted on the test bed with strut mounted clamps and rod mounted loop hangers to ensure their alignment. Grooved sections were fabricated with a roll grooving machine. Flanged sections and threaded or plain weldolet fittings to house instruments, support draining or filling, and connect equipment were welded with a shielded metal arc welder using 7018 flux coated electrodes. Threaded connections up to 50 mm were cut with a threading machine. There were no capabilities in house to thread diameters above this value, thus, larger threaded sections were purchased prefabricated and cut down on a bandsaw to an appropriate size. Weldolet fittings of 6 mm were welded to drilled ports into main piping sections while larger fittings were attached to ports cut with an oxyacetylene cutting torch. Welded connections were tested for tightness with shop air and a soap-water solution before they were hydrostatically tested for continuous operation at the critical design pressure with a compressed, pressure regulated nitrogen bottle. Threaded connections were wrapped

with pipe tape and coated with thread sealant (both compatible with all working fluids and process temperatures) before they were installed. Grooved connection surfaces were cleaned with a wire brush attachment on a hand grinder before their gaskets were lubricated, installed, and secured with clamps in accordance with manufacturer guidelines. Flanged connections used Teflon gaskets and were torqued to specification with Grade 5 hardware. Union threads were coated with anti-seize before installation. Once the major piping routes were established, stainless steel tubing was used with compression fittings and threaded flexible hoses to complete the system. Figure B-18 shows the connection strategies used throughout the test facility.

Figure B-18 Coupling strategies implemented throughout the test facility

Appendix C Test Facility Operational Procedures

Test facility operation is currently a highly involved process requiring a minimum of three trained personnel to complete. Until further controls or automated equipment is implemented and verified, the following procedures must be followed to test the operation of the prototype with combined condensers. First, a number of equipment checks must be performed to ensure the prototype is ready for operation (C.1.). Once all the safety checks are complete, the system startup can be initiated (C.2.). Once started, prototype operation can be tuned to a specified condition (C.3.). Once all desired operational points are tested, the system shutdown procedure should be followed (C.4.). If an emergency occurs, a rapid system shutdown procedure can be followed to reduce risk to personnel and equipment (C.5.).

C.1. Pretest Equipment Checks

Prior to experimentation, a number of equipment checks must be performed to ensure the prototype can be operated. First, the virtual interface must be opened and operated on the computer adjacent to the prototype. To open the interface, follow path file “C:\Program Files (x86)\National Instruments\LabVIEW 2018\LabVIEW.exe” to open the software package. Once the program is started, the project relating to the prototype is accessed through opening file “TCCS-2.lvproj”. “TCCS-2-RIO RT.vi” under “TCCS-2-RIO9066 (129.82.106.71)” must then be opened and run to begin communication between the data acquisition system and the computer. The virtual interface can then be opened through file “TCCS-2 Main R5.vi”. The main interface “Overview” is shown in Figure C-1 for reference. Input the desired sampling frequency for data collection (2 Hz was standard for this investigation) and a test length in minutes which will cover the length of the entire testing period (Item A in Figure C-1). Once complete, run the program and set the file location and name in the resulting popup window. Then, hit “GO!” to monitor the system in real time through the virtual interface and begin the recording of data. If the virtual interface

was already running without data collection, the same procedure is followed except the record button must be depressed (Item A in Figure C-1) to open the file path popup window.

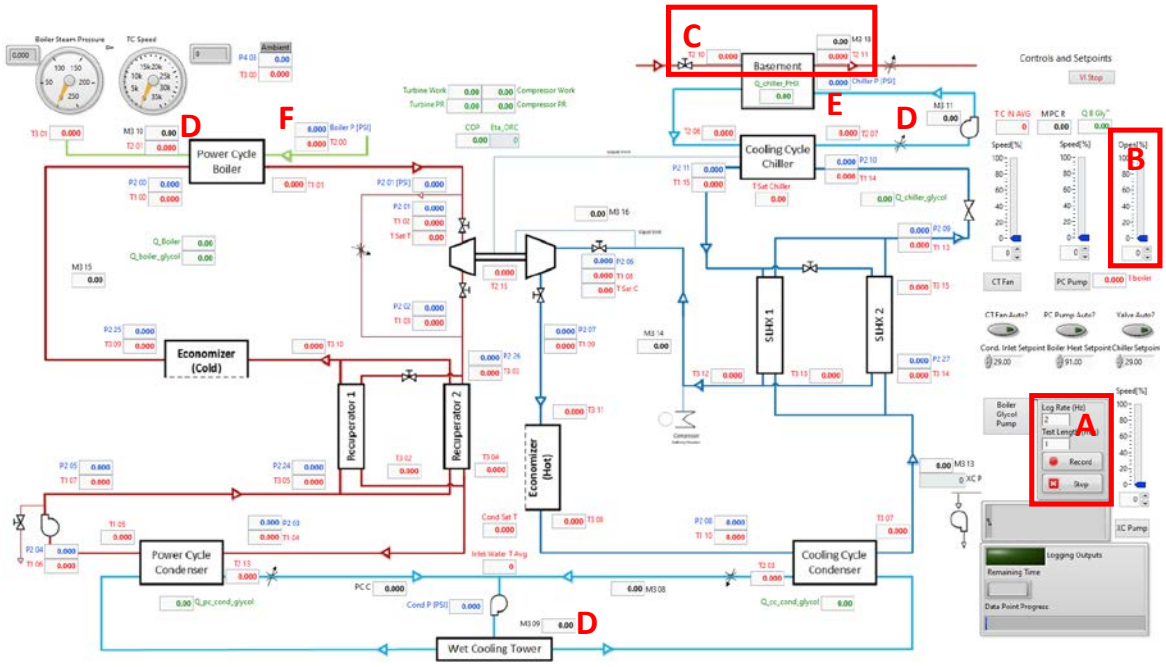

Figure C-1 Labeled virtual interface screenshot to discuss pretest procedures

With data recording and system operation being monitored in real time, the prototype pre-experimentation equipment checks can be complete. First, the heat line operation must be ensured such that the prototype is able to reject its cooling load. Open Valve 3 and 30 to determine the functionality of the heat line. If the automated valve for Valve 30 is closed, power the unit using the switch near the computer and set the slider controlling its position to 100% open in the virtual interface (Item B in Figure C-1). The flow through the heat line should read above 20 m^3 hr^{-1} if functioning properly. The temperature should also increase to around 70°C. The heat line flow and temperature readings (Item C in Figure C-1) respectively show the heat line circulation pumps and heater are functioning properly. Close Valve 30 until later detailed.

Next, check the operation of the circulation pumps on the external loops. Simply power each unit using the respective breakers located in the panel board across from the data acquisition enclosure. Set

each loop flowrate (Item D in Figure C-1) close to the desired value using the flow control valves on each loop. The flow can be increased in the evaporator and generator loop by pressurizing the loop with shop air. Never pressurize the evaporator loop beyond 690 kPa (Item E in Figure C-1). Never pressurize the generator loop without a safety valve installed on the atmospheric vent on the loop surge tank. If the generator loop is to be pressurized, never do so beyond 275 kPa (Item F in Figure C-1). The safety valve vent should be routed into an empty glycol drum to avoid the potential of leaking scalding liquid. Never operate the generator loop circulation pump while the loop is under vacuum. Doing so will cause cavitation in the circulation pump. The condenser loop should not be pressurized as there is already a prohibitive pressure loss through the loop which results in high circulation pump discharge pressures. Once operational and the flowrates set, the pumps can remain in operation. If not already complete from previous tests, the differential pressure lines of the external loops should also be purged of air.

With the operation of the circulation pumps in the external loops verified, the cooling tower must be prepared for operation. Connect the water makeup hose to the basin from the sink at the northmost section of the room the prototype is located within. Ensure water flows freely from the sink to the cooling tower basin. This is especially important in winter months when lines can freeze. If frozen, thaw lines until water flows freely. At this point, the basin pump of the cooling tower can be engaged unless there is risk of freezing. If there is risk of freezing, ensure the operation of the pump by operating it momentarily, then disconnect the unit. Only power the basin pump when the cooling tower fans are engaged as later detailed.

For the generator loop, ensure Valve 28 is open and all other valves leading to other steam processes are closed. In addition to Valve 28, there are two globe valves located at the steam line discharge port of the steam heat exchanger, these should be fully open. Ensure the functionality of the steam generator makeup water system by checking the supply pump and reverse osmosis water tank. Check to ensure the steam generator exhaust fan is operational and that there is fuel pressure at the unit.

If valves to other steam processes are open or other equipment is not operational, consult control room personal.

The next process is to ensure the prototype is ready for experimentation. Regarding the organic Rankine vapor compression system, all valves should be open except Valves 1, 4, 9, 10, 19, 20, and 34 through 48. A shop air line should be attached to a port at Valve 49 such that the accumulator can be pressurized at any time (through opening Valve 48) to avoid power cycle pump cavitation. All components relating to the compressor inlet liquid trap should be powered. There should be little to no refrigerant in the evaporator as indicated by the sight glass installed on its shell. If there is excess refrigerant in the evaporator, it can be drained by opening Valves 9 and 30. This sends heat into the evaporator which vaporizes the refrigerant. The vapor escapes the evaporator and is transferred to the cooling cycle condenser. Once empty, shutoff Valves 9 and 30 once more. At this point, the prototype is prepared for experimentation and startup can be initiated.

C.2. Startup

The first step in initiating system startup is to engage the steam generator. Flip all switches on the unit to on or auto except the burner switch and the manual blowdown switch. Hit escape on the control panel until no further changes to the menu occur. Then, select operation, boiler setpoint, and setpointw1. Enter (200 PSI) as this setpoint if not already done so. Once again, hit escape on the control panel until no further changes to the menu occur. Then, select operation, user maxload, and user maxloadmod. Enter 100% as this setpoint if not already done so. These two changes set the safety trip pressure to 1,375 kPa and the steam generator load to 100% respectively. Operation of the steam generator should never exceed 1,375 kPa due to component pressure ratings. The generator load can be decreased during turndown operation but must be started at 100%. With these settings confirmed, flip the burner switch to the on position to start the steam generator. Monitor the unit as it is starting at its location. Once its

load hits 40%, engage the unit exhaust fan. Failure to do so will lead to a buildup of carbon monoxide in the building. Engaging the fan before the load reaches 40% could extinguish the burner flame. If the burner is extinguished, an alarm will sound, and the unit must be restarted. The steam generator is fully operational at this point. It will take some time for the unit to reach its operational pressure (~350 kPa). However, it will be heating the generator loop fluid while this is occurring. Additional heat can be input to the generator loop using any number of the loop circulation heaters to match the desired heat duty of the testing conditions to be explored. The temperatures within the generator loop are monitored on the virtual interface as shown in Item A in Figure C-2.

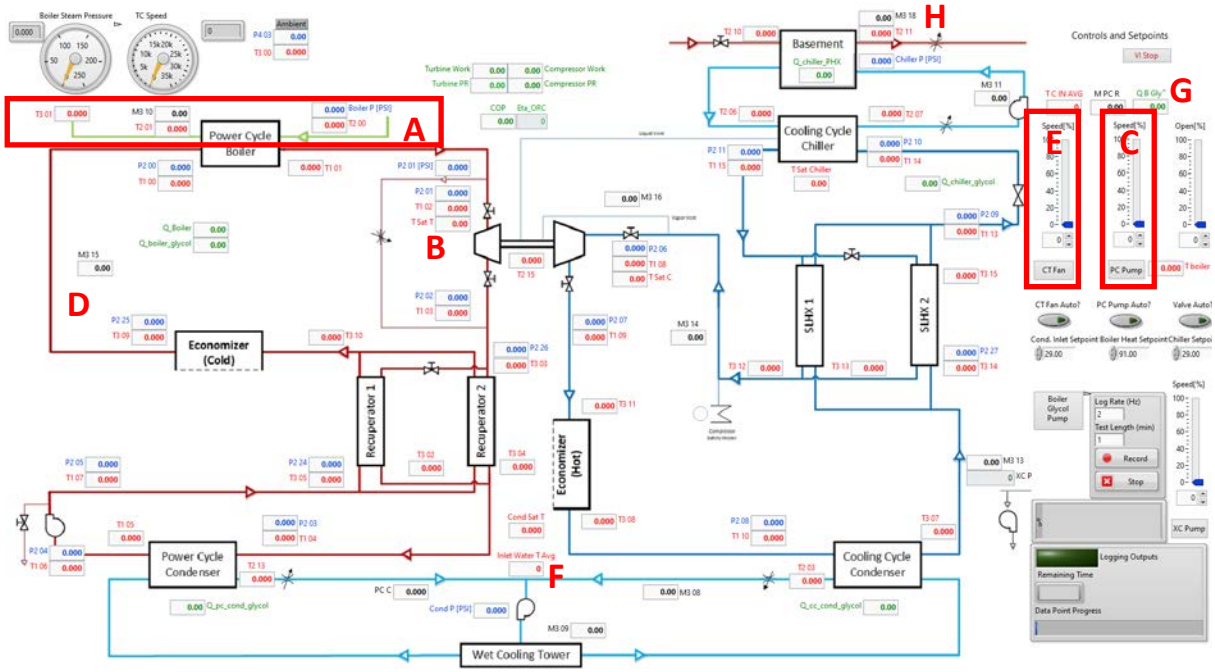

Figure C-2 Labeled virtual interface screenshot to discuss startup procedures

Once the temperature in the generator loop surpasses the refrigerant saturation temperature by ~10°C (Item B in Figure C-2), the power cycle pump can be powered through the virtual interface (Item C in Figure C-2) to begin circulation through the organic Rankine cycle via the turbine bypass. Power cycle flow (Item D in Figure C-2) may oscillate while vapor generated in the generators displaces liquid throughout the system. Ensure the flow is low enough that the generator loop continues to heat. Once a

flow steadies, restrict the flow through the turbine bypass using Valve 2. This increases the pressure ratio in the power cycle and brings the cycle closer to a realistic operating condition. Never fully close Valve 2 while Valves 4 and 10 are also closed. This will cause the pump to deliver its shutoff head which could over pressurize the power cycle. As soon as refrigerant is circulating within the power cycle, heat is being rejected to the condenser loop via the power cycle condenser. The temperature of this loop must be monitored and maintained at a desired value using the cooling tower fans. Power the fans through the virtual interface using the manual slider controlling their speed via the cooling tower fan variable frequency drive (Item E in Figure C-2). If the cooling tower basin pump was not yet engaged, do so now. This will result in a sharp decrease in condenser loop temperature (Item F in Figure C-2) until the water within the basin is heated to match the loop thermal quality.

Once the generator loop temperatures reach the desired conditions, the power cycle pump speed can be increased such that the load of the steam generator and generator loop circulation heaters (Item G in Figure C-2) match the energy removed by the power cycle refrigerant in the generators. Monitor any one of the high-side pressures in the power cycle as this flow is increased. Valve 2 may need to be opened slightly with increasing power cycle mass flow if the refrigerant saturation pressure in the generator approaches the generator loop supply temperature. Failure to recognize this could result in an over pressurization or a loss of vapor generation (through generator pinch limitations) and, thus, a loss in system controllability. It is likely the generator temperature stabilizes to the desired value before the condenser loop temperature. Regardless, when the condenser loop temperature reaches its desired value, the cooling tower fan variable frequency drive should be modulated to hold the operating condition at the desired value.

At this point, the steam generator and generator loop heaters should be delivering a steady heat duty at a fixed thermal quality by matching heat supplied with heat absorbed via the power cycle pump variable frequency drive. Also, the heat rejected from the condensers should match the heat rejected at

the cooling tower at a fixed thermal quality through modulating the cooling tower fan variable frequency drive. If this steady operation is achieved, power cycle flow can be directed through the turbine to enable cooling cycle operation. However, a number of tasks must be rapidly completed to do so without risk of damage to the system.

First, Valves 19 and 20 should be fully opened to allow coolant supply to the turbo-compressor. Failure to complete this task will result in damage to the unit. Next, Valve 30 must be cracked to allow heat transfer from the heat line to the evaporator loop. If this is not complete, operation of the cooling cycle could result in freezing of the evaporator loop which could damage the system. Then, Valve 1 must be cracked to allow refrigerant flow from the cooling cycle condenser to gravity feed into the evaporator. Opening the valve too much will flood the unit and potentially cause cavitation in the power cycle pump. Opening the valve too little will result in evaporator dry out which would reduce the load on the turbine and could cause turbine runaway. Next, in this order, Valves 9, 4, and 10 need to be opened in rapid succession. This allows flow through the turbine and compressor while still allowing some refrigerant to bypass the turbine through Valve 2. Thus, the load produced by the turbine is low and there is no rapid energy transfer through the turbo-compressor which could damage the unit. Finally, Valve 2 is slowly shutoff to allow all the power cycle flow to enter the turbine.

While the system is fully operational at this point, care must be taken to modulate Valve 1 and Valve 30 to bring the system to steady operation. Valve 1 is used to maintain the refrigerant level within the evaporator at the top of the sight glass indicator installed on the evaporator shell. Valve 30 is used to fix the evaporator chilled water delivery temperature at the desired value (Item H in Figure C-2). This modulation requires the full attention of a single operator as the refrigerant level within the evaporator and the evaporator chilled water delivery temperature are interdependent.

C.3. Operation

Once the prototype is fully operational following startup, operational conditions must be tuned to those desired for experimentation. To tune generator heat duty, operators must determine how many glycol heaters are required to just surpass the desired load. All but one of these units must be powered continuously, while the final unit must be cyclically powered and disconnected to match the desired heat duty. If the heat duty is maintained at the appropriate value but the loop temperature is steadily decreasing, the power cycle pump speed must be slightly decreased and vice versa. Alternatively, the steam generator load can be reduced to match the desired thermal load. In some instances (during turndown testing) the load of the steam generator had to be reduced. To do so, the same procedure to set the load at 100% can be followed to change the loading condition. Loading condition cannot be decreased below 40% or the unit will trip. If operation at elevated generator loop temperatures is desired, the steam pressure input to the steam heat exchanger may need to be increased to increase the temperature at which steam is condensing within the heat exchanger. This is accomplished through modulating the two valves on the steam line discharge port of the steam heat exchanger. Closely monitor the pressure as it increases to ensure the steam generator does not exceed a supply pressure of 1,375 kPa. This will cause the unit to trip. Considering the density in the generator loop may have changed, the pressure within the loop or the position of Valve 29 may need to be modulated to set the proper flowrate.

With the generator loop at the desired conditions, the condenser loop conditions can be set. The variable frequency drive controlling the cooling tower fans can be modulated manually or with a proportional-integral-derivative controller to set the average condenser glycol inlet temperature through the virtual interface. The control variables are accessed on another virtual interface tab labeled “PID Controls”. With the proper variables input, set the condenser inlet setpoint to the desired value and depress the button labeled “CTFan Auto?” (Item A in Figure C-3). Flow through the condensers can be balanced with Valves 32 and 33 if desired. Finally, the evaporator loop conditions must be set while

maintaining the refrigerant level within the evaporator. The chilled water delivery temperature can be set at the desired value using the heat line control valves. The automated valve can only be powered for 45 minutes before it must be disconnected for 15 minutes to avoid damage. The automated valve can be controlled with a proportional-integral-derivative controller during experimentation through the virtual interface (Item B in Figure C-3) similarly to the cooling tower fan variable frequency drive. Valve 31 can then be modulated to achieve the desired chilled water temperature difference at the produced chilling load. After the external loops have been set, operators can modulate Valves 12 and 13 to balance the thermal loads of the recuperators and suction line heat exchangers, respectively. This is accomplished once the recuperator vapor outlet temperatures (Item C in Figure C-3) and the suction line heat exchanger vapor outlet temperatures (Item D in Figure C-3) equate to one another.

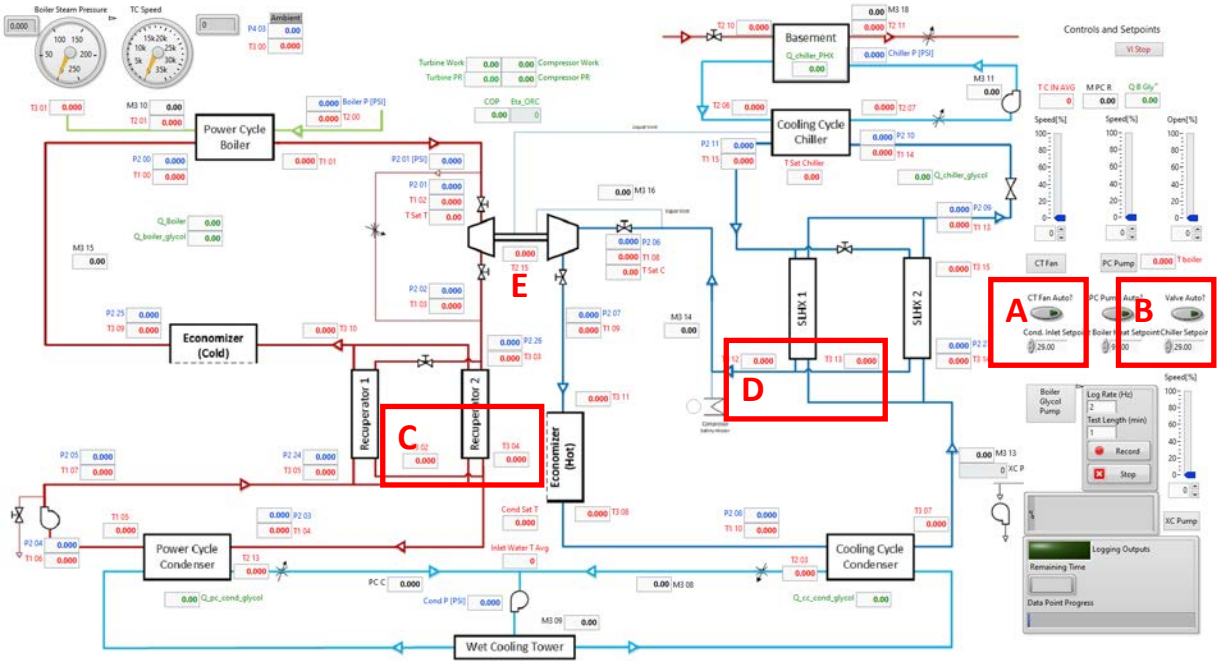

Figure C-3 Labeled virtual interface screenshot to discuss operational procedures

Once steady operation at the desired conditions is obtained and all flows have been balanced, the operators can take a data point. First, operators must note the exact time at which the data point was started so that the respective data can later be pulled from the master file for analysis. The operating

conditions must then be maintained for a specified time to ensure the data conforms to stability criteria. Stability can be monitored in the "PID Controls" tab of the virtual interface where generator glycol mixture inlet temperature, evaporator water outlet temperature, and average condenser glycol mixture inlet temperature are plotted in real time. Testing can continue in this manner until all conditions desired to be investigated were tested, operators must leave, or an emergency shutdown is required. In addition to monitoring the operating conditions and balancing flows, operators must also monitor additional items during experimentation to ensure the continued operation of the unit as well as its health. Turbo-compressor cavity temperature (Item E in Figure C-3) must be closely monitored to ensure coolant is being continuously delivered to the bearings. The cooling tower basin water level must also be monitored to ensure the continued operation of the condensers. The pressures within the external loops must be monitored to ensure over pressurization does not occur. Lastly, the steam generator makeup water tank should be monitored to ensure the generator does not run dry causing it to trip.

C.4. Shutdown

The standard shutdown procedure begins with the disconnect of the generator loop heat sources. Disconnect all breakers powering generator loop electric heaters and trip the burner switch on the steam generator. While one operator is decommissioning the generator loop heat sources, another can partially open Valve 2 to reduce the loading of the cooling cycle. Valve 30 should be modulated accordingly to ensure the evaporator loop does not heat unnecessarily. At this point, Valve 1 should be closed entirely to transfer the refrigerant charge in the evaporator to the condensers. This aids in draining operations or for a subsequent experimental effort. As soon as the refrigerant charge in the evaporator is below the bottommost portion of the sight glass indicator installed on the evaporator shell, close Valves 10, 4, and 9 in order in rapid succession. Never complete this process without ensuring flow can bypass the turbine through Valve 2. Failure to do so could result in an over pressurization event as the power cycle pump will deliver its shutoff head. With the turbo-compressor isolation valves closed, fully close Valves 19 and 20 as

turbo-compressor coolant is no longer needed. Failure to do so will result in refrigerant charge transfer to the evaporator which must later be transferred.

At this point, the valves associated with the heat line should be fully closed and the circulation pump for the evaporator loop can be disconnected. The cooling cycle is now decommissioned, and the power cycle is operating independently with flow bypassing the turbine. While the generator loop heat sources have been disconnected, there remains a significant amount of sensible thermal energy in the loop. The loop should be cooled to avoid risk to equipment. Thus, continue circulation of the power cycle with the cooling tower variable frequency drive set to 100% to reject energy. Either open Valve 2 or turn down the power cycle pump variable frequency drive as the system cools to avoid a pinch limitation in the generator. Once the generators are cooled such that they are safe to the touch, the power cycle pump variable frequency drive speed can be brought to zero. The cooling tower fan variable frequency drive can also be brought to zero and the cooling tower basin pump, condenser loop circulation pump, generator loop circulation pump, compressor inlet liquid trap systems, and cooling tower basin water makeup can be disconnected. At this point, the system is entirely at rest and data collection can be halted. Stop data collection through the stop button collocated with the test time and sample frequency inputs on the virtual interface. If data collection is halted through another method, the timestamp for each datapoint will not populate into the resulting data file. Equipment isolation valves can be shut throughout the system to reduce the risk of refrigerant loss and the generator loop can be vacuumed to finalize shutdown.

C.5. Emergency Shutdown

In some instances, an emergency shutdown may be required. The focus of an emergency shutdown is to bring the system to rest as quickly as possible with focus on variables which could harm personnel or equipment. Several examples of emergency scenarios include a frozen computer, loss of heat input at the generators or evaporator, or detection of a leak to list a few. The simplest emergency

shutdown entails one operator disconnecting all system electrical components at the switchgear feeding the facility, a second operator disconnecting all system electrical components for the cooling tower at the unit, and a third operator decommissioning the steam generator. This will bring all systems to an immediate rest except the heat line (which can be shut off by the first operator using Valve 3 at the test facility), the cooling tower basin makeup water system (which can be shut off by the second operator as the cooling tower electrical equipment is disconnected), and the generator loop circulation pump (which can be disconnected by the third operator at the unit).

While this procedure is the most rapid solution to an emergency, it is also the most dangerous to system components, specifically the turbo-compressor. The tripping of prototype electrical equipment will cause the power cycle pump to trip. The rapid change of the pump speed to zero will result in a rapid decrease in turbine load. A decrease in the turbine load while the compressor is still loaded will cause the compressor to surge, potentially causing damage. Thus, it is preferred to open Valve 2 and/or incrementally decrease the power cycle pump variable frequency drive speed prior to tripping the prototype electrical systems if possible. If the emergency is a refrigerant leak which cannot be isolated, operators should open Valve 26 and/or 27 to direct refrigerant away from personal.

Appendix D Test Facility Maintenance Procedures

This appendix presents maintenance procedures for the prototype organic Rankine vapor compression system. The most common procedures are filling and draining the prototype and supporting test loops during construction activities which are presented in Section D.1. Additional maintenance activities include altering calibration variables or virtual interface operations (D.2.) and preparing the system for cessation in experimentation or experimentation after a period of cessation (D.3.).

D.1. Fill and Drain Procedures

This section details considerations for draining and filling the prototype and its supporting systems. Before filling occurs, ensure the system or loop being filled is tight by pressurizing it with shop air. A system is considered leak free if the density within the loop under pressurization (and, thus, mass considering a fixed volume) remains constant over the course of 72 hours. Density is calculated using pressure and temperature instrumentation measurements recorded through the data acquisition system with the ideal gas equation. Simply, the ratio of absolute pressure to absolute temperature should not vary over the course of the leak down. Measurements should be taken at several locations (and averaged) at a time which the temperature throughout the investigated loop/system is homogeneous. If a leak is present, it must be located and sealed prior to filling. The detection of leaks can be complete with a soap/water solution or with a refrigerant detector. To detect a leak with soap/water, simply spray the solution over each connection. If bubbles form, the connection is leaking. For smaller leaks, the system/loop investigated can be charged with a trace amount of refrigerant while using the leak detector at each connection until the leak is found and sealed. Both a soap/water solution in a spray bottle and a refrigerant leak detector can be located within the storage cabinet collocated with the prototype.

D.1.1. Generator Loop

The generator loop is fitted with a number of drain/fill ports. The locations of these ports are at the base of the generator loop surge tank, the process connection between the surge tank and the generator loop, the glycol outlet port of the generators, the drain port of the lowest generator loop heater, the generator glycol inlet piping connection near the loop flow meter, the drain port on the circulation pump, and at the steam heat exchanger glycol outlet piping connection. Each port is terminated at a threaded ball valve with a garden hose fitting accessible to operators. To drain fluid from each location, attach a garden hose to the ball valve and route the hose into a storage drum as shown in Item A in Figure D-1. Once the hose is routed to the storage drum, open the drain valve to allow the fluid within the loop to exit the system. The loop can be open to the atmosphere during draining to allow air to displace the fluid leaving. The atmospheric vent to accomplish this is located on the generator loop surge tank above the test facility. If fluid does not flow freely from gravity, a liquid transfer pump can be used to aid in transferring fluid as shown in Item B in Figure D-1. Hoses and the transfer pump are generally stored on the evaporator loop skid. Drums for ethylene glycol-water mixture are located at the eastmost portion of the utility yard near the gate. If an ethylene glycol-water mixture must be stored for an extended period, it must be located within the building or on a containment pallet in the utility yard. If water is the only fluid within the generator loop, the liquid can be drained outside the building or into a floor drain using an extended hose. While this procedure will remove the majority of fluid from the loop, care must be taken while undoing piping couplings or removing instrumentation from ports as trace amounts of fluid can remain. To account for this, place a container under the fittings or couplers being removed following draining to catch any residual liquid. If water, this fluid can be discarded. If a glycol mixture, the fluid can be added to a storage barrel using a funnel which is generally located underneath the sinks at the northmost area of the same room the prototype is located.

To fill the generator loop, ensure all drain ports are closed and the atmospheric vent on the surge tank is open. If water is to be input to the loop, attach an extended hose from a water supply to a drain connection and fill the loop. Do not allow the liquid level within the loop to exceed the lowest sight indicator on the generator loop surge tank. This allows space for the fluid to expand as it is heated by the steam generator and/or electric heaters. Once the loop is filled, close the atmospheric vent and circulate the fluid within the loop with the generator loop circulation pump until the flow stabilizes. If the fluid level drops (as indicated by the lower sight glass on the generator loop surge tank), top off the loop until it is full once more. Repeat this process until the fluid level remains level with the sight indicator.

A similar procedure is used if an ethylene glycol-water mixture is to be added to the generator loop. To add such a mixture from a storage drum, attach a hose from a connection port to the drum transfer pump as shown in Item C in Figure D-1. The drum transfer pump simply inserts into a glycol drum and is generally located above the storage cabinet collocated with the prototype. The straw used to siphon fluid from the drum must be threaded into the base of the drum transfer pump and extended to reach the bottom of the drum. The straw is collocated with the drum transfer pump. If the drum transfer pump is not flowing properly, disengage the unit and clean the filter which is accessed by removing the strainer access cap on the side of the unit. If the concentration of the glycol solution was changed from a known value (whether through adding concentrate or water to an existing mixture), the new concentration can be determined using the concentration measurement tool within the cabinet collocated with the prototype. A change in concentration from 50% ethylene glycol-water will require representative changes to the virtual interface and data reduction model to ensure data fidelity.

To avoid risk to the generator loop pump, the disconnect powering the unit should be tripped while the loop is drained. This pump, and all other pumps within the system, should never be run dry unless done so for a fraction of a second to check the rotational direction of the device. Disconnecting the generator loop pump is especially relevant as it can be accidentally powered from the virtual interface

while other equipment requires manual actuation for power/deactivation. Also to be tripped during the draining of the generator loop is the generator loop electric circulation heaters. Maintenance should not be performed on the steam generator without consulting the control room personal as the equipment is shared amongst several users.

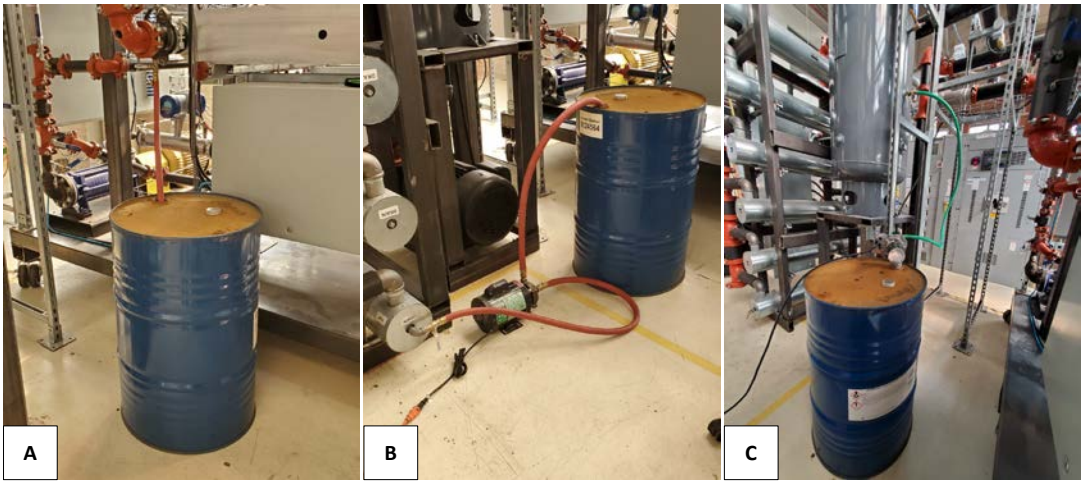

Figure D-1 Fill and drain configurations for prototype auxiliary loops

D.1.2. Condenser Loop

Fill and drain procedures for the condenser loop closely follow that of the generator loop. The drain locations for the condenser loop are at the loop pump drain connection, the side of the loop surge tank, the glycol inlet ports to the condensers, and at the pipe runs exiting/entering the building through the foundation. The atmospheric vent locations for the loop are at the discharge connection on the cooling tower and at the top of the condenser loop surge tank. These require the lift truck with a man basket and an extension ladder to access, respectively. Never open the vent atop the condenser loop surge tank unless the liquid level in the loop is below the vent. Failure to follow this guideline will result in a leak of the loop fluid onto adjacent equipment.

When filling the condenser loop, ensure there is space remaining in the surge tank similar to filling the generator loop. This allows the fluid to expand as it is heated in the condensers and prevents risk of

an over pressurization event. The condenser loop pump can be disconnected while its loop is drained through unplugging its power cord at the stand supporting the piping runs entering the basement at the northmost section of the test facility. Several maintenance tasks will also require the cooling tower to be drained. This can simply be accomplished through siphoning the water in the basin over the edge of the device or through opening the drain ports on the eastmost side of the device (one on the basin and one on the pump casing). Siphoning is preferred however considering the siphoned fluid will be directed into the storm drain instead of flooding the utility yard.

D.1.3. Evaporator Loop

Fill and drain procedures for the evaporator loop closely follow that of the generator and condenser loop. The drain locations for the evaporator loop are at the water inlet port to the evaporator, the loop pump inlet, the side of the loop surge tank, and the water inlet port to the basement heat exchanger. The atmospheric vent for the evaporator loop is located on its surge tank. The charge in this loop is monitored similarly to the generator loop where a sight glass is installed at the base of the surge tank. If maintenance is to be performed on the basement heat exchanger, the valves directly adjacent to the unit can be closed and the heat line can be drained from the drain port at the basement heat exchanger heat line outlet. This fluid must not be drained into the same containers used for ethylene glycol mixtures as it is a propylene glycol mixture. Failure to follow this will result in fluid contamination and heightened systematic uncertainty in the fluid properties if added back to the system. If the heat lines are required to be fully drained, the lines can be traced back to the REACH CoLab in the basement where an additional set of isolation and drain valves exist. If the heat lines are drained, they must be refilled from the mezzanine prior to opening the isolation valves in the basement or air will enter the building heating system which can damage its circulation pumps. The evaporator loop pump can be disconnected while its loop is drained through unplugging its power cord at the stand supporting the piping runs entering the basement at the northmost section of the test facility.

D.1.4. Prototype

Draining and filling the prototype with refrigerant is much more involved than the loops external to the system. To charge the prototype with refrigerant, it must first be ensured leak free. Then, the system must be evacuated using a vacuum pump. Removing the air and moisture from the system using these methods ensures the purity of the refrigerant during experimentation and the accuracy of thermophysical property calculations used in the data reduction model. To evacuate the prototype, all valves which are part of the organic Rankine and vapor compression cycles are to be open except valves relating to the blowdown subsystem (26 and 27). This closes the system from the atmosphere and ensures there are no pockets of air trapped within the prototype during evacuation. Regarding the fluid management subsystem, all valves are to be open during evacuation except Valves 41, 44, 45, 46, and 49. With the valves positioned for evacuation, the vacuum pump can be powered. Evacuation typically takes around 24 hours to complete. The vacuum pump oil level must be monitored during this time, and fluid must be added or removed as needed. If the vacuum pump becomes hot from operation, delay further evacuation until the unit has cooled. The system evacuation is complete when the analog vacuum gauge within the fill/drain station reads “29.92 “Hg”. If further confirmation of system evacuation is desired, a higher accuracy vacuum gauge may be placed in either the drain or fill port connection while the valve respective to the gauge is opened. Furthermore, the exhaust plug on the vacuum pump can be inserted on the unit. If the vacuum pump discharges this plug, it is still evacuating fluid. If the unit fails to discharge the plug, the system is evacuated and Valve 37, 40, 42, 43, 47, and 48 can be closed before disengaging the vacuum pump.

Once the prototype is fully evacuated, charging of refrigerant should immediately commence to reduce the risk of air leaking into the system. The valving configuration at the beginning of this process should be the same as the final evacuation configuration (all organic Rankine vapor compression system valves open except Valves 26, 27, 37, and 40 through 49). From here, a high pressure, flexible, stainless

braided, fill/drain hose (stored on the windowsill nearest the fill/drain station) can be inserted into the main system fill port. The other connection can be inserted into the discharge port of the refrigerant recovery device which is used in this instance to transfer refrigerant from pressurized refrigerant bottles to the system. An additional fill/drain hose can be inserted into the intake port of the refrigerant recovery device while its other connection can be inserted into the bottle disconnect valve. The bottle disconnect valve is then inserted into the main system drain port using a jumper. Both the jumper and bottle disconnect valve are located within the fill/drain station. The aforementioned components in their corresponding locations are shown in Figure D-2.

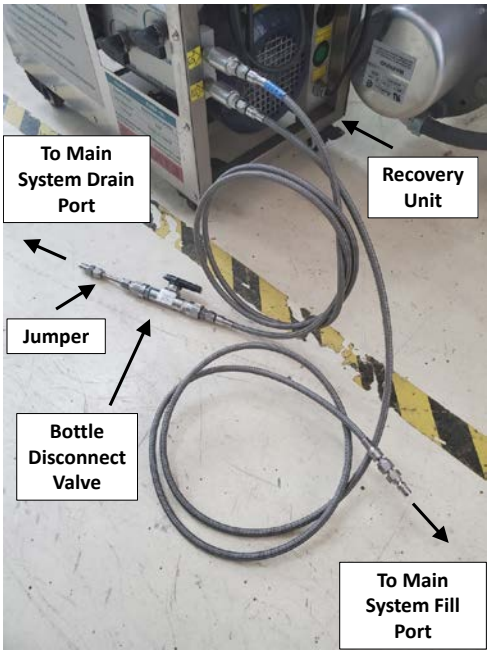

Figure D-2 Initial recovery unit configuration for refrigerant charging procedure

With the recovery unit configured as shown in Figure D-2, Valves 44, 45, 47, and the bottle disconnect valve can be opened after reengaging the vacuum pump to evacuate the fill lines with the recovery unit while it is operating. Once evacuated, close the bottle disconnect valve and Valves 45 and 47. Disconnect the vacuum pump and recovery unit and remove the jumper from both the bottle disconnect valve and the main system drain port and store for later use. At this point, a refrigerant bottle

can be prepared to add to the system. Place the bottle to be added to the system on a scale (stored atop the storage cabinet collocated with the prototype), remove the safety cap, and thread on the bottle connection with an appropriate pipe sealant (whether tape or puddy) as shown in Figure D-3. Each refrigerant bottle has two shutoff valves, a vapor valve on the top of the bottle and a liquid valve on the side. Crack the vapor shutoff valve on the prepared bottle to displace any air in the bottle connection with refrigerant and quickly attach the bottle disconnect valve to the bottle connection to avoid the discharge of refrigerant to the atmosphere. Close the vapor shutoff valve on the prepared bottle and record the mass readout of the scale. The bottle can then be added to the system by opening the liquid shutoff valve on the bottle and the bottle disconnect valve in addition to powering the vapor recovery unit and opening Valves 42 and 43. Close the liquid shutoff valve on the bottle and the bottle disconnect valve when the scale mass reading ceases to decrease further. At this point, the prepared refrigerant bottle is empty. Record the mass at this point to determine the amount of refrigerant added to the system.

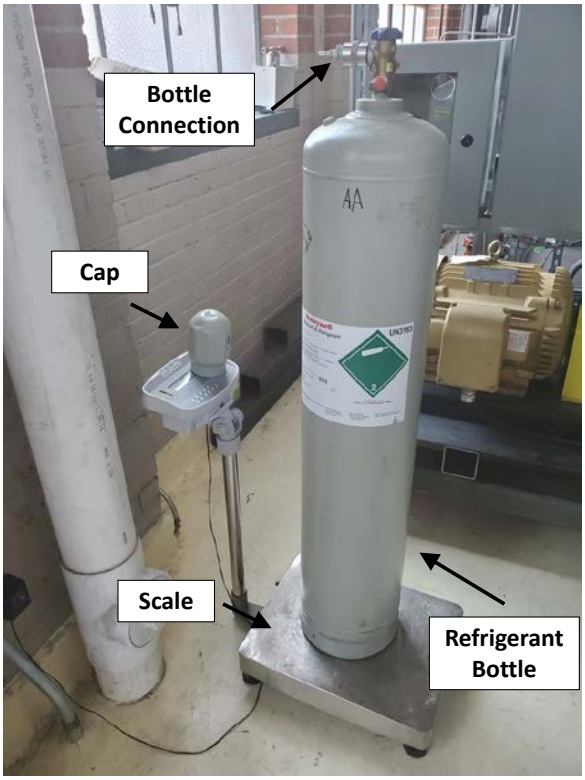

Figure D-3 Bottle preparation for draining/filling the prototype

To add another bottle, disconnect the bottle disconnect valve from the bottle connection. Wear insulated protective gloves while doing so to prevent injury from the discharge of any residual refrigerant. Store the empty refrigerant bottle and place another bottle to be added to the system on the scale. Repeat the aforementioned process until the desired system charge has been input to the system. Once the desired system charge is reached, disconnect the bottle disconnect valve from the bottle connection as previously mentioned and close Valves 42 and 43. Open Valve 46 to drain the charge from the filling lines while the recovery unit is running. Once the pressure is released, disengage the recovery unit, remove the fill/drain hose from the main system fill port, close Valves 44 and 46, open Valve 47, and engage the vacuum pump to evacuate the fill station lines. Once evacuated, close Valve 47 and disconnect the vacuum pump. At this point, the system is completely charged and free of air. Valve 37, 42, or 43 can be cracked at this point to displace the vacuum in the fill station tubing with refrigerant if desired. It is recommended to plug the main system fill and drain ports while the system is charged to reduce the risk of refrigerant release if Valve 44 or 45 is opened accidentally.

Draining the prototype of refrigerant is even more involved than filling it. First, Valves 37, 42, 43, 44, 45, 46, and 47 should be closed. Then, an empty refrigerant bottle must be prepared to be filled as shown previously in Figure D-3. Then, a fill/drain hose can be inserted into the main system fill port on one side, and the bottle disconnect valve on the other. The bottle disconnect valve can be open and attached to the prepared empty refrigerant bottle for evacuation (liquid and vapor shutoff valves closed). Opening Valves 44 and 47 while engaging the vacuum pump will evacuate the fill/drain station and the fill/drain hose leading to the empty prepared bottle. Once evacuated, close Valve 47 and disconnect the vacuum pump. Note the mass measured by the scale. At this point, refrigerant can be removed from the system using the fluid management pump. To accomplish this, ensure Valves 36, 38, 42, and 43 are closed while opening the refrigerant bottle liquid shutoff valve and Valves 34, 35, 37, and 39. Powering the fluid management pump will direct the fluid from the cooling cycle condenser refrigerant outlet, the suction

line heat exchanger liquid outlet, and power cycle pump outlet connections into the prepared bottle. Never fill the prepared bottle beyond the charge which it arrived from the manufacture. Never fill the prepared bottle when the refrigerant is at a temperature greater than the ambient. Doing either could result in an explosion due to an over pressurization of the bottle. A strategy to mitigate this risk is to open Valve 38 during draining such that excess refrigerant will be recirculated to the cooling cycle condenser if the prepared bottle is filled. Once a prepared bottle is filled, close the bottle liquid shutoff valve and the bottle disconnect valve while simultaneously disengaging the fluid management pump. Note the mass to determine how much refrigerant was removed and prepare another bottle to be filled. Repeat the draining process until the fluid management pump fails to increase the scale reading. At this point, there is insufficient fluid at the fluid management pump inlet to continue draining with this method. To maximize the amount of refrigerant recovered with the fluid management pump (and minimize the time and effort required to drain the system) it is recommended that refrigerant charge be stored in the cooling cycle condenser prior to this draining process.

To remove the refrigerant remaining in the system after the fluid management pump becomes starved, the refrigerant recovery unit must be utilized. Prior to assembling the recovery unit for use, the fill/drain hose must be purged of refrigerant and disconnected from the main system fill port. To do this, it is recommended the bottle disconnect valve be coupled to a refrigerant bottle with refrigerant within it. With the bottle disconnect valve, Valve 44 and either Valve 42 or 43 open, crack the refrigerant bottle vapor shutoff valve to displace the liquid in the line with vapor. This reduces refrigerant losses during the disconnect of the fill/drain hose. Close the vapor shutoff valve on the bottle and the bottle disconnect valve in addition to Valves 42, 37, and 43 if open. Then, open Valve 46 to purge the fill/drain hose and the fill/drain station. The fill/drain hose can now be safely removed, and the recovery unit can be prepared to fully evacuate the system of refrigerant.

To prepare the refrigerant recovery unit to evacuate the system of refrigerant, a fill/drain hose must be inserted into the main system drain port. The opposite connection of this fill/drain hose must be inserted into the intake port of the refrigerant recovery device. At the discharge port of the recovery device, another fill/drain hose must be inserted and routed to the makeshift condensing unit (stored atop the storage cabinet collocated with the prototype). The discharge port of the makeshift condensing unit is then routed to the inlet port of a small gear pump (stored on the windowsill nearest the fill/drain station) using another fill/drain hose. A final fill/drain hose is inserted at the gear pump outlet port and terminates at the bottle disconnect valve. The bottle disconnect valve is inserted into the jumper which is inserted into the main system fill port. The aforementioned components in their corresponding locations are shown in Figure D-4. There is no specified inlet or outlet connection for the makeshift condensing unit.

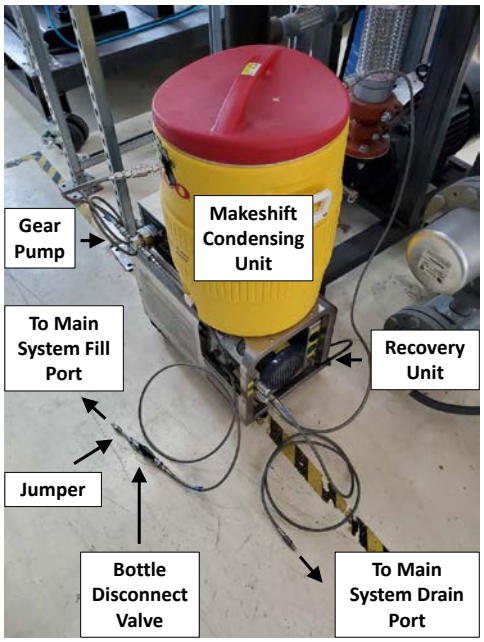

Figure D-4 Initial recovery unit configuration for refrigerant vapor draining procedure

With the recovery unit configured as shown in Figure D-4, Valves 44, 45, 47, and the bottle disconnect valve can be opened after reengaging the vacuum pump to evacuate the drain lines. Once evacuated, close the bottle disconnect valve and Valves 44 and 47. Disconnect the vacuum pump and

remove the jumper from both the bottle disconnect valve and the main system fill port and store for later use. At this point, the bottle disconnect valve can be attached to a prepared refrigerant bottle to further drain the system. However, before the system can be drained (through engaging the recovery unit and opening the bottle disconnect valve and Valve 37, 42, and/or 43), the makeshift condensing unit must be prepared. This unit simply consists of a tube bundle within an insulated vessel which condenses and sub cools the vapor recovered by the recovery unit after it has been pressurized. Without it, the refrigerant bottle would quickly overheat and over pressurize risking an explosion. The temperature of a recovery bottle should never feel hot to the touch. If a bottle overheats, immediately cease draining and allow the bottle temperature to normalize. To prevent this risk, fill the condensing unit with an ice and water mixture. As the ice melts, add additional ice and drain the water off it displaces. Ice can be taken from the breakroom ice maker. Repeat this process until the system is fully drained of refrigerant as indicated by a stagnant mass reading on the refrigerant bottle scale.

D.2. Calibration Variable and Virtual Interface Alteration Procedures

Another common maintenance procedure is to alter the design of the virtual interface (D.2.1.) or calibration variables for instrumentation (D.2.2.). The virtual interface is continuously modified following experimental investigation to improve the operability of the prototype and methods of data collection/analysis. Calibration variables require alteration if a new instrument is installed to assess the implications of new construction or if there was a modification to an existing instrument that warranted it to be recalibrated (i.e. broken wiring, damaged resistor for current signals, and changes in flow area for volumetric meters to list several examples).

D.2.1. Virtual Interface Alteration

The virtual interface is accessed on the computer adjacent to the prototype by following file path "C:\Program Files (x86)\National Instruments\LabVIEW 2018\LabVIEW.exe". Once the program is started,

the project relating to the prototype is accessed through opening file “TCCS-2.lvproj”. With the project file open, the virtual interface for this investigation “TCCS-2 Main R5” can be opened and modified. Prior to modification, save the file with a new name (i.e. TCCS-2 Main R6) using “substitute copy for original”. This will ensure the original file is unaltered and can be used for experimentation if the modifications to the new file result in errors which cannot be resolved. The new copy with a new file name can then be altered as desired. Common alterations included adding/removing displays for measurements and readouts for data analysis. If a new variable is to be recorded during experimentation, the data reduction model must be updated to accommodate the new variable which will be populated at the end of a data file next to the time stamp. Alternatively, if a variable is no longer relevant, the data file must also be updated to remove any analysis relating to the variable. Avoid the use of local variables in all instances as their values may not correlate to their source. Consult control room personal if challenges occur as modifications to the virtual interface are attempted. Never remove safety provisions which aid in the prevention of an over pressurization of the prototype during experimentation.

D.2.2. Calibration Variable Alteration

If a new instrument is installed, or the calibration of an existing instrument is modified, the new calibration variables (gain and offset) must be input into the data acquisition system to ensure data fidelity. Calibration variables, their respective bias errors, and the range over which the biases hold true must be documented in file path “T:\Projects\TCCS\DOE EERE TCCS\Instrumentation” under the respective data acquisition channel. The bias error for the measurement using the appropriate units must also be input to the data reduction model such that the appropriate total measurement uncertainty is determined, and the variable name must be updated to represent the measurement for clarity including the units of the variable. Variable names can also be altered in the virtual interface such that raw data files display what values relate to a measurement in addition to what the units of the measurement are.

To update the calibration factors for the instruments that collect data in the test facility, first log in to Internet Explorer and type in “129.82.106.71” to the address bar. The National Instruments data acquisition system page should appear. Then, login at the top right of the page with the appropriate credentials. After logging in, click on the file explorer and magnifying glass icon on the left panel (i.e. Remote File Browser). From here, expand the folder tree and open the **“C”** folder. The pressure and thermocouple calibration factor text files should be here. You can now upload new calibration factor text files to this location by clicking the left most button in the top panel. It is very important that the new calibration files have the exact same format as the originals. To ensure this, download the original files and open them in Microsoft Excel. Once open in Microsoft Excel, you can edit the calibration factors for each channel and then save the new document as a text file.

D.3. Recommissioning and Decommissioning Procedures

In addition to draining and filling, there are a number of additional procedures which must be complete during the decommissioning or recommissioning of the prototype prior to or following a cessation in experimentation. To prepare the facility for an extended period of cessation in experimentation, the main system must be drained of refrigerant following the processes outlined in D.1.4. This reduces the risk to the refrigerant which could leak through undetectable orifices in the piping network or through the blowdown system if it is tampered with. Fluid does not need to be drained from the auxiliary loops unless maintenance tasks require so. However, a slight vacuum should be pulled on the generator loop to prevent the potential leak of glycol from the generator hose connections. It was found these connections provide a tight seal while the generator loop fluid is heated, but, at ambient temperatures, will weep fluid. This is accomplished by removing the vacuum pump from the fluid management subsystem and attaching it to the ventilation port at the generator loop surge tank with a flexible hose. The disconnect for the generator loop circulation pump must be tripped while the loop is under vacuum as accidental powering of the unit under this condition will cause it to cavitate. In fact, all

equipment should be disconnected during decommissioning. This includes the external loop circulation pumps, the power cycle and fluid management pump, the generator loop circulation heaters, the liquid trap heater, and the cooling tower systems.

The cooling tower basin should always be drained during a decommission. Stagnant water creates a risk to human health and could freeze in winter months, which would ruin the basin if the basin heater failed to operate. Enclosures should be locked, and equipment should be properly stored. The heat line shutoffs in the REACH CoLab basement facilities can be utilized to prevent tampering with the heat line control valves which could cause hot fluid to be needlessly circulated through the building heating system. Valve 28 should be closed such that steam is not accidently fed to the steam heat exchanger by another lab group which could boil the generator loop fluid and cause an over pressurization of the loop.

In addition, a number of maintenance procedures can be complete during decommissioning or recommissioning. This includes replacing the filters within the system. Micron filters and filter dryers are located on the windowsill near the fill/drain station. Once the new filters are installed, they must be leak checked. All pumps should be greased with the grease gun located underneath the main workbench in the room the prototype is located within. If the grease gun is empty or cannot be located, consult control room personnel. The cooling tower systems should be inspected including the spray nozzles, basin heater, basin heater level probe, and the tower tube bundle. Spray nozzles and the tube bundle require the lift truck with a man basket to inspect. If nozzles are damaged or missing, they must be replaced to ensure the performance of the cooling tower. If the tubes are fouled, the cooling tower can be flushed with a cleaner, rinsed, and drained to improve their performance. The basin heater should be cleaned to prevent it from overheating. The probe controlling the heater should also be cleaned. Failure to do so could result in its malfunction which, during winter months, could result in freezing of the tower basin. The readout of instrumentation should also be checked before recommissioning the system. Within error, all temperature and pressure measurements should be identical when the system is drained and opened to

the atmosphere. If an instrument reads an illogical value, check the wiring to/from the component and (if equipped) the resistance of the resistor used to convert amperage signals to current signals. If these items are normal, replace the instrument with a new component and recalibrate if required. The functionality of Valves 24 and 25 should also be verified before recommissioning to ensure refrigerant is not lost unnecessarily. Finally, the external loop sides of the generators, condensers, and evaporator can be flushed with a cleaner to ensure their performance. This requires draining each loop.

Appendix E Instrumentation Calibration Methods

Instrumentation to monitor system performance was selected considering the operating conditions of the experimental facility, the capabilities of the selected data acquisition hardware, and the recommendations/requirements of the referenced commercial chiller performance rating standards. The instrumentation criteria from the performance rating standards used to guide experimentation are summarized in Table E-1.

Table E-1 Instrumentation bias and resolution requirements (Adapted from [45,190])

Measurement	***Minimum Bias Requirements***	***Minimum Resolution Requirements***
Temperature	±0.11 °C	0.005 °C
Flow Rate	±1.0% Reading	4 Significant Figures
Differential Pressure	±1.0% Reading	3 Significant Figures
Atmospheric Pressure	±1.0 kPa	0.1 kPa
Electric Power	±2.0% Reading	4 Significant Figures

It is noted that the instrumentation criteria from the performance rating standards only apply to external stream measurement devices. This is because external stream temperature, pressure, and flow measurements are the only values required to rate the performance of a commercial chiller. For this research effort, the instrument criteria were met for all devices installed in the generator, condenser, and evaporator loops. An attempt was also made to extend instrumentation criteria to measurement devices within the experimental prototype to accurately quantify performance characteristics beyond evaporator heat duty, thermal/electrical equivalent COP, and heat exchanger pressure loss.

The factory bias error of the prototype absolute pressure transducer (±0.5 kPa) surpassed the cutoff criteria from the commercial rating standards without calibration. Gauge pressure transmitters are not required for commercial chiller performance rating as the calculations are irrespective of pressure. Therefore, no accuracy criteria were explicitly specified for the prototype pressure transmitters, and a

criteria of Grade 3A (accuracy of ±0.25% of the span) was set. To achieve Grade 3A accuracy, the prototype system pressure transmitters were calibrated with an Ametek Type T deadweight tester with a bias of ±0.1% of the span. Figure E-1 shows the setup of the deadweight tester during calibration.

Figure E-1 Calibration of pressure transmitters using a deadweight tester

To calibrate the pressure transmitters, a known mass is added to a 10:1 piston to generate a known hydrostatic pressure on each device. The known pressure was documented along with the voltage signal each device produced at each interval as measured at the data acquisition system. This data was then used to determine calibration factors and bias errors for each transmitter. Calibration factors (slope and intercept) are determined using linear regression assuming a linear relationship between the pressure applied to the transmitter (independent variable) and the voltage reading taken at the data acquisition system (dependent variable). The resulting slope ($\hat{\beta}_1$) and intercept ($\hat{\beta}_0$) from the regression is then used to better estimate, or correct, the reading from the transmitter. The least squares estimate was utilized to perform linear regression [189]. The least squares estimate relationships are outlined in Equation (E.1) to Equation (E.3) where *y* represents the pressure produced by the calibration standard, *x* represents the transmitter reading, *N* represents the number of data points collected, and *z* represents the corrected transmitter reading using the transmitter reading and calibration factors.

$$\hat{\beta}_0 = \overline{y} - \hat{\beta}_1 \cdot \overline{x} \tag{E.1}$$

$$\hat{\beta}_1 = \frac{N \cdot \sum_{i=1}^{n}(x_i \cdot y_i) - \sum_{i=1}^{n}(x_i) \cdot \sum_{i=1}^{n}(y_i)}{N \cdot \sum_{i=1}^{n}(x_i^2) - \left(\sum_{i=1}^{n}(x_i)\right)^2} \tag{E.2}$$

$$z_i = \hat{\beta}_1 x_i + \hat{\beta}_0 \tag{E.3}$$

Once the calibration factors for an instrument are determined, the device bias error can be found. The standard error of estimate methodology was followed to determine the accuracies of the transmitters over their entire operating ranges [198]. The first step in calculating a calibrated instrument bias is to determine the standard error of estimate (*SEE*) using Equation (E.4).

$$SEE = \sqrt{\frac{\sum_{i=1}^{n}\left(y_i - z_i\right)^2}{N-2}} \tag{E.4}$$

This value is used in conjuncture with the total bias of the calibration standard ($E_{B,cs}$) and the Student T coverage factor for a 95% confidence two-tailed distribution (k) in Equation (E.5) to determine the new bias of the transmitter.

$$E_B = \sqrt{E_{B,cs}^2 + (k \cdot SEE)^2} \tag{E.5}$$

As the readings of the gauge transmitters are scaled by the reading of the absolute transmitter, the bias of the absolute transmitter must also be accounted for in the measurement. Equation (E.6) shows how the error of the combined reading is adjusted using the bias of both instruments.

$$E_{B,adj} = \sqrt{E_B^2 + E_{B,abs}^2} \tag{E.6}$$

Table E-2 shows the data set, calibration factors, and bias error for the compressor inlet pressure transmitter. The calculation presented in this table was done by hand to calibrate a model which calculated these factors for the remaining calibrated instruments.

Table E-2 Hand calculation for bias error and calibration variables

Data Point	*y* *[kPa]*	*x* *[VDC]*	x^2 *[VDC²]*	*xy* *[kPa-VDC]*	*z* *[kPa]*	$(y-z)^2$ *[kPa²]*
1	34.47	1.185	1.404	40.85	33.94	0.288
2	68.95	1.390	1.932	95.84	69.44	0.242
3	103.4	1.588	2.522	164.2	103.7	0.094
4	137.9	1.786	3.190	246.3	138.0	0.015
5	172.4	1.984	3.936	342.0	172.3	0.004
6	206.8	2.183	4.765	451.5	206.8	0.005
7	241.3	2.387	5.698	576.0	242.1	0.613
8	275.8	2.582	6.667	712.1	275.9	0.006
9	310.3	2.780	7.728	862.5	310.2	0.011
10	344.7	2.978	8.868	1027	344.4	0.083
11	379.2	3.178	10.10	1205	379.1	0.016
12	413.7	3.375	11.39	1396	413.2	0.234
13	448.2	3.576	12.79	1603	448.0	0.022
14	482.6	3.773	14.24	1821	482.1	0.256
15	517.1	3.976	15.81	2056	517.3	0.031
16	551.6	4.177	17.45	2304	552.1	0.261
17	586.1	4.363	19.04	2557	584.3	3.066
18	620.5	4.572	20.90	2837	620.5	0.001
19	655.0	4.775	22.80	3128	655.7	0.424
20	689.5	4.976	24.76	3431	690.5	0.974
Sum	7239	61.58	216.0	26855	7239	6.648
Average	362.0	3.079	10.80	1343	362.0	0.332

$\hat{\beta}_1$ *[kPa VDC^{-1}]*	$\hat{\beta}_0$ *[kPa]*	*k* *[-]*	*SEE* *[kPa]*	$E_{B,cs}$ *[kPa]*	E_B *[kPa]*	$E_{B,adj}$ *[kPa]*
173.180	-171.281	2.093	0.6077	1.379	1.876	2.126

Thermocouples also required calibration to meet test criteria. The calibration standard for the thermocouples was a 5615 Hart Scientific platinum resistance thermometer with an accuracy of ± 0.013°C. A Fluke 1502A thermometer readout was used to display and record the platinum resistance thermometer

temperature. Thermocouples were calibrated in an insulated beaker filled with water or mineral oil on a magnetically stirred hot plate. Each thermocouple was calibrated over its entire operating range to achieve sufficient accuracy while the beaker was stirred to maintain thermal homogeneity during calibration. The thermocouple calibration setup is shown in Figure E-2.

Figure E-2 Calibration of thermocouples using a platinum resistance thermometer

Differential pressure transmitters were factory calibrated. The differentials with a range of 186.6 kPa were accurate to 1.0% of the reading down to 60.65 kPa, while units with a range of 37.33 kPa were accurate to 1.0% of the reading down to 12.13 kPa. Flow meters and power meters were factory calibrated and met instrumentation criteria over the range of conditions presented in Table 4-3.

Appendix F Sample Calculations for Data Reduction

This appendix presents sample calculations used to validate the data reduction model discussed in Chapter 4 and investigated in Chapter 5 to assess experimental data collected during the operation of the manufactured prototype system. All hand calculations were performed assuming the measurement values in Table F-1 for consistency unless otherwise noted. These values are representative of the datapoint presented in Section 5.1. for the baseline, full-load performance of the prototype. Cooling cycle state point 15 was determined assuming a vapor mass quality of unity. The temperature at the outlet of the evaporator was artificially inflated 2°C to allow performance calculations.

Table F-1 Averaged state point values at baseline testing conditions for hand calculations

	Power Cycle			***Mass Flow [kg s^{-1}]***	***3.145***
State Point	***Temperature [°C]***	***Pressure [kPa]***	***Differential Pressure [kPa]***	***Enthalpy [kJ kg^{-1}]***	***Entropy [kJ kg^{-1} K^{-1}]***
1	90.22	2,241	-	437.9	1.706
2	50.45	743.3		422.0	1.721
3	50.49	743.0	11.745	422.1	1.721
4	39.28	731.3		410.5	1.686
5	39.08	731.4		410.3	1.685
6	37.97	725.2	18.697	409.2	1.682
7	37.66	718.9		252.3	1.178
8	35.26	712.7		248.8	1.167
9	35.36	724.6	-	249.0	1.167
10	38.34	2,459		253.3	1.176
11	38.42	2,364	8.685	253.4	1.177
12	46.15	2,355		264.6	1.212
13	46.15	2,302	7.775	264.6	1.212
14	56.09	2,294		279.3	1.258
15	56.06	2,299		279.3	1.258
16	86.17	2,287	36.502	329.2	1.403
17	85.92	2,275		429.8	1.683
18	90.83	2,263		438.3	1.706

Cooling Cycle				*Mass Flow [kg s^{-1}]*	-
State Point	***Temperature [°C]***	***Pressure [kPa]***	***Differential Pressure [kPa]***	***Enthalpy [kJ kg^{-1}]***	***Entropy [kJ kg^{-1} K^{-1}]***
1	35.69	244.6	-	416.5	1.777
2	73.29	759.5		445.6	1.790
3	73.20	759.5	13.738	445.5	1.790
4	47.40	745.8		418.8	1.711
5	47.26	722.8		419.1	1.714
6	37.56	717.0	17.416	409.0	1.682
7	37.27	711.2		251.7	1.176
8	36.84	705.4		251.1	1.174
9	36.62	708.0	6.181	250.8	1.173
10	24.14	701.8		233.1	1.115
11	24.14	710.7		233.1	1.115
12	21.74	463.9		233.1	1.115
13	6.031	269.0	-	233.1	1.119
14	6.031	269.0		388.5	1.676
15	7.722	269.0		390.1	1.682
16	5.722	269.0	18.704	388.5	1.676
17	35.85	250.3		416.5	1.776

External Streams	***Inlet Temperature***	***Outlet Temperature***	***Inlet Pressure [kPa]***	***Differential Pressure [kPa]***	***Volumetric Flow [m^3 hr^{-1}]***
Generator	91.18°C	86.24°C	350.843	33.126	94.33
Power Cycle Condenser	29.91°C	36.58°C	320.853	62.054	-
Cooling Cycle Condenser	30.05°C	36.82°C	317.866	62.547	43.65
Evaporator	12.12°C	6.996°C	526.412	34.635	44.20
Condenser Loop Pump	36.63°C	-	249.263	-	109.77

Table F-2 presents the hand calculations to validate the data reduction model. The calculations include the determination of cooling cycle refrigerant and power cycle condenser glycol mass flow, component and system wide performance characteristics, turbo-compressor mapping variables, and adjusted temperatures for heat exchanger fouling experimentation.

Table F-2 Hand calculations verifying accuracy of data reduction model

Calculation	*Formulation*	*Hand Calculation*	*Model Result*	*Hand Value*	*Units*
Economizer Liquid Heat Transfer	$\dot{Q}_{\text{econ}} = \dot{m}_{\text{pc}} \, (\text{h}_{\text{pc,14}} - \text{h}_{\text{pc,13}})$	$\dot{Q}_{\text{econ}} = 3.145 \, (279.3 - 264.6)$	46.38	46.23	kW
Cooling Cycle Refrigerant Mass Flow	$\dot{Q}_{\text{econ}} = \dot{m}_{\text{cc}} \, (\text{h}_{\text{cc,3}} - \text{h}_{\text{cc,4}})$	$46.36 = \dot{m}_{\text{cc}} \, (445.5 - 418.8)$	1.737	1.736	kg s^{-1}
Evaporator Loop Mass Flow	$\dot{m}_{\text{evap,w}} = \frac{\dot{V}_{\text{evap,w}}}{3600} \, \rho_{\text{evap,w,in}}$	$\dot{m}_{\text{evap,w}} = \frac{44.20}{3600} \, 999.69$	12.27	12.27	kg s^{-1}
Generator Ethylene Glycol-Water Inlet Density	$\rho_{\text{gen,eg,in}} = (-0.00151876 \, T_{\text{gen,eg,in}}^2 - 0.490119 \, T_{\text{gen,eg,in}} + 1096.64)$	$\rho_{\text{gen,eg,in}} = (-0.00151876 \, 91.18^2 - 0.490119 \, 91.18 + 1096.64)$	1039.33	1039.32	kg m^{3}
Generator Loop Mass Flow	$\dot{m}_{\text{gen,eg}} = \frac{\dot{V}_{\text{gen,eg}}}{3600} \, \rho_{\text{gen,eg,in}}$	$\dot{m}_{\text{gen,eg}} = \frac{94.33}{3600} 1039.33$	27.23	27.23	kg s^{-1}
Vapor Compression Condenser Ethylene Glycol-Water Outlet Density	$\rho_{\text{ccond,eg,out}} = (-0.00151876 \, T_{\text{ccond,eg,out}}^2 - 0.490119 \, T_{\text{ccond,eg,out}} + 1096.64)$	$\rho_{\text{ccond,eg,out}} = (-0.00151876 \, 36.82^2 - 0.490119 \, 36.82 + 1096.64)$	1076.53	1076.53	kg m^{3}
Vapor Compression Condenser Ethylene Glycol-Water Mass Flow	$\dot{m}_{\text{ccond,eg}} = \frac{\dot{V}_{\text{ccond,eg}}}{3600} \, \rho_{\text{ccond,eg,out}}$	$\dot{m}_{\text{ccond,eg}} = \frac{43.65}{3600} 1076.53$	13.05	13.05	kg s^{-1}
Condenser Loop Pump Inlet Density	$\rho_{\text{condp,eg,in}} = (-0.00151876 \, T_{\text{condp,eg,in}}^2 - 0.490119 \, T_{\text{condp,eg,in}} + 1096.64)$	$\rho_{\text{condp,eg,in}} = (-0.00151876 \, 36.63^2 - 0.490119 \, 36.63 + 1096.64)$	1076.65	1076.65	kg m^{3}
Condenser Loop Mass Flow	$\dot{m}_{\text{condp,eg}} = \frac{\dot{V}_{\text{condp,eg}}}{3600} \, \rho_{\text{condp,eg,in}}$	$\dot{m}_{\text{condp,eg}} = \frac{109.77}{3600} 1076.65$	32.83	32.83	kg s^{-1}
Organic Rankine Condenser Ethylene Glycol-Water Mass Flow	$\dot{m}_{\text{pcond,eg}} = \dot{m}_{\text{condp,eg}} - \dot{m}_{\text{ccond,eg}}$	$\dot{m}_{\text{pcond,eg}} = 32.83 - 13.05$	19.78	19.78	kg s^{-1}
Evaporator Heat Transfer	$\dot{Q}_{\text{evap},w} = \dot{m}_{\text{evap,w}} \, Cp_{\text{evap,w,avg}} \, (T_{\text{evap,w},\,in} - T_{\text{evap,w,out}})$	$\dot{Q}_{\text{evap},w} = 12.27 \, 4.194 \, (12.12 - 6.996)$	263.8	263.7	kW

Calculation	*Formulation*	*Hand Calculation*	*Model Result*	*Hand Value*	*Units*
	$\dot{Q}_{\mathrm{evap,r}} = \dot{m}_{\mathrm{cc}}\ (\mathrm{h}_{\mathrm{cc},15} - \mathrm{h}_{\mathrm{cc},13})$	$\dot{Q}_{\mathrm{evap,r}} = 1.737\ (388.5 - 233.1)$	270.0	269.9	
Vapor Compression Condenser Ethylene Glycol-Water Average Specific Heat Capacity	$Cp_{\mathrm{ccond,eg,avg}} = -3.428\ 10^{-8}\left(\frac{T_{\mathrm{ccond,eg,in}} + T_{\mathrm{ccond,eg,out}}}{2}\right)^2 + 0.003957\left(\frac{T_{\mathrm{ccond,eg,in}} + T_{\mathrm{ccond,eg,out}}}{2}\right) + 3.170$	$Cp_{\mathrm{ccond,eg,avg}} = -3.428\ 10^{-8}\left(\frac{30.05 + 36.82}{2}\right)^2 + 0.003957\left(\frac{30.05 + 36.82}{2}\right) + 3.170$	3.302	3.302	kJ kg^{-1} K^{-1}
Vapor Compression Condenser Heat Duty	$\dot{Q}_{\mathrm{ccond,eg}} = \dot{m}_{\mathrm{ccond,eg}}\ Cp_{\mathrm{ccond,eg,avg}}\ (T_{\mathrm{ccond,eg,out}} - T_{\mathrm{ccond,eg,in}})$	$\dot{Q}_{\mathrm{ccond,eg}} = 13.05\ 3.302\ (36.82 - 30.05)$	291.8	291.7	kW
	$\dot{Q}_{\mathrm{ccond,r}} = \dot{m}_{\mathrm{cc}}\ (\mathrm{h}_{\mathrm{cc},5} - \mathrm{h}_{\mathrm{cc},8})$	$\dot{Q}_{\mathrm{ccond,r}} = 1.737\ (419.1 - 251.1)$	291.7	291.8	
Organic Rankine Condenser Ethylene Glycol-Water Average Specific Heat Capacity	$Cp_{\mathrm{pcond,eg,avg}} = -3.428\ 10^{-8}\left(\frac{T_{\mathrm{pcond,eg,in}} + T_{\mathrm{pcond,eg,out}}}{2}\right)^2 + 0.003957\left(\frac{T_{\mathrm{pcond,eg,in}} + T_{\mathrm{pcond,eg,out}}}{2}\right) + 3.170$	$Cp_{\mathrm{pcond,eg,avg}} = -3.428\ 10^{-8}\left(\frac{29.91 + 36.58}{2}\right)^2 + 0.003957\left(\frac{29.91 + 36.58}{2}\right) + 3.170$	3.302	3.302	kJ kg^{-1} K^{-1}
Organic Rankine Condenser Heat Duty	$\dot{Q}_{\mathrm{pcond,eg}} = \dot{m}_{\mathrm{pcond,eg}}\ Cp_{\mathrm{pcond,eg,avg}}\ (T_{\mathrm{pcond,eg,out}} - T_{\mathrm{pcond,eg,in}})$	$\dot{Q}_{\mathrm{pcond,eg}} = 19.78\ 3.302\ (36.58 - 29.91)$	435.7	435.6	kW
	$\dot{Q}_{\mathrm{pcond,r}} = \dot{m}_{\mathrm{pc}}\ (\mathrm{h}_{\mathrm{pc},5} - \mathrm{h}_{\mathrm{pc},8})$	$\dot{Q}_{\mathrm{pcond,r}} = 3.145\ (410.3 - 248.8)$	507.6	507.9	
Generator Ethylene Glycol-Water Average Specific Heat Capacity	$Cp_{\mathrm{gen,eg,avg}} = -3.428\ 10^{-8}\left(\frac{T_{\mathrm{gen,eg,in}} + T_{\mathrm{gen,eg,out}}}{2}\right)^2 + 0.003957\left(\frac{T_{\mathrm{gen,eg,in}} + T_{\mathrm{gen,eg,out}}}{2}\right) + 3.170$	$Cp_{\mathrm{gen,eg,avg}} = -3.428\ 10^{-8}\left(\frac{91.18 + 86.24}{2}\right)^2 + 0.003957\left(\frac{91.18 + 86.24}{2}\right) + 3.170$	3.521	3.521	kJ kg^{-1} K^{-1}
Generator Heat Duty	$\dot{Q}_{\mathrm{gen,eg}} = \dot{m}_{\mathrm{gen,eg}}\ Cp_{\mathrm{gen,eg,avg}}\ (T_{\mathrm{gen,eg,in}} - T_{\mathrm{gen,eg,out}})$	$\dot{Q}_{\mathrm{gen,eg}} = 27.23\ 3.521\ (91.18 - 86.24)$	473.0	473.6	kW
	$\dot{Q}_{\mathrm{gen,r}} = \dot{m}_{\mathrm{pc}}\ (\mathrm{h}_{\mathrm{pc},18} - \mathrm{h}_{\mathrm{pc},15})$	$\dot{Q}_{\mathrm{gen,r}} = 3.145\ (438.3 - 279.3)$	500.1	500.1	

Calculation	*Formulation*	*Hand Calculation*	*Model Result*	*Hand Value*	*Units*
Pump Work	$\dot{W}_{\text{pump}} = \dot{m}_{\text{pc}}(\text{h}_{\text{pc,10}} - \text{h}_{\text{pc,9}})$	$\dot{W}_{\text{pump}} = 3.145\ \ (253.3 - 249.0)$	13.53	13.52	kW
Pump Efficiency	$\eta_{\text{pump}} = \frac{\text{h}_{\text{pc,s,10}} - \text{h}_{\text{pc,9}}}{\text{h}_{\text{pc,10}} - \text{h}_{\text{pc,9}}}$	$\eta_{\text{pump}} = \frac{250.5 - 249.0}{253.3 - 249.0}$	0.3564	0.3488	-
Thermal COP	$COP_{\text{TH}} = \frac{\dot{Q}_{\text{evap,w}}}{\dot{Q}_{\text{gen,eg}}}$	$COP_{\text{TH}} = \frac{263.8}{473.0}$	0.5577	0.5577	-
Electrical Equivalent COP	$COP_{\text{EC}} = \frac{\dot{Q}_{\text{evap}}}{\dot{W}_{\text{pump,e}}}$	$COP_{\text{EC}} = \frac{263.8}{13.62}$	19.37	19.37	-
Energy Balance	$EB = 2\frac{\dot{Q}_{\text{gen,eg}} + \dot{Q}_{\text{evap,w}} + \dot{W}_{\text{pump}} - \dot{Q}_{\text{pcond,eg}} - \dot{Q}_{\text{ccond,eg}}}{\dot{Q}_{\text{gen,eg}} + \dot{Q}_{\text{evap,w}} + \dot{W}_{\text{pump}} + \dot{Q}_{\text{pcond,eg}} + \dot{Q}_{\text{ccond,eg}}}$	$EB = 200\frac{473.0 + 263.8 + 13.52 - 435.7 - 291.8}{473.0 + 263.8 + 13.52 + 435.7 + 291.8}$	3.080	3.088	-
Turbine Work	$\dot{W}_{\text{turb}} = \dot{m}_{\text{pc}}(\text{h}_{\text{pc,1}} - \text{h}_{\text{pc,2}})$	$\dot{W}_{\text{turb}} = 3.145\ (437.9 - 422.0)$	50.07	50.01	kW
Turbine Efficiency	$\eta_{\text{turb}} = \frac{\text{h}_{\text{pc,1}} - \text{h}_{\text{pc,2}}}{\text{h}_{\text{pc,1}} - \text{h}_{\text{pc,s,2}}}$	$\eta_{\text{turb}} = \frac{437.9 - 422.0}{437.9 - 417.2}$	0.7670	0.7681	-
Compressor Work	$\dot{W}_{\text{comp}} = \dot{m}_{\text{cc}}(\text{h}_{\text{cc,2}} - \text{h}_{\text{cc,1}})$	$\dot{W}_{\text{comp}} = 1.737\ \ (445.6 - 416.5)$	50.50	50.55	kW
Compressor Efficiency	$\eta_{\text{comp}} = \frac{\text{h}_{\text{cc,s,2}} - \text{h}_{\text{cc,1}}}{\text{h}_{\text{cc,2}} - \text{h}_{\text{cc,1}}}$	$\eta_{\text{comp}} = \frac{441.1 - 416.5}{445.6 - 416.5}$	0.8483	0.8454	-
Shaft Efficiency	$\eta_{\text{shaft}} = \frac{\dot{W}_{\text{comp}}}{\dot{W}_{\text{turb}}}$	$\eta_{\text{shaft}} = \frac{50.50}{50.07}$	1.009	1.009	-
Organic Rankine Cycle Electrical Efficiency	$\eta_{\text{ORC}} = \frac{\dot{W}_{\text{turb}} - \dot{W}_{\text{pump,e}}}{\dot{Q}_{\text{gen,eg}}}$	$\eta_{\text{ORC}} = \frac{50.07 - 13.62}{473.0}$	0.0771	0.0771	-
Vapor Compression Cycle COP	$COP_{\text{VC}} = \frac{\dot{Q}_{\text{evap,w}}}{\dot{W}_{\text{comp}}}$	$COP_{\text{VC}} = \frac{263.8}{50.50}$	5.223	5.224	-

Calculation	*Formulation*	*Hand Calculation*	*Model Result*	*Hand Value*	*Units*
Suction Line Heat Exchanger Heat Transfer	$\dot{Q}_{\text{slhx,cold}} = \dot{m}_{\text{cc}} \left(\text{h}_{\text{cc,17}} - \text{h}_{\text{cc,16}}\right)$	$\dot{Q}_{\text{slhx,cold}} = 1.737 \left(416.5 - 388.5\right)$	48.58	48.64	kW
	$\dot{Q}_{\text{slhx,hot}} = \dot{m}_{\text{cc}} \left(\text{h}_{\text{cc,9}} - \text{h}_{\text{cc,10}}\right)$	$\dot{Q}_{\text{slhx,hot}} = 1.737 \left(250.8 - 233.1\right)$	30.75	30.74	
Recuperator Heat Transfer	$\dot{Q}_{\text{recup,cold}} = \dot{m}_{\text{pc}} \left(\text{h}_{\text{pc,12}} - \text{h}_{\text{pc,11}}\right)$	$\dot{Q}_{\text{recup,cold}} = 3.145 \left(264.6 - 253.4\right)$	35.10	35.22	kW
	$\dot{Q}_{\text{recup,hot}} = \dot{m}_{\text{pc}} \left(\text{h}_{\text{pc,3}} - \text{h}_{\text{pc,4}}\right)$	$\dot{Q}_{\text{recup,hot}} = 3.145 \left(422.1 - 410.5\right)$	36.38	36.48	
Generator Superheated Heat Duty Fraction	$\dot{Q}_{\text{gen,sh,fract}} = \frac{\text{h}_{\text{pc,18}} - \text{h}_{\text{pc,17}}}{\text{h}_{\text{pc,18}} - \text{h}_{\text{pc,15}}}$	$\dot{Q}_{\text{gen,sh,fract}} = \frac{438.3 - 429.8}{438.3 - 279.3}$	0.0531	0.0535	-
Generator Ethylene Glycol-Water Two-Phase/Superheated Transition Temperature	$\dot{Q}_{\text{gen,sh,fract}} = \frac{T_{\text{gen,eg,in}} - T_{\text{gen,eg,tpsh}}}{T_{\text{gen,eg,in}} - T_{\text{gen,eg,out}}}$	$0.0531 = \frac{91.18 - T_{\text{gen,eg,tpsh}}}{91.18 - 86.24}$	90.91	90.92	°C
Generator Superheated Heat Duty	$\dot{Q}_{\text{gen,sh,hot}} = \dot{m}_{\text{gen,eg}} \, Cp_{\text{gen,eg,avg}} \left(T_{\text{gen,eg, in}} - T_{\text{gen,eg,tpsh}}\right)$	$\dot{Q}_{\text{gen,sh,hot}} = 27.23 \; 3.521 \left(91.18 - 90.91\right)$	25.12	25.89	kW
	$\dot{Q}_{\text{gen,sh,cold}} = \dot{m}_{\text{pc}} \left(\text{h}_{\text{pc,18}} - \text{h}_{\text{pc,17}}\right)$	$\dot{Q}_{\text{gen,sh,cold}} = 3.145 \left(438.3 - 429.8\right)$	26.56	26.73	
Generator Subcooled Heat Duty Fraction	$\dot{Q}_{\text{gen,sc,fract}} = \frac{\text{h}_{\text{pc,16}} - \text{h}_{\text{pc,15}}}{\text{h}_{\text{pc,18}} - \text{h}_{\text{pc,15}}}$	$\dot{Q}_{\text{gen,sc,fract}} = \frac{329.2 - 279.3}{438.3 - 279.3}$	0.3143	0.3138	-
Generator Ethylene Glycol-Water Two-Phase/Subcooled Transition Temperature	$\dot{Q}_{\text{gen,sc,fract}} = \frac{T_{\text{gen,eg,tpsc}} - T_{\text{gen,eg,out}}}{T_{\text{gen,eg,in}} - T_{\text{gen,eg,out}}}$	$0.3143 = \frac{T_{\text{gen,eg,tpsc}} - 86.24}{91.18 - 86.24}$	87.79	87.79	°C
Generator Subcooled Heat Duty	$\dot{Q}_{\text{gen,sc,hot}} = \dot{m}_{\text{gen,eg}} \, Cp_{\text{gen,eg,avg}} \left(T_{\text{gen,eg,tpsc}} - T_{\text{gen,eg,in}}\right)$	$\dot{Q}_{\text{gen,sc,hot}} = 27.23 \; 3.521 \left(87.79 - 86.24\right)$	148.7	148.6	kW
	$\dot{Q}_{\text{gen,sc,cold}} = \dot{m}_{\text{pc}} \left(\text{h}_{\text{pc,16}} - \text{h}_{\text{pc,15}}\right)$	$\dot{Q}_{\text{gen,sc,cold}} = 3.145 \left(329.2 - 279.3\right)$	157.2	156.9	

Calculation	*Formulation*	*Hand Calculation*	*Model Result*	*Hand Value*	*Units*
Generator Two-Phase Heat Duty	$\dot{Q}_{\text{gen,tp,hot}} = \dot{m}_{\text{gen,eg}}\, Cp_{\text{gen,eg,avg}}\, (T_{\text{gen,eg,tpsh}} - T_{\text{gen,eg,tpsc}})$	$\dot{Q}_{\text{gen,tp,hot}} = 27.23\ 3.521\ (90.91 - 87.79)$	299.2	299.1	kW
	$\dot{Q}_{\text{gen,tp,cold}} = \dot{m}_{\text{pc}}\, (\text{h}_{\text{pc,17}} - \text{h}_{\text{pc,16}})$	$\dot{Q}_{\text{gen,tp,cold}} = 3.145\ (429.8 - 329.2)$	316.3	316.4	
Generator Pinch Temperature	$T_{\text{gen,pinch}} = T_{\text{gen,eg,tpsc}} - T_{\text{pc,16}}$	$T_{\text{gen,pinch}} = 87.79 - 86.17$	1.62	1.62	°C
Organic Rankine Condenser Superheated Heat Duty Fraction	$\dot{Q}_{\text{pcond,sh,fract}} = \frac{\text{h}_{\text{pc,5}} - \text{h}_{\text{pc,6}}}{\text{h}_{\text{pc,5}} - \text{h}_{\text{pc,8}}}$	$\dot{Q}_{\text{pcond,sh,fract}} = \frac{410.3 - 409.2}{410.3 - 248.8}$	0.0064	0.0068	-
Organic Rankine Condenser Ethylene Glycol-Water Two-Phase/Superheated Transition Temperature	$\dot{Q}_{\text{pcond,sh,fract}} = \frac{T_{\text{pcond,eg,out}} - T_{\text{pcond,eg,tpsh}}}{T_{\text{pcond,eg,out}} - T_{\text{pcond,eg,in}}}$	$0.0064 = \frac{36.58 - T_{\text{pcond,eg,tpsh}}}{36.58 - 29.91}$	36.54	36.54	°C
Organic Rankine Condenser Superheated Heat Duty	$\dot{Q}_{\text{pcond,sh,hot}} = \dot{m}_{\text{pc}}\, (\text{h}_{\text{pc,5}} - \text{h}_{\text{pc,6}})$	$\dot{Q}_{\text{pcond,sh,hot}} = 3.145\ (410.3 - 409.2)$	3.26	3.46	kW
	$\dot{Q}_{\text{pcond,sh,cold}} = \dot{m}_{\text{pcond,eg}}\, Cp_{\text{pcond,eg,avg}}\, (T_{\text{pcond,eg,out}} - T_{\text{pcond,eg,tpsh}})$	$\dot{Q}_{\text{pcond,sh,cold}} = 19.78\ 3.302\ (36.58 - 36.54)$	2.80	2.61	
Organic Rankine Condenser Subcooled Heat Duty Fraction	$\dot{Q}_{\text{pcond,sc,fract}} = \frac{\text{h}_{\text{pc,7}} - \text{h}_{\text{pc8}}}{\text{h}_{\text{pc,5}} - \text{h}_{\text{pc,8}}}$	$\dot{Q}_{\text{pcond,sc,fract}} = \frac{252.3 - 248.8}{410.3 - 248.8}$	0.0214	0.0217	-
Organic Rankine Condenser Ethylene Glycol-Water Two-Phase/Subcooled Transition Temperature	$\dot{Q}_{\text{pcond,sc,fract}} = \frac{T_{\text{pcond,eg,tpsc}} - T_{\text{pcond,eg,in}}}{T_{\text{pcond,eg,out}} - T_{\text{pcond,eg,in}}}$	$0.0214 = \frac{T_{\text{pcond,eg,tpsc}} - 29.91}{36.58 - 29.91}$	30.05	30.05	°C
Organic Rankine Condenser Subcooled Heat Duty	$\dot{Q}_{\text{pcond,sc,hot}} = \dot{m}_{\text{pc}}\, (\text{h}_{\text{pc,7}} - \text{h}_{\text{pc,8}})$	$\dot{Q}_{\text{pcond,sc,hot}} = 3.145\ (252.3 - 248.8)$	10.85	11.01	kW
	$\dot{Q}_{\text{pcond,sc,cold}} = \dot{m}_{\text{pcond,eg}}\, Cp_{\text{pcond,eg,avg}}\, (T_{\text{pcond,eg,tpsc}} - T_{\text{pcond,eg,in}})$	$\dot{Q}_{\text{pcond,sc,cold}} = 19.78\ 3.302\ (30.05 - 29.91)$	9.31	9.14	

Calculation	*Formulation*	*Hand Calculation*	*Model Result*	*Hand Value*	*Units*
Organic Rankine Condenser Two-Phase Heat Duty	$\dot{Q}_{\mathrm{pcond,tp,hot}} = \dot{m}_{\mathrm{pc}} \left(\mathrm{h}_{\mathrm{pc,6}} - \mathrm{h}_{\mathrm{pc,7}}\right)$	$\dot{Q}_{\mathrm{pcond,tp,hot}} = 3.145 \left(409.2 - 252.3\right)$	493.5	493.5	kW
	$\dot{Q}_{\mathrm{pcond,tp,cold}} = \dot{m}_{\mathrm{pcond,eg}} \, Cp_{\mathrm{pcond,eg,avg}} \left(T_{\mathrm{pcond,eg,tpsh}} - T_{\mathrm{pcond,eg,tpsc}}\right)$	$\dot{Q}_{\mathrm{pcond,tp,cold}} = 19.78 \; 3.302 \left(36.54 - 30.05\right)$	423.6	423.9	
Organic Rankine Condenser Pinch Temperature	$T_{\mathrm{pcond,pinch}} = T_{\mathrm{pc,6}} - T_{\mathrm{pcond,eg,tpsh}}$	$T_{\mathrm{pcond,pinch}} = 37.97 - 36.54$	1.43	1.43	°C
Vapor Compression Condenser Superheated Heat Duty Fraction	$\dot{Q}_{\mathrm{ccond,sh,fract}} = \dfrac{\mathrm{h}_{\mathrm{cc,5}} - \mathrm{h}_{\mathrm{cc,6}}}{\mathrm{h}_{\mathrm{cc,5}} - \mathrm{h}_{\mathrm{cc,8}}}$	$\dot{Q}_{\mathrm{ccond,sh,fract}} = \dfrac{419.1 - 409.0}{419.1 - 251.1}$	0.0600	0.0601	-
Vapor Compression Condenser Ethylene Glycol-Water Two-Phase/Superheated Transition Temperature	$\dot{Q}_{\mathrm{ccond,sh,fract}} = \dfrac{T_{\mathrm{ccond,eg,out}} - T_{\mathrm{ccond,eg,tpsh}}}{T_{\mathrm{ccond,eg,out}} - T_{\mathrm{ccond,eg,in}}}$	$0.0600 = \dfrac{36.82 - T_{\mathrm{ccond,eg,tpsh}}}{36.82 - 30.05}$	36.41	36.41	°C
Vapor Compression Condenser Superheated Heat Duty	$\dot{Q}_{\mathrm{ccond,sh,hot}} = \dot{m}_{\mathrm{cc}} \left(\mathrm{h}_{\mathrm{cc,5}} - \mathrm{h}_{\mathrm{cc,6}}\right)$	$\dot{Q}_{\mathrm{ccond,sh,hot}} = 1.737 \left(419.1 - 409.0\right)$	17.51	17.54	kW
	$\dot{Q}_{\mathrm{ccond,sh,cold}} = \dot{m}_{\mathrm{ccond,eg}} \, Cp_{\mathrm{ccond,eg,avg}} \left(T_{\mathrm{ccond,eg,out}} - T_{\mathrm{ccond,eg,tpsh}}\right)$	$\dot{Q}_{\mathrm{ccond,sh,cold}} = 13.05 \; 3.302 \left(36.82 - 36.41\right)$	17.52	17.67	
Vapor Compression Condenser Subcooled Heat Duty Fraction	$\dot{Q}_{\mathrm{ccond,sc,fract}} = \dfrac{\mathrm{h}_{\mathrm{cc,7}} - \mathrm{h}_{\mathrm{cc8}}}{\mathrm{h}_{\mathrm{cc,5}} - \mathrm{h}_{\mathrm{cc,8}}}$	$\dot{Q}_{\mathrm{ccond,sc,fract}} = \dfrac{251.7 - 251.1}{419.1 - 251.1}$	0.0037	0.0036	-
Vapor Compression Condenser Ethylene Glycol-Water Two-Phase/Subcooled Transition Temperature	$\dot{Q}_{\mathrm{ccond,sc,fract}} = \dfrac{T_{\mathrm{ccond,eg,tpsc}} - T_{\mathrm{ccond,eg,in}}}{T_{\mathrm{ccond,eg,out}} - T_{\mathrm{ccond,eg,in}}}$	$0.0037 = \dfrac{T_{\mathrm{ccond,eg,tpsc}} - 30.05}{36.82 - 30.05}$	30.08	30.08	°C
Vapor Compression Condenser Subcooled Heat Duty	$\dot{Q}_{\mathrm{ccond,sc,hot}} = \dot{m}_{\mathrm{cc}} \left(\mathrm{h}_{\mathrm{cc,7}} - \mathrm{h}_{\mathrm{cc,8}}\right)$	$\dot{Q}_{\mathrm{ccond,sc,hot}} = 1.737 \left(251.7 - 251.1\right)$	1.06	1.04	kW
	$\dot{Q}_{\mathrm{ccond,sc,cold}} = \dot{m}_{\mathrm{ccond,eg}} \, Cp_{\mathrm{ccond,eg,avg}} \left(T_{\mathrm{ccond,eg,tpsc}} - T_{\mathrm{ccond,eg,in}}\right)$	$\dot{Q}_{\mathrm{ccond,sc,cold}} = 13.05 \; 3.302 \left(30.08 - 30.05\right)$	1.07	1.29	

Calculation	*Formulation*	*Hand Calculation*	*Model Result*	*Hand Value*	*Units*
Vapor Compression Condenser Two-Phase Heat Duty	$\dot{Q}_{\text{ccond,tp,hot}} = \dot{m}_{\text{cc}}\ (\text{h}_{\text{cc,6}} - \text{h}_{\text{cc,7}})$	$\dot{Q}_{\text{ccond,tp,hot}} = 1.737\ (409.0 - 251.7)$	273.1	273.2	kW
	$\dot{Q}_{\text{ccond,tp,cold}} = \dot{m}_{\text{ccond,eg}}\ Cp_{\text{ccond,eg,avg}}\ (T_{\text{ccond,eg,tpsh}} - T_{\text{ccond,eg,tpsc}})$	$\dot{Q}_{\text{ccond,tp,cold}} = 13.05\ 3.302\ (36.41 - 30.08)$	273.3	272.8	
Vapor Compression Condenser Pinch Temperature	$T_{\text{ccond,pinch}} = T_{\text{cc,6}} - T_{\text{ccond,eg,tpsh}}$	$T_{\text{ccond,pinch}} = 37.56 - 36.41$	1.15	1.15	°C
Evaporator Pinch Temperature	$T_{\text{evap,pinch}} = T_{\text{evap,w,out}} - T_{\text{cc,13}}$	$T_{\text{evap,pinch}} = 6.996 - 6.031$	0.97	0.97	°C
Evaporator Superheated Heat Duty Fraction	$\dot{Q}_{\text{evap,sh,fract}} = \frac{\text{h}_{\text{cc,15}} - \text{h}_{\text{cc,14}}}{\text{h}_{\text{cc,15}} - \text{h}_{\text{cc,13}}}$	$\dot{Q}_{\text{evap,sh,fract}} = \frac{390.1 - 388.5}{390.1 - 233.1}$	0.0099	0.0102	-
Evaporator Water Two-Phase/Superheated Transition Temperature	$\dot{Q}_{\text{evap,sh,fract}} = \frac{T_{\text{evap,w,in}} - T_{\text{evap,w,tpsh}}}{T_{\text{evap,w,in}} - T_{\text{evap,w,out}}}$	$0.0099 = \frac{12.12 - T_{\text{evap,w,tpsh}}}{12.12 - 6.996}$	12.07	12.07	°C
Evaporator Superheated Heat Duty	$\dot{Q}_{\text{evap,sh,hot}} = \dot{m}_{\text{evap,w}}\ Cp_{\text{evap,w,avg}}\ (T_{\text{evap,w, in}} - T_{\text{evap,w,tpsh}})$	$\dot{Q}_{\text{evap,sh,hot}} = 12.27\ 4.194\ (12.12 - 12.07)$	2.61	2.57	kW
	$\dot{Q}_{\text{evap,sh,cold}} = \dot{m}_{\text{cc}}\ (\text{h}_{\text{cc,15}} - \text{h}_{\text{cc,14}})$	$\dot{Q}_{\text{ccond,sh,cold}} = 1.737\ (390.1 - 388.5)$	2.69	2.78	
Evaporator Two-Phase Heat Duty	$\dot{Q}_{\text{evap,tp,hot}} = \dot{m}_{\text{evap,w}}\ Cp_{\text{evap,w,avg}}\ (T_{\text{evap,w,tpsh}} - T_{\text{evap,w,in}})$	$\dot{Q}_{\text{evap,tp,hot}} = 12.27\ 4.194\ (12.07 - 6.996)$	261.2	261.1	kW
	$\dot{Q}_{\text{evap,tp,cold}} = \dot{m}_{\text{cc}}\ (\text{h}_{\text{cc,14}} - \text{h}_{\text{cc,13}})$	$\dot{Q}_{\text{evap,tp,cold}} = 1.737\ (388.5 - 233.1)$	270.0	269.9	
Turbine Inlet Velocity	$\vec{V}_{\text{turb,in}} = \frac{\dot{m}_{\text{pc}}}{\rho_{\text{turb,in}}\ A_{\text{turb,in}}}$	$\vec{V}_{\text{turb,in}} = \frac{3.145}{129.5\ 0.002168}$	11.20	11.20	$m\ s^{-1}$
Turbine Outlet Velocity	$\vec{V}_{\text{turb,out}} = \frac{\dot{m}_{\text{pc}}}{\rho_{\text{turb,out}}\ A_{\text{turb,out}}}$	$\vec{V}_{\text{turb,out}} = \frac{3.145}{36.85\ 0.008213}$	10.39	10.39	$m\ s^{-1}$

Calculation	*Formulation*	*Hand Calculation*	*Model Result*	*Hand Value*	*Units*
Turbine Isentropic Outlet Velocity	$\vec{V}_{\text{turb,out,s}} = \frac{\dot{m}_{\text{pc}}}{\rho_{\text{turb,out,s}}\, A_{\text{turb,out}}}$	$\vec{V}_{\text{turb,out,s}} = \frac{3.145}{37.79\ 0.008213}$	10.13	10.13	$m\ s^{-1}$
Turbine Inlet Total Pressure	$P_{\text{turb,in,o}} = P_{\text{turb,in}} + \frac{\rho_{\text{turb,in}}\, \vec{V}^2_{\text{turb,in}}}{2000}$	$P_{\text{turb,in,o}} = 2241 + \frac{129.5\ 11.20^2}{2000}$	2249	2249	kPa
Turbine Outlet Total Pressure	$P_{\text{turb,out,o}} = P_{\text{turb,out}} + \frac{\rho_{\text{turb,out}}\, \vec{V}^2_{\text{turb,out}}}{2000}$	$P_{\text{turb,out,o}} = 743.3 + \frac{36.85\ 10.39^2}{2000}$	745.3	745.3	kPa
Turbine Inlet Total Temperature	$T_{\text{turb,in,o}} = T_{\text{turb,in}} + \frac{\vec{V}^2_{\text{turb,in}}}{2000\ Cp_{\text{turb,in}}}$	$T_{\text{turb,in,o}} = 90.22 + \frac{11.20^2}{2000\ 1.541}$	90.26	90.26	°C
Turbine Outlet Total Temperature	$T_{\text{turb,out,o}} = T_{\text{turb,out}} + \frac{\vec{V}^2_{\text{turb,out}}}{2000\ Cp_{\text{turb,out}}}$	$T_{\text{turb,out,o}} = 50.45 + \frac{10.39^2}{2000\ 1.047}$	50.50	50.50	°C
Total Turbine Inlet Enthalpy	$\text{h}_{\text{turb,in,o}} = \text{h}_{\text{turb,in}} + \frac{\vec{V}^2_{\text{turb,in}}}{2000}$	$\text{h}_{\text{turb,in,o}} = 437.9 + \frac{11.22^2}{2000}$	438.0	438.0	$kJ\ kg^{-1}$
Total Turbine Outlet Enthalpy	$\text{h}_{\text{turb,out,o}} = \text{h}_{\text{turb,out}} + \frac{\vec{V}^2_{\text{turb,out}}}{2000}$	$\text{h}_{\text{turb,out,o}} = 422.0 + \frac{10.39^2}{2000}$	422.1	422.1	$kJ\ kg^{-1}$
Total Turbine Isentropic Outlet Enthalpy	$\text{h}_{\text{turb,out,s,o}} = \text{h}_{\text{turb,out,s}} + \frac{\vec{V}^2_{\text{turb,out,s}}}{2000}$	$\text{h}_{\text{turb,out,s,o}} = 417.2 + \frac{10.13^2}{2000}$	417.2	417.2	$kJ\ kg^{-1}$
Total to Total Turbine Work	$\dot{W}_{\text{turb,tt}} = \dot{m}_{\text{pc}}(\text{h}_{\text{turb,in,o}} - \text{h}_{\text{turb,out,o}})$	$\dot{W}_{\text{turb,tt}} = 3.145\ (438.0 - 422.1)$	50.10	50.01	kW
Total to Total Turbine Efficiency	$\eta_{\text{turb,tt}} = \frac{\text{h}_{\text{turb,in,o}} - \text{h}_{\text{turb,out,o}}}{\text{h}_{\text{turb,in,o}} - \text{h}_{\text{turb,out,s,o}}}$	$\eta_{\text{turb,tt}} = \frac{438.0 - 422.1}{438.0 - 417.2}$	0.7670	0.7644	-
Total to Static Turbine Efficiency	$\eta_{\text{turb,ts}} = \frac{\text{h}_{\text{turb,in,o}} - \text{h}_{\text{turb,out}}}{\text{h}_{\text{turb,in,o}} - \text{h}_{\text{turb,out,s}}}$	$\eta_{\text{turb,ts}} = \frac{438.0 - 422.0}{438.0 - 417.2}$	0.7677	0.7692	-
Compressor Inlet Velocity	$\vec{V}_{\text{comp,in}} = \frac{\dot{m}_{\text{cc}}}{\rho_{\text{comp,in}}\, A_{\text{comp,in}}}$	$\vec{V}_{\text{comp,in}} = \frac{1.737}{11.46\ 0.008213}$	18.45	18.45	$m\ s^{-1}$

Calculation	*Formulation*	*Hand Calculation*	*Model Result*	*Hand Value*	*Units*
Compressor Outlet Velocity	$\vec{V}_{\text{comp,out}} = \frac{\dot{m}_{\text{cc}}}{\rho_{\text{comp,out}} A_{\text{comp,out}}}$	$\vec{V}_{\text{comp,out}} = \frac{1.737}{33.90\ 0.008213}$	6.237	6.239	$m\ s^{-1}$
Compressor Isentropic Outlet Velocity	$\vec{V}_{\text{comp,out,s}} = \frac{\dot{m}_{\text{cc}}}{\rho_{\text{comp,out,s}} A_{\text{comp,out}}}$	$\vec{V}_{\text{comp,out,s}} = \frac{1.737}{34.54\ 0.008213}$	6.122	6.123	$m\ s^{-1}$
Compressor Inlet Total Pressure	$P_{\text{comp,in,o}} = P_{\text{comp,in}} + \frac{\rho_{\text{comp,in}} \vec{V}^2_{\text{comp,in}}}{2000}$	$P_{\text{comp,in,o}} = 244.6 + \frac{11.46\ 18.45^2}{2000}$	246.6	246.6	kPa
Compressor Outlet Total Pressure	$P_{\text{comp,out,o}} = P_{\text{comp,out}} + \frac{\rho_{\text{comp,out}} \vec{V}^2_{\text{comp,out}}}{2000}$	$P_{\text{comp,out,o}} = 759.5 + \frac{33.90\ 6.237^2}{2000}$	760.2	760.2	kPa
Compressor Inlet Total Temperature	$T_{\text{comp,in,o}} = T_{\text{comp,in}} + \frac{\vec{V}^2_{\text{comp,in}}}{2000\ Cp_{\text{comp,in}}}$	$T_{\text{comp,in,o}} = 35.69 + \frac{18.45^2}{2000\ 0.9363}$	35.87	35.87	°C
Compressor Outlet Total Temperature	$T_{\text{comp,out,o}} = T_{\text{comp,out}} + \frac{\vec{V}^2_{\text{comp,out}}}{2000\ Cp_{\text{comp,out}}}$	$T_{\text{comp,out,o}} = 73.29 + \frac{6.237^2}{2000\ 1.043}$	73.31	73.31	°C
Total Compressor Inlet Enthalpy	$\text{h}_{\text{comp,in,o}} = \text{h}_{\text{comp,in}} + \frac{\vec{V}^2_{\text{comp,in}}}{2000}$	$\text{h}_{\text{comp,in,o}} = 416.5 + \frac{18.45^2}{2000}$	416.6	416.7	$kJ\ kg^{-1}$
Total Compressor Outlet Enthalpy	$\text{h}_{\text{comp,out,o}} = \text{h}_{\text{comp,out}} + \frac{\vec{V}^2_{\text{comp,out}}}{2000}$	$\text{h}_{\text{comp,out,o}} = 445.6 + \frac{6.237^2}{2000}$	445.6	445.6	$kJ\ kg^{-1}$
Total Compressor Isentropic Outlet Enthalpy	$\text{h}_{\text{comp,out,s,o}} = \text{h}_{\text{comp,out,s}} + \frac{\vec{V}^2_{\text{comp,out,s}}}{2000}$	$\text{h}_{\text{comp,out,s,o}} = 441.1 + \frac{6.122^2}{2000}$	441.2	441.1	$kJ\ kg^{-1}$
Total to Total Compressor Work	$\dot{W}_{\text{comp,tt}} = \dot{m}_{\text{cc}}(\text{h}_{\text{comp,out,o}} - \text{h}_{\text{comp,in,o}})$	$\dot{W}_{\text{comp,tt}} = 1.737\ (445.6 - 416.6)$	50.24	50.37	kW
Total to Total Compressor Efficiency	$\eta_{\text{comp,tt}} = \frac{\text{h}_{\text{comp,out,s,o}} - \text{h}_{\text{comp,in,o}}}{\text{h}_{\text{comp,out,o}} - \text{h}_{\text{comp,in,o}}}$	$\eta_{\text{comp,tt}} = \frac{441.2 - 416.6}{445.6 - 416.6}$	0.8475	0.8483	-
Total to Total Shaft Efficiency	$\eta_{\text{shaft,tt}} = \frac{\dot{W}_{\text{comp,oo}}}{\dot{W}_{\text{turb,oo}}}$	$\eta_{\text{shaft,tt}} = \frac{50.24}{50.10}$	0.1003	0.1003	-

Calculation	*Formulation*	*Hand Calculation*	*Model Result*	*Hand Value*	*Units*
Pump Inlet Velocity	$\vec{V}_{\text{pump,in}} = \frac{\dot{m}_{\text{pc}}}{\rho_{\text{pump,in}}\, A_{\text{pump,in}}}$	$\vec{V}_{\text{pump,in}} = \frac{3.145}{1127.5\ 0.004768}$	0.5850	0.5850	m s^{-1}
Pump Outlet Velocity	$\vec{V}_{\text{pump,out}} = \frac{\dot{m}_{\text{pc}}}{\rho_{\text{pump,out}}\, A_{\text{pump,out}}}$	$\vec{V}_{\text{pump,out}} = \frac{3.145}{1127.9\ 0.001316}$	2.118	2.119	m s^{-1}
Pump Isentropic Outlet Velocity	$\vec{V}_{\text{pump,out,s}} = \frac{\dot{m}_{\text{pc}}}{\rho_{\text{pump,out,s}}\, A_{\text{pump,out}}}$	$\vec{V}_{\text{pump,out,s}} = \frac{3.145}{1134.7\ 0.001316}$	2.106	2.106	m s^{-1}
Pump Inlet Total Pressure	$P_{\text{pump,in,o}} = P_{\text{pump,in}} + \frac{\rho_{\text{pump,in}}\, \vec{V}^2_{\text{pump,in}}}{2000}$	$P_{\text{pump,in,o}} = 724.6 + \frac{1127.5\ 0.5850^2}{2000}$	724.8	724.8	kPa
Pump Outlet Total Pressure	$P_{\text{pump,out,o}} = P_{\text{pump,out}} + \frac{\rho_{\text{pump,out}}\, \vec{V}^2_{\text{pump,out}}}{2000}$	$P_{\text{pump,out,o}} = 2459 + \frac{1127.9\ 2.118^2}{2000}$	2462	2462	kPa
Pump Inlet Total Temperature	$T_{\text{pump,in,o}} = T_{\text{pump,in}} + \frac{\vec{V}^2_{\text{pump,in}}}{2000\ Cp_{\text{pump,in}}}$	$T_{\text{pump,in,o}} = 35.36 + \frac{0.5850^2}{2000\ 1.437}$	35.36	35.36	°C
Pump Outlet Total Temperature	$T_{\text{pump,out,o}} = T_{\text{pump,out}} + \frac{\vec{V}^2_{\text{pump,out}}}{2000\ Cp_{\text{pump,out}}}$	$T_{\text{pump,out,o}} = 38.34 + \frac{2.118^2}{2000\ 1.427}$	38.35	38.34	°C
Total Pump Inlet Enthalpy	$\text{h}_{\text{pump,in,o}} = \text{h}_{\text{pump,in}} + \frac{\vec{V}^2_{\text{pump,in}}}{2000}$	$\text{h}_{\text{pump,in,o}} = 249.0 + \frac{0.5850^2}{2000}$	249.0	249.0	kJ kg^{-1}
Total Pump Outlet Enthalpy	$\text{h}_{\text{pump,out,o}} = \text{h}_{\text{pump,out}} + \frac{\vec{V}^2_{\text{pump,out}}}{2000}$	$\text{h}_{\text{pump,out,o}} = 253.3 + \frac{2.118^2}{2000}$	253.3	253.3	kJ kg^{-1}
Total Pump Isentropic Outlet Enthalpy	$\text{h}_{\text{pump,out,s,o}} = \text{h}_{\text{pump,out,s}} + \frac{\vec{V}^2_{\text{pump,out,s}}}{2000}$	$\text{h}_{\text{pump,out,s,o}} = 250.5 + \frac{2.106^2}{2000}$	250.5	250.5	kJ kg^{-1}
Total to Total Pump Work	$\dot{W}_{\text{pump,tt}} = \dot{m}_{\text{pc}}(\text{h}_{\text{pump,out,o}} - \text{h}_{\text{pump,in,o}})$	$\dot{W}_{\text{pump,tt}} = 3.145\ (253.3 - 249.0)$	13.54	13.52	kW
Total to Total Pump Efficiency	$\eta_{\text{pump,tt}} = \frac{\text{h}_{\text{pump,out,s,o}} - \text{h}_{\text{pump,in,o}}}{\text{h}_{\text{pump,out,o}} - \text{h}_{\text{pump,in,o}}}$	$\eta_{\text{pump,tt}} = \frac{250.5 - 249.0}{253.3 - 249.0}$	0.3567	0.3488	-

Calculation	*Formulation*	*Hand Calculation*	*Model Result*	*Hand Value*	*Units*
Compressor Critical Velocity Reference	$\vec{V}_{\text{crit,comp,ref}} = \sqrt{\frac{2\,\gamma_{\text{comp,ref}}}{\gamma_{\text{comp,ref}}+1} G\, Z_{\text{comp,ref}}\, R_{\text{comp,ref}}\, TA_{\text{comp,in,o,ref}}}$	$\vec{V}_{\text{crit,comp,ref}} = \sqrt{\frac{2\,1.115}{1.115+1} 9.81\ 0.9415\ 72.91\ 307.19}$	467.1	467.0	$m\ s^{-1}$
Compressor Critical Velocity Actual	$\vec{V}_{\text{crit,comp,test}} = \sqrt{\frac{2\,\gamma_{\text{comp,test}}}{\gamma_{\text{comp,test}}+1} G\, Z_{\text{comp,test}}\, R_{\text{comp,test}}\, TA_{\text{comp,in,o,test}}}$	$\vec{V}_{\text{crit,comp,test}} = \sqrt{\frac{2\,1.112}{1.112+1} 9.81\ 0.9480\ 72.91\ 309.02}$	469.7	469.7	$m\ s^{-1}$
Epsilon Compressor	$\psi_{\text{comp}} = \frac{\gamma_{\text{comp,ref}} \left(\frac{2}{\gamma_{\text{comp,ref}}+1}\right)^{\frac{\gamma_{\text{comp,ref}}}{\gamma_{\text{comp,ref}}-1}}}{\gamma_{\text{comp,test}} \left(\frac{2}{\gamma_{\text{comp,test}}+1}\right)^{\frac{\gamma_{\text{comp,test}}}{\gamma_{\text{comp,test}}-1}}}$	$\psi_{\text{comp}} = \frac{1.115 \left(\frac{2}{1.115+1}\right)^{\frac{1.115}{1.115-1}}}{1.112 \left(\frac{2}{1.112+1}\right)^{\frac{1.112}{1.112-1}}}$	1.002	1.002	-
Theta Compressor	$\theta_{\text{comp}} = \left(\frac{\vec{V}_{\text{crit,comp,test}}}{\vec{V}_{\text{crit,comp,ref}}}\right)^2$	$\theta_{\text{comp}} = \left(\frac{469.7}{467.1}\right)^2$	1.011	1.011	-
Del Compressor	$\delta_{\text{comp}} = \frac{P_{\text{comp,in,o,test}}}{P_{\text{comp,in,o,ref}}}$	$\delta_{\text{comp}} = \frac{246.6}{270.0}$	0.9132	0.9133	-
Equivalent Compressor Speed	$\omega_{\text{cor,comp}} = \frac{\omega_{\text{comp}}}{\sqrt{\theta_{\text{comp}}}}$	$\omega_{\text{cor,comp}} = \frac{31.472}{\sqrt{1.011}}$	31.297	31.300	kRPM
Equivalent Compressor Mass Flow	$\dot{m}_{\text{cor,comp}} = \frac{\dot{m}_{\text{comp,test}} \sqrt{\theta_{\text{comp}}} \psi_{\text{comp}}}{\delta_{\text{comp}}}$	$\dot{m}_{\text{cor,comp}} = \frac{1.737 \sqrt{1.011}\ 1.002}{0.9132}$	1.916	1.916	$kg\ s^{-1}$
Equivalent Ideal Compressor Enthalpy Difference	$\Delta h_{\text{s,eq,comp,o}} = \frac{\Delta h_{\text{s,comp,o}}}{\theta_{\text{comp}}}$	$\Delta h_{\text{s,eq,comp,o}} = \frac{441.2 - 416.6}{1.011}$	24.25	24.33	$kJ\ kg^{-1}$
Turbine Critical Velocity Reference	$\vec{V}_{\text{crit,turb,ref}} = \sqrt{\frac{2\,\gamma_{\text{turb,ref}}}{\gamma_{\text{turb,ref}}+1} G\, Z_{\text{turb,ref}}\, R_{\text{turb,ref}}\, TA_{\text{turb,in,o,ref}}}$	$\vec{V}_{\text{crit,turb,ref}} = \sqrt{\frac{2\,1.426}{1.426+1} 9.81\ 0.6762\ 72.91\ 364.08}$	455.0	455.0	$m\ s^{-1}$
Turbine Critical Velocity Actual	$\vec{V}_{\text{crit,turb,test}} = \sqrt{\frac{2\,\gamma_{\text{turb,test}}}{\gamma_{\text{turb,test}}+1} G\, Z_{\text{turb,test}}\, R_{\text{turb,test}}\, TA_{\text{turb,in,o,test}}}$	$\vec{V}_{\text{crit,turb,test}} = \sqrt{\frac{2\,1.504}{1.504+1} 9.81\ 0.6513\ 72.91\ 363.41}$	451.0	451.1	$m\ s^{-1}$

Calculation	*Formulation*	*Hand Calculation*	*Model Result*	*Hand Value*	*Units*
Epsilon Turbine	$\psi_{\text{turb}} = \frac{\gamma_{\text{turb,ref}} \left(\frac{2}{\gamma_{\text{turb,ref}}+1}\right)^{\frac{\gamma_{\text{turb,ref}}}{\gamma_{\text{turb,ref}}-1}}}{\gamma_{\text{turb,test}} \left(\frac{2}{\gamma_{\text{turb,test}}+1}\right)^{\frac{\gamma_{\text{turb,test}}}{\gamma_{\text{turb,test}}-1}}}$	$\psi_{\text{turb}} = \frac{1.426 \left(\frac{2}{1.426+1}\right)^{\frac{1.426}{1.426-1}}}{1.504 \left(\frac{2}{1.504+1}\right)^{\frac{1.504}{1.504-1}}}$	0.9714	0.9714	-
Theta Turbine	$\theta_{\text{turb}} = \left(\frac{\vec{V}_{\text{crit,turb,test}}}{\vec{V}_{\text{crit,turb,ref}}}\right)^2$	$\theta_{\text{turb}} = \left(\frac{451.0}{455.0}\right)^2$	0.9824	0.9825	-
Del Turbine	$\delta_{\text{turb}} = \frac{P_{\text{turb,in,o,test}}}{P_{\text{turb,in,o,ref}}}$	$\delta_{\text{turb}} = \frac{2249}{2160}$	1.041	1.041	-
Equivalent Turbine Speed	$\omega_{\text{cor,turb}} = \frac{\omega_{\text{turb}}}{\sqrt{\theta_{\text{comp}}}}$	$\omega_{\text{cor,turb}} = \frac{31.472}{\sqrt{0.9825}}$	31.752	31.751	kRPM
Equivalent Turbine Mass Flow	$\dot{m}_{\text{cor,turb}} = \frac{\dot{m}_{\text{turb,test,adj}} \sqrt{\theta_{\text{turb}}} \psi_{\text{turb}}}{\delta_{\text{turb}}\ \omega_{\text{cor,turb}}}$	$\dot{m}_{\text{cor,turb}} = \frac{6.933\sqrt{0.9824}\ 0.9714}{1.041\ 31.752}$	0.2019	0.2019	kg s^{-1}
Equivalent Ideal Turbine Enthalpy Difference	$\Delta h_{\text{s,eq,turb,o}} = \frac{\Delta h_{\text{s,turb,o}}}{\theta_{\text{turb}}}$	$\Delta h_{\text{s,eq,turb,o}} = \frac{438.0 - 417.2}{0.9825}$	21.14	21.17	kJ kg^{-1}
Range Temperature Difference Generator	$T_{\text{range,gen}} = \lvert T_{\text{gen,eg,in}} - T_{\text{gen,eg,out}} \rvert$	$T_{\text{range,gen}} = \lvert 91.18 - 86.24 \rvert$	4.93	4.94	°C
Small Temperature Difference Generator	$T_{\text{small,gen}} = \lvert T_{\text{gen,r,sat}} - T_{\text{gen,eg,out}} \rvert$	$T_{\text{small,gen}} = \lvert 86.05 - 86.24 \rvert$	0.20	0.19	°C
Fouling LMTD Generator	$T_{\text{LMTD,gen}} = \frac{T_{\text{range,gen,}}}{\ln\left(1 + \frac{T_{\text{range,gen}}}{T_{\text{small,gen}}}\right)}$	$T_{\text{LMTD,gen}} = \frac{4.93}{\ln\left(1 + \frac{4.93}{0.20}\right)}$	1.51	1.52	°C
Fouling ILMTD Generator	$T_{\text{ILMTD,gen}} = FP_{\text{gen}} \frac{\dot{Q}_{\text{gen,eg}}}{A_{\text{gen,ext}}}$	$T_{\text{ILMTD,gen}} = 0.018 \frac{473.0}{77.63}$	0.11	0.11	°C
Generator Fouling Coefficient	$FC_{\text{gen}} = \frac{T_{\text{range,gen}}}{T_{\text{LMTD,gen}} - T_{\text{ILMTD,gen}}}$	$FC_{\text{gen}} = \frac{4.93}{1.51 - 0.11}$	3.52	3.52	-
Small Clean Temperature Difference Generator	$T_{\text{clean,gen}} = \frac{T_{\text{range,gen}}}{e^{FC_{\text{gen}}} - 1}$	$T_{\text{clean,gen}} = \frac{4.93}{e^{3.52} - 1}$	0.15	0.15	°C

Calculation	*Formulation*	*Hand Calculation*	*Model Result*	*Hand Value*	*Units*
Generator Adjusted Temperature	$T_{\text{gen,adj}} = T_{\text{small,gen}} - T_{\text{clean,gen}}$	$T_{\text{gen,adj}} = 0.20 - 0.15$	0.05	0.05	°C
Range Temperature Difference Evaporator	$T_{\text{range,evap}} = \lvert T_{\text{evap,w,in}} - T_{\text{evap,w,out}} \rvert$	$T_{\text{range,evap}} = \lvert 12.12 - 6.996 \rvert$	5.12	5.12	°C
Small Temperature Difference Evaporator	$T_{\text{small,evap}} = \lvert T_{\text{evap,r,sat}} - T_{\text{evap,w,out}} \rvert$	$T_{\text{small,evap}} = \lvert 6.031 - 6.996 \rvert$	0.96	0.97	°C
Fouling LMTD Evaporator	$T_{\text{LMTD,evap}} = \frac{T_{\text{range,evap}}}{\ln\left(1 + \frac{T_{\text{range,evap}}}{T_{\text{small,evap}}}\right)}$	$T_{\text{LMTD,evap}} = \frac{5.12}{\ln\left(1 + \frac{5.12}{0.96}\right)}$	2.78	2.77	°C
Fouling ILMTD Evaporator	$T_{\text{ILMTD,evap}} = FP_{\text{evap}} \frac{\dot{Q}_{\text{evap,w}}}{A_{\text{evap,ext}}}$	$T_{\text{ILMTD,evap}} = 0.018 \frac{263.8}{18.97}$	0.25	0.25	°C
Evaporator Fouling Coefficient	$FC_{\text{evap}} = \frac{T_{\text{range,evap}}}{T_{\text{LMTD,evap}} - T_{\text{ILMTD,evap}}}$	$FC_{\text{evap}} = \frac{5.12}{2.78 - 0.25}$	2.02	2.02	-
Small Clean Temperature Difference Evaporator	$T_{\text{clean,evap}} = \frac{T_{\text{range,evap}}}{e^{FC_{\text{evap}}} - 1}$	$T_{\text{clean,evap}} = \frac{5.12}{e^{2.02} - 1}$	0.78	0.78	°C
Evaporator Adjusted Temperature	$T_{\text{evap,adj}} = T_{\text{small,evap}} - T_{\text{clean,evap}}$	$T_{\text{evap,adj}} = 0.96 - 0.78$	0.19	0.18	°C
Range Temperature Difference Power Condenser	$T_{\text{range,pcond}} = \lvert T_{\text{pcond,eg,in}} - T_{\text{pcond,eg,out}} \rvert$	$T_{\text{range,pcond}} = \lvert 29.91 - 36.58 \rvert$	6.67	6.67	°C
Small Temperature Difference Power Condenser	$T_{\text{small,pcond}} = \lvert T_{\text{pcond,r,sat}} - T_{\text{pcond,eg,out}} \rvert$	$T_{\text{small,pcond}} = \lvert 37.81 - 36.58 \rvert$	1.23	1.23	°C
Fouling LMTD Power Condenser	$T_{\text{LMTD,pcond}} = \frac{T_{\text{range,pcond}}}{\ln\left(1 + \frac{T_{\text{range,pcond}}}{T_{\text{small,pcond}}}\right)}$	$T_{\text{LMTD,pcond}} = \frac{6.67}{\ln\left(1 + \frac{6.67}{1.23}\right)}$	3.59	3.59	°C
Fouling ILMTD Power Condenser	$T_{\text{ILMTD,pcond}} = FP_{\text{pcond}} \frac{\dot{Q}_{\text{pcond,eg}}}{A_{\text{pcond,ext}}}$	$T_{\text{ILMTD,pcond}} = 0.044 \frac{435.7}{42.62}$	0.45	0.45	°C

Calculation	*Formulation*	*Hand Calculation*	*Model Result*	*Hand Value*	*Units*
Power Condenser Fouling Coefficient	$FC_{\text{pcond}} = \frac{T_{\text{range,pcond}}}{T_{\text{LMTD,pcond}} - T_{\text{ILMTD,pcond}}}$	$FC_{\text{pcond}} = \frac{6.67}{3.59 - 0.45}$	2.12	2.12	-
Small Clean Temperature Difference Power Condenser	$T_{\text{clean,pcond}} = \frac{T_{\text{range,pcond}}}{e^{FC_{\text{pcond}}} - 1}$	$T_{\text{clean,pcond}} = \frac{6.67}{e^{2.12} - 1}$	0.91	0.91	°C
Power Condenser Adjusted Temperature	$T_{\text{pcond,adj}} = T_{\text{small,pcond}} - T_{\text{clean,pcond}}$	$T_{\text{pcond,adj}} = 1.23 - 0.91$	0.33	0.32	°C
Range Temperature Difference Cooling Condenser	$T_{\text{range,ccond}} = \lvert T_{\text{ccond,eg,in}} - T_{\text{ccond,eg,out}} \rvert$	$T_{\text{range,ccond}} = \lvert 30.05 - 36.82 \rvert$	6.77	6.77	°C
Small Temperature Difference Cooling Condenser	$T_{\text{small,ccond}} = \lvert T_{\text{ccond,r,sat}} - T_{\text{ccond,eg,out}} \rvert$	$T_{\text{small,ccond}} = \lvert 37.41 - 36.82 \rvert$	0.59	0.59	°C
Fouling LMTD Cooling Condenser	$T_{\text{LMTD,ccond}} = \frac{T_{\text{range,ccond}}}{\ln\left(1 + \frac{T_{\text{range,ccond}}}{T_{\text{small,ccond}}}\right)}$	$T_{\text{LMTD,ccond}} = \frac{6.77}{\ln\left(1 + \frac{6.77}{0.59}\right)}$	2.69	2.68	°C
Fouling ILMTD Cooling Condenser	$T_{\text{ILMTD,ccond}} = FP_{\text{ccond}} \frac{\dot{Q}_{\text{ccond,eg}}}{A_{\text{ccond,ext}}}$	$T_{\text{ILMTD,ccond}} = 0.044 \frac{291.8}{28.30}$	0.45	0.45	°C
Cooling Condenser Fouling Coefficient	$FC_{\text{ccond}} = \frac{T_{\text{range,ccond}}}{T_{\text{LMTD,ccond}} - T_{\text{ILMTD,ccond}}}$	$FC_{\text{ccond}} = \frac{6.77}{2.69 - 0.45}$	3.03	3.02	-
Small Clean Temperature Difference Cooling Condenser	$T_{\text{clean,ccond}} = \frac{T_{\text{range,ccond}}}{e^{FC_{\text{ccond}}} - 1}$	$T_{\text{clean,ccond}} = \frac{6.77}{e^{3.03} - 1}$	0.34	0.34	°C
Cooling Condenser Adjusted Temperature	$T_{\text{ccond,adj}} = T_{\text{small,ccond}} - T_{\text{clean,ccond}}$	$T_{\text{ccond,adj}} = 0.59 - 0.34$	0.25	0.25	°C